POINT OF CARE DIAGNOSTICS FOR TRAUMATIC BRAIN INJURY

By

CARL BANBURY

A thesis submitted to
the University of Birmingham
for the degree of
DOCTOR OF PHILOSOPHY

Advanced Nano-Materials Structures and Applications Group
School of Chemical Engineering
College of Engineering and Physical Sciences
University of Birmingham
Jul 2020

ABSTRACT

Traumatic brain injury (TBI) is a major burden on healthcare services worldwide, which currently lacks an effective method for point-of-care (PoC) diagnostics and monitoring. In this thesis, the prospect of using Raman spectroscopy, as a non-invasive means to measure chemical changes indicative of TBI from the back of the eye is explored. Through the development of multivariate analysis methods, self-organising maps are highlighted as a superior alternative to principal component analysis and are successfully used to introduce a new means of classification. A classification accuracy of > 93 % is demonstrated over five tissue types applied to anatomical layers of ocular porcine eyes. Subsequently, in a clinically relevant murine model of TBI, an ability to accurately identify TBI and injury severity from Raman spectra of the retina is demonstrated for the first time. Using feature extraction, intrinsically linked to the classification result, the findings are associated with a decrease in cardiolipin linked to metabolic distress, which is a hallmark of TBI. Finally, in an effort to translate the technology, a (patent pending) handheld system has been developed. Simultaneously, fundus photography is combined with eye safe Raman spectroscopy, measuring high wavenumber bands from a three-dimensional printed tissue phantom of the undilated human eye.

ACKNOWLEDGEMENTS

The work in this thesis was carried out in the Advanced Nano-Materials Structures and Applications (ANMSA) group, led by Dr. Pola Goldberg Oppenheimer and as part of the EPSRC Sci-Phy-4-Health Centre for Doctoral Training studentship (EP/L016346/1). I would like to begin by thanking everyone that has been involved in the Sci-Phy centre. The diversity of expertise, personalities, equipment and open doors that have been available throughout the programme will be sorely missed. I would like to take the opportunity to thank each of my supervisors: Dr. Pola Goldberg Oppenheimer, Prof. Iain Styles, Mr. Neil Eisenstein, Prof. Ann Logan and Prof. Antonio Belli.

As my primary supervisor, Dr. Goldberg Oppenheimer has energetically provided inspiration and support from the very first year of the programme. The ANMSA group has provided a dynamic and engaging environment to work in, within the broader community of Chemical Engineering at the University of Birmingham. The group promotes freedom of ideas and creativity, whilst holding each other to account. Dr. Goldberg Oppenheimer does this with a level of ease that often seems to go unnoticed, but has always been appreciated.

As my computational supervisor, I thank Prof. Iain Styles for his unwavering patience and logical approach. Throughout the project, interactions with Prof. Styles have been a comforting reminder to the world I know, as I've explored new scientific disciplines. For each of my clinical supervisors, Mr. Neil Eisenstein, Prof. Ann Logan and Prof. Antonio Belli I am thankful for the glimpse into their world, which is as far removed from my prior

experience in tech startups as I can imagine. Having such a broad range of supervisors for this project has been essential to steer through a maze of multidisciplinary boundaries.

Within each supervisor's research groups, there have been those that took the time to introduce this software engineer to totally alien fields and environments. To this end, I am especially grateful to Dr. JJ Rickard, Dr. Georgios Gkotsis, Dr. Chiara Busà, Lt. Col. Richard Blanch and Dr. Chloe Thomas. Thank you to Dr. Paolo Passaretti, Mr. Paulo De Carvalho Gomes, Dr. Martin Chu, Dr. Mike Hardy and Dr. Liam Kelleher for proof reading sections of this thesis. Finally, I would like to make a special mention to Dr. Michael Clancy, for sharing several moments of frustration and confusion in the laboratory alongside endless cups of coffee. Thank you all!

CONTENTS LISTINGS

- List of papers and abstracts
- Contents
- List of figures
- List of tables
- List of abbreviations

LIST OF PAPERS AND ABSTRACTS

The following three papers and patent application form the basis of this thesis:

- **Banbury C.**, Mason R., Styles I., Eisenstein N., Clancy M., Belli A., Logan A. and Goldberg Oppenheimer P. [2019], 'Development of the self optimising kohonen index network (SKiNET) for Raman spectroscopy based detection of anatomical eye tissue.', *Scientific Reports* **9**, 10812

- **Banbury C.**, Styles I., Eisenstein N., Zanier E. R., Vegliante G., Belli A., Logan A. and Goldberg Oppenheimer P. [2020], 'Spectroscopic detection of traumatic brain injury severity and biochemistry from the retina.', *Biomedical Optics Express* **11**(11), 6249-6261

- **Banbury C.**, Clancy M., Eisenstein N., Styles I., Belli A., Logan A. and Goldberg Oppenheimer P., 'Simultaneous fundus photography and eye safe Raman spectroscopy for handheld neurological point-of-care diagnostics.', (In submission)

- **Banbury, C.**, Clancy, M., Eisenstien, N. and Goldberg Oppenheimer, P. [2019], 'Traumatic brain injury detection.', HGF Ref. P276184GB / CM / CH, UK Patent Application No 1913476.6

In addition the following papers were published:

- **Banbury, C.**, Rickard, J.J.S., Mahajan, S. and Goldberg Oppenheimer, P. [2019], 'Tuneable metamaterial-like platforms for surface-enhanced Raman scattering via

three-dimensional block co-polymer-based nanoarchitectures.' *ACS Applied Materials and Interfaces* **11**(15), 14437-14444

- Smith S.C.L., **Banbury C.**, Zardo D, Cannatelli R, Nardone O.M., Shivaji U., Ghosh S., Goldberg Oppenheimer P., and Iacucci M. 'Raman Spectroscopy can accurately differentiate mucosal healing from non-healing in inflammatory bowel disease.' (In submission)

In addition, the following conference abstracts were accepted for presentation:

- **Banbury C.**, Eisenstein N., Styles I., Belli A., Logan A. and Goldberg Oppenheimer P. [2017], 'Homebrew Raman systems from 3D printed parts.', *WITec Raman Symposium* Ulm, Germany (Poster)

- **Banbury C.**, Eisenstein N., Styles I., Belli A., Logan A. and Goldberg Oppenheimer P. [2018], 'Raman spectroscopy of eye tissue to aid diagnostics.', *International Conference on Raman Spectroscopy* Jeju, Korea. (Presentation)

- **Banbury C.**, Eisenstein N., Styles I., Belli A., Logan A. and Goldberg Oppenheimer P. [2019], 'Diagnostics for traumatic brain injury: Raman spectroscopy of the retina and optic Nerve.', *SelectBIO Point-of-Care, Biosensors and Mobile Diagnostics Europe* Rotterdam, Netherlands (Poster)

- Smith S.C.L., **Banbury C.**, Zardo D, Cannatelli R, Nardone O.M., Shivaji U., Ghosh S., Goldberg Oppenheimer P., and Iacucci M. [2020], 'Raman Spectroscopy demonstrates biomolecular changes and predicts response to biological therapy in inflammatory bowel disease (IBD).', *Endoscopy ESGE Days* (ePoster)

- Smith S.C.L., **Banbury C.**, Zardo D, Cannatelli R, Nardone O.M., Shivaji U., Ghosh S., Goldberg Oppenheimer P., and Iacucci M. [2020], 'Raman Spectroscopy can differentiate mucosal healing from non-healing in inflammatory bowel disease.', *Endoscopy ESGE Days* (ePoster)

A copy of each published article is included in the appendix.

CONTENTS

LIST OF FIGURES

LIST OF TABLES

LIST OF ABBREVIATIONS

AMD age-related macular degeneration

ANMSA Advanced Nano-Materials Structures and Applications

ANN artifical neural network

ANOVA analysis of variance

BBB blood-brain barrier

BMU best matching unit

CAD computer aided design

CBF cerebral blood flow

CCD charge coupled device

CE Conformité Européenne

CNS central nervous system

CSF cerebrospinal fluid

CT computed tomography

CTE chronic traumatic encephalopathy

DAI diffuse axonal injury

ELISA enzyme linked immunosorbent assay

EVD external ventricular drain

GCS Glasgow coma scale

GFAP glial fibrillary acidic protein

ICP intracranial pressure

IPM intraparenchymal fiberoptic monitor

kNN k-nearest neighbours

LVQ learning vector quantisation

MLP multi-layer perceptrons

MPE maximum permissible exposure

MRI magnetic resonance imaging

MRS magnetic resonance spectroscopy

MS multiple sclerosis

mTBI moderate TBI

NAA n-acetyl aspartate

NIRS near infrared spectroscopy

NMR nuclear magnetic resonance

NNLS non-negative least squares

OCT optical coherence tomography

ONSD optic nerve sheath diameter

PBS phosphate-buffered saline

PCA principal component analysis

PFA paraformaldehyde

PLS-DA partial least squares discriminant analysis

PoC point-of-care

SERS surface enhanced Raman spectroscopy

SKiNET self optimising Kohonen index network

SOM self organising map

SOMDI self organising map discriminant index

SORS spatially offset Raman spectroscopy

sTBI severe TBI

SVM support vector machines

TBI traumatic brain injury

UCHL-1 ubiquitin C-terminal hydrolase -L1

CHAPTER 1

INTRODUCTION

Traumatic brain injury (TBI) is the leading cause of death under the age of 40 and represents a major burden on healthcare services worldwide [1, 2]. The severity of TBI ranges from mild concussion to severe and chronic loss of cognitive and motor function, resulting from sudden impact to the head. Timely initial diagnosis followed by close patient monitoring (for severe cases) are crucial to favourable patient outcomes. Currently, clinical triaging and monitoring relies heavily on subjective visual assessment of the patient, which lacks quantitative mechanistic insight [4]. The aim of this work is to develop a device for real-time, quantitative point-of-care (PoC) diagnostics for TBI by spanning across traditional scientific boundaries.

By evolutionary 'design', the brain is protected from external trauma by the skull, and isolated from the rest of the body *via* the blood-brain barrier (BBB). As a result, methods to study physical and chemical changes to the brain are either highly invasive, or require radiative sources that are tethered to a location and are highly resource intensive. Central to our inquiry, is the fact that a small part of the central nervous system (CNS) is visible at the back of the eye (retina), where photoreceptive cells capture and transmit light from the world to the brain [3]. Given the optical transparency of the eye, and natural function of focusing light onto retina, we hypothesise that a form of optical spectroscopy may be able to measure neurochemical information. Optical spectroscopy is used to measure properties of light, and how these change through interaction with matter. In much the same way that it is possible to determine the chemical composition of distant stars and planets by studying the light that reaches Earth, it may be possible to study brain function.

1.1 Thesis Overview

The structure of this thesis begins with an introduction to TBI diagnostics, covering clinically adopted methods and highlighting novel approaches being pursued in the literature. This is followed by an introduction to Raman spectroscopy, which forms the basis for our experimental study. Applications of Raman spectroscopy in neurology and opthalmology are shown, highlighting recent progress, shortcomings and limitations. The main results are described by Chapters 4-6, which are self contained articles published during the duration of study. Together, the results chapters address the following three key questions:

- Chapter 4: How can the analysis of Raman spectroscopy be improved to reliably measure subtle chemical changes from biological samples?
- Chapter 5: Can Raman spectroscopy of the retina detect biochemical changes indicative of TBI from the retina?
- Chapter 6: How can the technology be effectively translated from a laboratory setting to a handheld PoC diagnostic device?

Chapter 4 describes the importance and use of machine learning in the analysis of Raman spectra, developing a new methodology that simultaneously aids presentation, comprehension and classification of large hyperdimensional datasets. In Chapter 5, the computational methods developed in Chapter 4 are used to fundamentally assess whether Raman spectroscopy of the eye can be used to identify TBI, in a clinically relevant *ex-vivo* murine model. Finally, Chapter 6 attempts to bridge the gulf that exists between benchtop Raman spectroscopy and a portable clinical device for *in-vivo* diagnostics of TBI from the eye. The

device design in Chapter 6 resulted in a patent application for the simultaneous acquisition of Raman spectra from the retina and fundus photography, which is of critical importance for future development. Whilst the format of the thesis results in some natural overlap and redundancy, each chapter touches on very different scientific fields, which form interconnected dependencies between each other. Thereby, we emphasise the multidisciplinary nature of the work by bracketing the central healthcare challenge by developments in computer science and optics.

1.2 References

[1] Lawrence, T., Helmy, A., Bouamra, O., Woodford, M., Lecky, F. and Hutchinson, P. J. [2016], 'Traumatic brain injury in England and Wales: prospective audit of epidemiology, complications and standardised mortality.', *BMJ open* **6**(11), e012197.

[2] Popescu, C., Anghelescu, A., Daia, C. and Onose, G. [2015], 'Actual data on epidemiological evolution and prevention endeavours regarding traumatic brain injury.', *Journal of medicine and life* **8**(3), 272–7.

[3] Purves, D., Augustine, G. J., Fitzpatrick, D., Katz, L. C., LaMantia, A., McNamara, J. O. and Williams, M. [2001], *Neuroscience*, 2 edn, Sunderland (MA): Sinauer Associates.

[4] Teasdale, G., Maas, A., Lecky, F., Manley, G., Stocchetti, N. and Murray, G. [2014], 'The Glasgow coma scale at 40 years: standing the test of time', *The Lancet Neurology* **13**(8), 844–854.

CHAPTER 2

TRAUMATIC BRAIN INJURY

TBI is defined as ‘alteration in brain function, or other evidence of brain pathology, caused by an external force’, but is distinct from the more broad category of head injury, which includes damage to other areas such as the skull. Alteration in brain function is further specified as either: a loss of consciousness; loss of memory immediately before or after injury; neurological deficits (e.g. loss of balance, change in vision); or altered mental state at the time of injury (e.g. confusion, disorientation) [30]. Common causes include falls, assault, road traffic accidents, contact sports and military combat [17, 42]. In the absence of external physical damage, TBI is extremely difficult to identify. At the point of injury, tests such as the Glasgow coma scale (GCS) are routinely used, relying on downstream changes to visual, motor and verbal response as indicators of damage to the brain [47]. The GCS is used to stratify TBI according to severity as either mild, moderate or severe. Mild TBI can be as simple as minor concussion, but the long term damaging effects of even minor injuries (which have a higher tendency to go undetected) have recently been highlighted by a number of high profile cases. A major concern is the effect of repetitive injuries, such as those sustained from contact sports (e.g. boxing) [7, 8]. There are links between TBI and chronic conditions such as chronic traumatic encephalopathy (CTE), a degenerative disease, presenting with similar symptoms to Alzheimer’s disease [49].

More generally, TBI has been dubbed the ‘silent epidemic’, with an estimated 69 million cases per year worldwide [14]. In the UK, there are over one million incidents of TBI needing emergency medical treatment every year, placing a major burden on healthcare services [25]. Importantly, patients often arrive at emergency centres an unknown time after injury and without witnesses to the event. In these circumstances, diagnosis relies on self reporting from patients, which is naturally confounded by confusion or disorientation

resulting from TBI [30]. This is commonly complicated further by drug or alcohol intoxication, which also causes a loss of balance and disorientation. In such cases patients can be referred for a computed tomography (CT) scan as a precaution, however guidelines vary between regions and countries [53].

2.1 Pathophysiology and Pathobiology

All of the functions in the brain from perception, to conscious thought and motor control are determined through a complex network of billions of neurons, which communicate by transmitting electrical signals across synapses to other neurons. The bias inside a neuron relative to the surrounding interstitial fluid is determined by the relative concentrations of ions such as potassium and sodium inside and outside the cell. This crucial balance is controlled by a number of channels within the cell membrane that actively pump ions according to its state [51]. Since neurons communicate *via* electrical signals, this balance of charge is crucial to maintaining the architectural circuitry in the brain, not dissimilar from an electronic circuit board. TBI fundamentally disrupts the balance of charge within the brain, causing immediate damage (primary injury), but additionally results in a cascading cellular response, which can lead to lasting effects over hours, days or months (secondary injury) [28].

Neurons are perhaps the most well known cell type in the brain, however, are outnumbered by a group of cells known as glial cells, which were originally thought to provide only structural ‘glue’ for neurons [50]. Glial cells consist of astrocytes, oligodendrocytes and microglia, which together provide a number of supporting functions to neurons. Astrocytes

perform some of the most important regulatory roles in the brain: providing skeletal support for neurons, helping to reset synaptic junctions, and actively controlling movement of large molecules between the bloodstream and brain (the BBB). Furthermore, astrocytes form their own network and communicate with each other, but the extent to which this impacts neurological behaviour is not yet fully understood [40]. Oligodendrocytes produce the insulating myelin sheath, which covers axons and allows electrical impulses to be transmitted rapidly along the length of the axon. Finally, microglia are immune cells (macrophages) of the CNS that scavenge, consume and digest debris, damaged cells or foreign bodies [51]. A cartoon illustration of each cell type and their interaction is shown in Fig. 2.1.

2.1.1 Primary Injury

Even in the absence of direct tissue and cellular destruction (present in moderate or severe injury), TBI causes stretching of cell membranes, leading to a loss of homeostasis. This forces neurons into a metabolically distressed state as ions are actively pumped across the cell membrane to restore the resting potential [36]. Furthermore, the axons of each neuron, which can project over large distances and form the wires between neuronal circuitry can be sheared; termed diffuse axonal injury (DAI). Neurons that become orphaned from the rest of the network in this way quickly die, releasing neurotransmitters and other signalling molecules (cytokines) that causes further damage to neighbouring cells [3]. Macroscopically, under sudden change in momentum, the brain ricochets back and forth along the direction of the applied force, pivoting about the brainstem and colliding with the skull, which can lead to bruising on opposing sides of the brain [29]. A small amount of cushioning is provided by a thin layer of cerebrospinal fluid (CSF) which surrounds the brain and

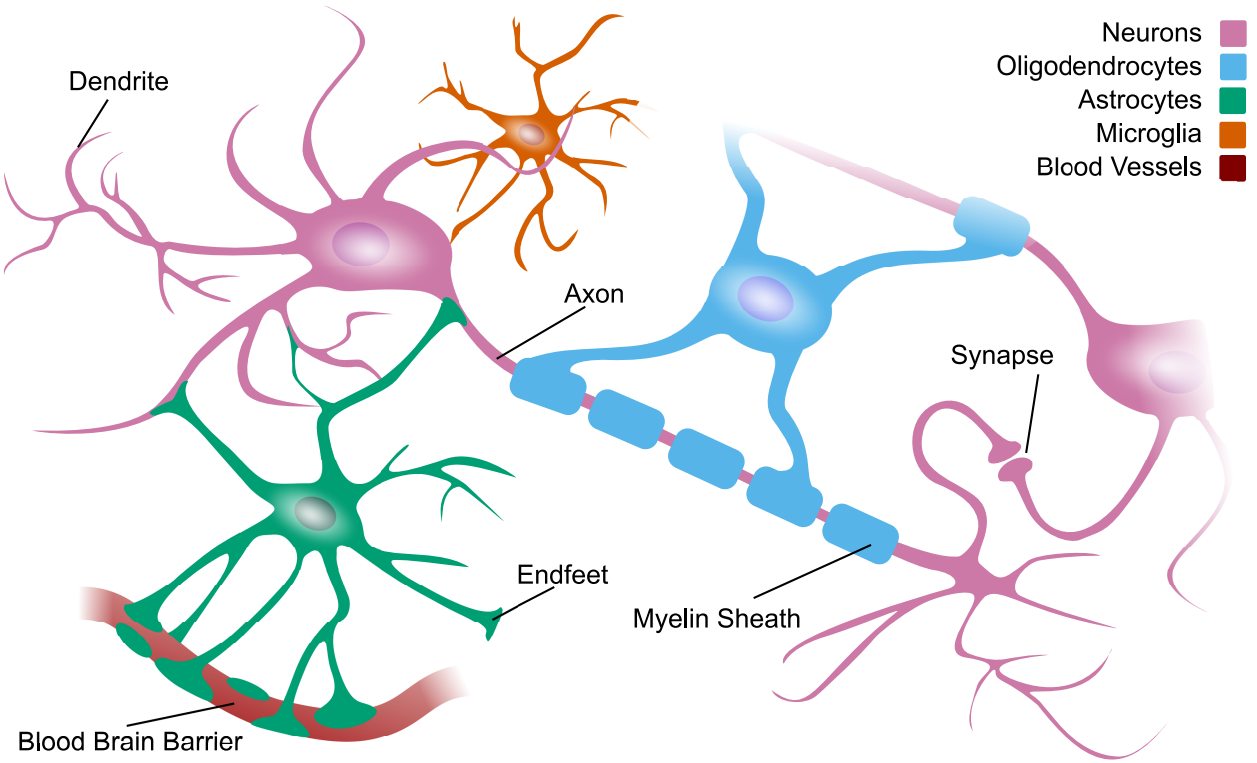

Figure 2.1: Illustration of the main neuronal cell types and their inter-connections in the CNS.

consists of mostly water filtered from the bloodstream [39].

2.1.2 Secondary Injury

Secondary injury is described by neurodegeneration in the hours, days and months following TBI, which is often caused by increased intracranial pressure (ICP) that restricts cerebral blood flow (CBF) [20]. Since the brain occupies a fixed volume, ICP can quickly become increased to levels that the brain struggles to deal with by the presence of excessive inflammation or fluid build-up [33]. Common sources of fluid in the brain are ac-

cumulation of CSF (hydrocephalus) and blood (haematoma). A lack of oxygen to neurons (ischaemia) caused by reduced CBF and ICP leads to further cell loss and continues the cascade of damage to surrounding neurons (excitotoxicity) [52]. Poor blood flow and haematoma are caused by breakdown of the BBB, resulting from damage to endothelial cells in blood vessels and astrocytes, which form tight junctions around blood vessels in the brain and strictly limits the movement of large molecules from the bloodstream to the brain [51].

2.2 Diagnostics Methods

In this section, the diagnostic tools that are currently adopted clinically are introduced, outlining their advantages and shortcomings alongside the impact this has both clinically and for future research. We then review recent and novel methods that have been attempted in the literature, including: blood biomarker tests, ICP monitoring, advances in neuroimaging and optics.

2.2.1 Established Techniques

2.2.1.1 Glasgow Coma Scale

What is now known as the GCS was first described in 1974 by Sir Graham Teasdale and Bryan Jennett based on simple assessment of a patient's visual, verbal and motor response [45]. The original definition was updated two years later to include further granularity in motor response and is the scale most widely used today (however, the original

article remains the most cited) [46]. Visual response is ranked from 1-4, verbal response, 1-5 and motor response, 1-6. The three areas of assessment are independently routed in an anatomical basis, with increasing severity being related to deeper and more primal regions of the brain. Not only does this give a good predictor for which parts of the brain are damaged, but provides an internal cross check of the assessment (i.e. scores for independent components should not differ greatly) [34]. In-hospital, the independent scores can be routinely monitored and recorded on observational charts over time, allowing for immediate visual identification of patient deterioration and improvement (Fig. 2.2). In addition to wide clinical adoption, the GCS forms the basis for standardised communication in scientific research. Retrospectively, this has shown a striking correlation to metabolomics, neuroimaging, biomarkers and patient outcomes [47]. Although the GCS has been enormously successful, it is not without criticisms. These primarily focus on inter-observer variability, especially between pre-hospital and in-hospital assessment. A major contributor to this effect is in-hospital sedation, which prevents meaningful measurements for visual and verbal response. There are numerous approaches to dealing with this issue, with a common method being to assign a score of 1 for both verbal and visual response. This has the effect of automatically exaggerating the severity of patients in hospital, which severely hampers the quality of clinical research [57].

2.2.1.2 Neuroimaging

Following initial assessment using the GCS, neuroimaging most commonly in the form of CT is used in moderate and severe cases, to identify abnormalities that require immediate intervention. CT combines X-ray images over different angles and computational recon-

NAME: J. CONNOR		01 JAN					2 JAN					3 JAN					4 JAN					Date
																						Time
Eyes Open	Spontaneously																		x	x	x	Eyes closed by swelling = C
	To peech								x	x	x						x	x				
	To pain						x	x				x	x		x	x						
	None	x	x	x	x	x								x								
Best Verbal Response	Oriented																					I tube or tracheostomy = T
	Confused																		x	x	x	
	Inappropriate															x	x	x				
	Incomprehensible												x	x	x							
	None	x	x	x	x	x	x	x	x	x	x	x										
Best Motor Response	Obey commands																x	x	x	x	x	Usually record the best arm response
	Localise pain											x	x	x	x	x						
	Flexion to pain						x	x	x	x	x											
	Extension to pain	x	x	x	x	x																
	None																					

Figure 2.2: Illustration of how the GCS can be used visually to represent patient changes over time based on repeat observations by nurses (based on illustration by Teasdale and Jennett [46]).

struction to create 2D slices and 3D volumes of the brain, which can be performed quickly and relatively cheaply [19]. CT is favoured over magnetic resonance imaging (MRI) for cost, speed and availability, but additionally has better sensitivity to identifying skull fractures. Furthermore, MRI carries an additional risk in cases where metallic debris (e.g. bullets) may be present in the brain. In paediatric TBI, neuroimaging is less commonly used as ionising radiation from CT poses a greater risk to children, and MRI often requires sedation due to the length of time the patient is required to remain still [53].

The main anatomical features identified using CT include skull fractures, excessive bleeding (haemorrhage and haematoma), bruising (contusion), accumulation of CSF (hy-

drocephalus) and displacement of brain tissue (herniation) [43]. The interpretation of CT requires an experienced radiologist, as shown in a study by Laalo *et al.* [24] who looked at inter-observer accuracy between on call radiologists and neuroradiologists. Importantly, only four out of the hundred patients in the study required immediate surgical intervention, which were all identified correctly. However, on call radiologists had a high false negative rate for contusions, missing 67 % [24]. Mistakes are often made as a result of imaging artefacts that occur due to a number of reasons, including: physical properties, reconstruction errors and incorrect patient placement [2]. Artificial intelligence is increasingly being looked at as the answer to reducing systematic and user error, by having computational algorithms automatically highlight regions of interest or perform diagnosis [21]. As previously mentioned, MRI is not widely used to perform initial diagnostics in acute settings, but is the primary modality for chronic injury, showing a greater percentage of lesions and DAI [53].

2.2.1.3 Intracranial Pressure Monitoring

ICP is monitored as a standard of care for patients with severe TBI, either by using an external ventricular drain (EVD) or an intraparenchymal fiberoptic monitor (IPM), where EVD is considered the gold standard and has been shown to lead to significantly better patient outcomes [26]. An EVD is a soft catheter inserted into one of the lateral ventricles *via* a small burr hole in the skull. The lateral ventricles are C shaped cavities containing CSF. A collection chamber and pressure scale measured in millimetres of water pressure allows ICP to be monitored and excess CSF controlled *via* a drainage bag (Fig. 2.3) [22]. ICP monitoring and CSF drainage plays a crucial role in intensive care for severe TBI

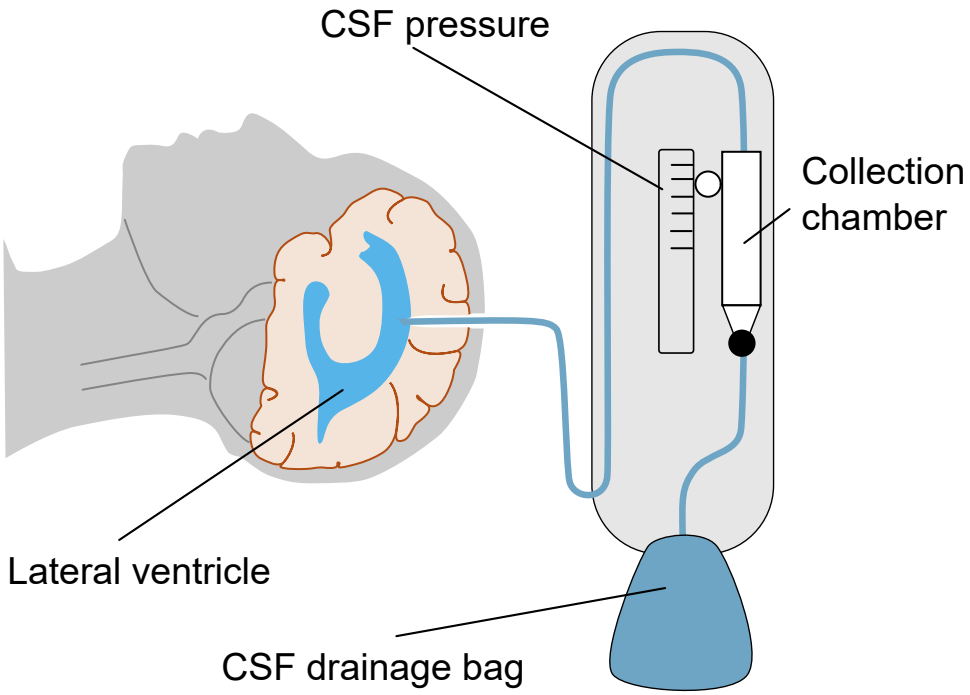

Figure 2.3: Illustration of CSF monitoring and drainage using EVD (based on illustration by Emily Humphrey [22]).

patients, but is a highly invasive procedure. The most common risks are infections and further damage from incorrect placement of the EVD catheter into the brain, which can have fatal consequences. The occurrence of complications associated with invasive ICP is uncertain (ranging from close to 0 % to near 100 %), coupled to a lack of standardisation and adherence to existing protocols [5, 44]. The use of EVDs clinically is unlikely to be replaced in intensive care, as CSF drainage provides an effective means for clinicians to simultaneously monitor and reduce increased ICP. However, given the obvious (but poorly quantified) risks, it is important that invasive methods are only used where absolutely necessary.

2.2.2 Proposed Methods

Fig. 2.4 gives a visual overview of current diagnostic modalities (GCS, CT/MRI, ICP) alongside broad categories for novel diagnostic tools (biomarkers, non-invasive ICP, CT/MRI), grouped according to desirable traits. The ideal technology would be a cheap and portable device to non-invasively and temporally measure changes to the CNS (indicated by δ in Fig. 2.4). In this section, these broad themes are expanded in more detail, highlighting recent progress and fundamental limitations in each category.

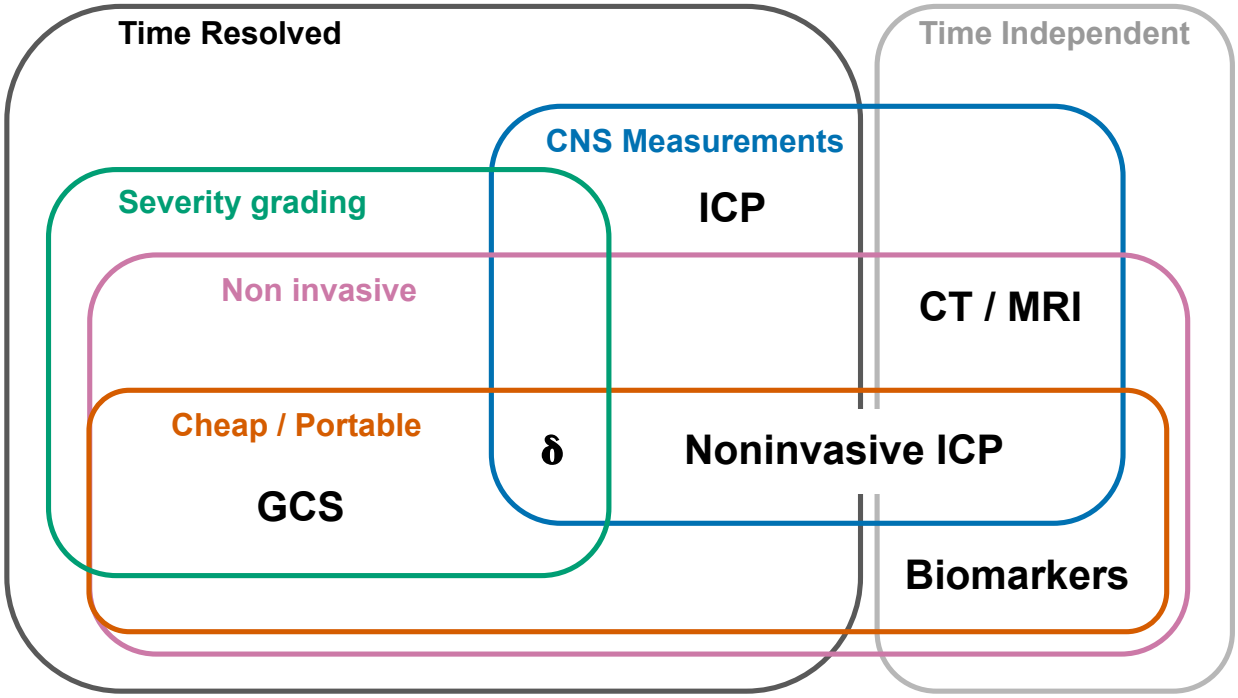

Figure 2.4: Technology landscape for TBI diagnostics.

Technology landscape showing existing diagnostic modalities (GCS, CT/MRI, ICP) and emerging technologies (biomarkers, non-invasive ICP, CT/MRI), grouped according to diagnostic conditions. The space occupied by δ where the ideal set of device properties would lie.

2.2.2.1 Biomarkers

Biomarker assays for diagnostics of TBI are a current hot topic, with several reviews on the subject [13, 18, 56]. The world health organisation defines a biomarker as 'any substance, structure, or process that can be measured in the body or its products and influence or predict the incidence of outcome or disease' [54]. For some time, chemical analysis of CSF has yielded some insight into the cellular processes involved in TBI and the integrity of the BBB. Levels of albumin in CSF, produced predominantly in the liver provides a good indicator for BBB integrity [41]. However, the collection of CSF requires highly invasive procedures such as a lumbar puncture or EVD, which carry their own risks. Instead, blood and more recently, saliva are targets that can be collected through minimally invasive or non-invasive means, and so have received much attention [13]. The challenges facing these approaches are that native quantities of molecules specific to TBI are found in extremely low concentrations, even with disruption to the BBB. Out of the pool of potential biomarkers, by far the most well studied to date are S100-B and glial fibrillary acidic protein (GFAP) [18].

S100-B is a calcium binding protein found abundantly within astrocytes in the CNS and performs regulatory functions within the cell. As previously mentioned, astrocytes are integral to the BBB, but more generically act as scaffolding for the CNS and help to maintain ionic homeostasis of interstitial fluid necessary for neurons to function correctly [12]. On injury, release of high concentrations of S100-B promotes programmed cell death (apoptosis) and serum concentrations of S100-B have been used clinically as diagnostic and prognostic markers of TBI [48]. However, quantitative assessment by Gan *et al.* [18]

pooled more than 60,000 observations and showed only modest diagnostic accuracy from S100-B alone. Although S100-B is found in high concentrations in astrocytes, the protein is not specific to the CNS, and increased levels of S100-B have been observed in the absence of brain injury. Since TBI is often accompanied by trauma to other regions of the body, S100-B as a biomarker cannot confirm the absence of brain trauma, in the presence of other injuries [1].

Conversely, GFAP is an intermediate filament protein specific to the CNS and plays important functional and structural roles, however, these are much less well understood. A review by Brenner [10] shows large discrepancies in the results from different laboratories, and takes the viewpoint that this may be due to regional roles within the brain. Regardless of the underlying role, GFAP is consistently observed as upregulated following TBI, and as a result of having a higher molecular weight (*vs* S100-B), takes longer to be cleared from the body [13]. One of the most promising tests builds on the prior success of GFAP as a biomarker of TBI, but employs a combination of multiple biomarkers to improve predictive outcomes. Diaz *et al.* [15] assessed the serum concentrations of GFAP in conjunction with ubiquitin C-terminal hydrolase -L1 (UCHL-1), a protein specific to neurons and that had previously been seen elevated with severe TBI. Moreover, UCHL-1 is associated with DAI, whereas GFAP is associated more with focal lesions, and so the two provide complementary information regarding injury and cell types specific to the CNS. Evaluation of biomarker concentrations was performed by an enzyme linked immunosorbent assay (ELISA), which provides a colorimetric change upon binding of antibodies specific to the target biomarker in solution [15]. The work has recently been repeated by Bazarian *et al.* [6], who found similar results with a sensitivity and specificity of 0.976 and 0.364 respec-

tively, similar to that obtained by CT. The authors estimate that such a test could save up to a third of unnecessary CT scans [6].

Research into TBI biomarkers to provide simple effective triaging has the potential to streamline diagnostic decisions, particularly in emergency settings where resources such as CT are overused. To truly leverage this benefit, new methods are required so that test results can be obtained in a timely fashion at the point of injury, which may be a remote location (e.g. military combat). However, tests from bodily fluids provides information at a single point in time, and there exists a narrow window of time following injury where the test can be conducted [13]. This allows biomarker assays to be integrated into existing workflows and augment patient triaging, but cannot completely replace continuous assessment such as the GCS and ICP monitoring.

2.2.2.2 Magnetic Resonance Spectroscopy

In the field of neuroimaging, there are several proposed variations to improve and extend the capabilities of existing technologies such as CT and MRI, which will largely be ignored here as the cost and portability requirements limit the opportunity for diagnostics in pre-hospital settings and at the PoC [43]. One modality that is noteworthy for its ability to sensitively and non-invasively detect metabolic species from the CNS *in-vivo* is magnetic resonance spectroscopy (MRS). In a conventional MRI scan atomic nuclei are aligned with a strong magnetic field, and then deflected by a pulse of electromagnetic radiation at the resonant frequency of the target element (hydrogen nuclei). As the pulse ends, nuclei relax to align with the magnetic field, emitting electromagnetic radiation, which is detected. Radio frequency pulses are used to detect hydrogen atoms from fat and water, which are

abundant in the body, and used to form the images used clinically [9]. The resonance frequency of the proton varies based on the local environment, and so by varying the frequency of the external radiation, molecules other than water and fat can be measured. By suppressing the more dominant contribution from water [16], MRS can be used to non-invasively measure metabolites within the brain *in-vivo* [35].

Although metabolic disruption plays a major role in secondary injury and patient outcomes, a recent meta analysis by Brown *et al.* [11] shows that there is a great deal of uncertainty and inconsistency across studies of TBI, with the exception of n-acetyl aspartate (NAA), which is used as a marker of neuronal activity. Specifically, NAA provides: osmotic regulation (acting as a molecular water pump) for neurons; stimulates astrocytes (which provide energy in the form of glycogen); and increases local blood flow and oxygen supply [4]. In response to TBI, a decrease in NAA can be observed *via* MRS proportional to injury severity, and correlating to decreased neuronal activity [32]. However, MRS studies have thus far only shown sensitivity to sub-acute and chronic injury [11]. As a result, MRS may be useful to further our understanding of the temporal evolution of TBI and patient outcomes, but is unlikely to offer a replacement diagnostic tool in acute emergency settings.

2.2.2.3 Non-invasive Intracranial Pressure Monitoring

Methods to non-invasively measure ICP take wildly varying approaches including measuring subtle deformations to the skull, cochlear fluid pressure, near infrared spectroscopy (NIRS) and a host of approaches that consider physical changes to the eye (such as the optic nerve sheath diameter (ONSD)) [23]. The number of publications dedicated to devel-

oping a new non-invasive standard of care illustrate both the importance of ICP monitoring in neurological intensive care, and difficultly to innovate in this space. Reoccurring issues amongst several of the most promising approaches are a lack of independent validation or follow on studies [31, 55]. In several cases, ICP measurements were limited to pre-screening applications, showing a change in ICP, but without quantification. In the review by Khan *et al.* [23], it was concluded that the most promising methods were two ophthalmic applications: pupillometry and ONSD.

Pupillometry is used to measure the amplitude, percentage and velocity in which the pupil constricts in response to light stimuli. Mariakakis *et al.* [27] took a modern approach by combining a simple smartphone camera and flash, with an artifical neural network (ANN) to track pupil diameter over time and in response to change in light (camera flash) [27]. By using ubiquitous technology, the authors hoped to make pupillometry more widely adopted, with the cost of existing commercial instruments being in excess of 4000 USD. In effect, pupillometry quantifies and standardises the visual response component of the GCS, but as a result is subject to the same limitations with sedation and intoxication [57].

Measurements of ONSD can be made using standard neuroimaging (CT, MRI), but also using bedside techniques such as an ultrasound probe placed over the closed eyelid of the patient [37]. In a recent clinical study of 100 patients, Robba *et al.* [38] used ultrasonography on admission to measure ONSD, and showed a good correlation to ICP and mortality. This followed a smaller prospective study by the same author, indicating that ONSD may be a useful tool in deciding if patients require invasive monitoring, or are at risk of poor outcomes (but is yet to be independently verified) [37].

2.2.2.4 Conclusions

In this section, we have shown that TBI results in heterogeneous cellular and tissue damage, making initial pre-hospital diagnostics, in-hospital monitoring and post-hospital care extremely difficult, but crucial to get right. As a result, the GCS remains the only modality able to temporally track severity in a non-invasive manor, and therefore span the entire patient journey. However, this relies on subjective assessment, which has been shown to vary across pre-hospital and in-hospital settings in particular [57], owing largely to the low scores for verbal and visual response associated with sedation. From the large pool of upcoming approaches to provide quantitative non-invasive monitoring for neurological dynamics, some of the most promising of these are from changes to physical properties of the eye [27, 38]. This sets a precedence that the effects of TBI can be seen and monitored from the eye, but an area that currently remains unexplored is to assess these changes from a chemical viewpoint. Such a device would ideally combine the ease of use and accessibility of methods such as ONSD with the chemical specificity of MRS, allowing for continuous real time monitoring of brain chemistry non-invasively.

2.3 References

[1] Anderson, R. E., Hansson, L.-O., Nilsson, O., Dijlai-Merzoug, R. and Settergren, G. [2001], 'High serum S100B levels for trauma patients without head injuries', *Neurosurgery* **48**(6), 1255–1260.

[2] Barrett, J. F. and Keat, N. [2004], 'Artifacts in CT: Recognition and avoidance', *Ra-*

dioGraphics **24**, 1679–1691.

[3] Barron, K. D. [2004], 'The axotomy response', *Journal of the Neurological Sciences* **220**(1-2), 119–121.

[4] Baslow, M. H. [2010], 'Evidence that the tri-cellular metabolism of N-acetylaspartate functions as the brain's "operating system": how NAA metabolism supports meaningful intercellular frequency-encoded communications', *Amino Acids* **39**(5), 1139–1145.

[5] Baum, G. R., Hooten, K. G., Lockney, D. T., Fargen, K. M., Turan, N., Pradilla, G., Murad, G. J. A., Harbaugh, R. E. and Glantz, M. [2017], 'External ventricular drain practice variations: results from a nationwide survey', *Journal of Neurosurgery* **127**(5), 1190–1197.

[6] Bazarian, J. J., Biberthaler, P., Welch, R. D., Lewis, L. M., Barzo, P., Bogner-Flatz, V., Gunnar Brolinson, P., Büki, A., Chen, J. Y., Christenson, R. H., Hack, D., Huff, J. S., Johar, S., Jordan, J. D., Leidel, B. A., Lindner, T., Ludington, E., Okonkwo, D. O., Ornato, J., Peacock, W. F., Schmidt, K., Tyndall, J. A., Vossough, A. and Jagoda, A. S. [2018], 'Serum GFAP and UCH-L1 for prediction of absence of intracranial injuries on head CT (ALERT-TBI): a multicentre observational study', *The Lancet Neurology* **17**(9), 782–789.

[7] BBC News [2016], 'Muhammad ali: Boxer's battle with Parkinson's', `https://www.bbc.co.uk/news/health-36455016`.

[8] BBC News [2018], 'Brain injury expert calls for ban on heading in football', `https://www.bbc.co.uk/sport/football/45110282`.

[9] Berger, A. [2002], 'How does it work?: Magnetic resonance imaging', *BMJ* **324**(7328), 35–35.

[10] Brenner, M. [2014], 'Role of GFAP in CNS injuries', *Neuroscience Letters* **565**, 7–13.

[11] Brown, M., Baradaran, H., Christos, P. J., Wright, D., Gupta, A. and Tsiouris, A. J. [2018], 'Magnetic resonance spectroscopy abnormalities in traumatic brain injury: A meta-analysis', *Journal of Neuroradiology* **45**(2), 123–129.

[12] Brozzi, F., Arcuri, C., Giambanco, I. and Donato, R. [2009], 'S100B protein regulates astrocyte shape and migration via interaction with src kinase', *Journal of Biological Chemistry* **284**(13), 8797–8811.

[13] Dadas, A., Washington, J., Diaz-Arrastia, R. and Janigro, D. [2018], 'Biomarkers in traumatic brain injury (TBI): a review', *Neuropsychiatric Disease and Treatment* **14**, 2989–3000.

[14] Dewan, M. C., Rattani, A., Gupta, S., Baticulon, R. E., Hung, Y. C., Punchak, M., Agrawal, A., Adeleye, A. O., Shrime, M. G., Rubiano, A. M., Rosenfeld, J. V. and Park, K. B. [2019], 'Estimating the global incidence of traumatic brain injury', *Journal of Neurosurgery* **130**(4), 1080–1097.

[15] Diaz-Arrastia, R., Wang, K. K., Papa, L., Sorani, M. D., Yue, J. K., Puccio, A. M., McMahon, P. J., Inoue, T., Yuh, E. L., Lingsma, H. F., Maas, A. I., Valadka, A. B., Okonkwo, D. O., Geoffrey, T. M., Casey, S. S., Cheong, M., Cooper, S. R., Dams-O'Connor, K., Gordon, W. A., Hricik, A. J., Menon, D. K., Mukherjee, P., Schnyer, D. M., Sinha, T. K. and Vassar, M. J. [2014], 'Acute biomarkers of traumatic brain

injury: Relationship between plasma levels of ubiquitin C-terminal hydrolase-L1 and glial fibrillary acidic protein', *Journal of Neurotrauma* **31**(1), 19–25.

[16] Dong, Z. [2015], 'Proton MRS and MRSI of the brain without water suppression', *Progress in Nuclear Magnetic Resonance Spectroscopy* **86-87**, 65–79.

[17] Faul, M., Xu, L., Wald, M. and Coronado, V. [2010], Traumatic brain injury in the United States: Emergency department visits, hospitalizations and deaths, U.S. Department of Health and Human Services Centers for Disease Control and Prevention.

[18] Gan, Z. S., Stein, S. C., Swanson, R., Guan, S., Garcia, L., Mehta, D. and Smith, D. H. [2019], 'Blood biomarkers for traumatic brain injury: A quantitative assessment of diagnostic and prognostic accuracy', *Frontiers in Neurology* **10**, 446.

[19] Goldman, L. W. [2007], 'Principles of CT and CT technology', *Journal of Nuclear Medicine Technology* **35**(3), 115–128.

[20] Greve, M. W. and Zink, B. J. [2009], 'Pathophysiology of traumatic brain injury', *Mount Sinai Journal of Medicine: A Journal of Translational and Personalized Medicine* **76**(2), 97–104.

[21] Hosny, A., Parmar, C., Quackenbush, J., Schwartz, L. H., Aerts, H. J. W. L. and Edu, H. H. [2018], 'Artificial intelligence in radiology', *Nat Rev Cancer* **18**(8), 500–510.

[22] Humphrey, E. [2018], 'Caring for neurosurgical patients with external ventricular drains', *Nursing Times [online]* **114**(4), 52–56.

[23] Khan, M., Shallwani, H., Khan, M. and Shamim, M. [2017], 'Noninvasive monitoring intracranial pressure – A review of available modalities', *Surgical Neurology International* **8**(1), 51.

[24] Laalo, J. P., Kurki, T. J., Sonninen, P. H. and Tenovuo, O. S. [2009], 'Reliability of diagnosis of traumatic brain injury by computed tomography in the acute phase', *Journal of Neurotrauma* **26**(12), 2169–2178.

[25] Lawrence, T., Helmy, A., Bouamra, O., Woodford, M., Lecky, F. and Hutchinson, P. J. [2016], 'Traumatic brain injury in England and Wales: prospective audit of epidemiology, complications and standardised mortality.', *BMJ open* **6**(11), e012197.

[26] Liu, H., Wang, W., Cheng, F., Yuan, Q., Yang, J., Hu, J. and Ren, G. [2015], 'External ventricular drains versus intraparenchymal intracranial pressure monitors in traumatic brain injury: A prospective observational study', *World Neurosurgery* **83**(5), 794–800.

[27] Mariakakis, A., Baudin, J., Whitmire, E., Mehta, V., Banks, M. A., Law, A., Mcgrath, L. and Patel, S. N. [2017], 'Pupilscreen: Using smartphones to assess traumatic brain injury', *Proceedings of the ACM on Interactive, Mobile, Wearable and Ubiquitous Technologies* **1**(3), 1–27.

[28] McAllister, T. W. [2011], 'Neurobiological consequences of traumatic brain injury.', *Dialogues in clinical neuroscience* **13**(3), 287–300.

[29] Mckee, A. C. and Daneshvar, D. H. [2015], The neuropathology of traumatic brain injury, *in* 'Handbook of Clinical Neurology', 1 edn, Vol. 127, Elsevier B.V., pp. 45–66.

[30] Menon, D. K., Schwab, K., Wright, D. W. and Maas, A. I. [2010], 'Position statement: Definition of traumatic brain injury', *Archives of Physical Medicine and Rehabilitation* **91**(11), 1637–1640.

[31] Michaeli, D. and Rappaport, Z. H. [2002], 'Tissue resonance analysis: a novel method for noninvasive monitoring of intracranial pressure', *Journal of Neurosurgery* **96**(6), 1132–1137.

[32] Moffett, J. R., Arun, P., Ariyannur, P. S. and Namboodiri, A. M. A. [2013], 'N-acetylaspartate reductions in brain injury: impact on post-injury neuroenergetics, lipid synthesis, and protein acetylation', *Frontiers in Neuroenergetics* **5**(DEC).

[33] Mokri, B. [2001], 'The Monro-Kellie hypothesis: Applications in CSF volume depletion', *Neurology* **56**(12), 1746–1748.

[34] Munakomi, S. and Kumar, B. M. [n.d.], 'Neuroanatomical basis of Glasgow coma scale — a reappraisal', *Neuroscience and Medicine* (03), 116–120.

[35] Mutch, C. A., Talbott, J. F. and Gean, A. [2016], 'Imaging evaluation of acute traumatic brain injury', *Neurosurgery Clinics of North America* **27**(4), 409–439.

[36] Prins, M., Greco, T., Alexander, D. and Giza, C. C. [2013], 'The pathophysiology of traumatic brain injury at a glance', *Disease Models & Mechanisms* **6**(6), 1307–1315.

[37] Robba, C., Cardim, D., Tajsic, T., Pietersen, J., Bulman, M., Donnelly, J., Lavinio, A., Gupta, A., Menon, D. K., Hutchinson, P. J. A. and Czosnyka, M. [2017], 'Ultrasound non-invasive measurement of intracranial pressure in neurointensive care: A prospective observational study', *PLOS Medicine* **14**(7), e1002356.

[38] Robba, C., Donnelly, J., Cardim, D., Tajsic, T., Cabeleira, M., Citerio, G., Pelosi, P., Smielewski, P., Hutchinson, P., Menon, D. K. and Czosnyka, M. [2020], 'Optic nerve sheath diameter ultrasonography at admission as a predictor of intracranial hypertension in traumatic brain injured patients: a prospective observational study', *Journal of Neurosurgery* **132**(4), 1279–1285.

[39] Sakka, L., Coll, G. and Chazal, J. [2011], 'Anatomy and physiology of cerebrospinal fluid', *European Annals of Otorhinolaryngology, Head and Neck Diseases* **128**(6), 309–316.

[40] Santello, M., Toni, N. and Volterra, A. [2019], 'Astrocyte function from information processing to cognition and cognitive impairment', *Nature Neuroscience* **22**(2), 154–166.

[41] Saw, M. M., Chamberlain, J., Barr, M., Morgan, M. P. G., Burnett, J. R. and Ho, K. M. [2014], 'Differential disruption of blood–brain barrier in severe traumatic brain injury', *Neurocritical Care* **20**(2), 209–216.

[42] Schmid, K. E. and Tortella, F. C. [2012], 'The diagnosis of traumatic brain injury on the battlefield', *Frontiers in Neurology* **3**(June), 1–5.

[43] Smith, L. G. F., Milliron, E., Ho, M.-L., Hu, H. H., Rusin, J., Leonard, J. and Sribnick, E. A. [2019], 'Advanced neuroimaging in traumatic brain injury: an overview', *Neurosurgical Focus* **47**(6), E17.

[44] Tavakoli, S., Peitz, G., Ares, W., Hafeez, S. and Grandhi, R. [2017], 'Complications of

invasive intracranial pressure monitoring devices in neurocritical care', *Neurosurgical Focus* **43**(5), E6.

[45] Teasdale, G. and Jennett, B. [1974], 'Assessment of coma and impaired consciousness. a practical scale', *The Lancet* **304**(7872), 81–84.

[46] Teasdale, G. and Jennett, B. [1976], 'Assessment and prognosis of coma after head injury', *Acta Neurochirurgica* **34**(1-4), 45–55.

[47] Teasdale, G., Maas, A., Lecky, F., Manley, G., Stocchetti, N. and Murray, G. [2014], 'The Glasgow coma scale at 40 years: standing the test of time', *The Lancet Neurology* **13**(8), 844–854.

[48] Thelin, E. P., Nelson, D. W. and Bellander, B.-M. [2017], 'A review of the clinical utility of serum S100B protein levels in the assessment of traumatic brain injury', *Acta Neurochirurgica* **159**(2), 209–225.

[49] Turner, R. C., Lucke-Wold, B. P., Robson, M. J., Omalu, B. I., Petraglia, A. L. and Bailes, J. E. [2012], 'Repetitive traumatic brain injury and development of chronic traumatic encephalopathy: a potential role for biomarkers in diagnosis, prognosis, and treatment?', *Frontiers in neurology* **3**, 186.

[50] Virchow, R. [1856], *Gesammelte Abhandlungen zur Wissenschaftlichen Medicin*, Frankfurt A. M. : Meidinger Sohn & Comp.

[51] Waxham, M. N. [2014], *From Molecules to Networks: An Introduction to Cellular and Molecular Neuroscience*, Elsevier.

[52] Werner, C. and Engelhard, K. [2007], 'Pathophysiology of traumatic brain injury', *British Journal of Anaesthesia* **99**(1), 4–9.

[53] Wintermark, M., Sanelli, P. C., Anzai, Y., Tsiouris, A. J. and Whitlow, C. T. [2015], 'Imaging evidence and recommendations for traumatic brain injury: Conventional neuroimaging techniques', *Journal of the American College of Radiology* **12**(2), e1–e14.

[54] World Health Organization [2001], 'Biomarkers in risk assessment : validity and validation'.

[55] Yue, X. and Wang, L. [2009], 'Deformation of skull bone as intracranial pressure changing', *African Journal of Biotechnology* **8**(5), 745–750.

[56] Zetterberg, H., Smith, D. H. and Blennow, K. [2013], 'Biomarkers of mild traumatic brain injury in cerebrospinal fluid and blood', *Nature Reviews Neurology* **9**(4), 201–210.

[57] Zuercher, M., Ummenhofer, W., Baltussen, A. and Walder, B. [2009], 'The use of Glasgow coma scale in injury assessment: A critical review', *Brain Injury* **23**(5), 371–384.

CHAPTER 3

RAMAN SPECTROSCOPY

Raman spectroscopy is a branch of optical spectroscopy that provides highly specific chemical information about a sample, which can be measured quickly and non-invasively. Furthermore, Raman spectrometers can be made compact, portable and have minimal energy requirements. These key advantages make Raman spectroscopy highly attractive in the field of biomedical imaging, but real-world applicability is hindered by a number of key issues [5, 22, 43]. This section provides a brief introduction to Raman spectroscopy, and highlights the challenges faced by Raman spectroscopy of biological tissue. Existing work from the literature is reviewed, with an emphasis on neurological and ophthalmic applications.

3.1 Raman Scattering

Raman spectroscopy is underpinned by Raman scattering, which describes the inelastic scattering of light through interaction with matter. The phenomenon was first predicted by Austrian physicist Adolf Smekal in 1923 and later shown experimentally by Kariamanikkam Srinivasa Krishnan and Sir Chandrashekhara Venkata Raman in 1928 [46, 49]. Smekal hypothesised based on an energy conservation argument for a system containing a photon of energy $h\nu$, and a molecule who's energy depends on a translational velocity, υ and it's quantum state E_m, the following:

$$\frac{M\upsilon^2}{2} + E_m + h\nu = \frac{M\upsilon'^2}{2} + E_n + h\nu' \tag{3.1}$$

where M is the mass of the molecule and n and m represent different quantum numbers. Conceptually, this process can be thought of as absorption of the photon by the molecule, promoting the molecule to a virtual energy state, followed by the instantaneous emission of a photon. The case where the final state is the same as the initial state for the molecule (m=n) is the more widely known Rayleigh or elastic scattering. The 1928 article by C.V. Raman showed the first experimental evidence of inelastic scattering [46]. Using a single spectrogram from a monochromatic light source incident on benzene, Krishnan and Raman demonstrated the presence of both red and blue shifted spectral lines. The latter describes the case where the scattered photon gains energy from the molecule in an existing excited state as 'negative absorption of radiation' [46].

Fundamental to quantum mechanics, is the notion that energy is quantised and can only occupy discrete energy states. In the case where the photon energy matches an allowed electronic transition, absorption occurs, followed by subsequent emission of a photon known as fluorescence as the electron returns to it's initial state. Both Raman scattering and fluorescence involve an energy exchange between a photon and a molecule, but are distinct optical processes. The important distinction is the timescale under which each phenomenon occurs. As previously stated, Raman scattering occurs instantaneously (i.e. the electron cannot occupy the virtual state), whereas for fluorescence there exists a real electron transition over a finite period of time. In the case of fluorescence, the emitted photon is always of lower energy (with the remaining energy dissipated as heat), and the change in wavelength termed the Stokes shift. Rather confusingly, Raman scattering inherits this nomenclature, but for Raman scattering the emitted photon may be of lower (Stokes) or higher (anti-Stokes) energy. The resultant energy transition of the molecule

($m \neq n$) occurs due to a change of the vibrational state of the molecule [10].

Molecular vibrational energy levels arise from degrees of freedom, which can be subdivided into translation, rotation and vibration. Translation and rotation refer to motion of the molecule as a whole in space, but the same degrees of freedom exist for each atom within the molecule, giving rise to vibrational states such as bond stretching or twisting [56]. At this point, it is useful to consider a molecular bond by a simple model of two masses connected by a spring, vibrating at some natural frequency. The Raman spectrum measures intensity against spatial frequency (wavenumber) with units of cm^{-1}. Using the mass on a spring example and given the quantisation of energy, the allowed vibrational states would appear as distinct lines in the spectrum. The spectrum of a molecule therefore provides a corresponding barcode or fingerprint based on chemical composition. Unfortunately the measured Raman spectrum does not appear as lines, but as bands with non-zero widths. This broadening occurs due to a number of reasons, which include the local environment of the molecule (temperature, pressure etc) and fundamentally limited by the uncertainty principle, since the lifetime of the excited state is finite and short lived, we cannot exactly measure the energy [21]. The Raman spectrum is commonly referred to in terms of discrete regions: the low wavenumber region (100-200 cm^{-1}); the fingerprint region (500-2000 cm^{-1}); and the high wavenumber region (2000-4000 cm^{-1}) [50]. In this section, we have briefly introduced the concept of Raman scattering alongside Rayleigh scattering and fluorescence (Fig. 3.1), but have not discussed how these may hinder or interfere with the measurement of Raman scattering. The reality is that Raman scattering yields by far the weakest signal of the three, with about one in every million scattering events being inelastic scatter. Furthermore, biological samples are inherently autofluorescent, but is

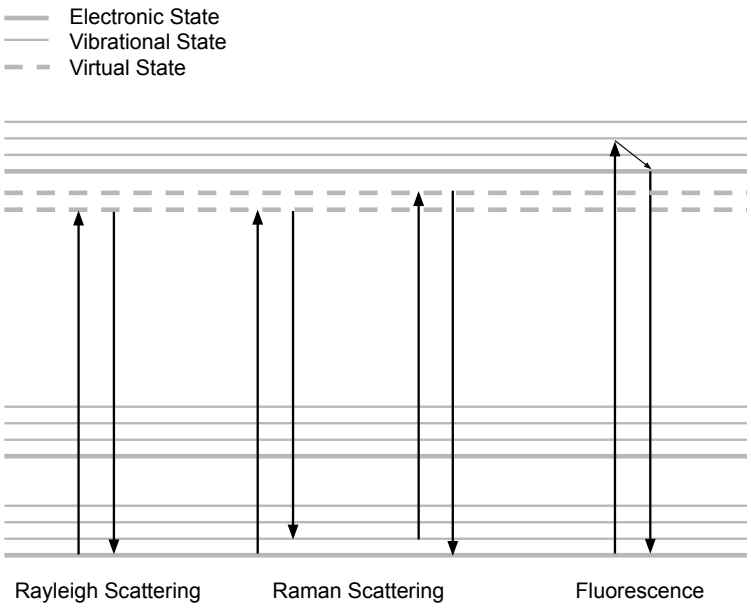

Figure 3.1: Overview of Rayleigh scattering, Raman (Stokes and anti-Stokes) scattering and fluorescence as energy level diagrams.

especially problematic in the retina, which contain lipofuscin pigments where fundus autofluorescence imaging is already used to detect some retinal abnormalities non-invasively [35]. A number of approaches can be employed to suppress fluorescence; one of the most promising of these being time resolved Raman spectroscopy [55]. This exploits the physical timescales under which each occurs as described previously, but requires more complicated instrumentation that at the present time remains niche in terms of commercially available systems.

3.2 Experimental Arrangement

As a result of the Raman effect being comparatively weak, a typical Raman instrument uses a laser focused through a high magnification microscope objective to illuminate a sample with monochromatic light. The high photon flux created at the focal point of the beam can then generate a detectable number of Raman scattering events. The scattered light is typically collected either *via* a forward-scattering (transmission) or back-scattering (reflection) geometry. An illustration of a typical back-scattering arrangement is shown in Fig. 3.2, where a laser is introduced into the optical path of a standard microscope, and the back-scattered light from the sample is collected *via* the microscope objective. Incident and collected light are typically separated by a dichroic beamsplitter. A confocal geometry is commonly applied, which rejects out of focus light, through the use of a slit. Before reaching the spectrometer, back-scattered Rayleigh light is suppressed by the introduction of a filter, such as a long pass filter. A number of spectrometer designs exist, but the most common uses a diffraction grating to spatially disperse the various Raman bands before being measured using a high sensitivity detector (usually a multi-stage cooled charge coupled device (CCD)) [50].

3.3 Raman Spectroscopy in Diagnostics

This section reviews both *ex-vivo* and *in-vivo* applications of Raman spectroscopy in the literature, with an emphasis on studies of tissue from the brain and the eye. Whilst our interest lies primarily in the use of Raman spectroscopy for *in-vivo* assessment, much

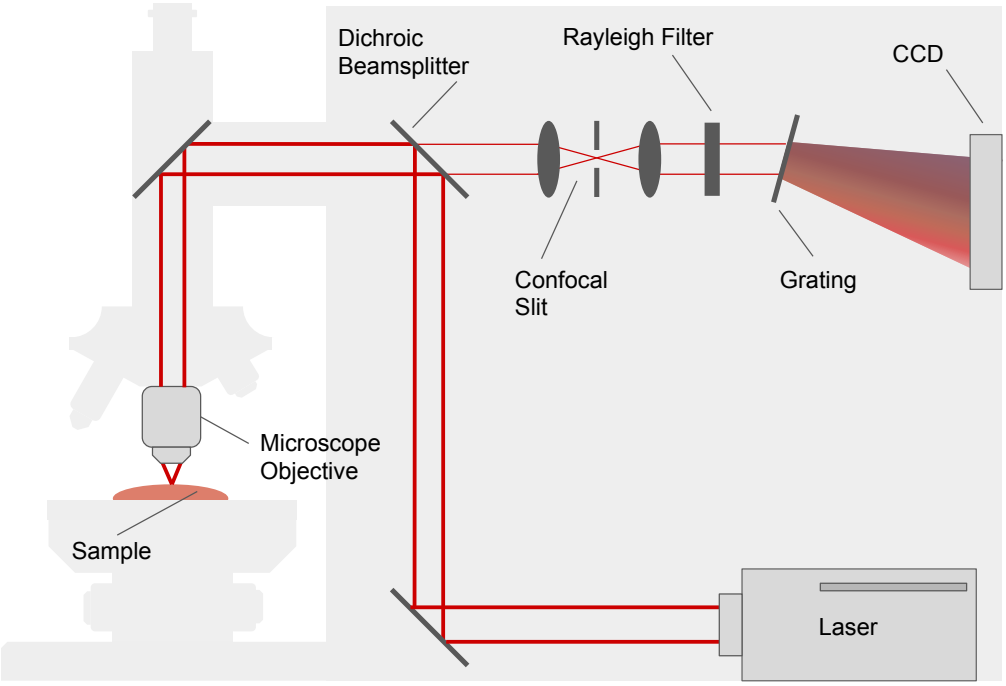

Figure 3.2: Illustration of typical confocal Raman spectroscopy arrangement.

of the current focus in the field is towards sensing applications using surface enhanced Raman spectroscopy (SERS) [15]. Bodily fluids such as blood, serum, saliva and urine are regularly collected clinically to aid in the diagnosis of a number of diseases. SERS allows for trace level detail to be detected from samples by exploiting optical effects, such as surface plasmon resonance from metallic nanoparticles, which enhance the local electric field and Raman signal in proximity to the sample [2]. The enhancement offered by SERS mitigates the inherent weakness of Raman spectroscopy and has the potential to provide timely diagnostics from trace levels of molecular disease biomarkers.

Despite these advantages, the issue of identifying target molecules in isolation remains a huge challenge from bodily fluid samples. Earlier, we asserted that Raman spectroscopy

provides a molecular fingerprint. However, for biological samples containing thousands of different compounds of varying sizes, the Raman spectrum begins to become convoluted as bands overlap. What results, is an unmixing problem not dissimilar from the classical cocktail party problem; where the challenge is to depict independent conversations amongst the noise of the room [13]. Numerous efforts have been made to address this issue, which can be broken down as either upstream or downstream to the measurement. Upstream efforts include the use of filtration, antibodies and physical methods to capture the molecules of interest and remove those which would confound the results [4, 9, 51]. Downstream methods use computational algorithms to decompose the signal or naively separate the data using multivariate techniques [4]. Multivariate methods used in Raman spectroscopy attempt to separate the data according to statistical properties inherent in the dataset, and are often essential to provide meaningful analysis from spectra of biological samples. The unmixing problem is further exacerbated by common sample preservation techniques for fluid and tissue samples (fixation, anti-coagulants, wax embedding and cryopreservation etc), which can dominate Raman spectra [12]. A final factor in the translation of SERS from laboratory to clinic has been a lack of reproducibility, in particular for nanoparticle based approaches [57].

A number of more recent studies have started to address these shortcomings, in efforts to scale up the technology [29, 33, 47]. Work by Rickard *et al.* demonstrated the efficacy of a SERS platform applied to TBI diagnostics, built using a one-step lithographic process and combined with microfluidics to physically separate plasma from whole blood [47]. By creating a library of Raman spectra for TBI biomarkers (S100-B, NAA, GFAP etc), concentration changes in severe TBI patients were identified with a high sensitivity, both

temporally and compared to control samples. The use of SERS has the potential to provide vast improvements over traditional assays (e.g. ELISA), with the ability to rapidly detect trace level (picomolar) concentrations of injury biomarkers, but comes with some of the same limitations identified in the previous chapter. Specifically, it is unclear whether the evolution of biomarker concentrations with time is related to patient recovery or associated with clearance from the body. Further work is also required to show that the method can be applied in discrimination between injury severity [47].

Here, we have given only an anecdotal introduction to SERS, to give a flavour for the current trends in the field of Raman spectroscopy. Unfortunately, SERS is fundamentally incompatible with our primary focus towards non-invasively identifying TBI *in-vivo* from the posterior of the eye. That said, many of the challenges in handling, storing and measuring biological samples remain relevant to our efforts, particularly for initial proof-of-concept studies using *ex-vivo* samples. By targeting tissue belonging to the CNS, we significantly reduce the need to filter out confounding compounds, where we technically measure from the brain side of the BBB.

3.3.1 Neurology

In neurology, there is a large emphasis on using Raman spectroscopy for cancer detection, in particular as an inter-operative guide during tumour resection [16, 26, 30]. The motivation for this partly comes from the diffuse nature of glioblastomas, where discrepancies between preoperative MRI scans lead to relapse from the resection margin. The availability of handheld Raman probes for industrial applications means that proof-of-concept interventions using Raman spectroscopy are straightforward to integrate into existing sur-

gical practice. The concept is highlighted across several publications by Jermyn *et al.* working in the group of Frederic Leblond [24–26]. The probe developed featured a compact concentric design, with a central excitation illumination fibre and peripheral collection fibres, which allowed for integration into existing surgical practice. By comparison to MRI, the use of Raman spectroscopy showed a greater specificity and sensitivity, centimetres beyond the region of detection using MRI. Following their initial *in-vivo* study, the group (perhaps somewhat confusingly) performed *ex-vivo* validation in a study that combined several different animal models and devices [16]. The work by Desroches *et al.* [16] extended the initial concept to show that high wavenumber bands alone can be used in the classification of cancerous tissue. Finally, the group have shown that the need to manually subtract background effects caused by fluorescent lights in the operating theatre can be ignored through the use of machine learning [25].

Along more fundamental lines of enquiry, the Raman spectra of different brain structures has been studied, with clear differences observable in the spectra of white matter and grey matter. The work by Kast *et al.* [31] acknowledges that Raman bands displaying key changes for white matter and grey matter come from a mixture of lipids and proteins. However, white matter contains a higher proportion of lipids and so by using peak ratios the authors were able to discriminate between tissue types. An unusual aspect, is the visual approach that was taken to present data from tissue biopsies. The bands at 1004, 1330:1344, and 1660 cm^{-1} were mapped to red, green and blue colour channels respectively, providing an immediate visual representation through colour mixing. These false colour images showed good agreement with histological staining, however, using this approach to visually show cancerous and necrotic tissue was less convincing. More work

in this study could have been done to show parity between the colours used in histology and the falsely coloured Raman map by creating a colour space mapping between histology images and Raman maps. This would allow clinical interpretation without the need for further user training, or to physically stain samples [31].

A similar analysis was performed by Koljenović *et al.* [34], using falsely coloured Raman image maps of tissue from both brain and bladder in a porcine model. In this study, the authors note design considerations when using fibre optics, which allows for the bulk laser/spectrometer setup to be kept away from tissue/patient measurements as discussed previously in the work by Desroches *et al.* [16]. As with later work in the Leblond group, Koljenović *et al.* highlight the practical importance of the high wavenumber region. Unlike the fingerprint region, the high wavenumber region is devoid of Raman scatter generated by silica fibres, which otherwise needs to be filtered out. Koljenović *et al.* show using false coloured Raman maps of porcine tissue, that the same diagnostic information can be generated from the high wavenumber region as fingerprint region [34]. This leads to the more general assertion that for preliminary studies, where the focus is on understanding the molecular changes observed and basic scientific understanding, the fingerprint region has higher value owing to having a greater number of peaks, and therefore deeper understanding of the underlying biochemistry. However, for translational applications, where the focus shifts to diagnostic discrimination and the physical design and dimensions of the device become more important; the high wavenumber region may serve as a better fit.

So far, we have discussed *in-vivo* and *ex-vivo* examples in the literature for using Raman spectroscopy to identify abnormalities in the brain, but these have all focused around the detection of cancer. In addition to cancer detection, Raman spectroscopy has been

shown to be sensitive to conformational changes in proteins, which has important implications for neurodegenerative diseases such as Alzheimer's and Parkinson's. Ji *et al.* [27] showed a blue shift of 10 cm^{-1} to the amide I band (1660 cm^{-1}) as a result of misfolded proteins in a murine model of Alzheimer's disease. Separately, Flynn *et al.* [20] studied the formation of α-synuclein amyloid fibrils associated with Parkinson's disease, as they aggregate from solution under differing pH levels and for mutant forms of the protein linked to early onset of the disease. As in the previous study, energy shifts to the amide I band were observed along with narrowing of the band with aggregation. These studies highlight the capability of Raman spectroscopy to show exquisite chemical information from biological samples, but the similarity in the observed changes between different diseases raises questions regarding specificity, which remain currently unanswered.

The first experiment showing that Raman spectroscopy is sensitive to biochemical changes following TBI was performed by Tay *et al.* [54] using a focal brain injury model (left motor cortex) in mice. Dramatic changes were observed in the spectral profile in response to injury, using the uninjured hemisphere as a control. Importantly, the authors showed that the results were largely unaffected by tissue fixation. Although the Raman analysis in this study was purely qualitative, immunohistology studies were also performed, showing that the observed changes may be linked to mitochondrial activity and apoptosis following injury [54]. More recent work by Surmacki *et al.* [53] has studied the temporal response to TBI at 2 and 7 days after injury, again in a murine model. In addition to changes from the hemisphere of injury (left), spectral changes were also observed from the contralateral hemisphere and seen to evolve with time. Unlike the previous study, attribution to the underlying biochemistry was made with reference to Raman spectra of brain specific lipids

to make qualitative attribution to a relative increase in cholesterol with injury.

Multivariate analysis was used in the form of principal component analysis (PCA), which is a dimensionality reduction technique using the inherent variance of the data. PCA projects the data onto the axis of greatest variance (the first principal component or PC1). Subsequent dimensions are along the direction of largest variance, subject to being orthogonal to the previous dimensions. Separation of data is usually displayed using scores plots as pairs of dimensions, which show how samples of different types (e.g. injured, control) lie in the PC space. These are accompanied by loadings plots, showing the spectral weighting associated with each component, allowing for identification of Raman bands in the spectra unique to each group (with reference to the scores plot) [11]. In the article by Surmacki *et al.* [53], the results displayed PC2 vs PC3 accounting for only 2.25 % and 0.78 % of the total variance in the data, and showed poor separation of the data. Although PC1 was not shown in the scores plot, the loadings were shown for PC1, PC2 and PC3, where PC1 accounted for 95.01 % of the total variance, indicating a large degree of similarity between the samples [53].

3.3.2 Ophthalmology

Surprisingly, given what may be a natural fear towards intentionally shining a laser into the eye, there has been a significant level of interest in the field of ophthalmology for the application of Raman spectroscopy [18]. This includes both the breadth of studies (with every anatomical layer of the eye being studied) to the degree of translation, including human clinical trials [41]. Encouragingly, some of the most promising results are from studies of the retina. These results show our initial aversion towards laser spectroscopy in

the eye may not be justified, with lasers being routinely used in ophthalmic applications for both diagnostics using optical coherence tomography (OCT) and corrective surgery [1, 42].

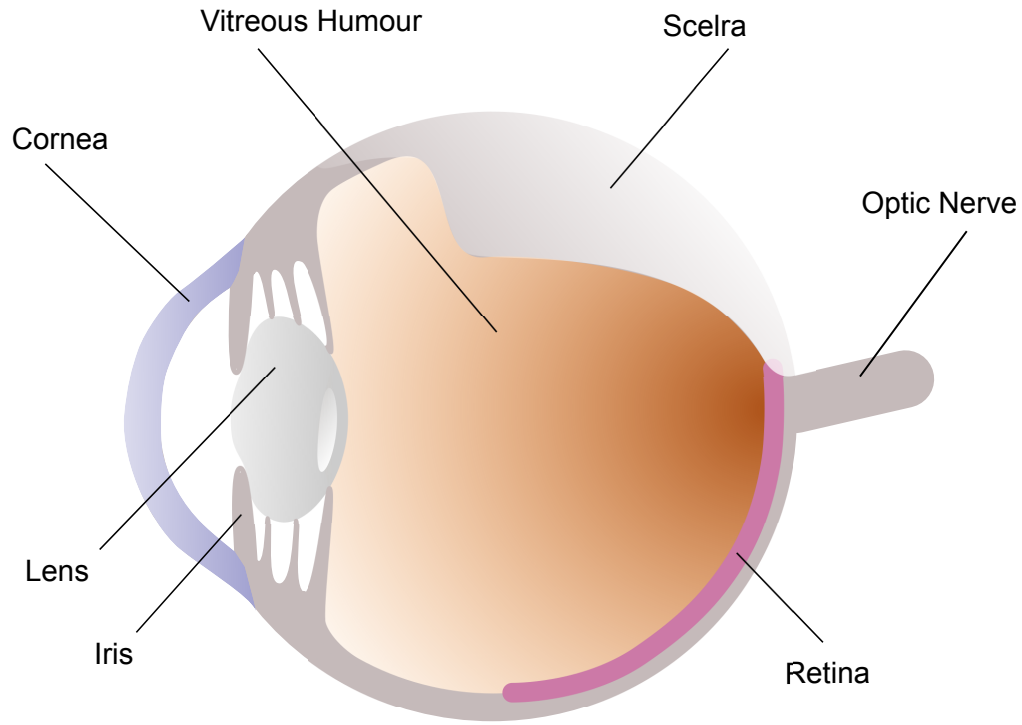

Figure 3.3: Illustration showing anatomy of the eye.

The eye is composed of several anatomical layers (Fig. 3.3), working together to capture and focus light onto the back of the eye, which is then converted to electrical signals interpreted by the brain. Forming a curved transparent barrier to the outside world, the cornea is responsible for over 70 % of the total refractive power of the eye. After passing through the cornea, light is further focused by the crystalline lens, which adjusts in shape to allow for focusing on near or distant objects. The main volume of the eye is occupied by the vitreous humour, composed mostly of water and containing a complex network of collagen. Finally, light is incident on the retina, which contains photoreceptive cells which

detect colour (cones) and intensity (rods) [3].

The cornea provides a tough external barrier, whilst simultaneously providing excellent transparency as a result of highly regulated collagen fibrils. Epithelial and endothelial cells at the anterior and posterior boundaries to the cornea actively maintain water levels, essential for optical clarity. An early study by Bauer *et al.* used the ratio of CH and OH bonds from the high wavenumber region to assess corneal hydration *in-vivo* in rabbits [7]. A small follow-up study was performed *in-vivo* in two legally blind humans, where hydration was manually controlled by the application of a mild dehydrating solution [6]. Targeting the cornea using Raman spectroscopy requires little modification from a laboratory setup, but there does not appear to be any further work beyond these preliminary studies. Most recently, a similar study in rabbits has been conducted, but using terahertz (far infrared) reflectometry, indicating that the measurement of corneal hydration remains a clinically unsolved problem [8].

The aqueous humour separates the cornea and lens, and consists of mostly water. Lambert *et al.* [36] suggested Raman spectroscopy of the aqueous humour could be used as an non-invasive method to monitor glucose levels in diabetics. Clinically relevant glucose concentrations were first measured in an artificial aqueous humour, followed by a study to compare eye safety trade-offs against measured signal in rabbits. *In-vitro* measurements from human aqueous humours were taken from patients undergoing cataract surgery, which was used to form a predictive model and mapping between blood glucose. [36, 37]. Again, there appear to be no further follow-on studies to show efficacy in humans. Instead, more recent work has focused on transcutaneous Raman measurements from skin [28]. The latter approach can be more easily incorporated into continuous un-

obtrusive patient monitoring through a wearable device, but requires more complex post processing to remove contributions from from skin tissue.

The crystalline lens contains a set of water-soluble proteins called crystallins, that form tightly packed aggregates to increase the refractive power, whilst maintaining transparency. The formation of cataracts (clouding of the lens) that leads to impaired vision, account for 50 % of all cases of blindness and is commonly associated with ageing [44]. Raman spectroscopy of the lens has focused primarily on *ex-vivo* investigations to study conformational changes to lens proteins with age [23]. It is curious that there are no examples of *in-vivo* Raman spectroscopy of the lens in the literature, given the number of *ex-vivo* studies.

The vitreous humour sits behind the crystalline lens and forms the largest tissue body in the eye, filling the space from the lens to the retina, having a gel-like structure and consisting mostly of water. A US patent exists for Raman spectroscopy of the vitreous, with a focus on the detection of glutamate as a marker of glaucoma or diabetic retinopathy [48]. Glaucoma is defined as damage to the optic nerve by pressure from fluid in the eye, and often has no symptoms. Diabetic retinopathy is a risk for patients with type I and II diabetes, where damage to blood vessels in the retina lead to a loss of vision [14, 45]. The data backing the patent are described by a publication in 2003, using *ex-vivo* porcine eyes spiked with glutamate. The results from this study are tenuous at best, with the authors admitting that contributions from the cornea and lens dominated the spectra. Measurements of glutamate were only successfully measured by using artificially high concentrations and removing the cornea and lens to leave an eye cup where the vitreous could be focused on directly. Unsurprisingly, the patent has since been abandoned [32].

Finally, light incident on the retina is captured somewhat like a camera by photoreceptive cells. The signal is transmitted along the optic nerve to the brain, which is interpreted as an image. A central area of the retina, known as the macula provides high resolution colour information, and another area of the eye subject to degradation with ageing (age-related macular degeneration (AMD)). In 2001, it was shown that resonance Raman spectroscopy could be applied to detect macular pigments from the retina, owing to the relatively unique property of the molecules to have electronic transitions in the visible spectrum (for obvious reasons). Resonance of the Raman effect occurs when the excitation laser energy is very close to the energy of an electronic transition, and so ideally suited to the task of detecting macular pigments. The results were shown to be successful *in-vivo* and have since gone on to clinical trials [19, 41].

More recently, Marro *et al.* [38] studied inflammation in murine retina cultures, and suggested the results could be applied to retinal damage in the case of multiple sclerosis (MS). An autoimmune disease of the nervous system, MS results in demyelination of axons mediated by microglia, resulting in visual, motor, sensory and psychological changes [17]. This is the first description of the use of Raman spectroscopy to study diseases effecting the brain, however, the primary focus in the study remained damage to the retina [38].

The tissue preparation method employed by Marro *et al.* is noteworthy, as this allowed the authors to model inflammatory responses over time *ex-vivo*. Retinae were dissected from mice, flat mounted into well plates, and cultured in cell media between spectroscopy measurements [39]. Changes to spectra were studied in terms of constituent biological components, by using multivariate analysis to fit from a ‘database’ of candidate molecules. Whilst this shows how Raman spectroscopy can be used to study cellular processes, the

authors acknowledged that this currently requires prior knowledge and assumptions, given limited completeness and availability of appropriate databases [38].

In 2019, Stiebing *et al.* [52] addressed the limitations of existing studies of the retina, where *in-vivo* measurements were only possible using resonant targets such as macular pigments. The experimental arrangement used optics that mimic the human eye in place of a microscope objective, and showed that Raman spectra could be measured from *ex-vivo* flat mounted human retina using a 785 nm excitation at eye safe laser powers [52]. Raman image maps over the retina were used to produce false colour images that show the spatial distribution of chemical species, and highlighting the fovea. However, the Raman maps took 6 hours to acquire, meaning that *in-vivo* acquisition would currently be limited to point measurements [52].

Despite large variation in the data caused by autofluorescence, major bands associated with lipids and proteins were identifiable through careful subtraction of the fluorescence signal. The authors presented the mean data smoothed to demonstrate comparison to a commercial confocal microscope. This effectively demonstrates the main Raman bands and proves the concept, but the applicability of such smoothing, which in effect removes data is questionable for any disease model. A final point of consideration is that the system assumed the pupil to be dilated, which can be performed by mydriatic drops, and is regularly used by opticians [40]. However, this would move a future diagnostic platform from non-invasive to minimally invasive, which would limit the usefulness in PoC TBI diagnostics. Paralysation using mydriatic drops dilates the pupil for hours to days, which would impede the monitoring of GCS measurements.

3.4 Conclusions

In this section we have shown that Raman spectroscopy can offer a label free mechanism for measuring changes to biochemistry, which can be applied *in-vivo* in invasive settings such as surgery, but has also shown promise for non-invasive measurement; in particular in the field of ophthalmology.

Given a rooting in more fundamental chemistry, the analysis of spectra from biological samples, formed of complex permutations of thousands of individual molecules in a single sample remains challenging. Historical chemometric analysis tools such as PCA are commonly used inappropriately in the literature in efforts to overcome the high dimensionality of the data, leaving both the author and reader underwhelmed and confused. By aiming to study posterior tissue through a thick heterogeneous sample (the eye), and indirectly detect subtle changes from brain injury, without the luxury of SERS, will require improvements to analysis methods.

The link between damage to the retina and CNS has been briefly noted in the literature [38], but this has not currently been applied to a specific model of disease or injury. In exploring whether it is fundamentally possible to study biochemical changes resultant from TBI, we will expand the possibilities of an emerging diagnostic platform.

3.5 References

[1] Adhi, M. and Duker, J. S. [2013], 'Optical coherence tomography – current and future applications', *Current Opinion in Ophthalmology* **24**(3), 213–221.

[2] Amendola, V., Pilot, R., Frasconi, M., Maragò, O. M. and Iatì, M. A. [2017], 'Surface plasmon resonance in gold nanoparticles: a review', *Journal of Physics: Condensed Matter* **29**(20), 203002.

[3] Artal, P. [2014], 'Optics of the eye and its impact in vision: a tutorial', *Advances in Optics and Photonics* **6**(3), 340.

[4] Atkins, C. G., Buckley, K., Blades, M. W. and Turner, R. F. [2017], 'Raman spectroscopy of blood and blood components', *Applied Spectroscopy* **71**(5), 767–793.

[5] Baker, M. J., Byrne, H. J., Chalmers, J., Gardner, P., Goodacre, R., Henderson, A., Kazarian, S. G., Martin, F. L., Moger, J., Stone, N. and Sulé-Suso, J. [2018], 'Clinical applications of infrared and Raman spectroscopy: state of play and future challenges', *The Analyst* **143**(8), 1735–1757.

[6] Bauer, N. J. C., Hendrikse, F. and March, W. F. [1999], 'In vivo confocal Raman spectroscopy of the human cornea', *Cornea* **18**(4), 483–488.

[7] Bauer, N. J., Wicksted, J. P., Jongsma, F. H., March, W. F., Hendrikse, F. and Motamedi, M. [1998], 'Noninvasive assessment of the hydration gradient across the cornea using confocal Raman spectroscopy.', *Investigative Ophthalmology & Visual Science* **39**(5), 831–5.

[8] Bennett, D., Taylor, Z., Tewari, P., Sung, S., Maccabi, A., Singh, R., Culjat, M., Grundfest, W., Hubschman, J.-P. and Brown, E. [2012], 'Assessment of corneal hydration sensing in the terahertz band: in vivo results at 100 GHz', *Journal of Biomedical Optics* **17**(9), 0970081.

[9] Bhamla, S., Benson, B., Chai, C., Katsikis, G., Johri, A. and Prakash, M. [2017], 'Hand-powered ultralow-cost paper centrifuge', *Nature Biomedical Engineering* **1**, 0009.

[10] Breit, G. [1932], 'Quantum theory of dispersion', *Reviews of Modern Physics* **4**(3), 504–576.

[11] Brereton, R. G. [2009], Exploratory data analysis, *in* 'Chemometrics for Pattern Recognition', John Wiley & Sons, Ltd, Chichester, UK, pp. 47–106.

[12] Butler, H. J., Ashton, L., Bird, B., Cinque, G., Curtis, K., Dorney, J., Esmonde-White, K., Fullwood, N. J., Gardner, B., Martin-Hirsch, P. L., Walsh, M. J., McAinsh, M. R., Stone, N. and Martin, F. L. [2016], 'Using Raman spectroscopy to characterize biological materials', *Nature Protocols* **11**(4), 664–687.

[13] Cherry, E. C. [1953], 'Some experiments on the recognition of speech, with one and with two ears', *The Journal of the Acoustical Society of America* **25**(5), 975–979.

[14] Cheung, N., Mitchell, P. and Wong, T. Y. [2010], Diabetic retinopathy, *in* 'The Lancet'.

[15] Chisanga, M., Muhamadali, H., Ellis, D. and Goodacre, R. [2019], 'Enhancing disease diagnosis: Biomedical applications of surface-enhanced Raman scattering', *Applied Sciences* **9**(6), 1163.

[16] Desroches, J., Jermyn, M., Pinto, M., Picot, F., Tremblay, M.-A., Obaid, S., Marple, E., Urmey, K., Trudel, D., Soulez, G., Guiot, M.-C., Wilson, B. C., Petrecca, K. and Leblond, F. [2018], 'A new method using Raman spectroscopy for in vivo targeted brain cancer tissue biopsy', *Scientific Reports* **8**(1), 1792.

[17] Dobson, R. and Giovannoni, G. [2019], 'Multiple sclerosis – a review', *European Journal of Neurology* **26**(1), 27–40.

[18] Erckens, R., Jongsma, F., Wicksted, J., Hendrikse, F., March, W. and Motamedi, M. [2001], 'Raman spectroscopy in ophthalmology: From experimental tool to applications in vivo', *Lasers in Medical Science* **16**(4), 236–252.

[19] Ermakov, I. V., McClane, R. W., Gellermann, W. and Bernstein, P. S. [2001], 'Resonant Raman detection of macular pigment levels in the living human retina', *Optics Letters* **26**(4), 202.

[20] Flynn, J. D., McGlinchey, R. P., Walker, R. L. and Lee, J. C. [2018], 'Structural features of α-synuclein amyloid fibrils revealed by Raman spectroscopy', *Journal of Biological Chemistry* **293**(3), 767–776.

[21] Gabrielse, G. and Dehmelt, H. [1985], 'Observation of inhibited spontaneous emission', *Physical Review Letters* **55**(1), 67–70.

[22] Hanlon, E. B., Manoharan, R., Koo, T.-W., Shafer, K. E., Motz, J. T., Fitzmaurice, M., Kramer, J. R., Itzkan, I., Dasari, R. R. and Feld, M. S. [2000], 'Prospects for in vivo Raman spectroscopy', **1**, 0–59.

[23] Huang, C. and Chen, W. [2018], 'Raman spectroscopic analysis of cataract lens: A compendious review', *Applied Spectroscopy Reviews* **53**(9), 689–702.

[24] Jermyn, M., Desroches, J., Mercier, J., St-Arnaud, K., Guiot, M.-C., Leblond, F. and Petrecca, K. [2016], 'Raman spectroscopy detects distant invasive brain can-

cer cells centimeters beyond MRI capability in humans', *Biomedical Optics Express* **7**(12), 5129.

[25] Jermyn, M., Desroches, J., Mercier, J., Tremblay, M.-A., St-Arnaud, K., Guiot, M.-C., Petrecca, K. and Leblond, F. [2016], 'Neural networks improve brain cancer detection with Raman spectroscopy in the presence of operating room light artifacts', *Journal of Biomedical Optics* **21**(9), 094002.

[26] Jermyn, M., Mok, K., Mercier, J., Desroches, J., Pichette, J., Saint-Arnaud, K., Bernstein, L., Guiot, M.-C., Petrecca, K. and Leblond, F. [2015], 'Intraoperative brain cancer detection with Raman spectroscopy in humans', *Science Translational Medicine* **7**(274).

[27] Ji, M., Arbel, M., Zhang, L., Freudiger, C. W., Hou, S. S., Lin, D., Yang, X., Bacskai, B. J. and Xie, X. S. [2018], 'Label-free imaging of amyloid plaques in Alzheimer's disease with stimulated Raman scattering microscopy', *Science Advances* **4**(11).

[28] Kang, J. W., Park, Y. S., Chang, H., Lee, W., Singh, S. P., Choi, W., Galindo, L. H., Dasari, R. R., Nam, S. H., Park, J. and So, P. T. C. [2020], 'Direct observation of glucose fingerprint using in vivo Raman spectroscopy', *Science Advances* **6**(4).

[29] Kanipe, K. N., Chidester, P. P. F., Stucky, G. D. and Moskovits, M. [2016], 'Large format surface-enhanced raman spectroscopy substrate optimized for enhancement and uniformity', *ACS Nano* **10**(8), 7566–7571. PMID: 27482725.

[30] Karabeber, H., Huang, R., Iacono, P., Samii, J. M., Pitter, K., Holland, E. C. and Kircher, M. F. [2014], 'Guiding brain tumor resection using surface-enhanced Raman

scattering nanoparticles and a hand-held Raman scanner', *ACS Nano* **8**(10), 9755–9766.

[31] Kast, R., Auner, G., Yurgelevic, S., Broadbent, B., Raghunathan, A., Poisson, L. M., Mikkelsen, T., Rosenblum, M. L. and Kalkanis, S. N. [2015], 'Identification of regions of normal grey matter and white matter from pathologic glioblastoma and necrosis in frozen sections using Raman imaging', *Journal of Neuro-Oncology* **125**(2), 287–295.

[32] Katz, A., Kruger, E. F., Minko, G., Liu, C. H., Rosen, R. B. and Alfano, R. R. [2003], 'Detection of glutamate in the eye by Raman spectroscopy', *Journal of Biomedical Optics* **8**(2), 167.

[33] Ko, J., Park, S.-G., Lee, S., Wang, X., Mun, C., Kim, S., Kim, D.-H. and Choo, J. [2018], 'Culture-free detection of bacterial pathogens on plasmonic nanopillar arrays using rapid raman mapping', *ACS Applied Materials & Interfaces* **10**(8), 6831–6840. PMID: 29405055.

[34] Koljenović, S., Bakker Schut, T. C., Wolthuis, R., de Jong, B., Santos, L., Caspers, P. J., Kros, J. M. and Puppels, G. J. [2005], 'Tissue characterization using high wave number Raman spectroscopy', *Journal of Biomedical Optics* **10**(3), 031116.

[35] Lam, L. A. [2012], Angioid Streaks, *in* 'Retina Fifth Edition', Vol. 2, Elsevier, pp. 1267–1273.

[36] Lambert, J. L., Morookian, J. M., Sirk, S. J. and Borchert, M. S. [2002], 'Measurement of aqueous glucose in a model anterior chamber using Raman spectroscopy', *Journal of Raman Spectroscopy* **33**(7), 524–529.

[37] Lambert, J. L., Pelletier, C. C. and Borchert, M. [2005], 'Glucose determination in human aqueous humor with Raman spectroscopy', *Journal of Biomedical Optics* **10**(3), 031110.

[38] Marro, M., Taubes, A., Abernathy, A., Balint, S., Moreno, B., Sanchez-Dalmau, B., Martínez-Lapiscina, E. H., Amat-Roldan, I., Petrov, D. and Villoslada, P. [2014], 'Dynamic molecular monitoring of retina inflammation by in vivo Raman spectroscopy coupled with multivariate analysis', *Journal of Biophotonics* **7**(9), 724–734.

[39] Mertsch, K., Hanisch, U., Kettenmann, H. and Schnitzer, J. [2001], 'Characterization of microglial cells and their response to stimulation in an organotypic retinal culture system', *The Journal of Comparative Neurology* **431**(2), 217–227.

[40] NICE [2020], 'Mydriatics and cycloplegics', `https://bnf.nice.org.uk/treatment-summary/mydriatics-and-cycloplegics.html`.

[41] Obana, A., Hiramitsu, T., Gohto, Y., Ohira, A., Mizuno, S., Hirano, T., Bernstein, P. S., Fujii, H., Iseki, K., Tanito, M. and Hotta, Y. [2008], 'Macular carotenoid levels of normal subjects and age-related maculopathy patients in a japanese population', *Ophthalmology* **115**(1), 147–157.

[42] Optical Express [2020], 'LASIK eye surgery', `https://www.opticalexpress.co.uk/laser-eye-surgery/lasik`.

[43] Owens, N. A., Laurentius, L. B., Porter, M. D., Li, Q., Wang, S. and Chatterjee, D. [2018], 'Handheld Raman spectrometer instrumentation for quantitative tuberculosis

biomarker detection: A performance assessment for point-of-need infectious disease diagnostics', *Applied Spectroscopy* **72**(7), 1104–1115.

[44] Pascolini, D. and Mariotti, S. P. [2012], 'Global estimates of visual impairment: 2010', *British Journal of Ophthalmology* **96**(5), 614–618.

[45] Quigley, H. A. [2011], Glaucoma, *in* 'The Lancet'.

[46] Raman, C. V. and Krishnan, K. S. [1928], 'The negative absorption of radiation', *Nature* **122**(3062), 12–13.

[47] Rickard, J. J., Di-Pietro, V., Smith, D. J., Davies, D. J., Belli, A. and Oppenheimer, P. G. [2020], 'Rapid optofluidic detection of biomarkers for traumatic brain injury via surface-enhanced Raman spectroscopy', *Nature Biomedical Engineering* .

[48] Rosen, R., Kruger, E., Katz, A. and Alfano, R. [2002], 'Method and system for detection by Raman measurements of bimolecular markers in the vitreous humor'. US Patent 2002/00952.57 A1.

[49] Smekal, A. [1923], 'Zur quantentheorie der dispersion', *Die Naturwissenschaften* **11**(43), 873–875.

[50] Smith, E. and Dent, G. [2005], *Modern Raman spectroscopy - A practical approach*, Wiley.

[51] Smolsky, J., Kaur, S., Hayashi, C., Batra, S. and Krasnoslobodtsev, A. [2017], 'Surface-enhanced Raman scattering-based immunoassay technologies for detection of disease biomarkers', *Biosensors* **7**(4), 7.

[52] Stiebing, C., Schie, I. W., Knorr, F., Schmitt, M., Keijzer, N., Kleemann, R., Jahn, I. J., Jahn, M., Kiliaan, A. J., Ginner, L., Lichtenegger, A., Drexler, W., Leitgeb, R. A. and Popp, J. [2019], 'Nonresonant Raman spectroscopy of isolated human retina samples complying with laser safety regulations for in vivo measurements', *Neurophotonics* **6**(04), 1.

[53] Surmacki, J. M., Woodhams, B. J., Haslehurst, A., Ponder, B. A. J. and Bohndiek, S. E. [2018], 'Raman micro-spectroscopy for accurate identification of primary human bronchial epithelial cells', *Scientific Reports* **8**(1), 12604.

[54] Tay, L., Tremblay, R. G., Hulse, J., Zurakowski, B., Thompson, M. and Bani-Yaghoub, M. [2011], 'Detection of acute brain injury by Raman spectral signature', *The Analyst* **136**(8), 1620.

[55] Timegate instruments Ltd [2020], 'Timegated technology', `https://www.timegate.com/timegated-technology`.

[56] Wartewig, S. [2003], *IR and Raman Spectroscopy*, Wiley.

[57] Xiong, M. and Ye, J. [2014], 'Reproducibility in surface-enhanced Raman spectroscopy', *Journal of Shanghai Jiaotong University (Science)* **19**(6), 681–690.

CHAPTER 4

DEVELOPMENT OF THE SELF OPTIMISING KOHONEN INDEX NETWORK (SKINET) FOR RAMAN SPECTROSCOPY BASED DETECTION OF ANATOMICAL EYE TISSUE

4.1 Abstract

Raman spectroscopy shows promise as a tool for timely diagnostics via *in-vivo* spectroscopy of the eye, for a number of ophthalmic diseases. By measuring the inelastic scattering of light, Raman spectroscopy is able to reveal detailed chemical characteristics, but is an inherently weak effect resulting in noisy complex signal, which is often difficult to analyse. Here, we embraced that noise to develop the self optimising Kohonen index network (SKiNET), and provide a generic framework for multivariate analysis that simultaneously provides dimensionality reduction, feature extraction and multi-class classification as part of a seamless interface. The method was tested by classification of anatomical *ex-vivo* eye tissue segments from porcine eyes, yielding an accuracy $>$ 93 % across 5 tissue types. Unlike traditional packages, the method performs data analysis directly in the web browser through modern web and cloud technologies as an open source extendable web app. The unprecedented accuracy and clarity of the SKiNET methodology has the potential to revolutionise the use of Raman spectroscopy for *in-vivo* applications.

4.2 Introduction

Raman spectroscopy is a non-invasive technique for immediate detection and analyses of the biochemical composition of analytes by measurement of the inelastic scattering of light. A schematic showing a typical experimental arrangement is shown in Fig. 4.1a, where longer wavelength inelastically scattered light from the sample is directed to a spectrometer via a beamsplitter. It is one of most sensitive optical spectroscopy methods yet

can be packaged as a hand-held device [19, 32]. Therefore, there is a considerable interest in applying Raman spectroscopy for the point-of-care detection of clinical biomarkers. Ophthalmic applications have received particular interest, as the optically clear nature of the eye provides a convenient route for *in-vivo* measurements [3, 12, 13, 26, 27, 31]. The

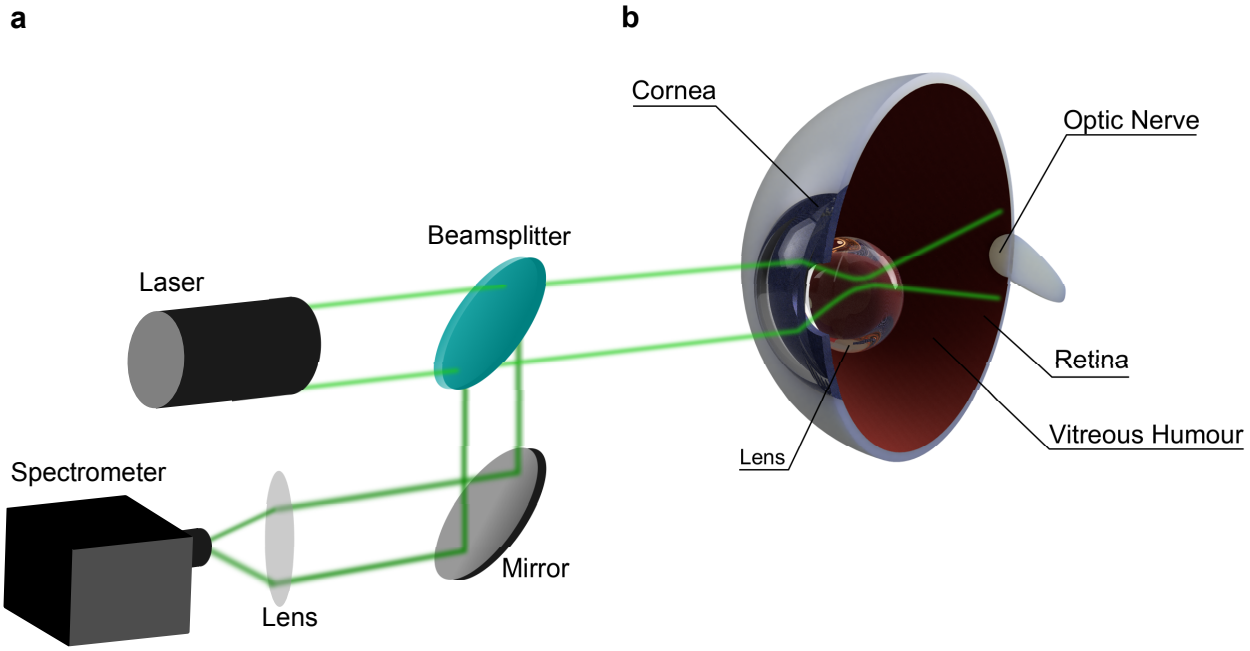

Figure 4.1: Illustration of Raman spectroscopy experimental arrangement and anatomy of the eye.

a, Illustration of typical Raman spectroscopy setup. Light from a laser is focused into the eye. Backscattered light is then directed via a beamsplitter to a spectrometer. **b**, Schematic of the eye.

eye consists of a number of anatomical layers (Fig. 4.1b), each with their own specific functions, which are biologically and chemically distinct. Despite studies highlighting the potential for early diagnostics of diseases that target a specific tissue type, there is currently no direct comparison of Raman spectra from each anatomical tissue layer. Whilst

Raman spectroscopy offers excellent chemical specificity, biological samples form complex permutations built from only a few amino acid building blocks, resulting in considerable spectral overlap and complex data analysis [7]. The problem is further compounded by poor signal to noise as a result of the Raman effect being relatively weak. Particularly for diagnostic applications, it is crucial to be able to accurately identify and understand the signal originating from different parts of the eye. In addition to eye tissue, the optic nerve was included as an additional class, as this represents a particularly interesting target for applications beyond ophthalmology. Forming part of the central nervous system, the optic nerve is technically part of the brain and lies at the same focal plane as the retina. The ability to spectrally isolate and characterise the optic nerve from the rest of the eye would lay foundations for further diagnostic possibilities of major neurological diseases including for instance: traumatic brain injury, multiple sclerosis or Alzheimer's disease.

The analysis of such datasets is often conducted as a workflow of three stages: projection, feature extraction and classification. The initial step (projection) aims to show spatial separation of data from spectra according to different types or classes in two or three dimensions. Feature extraction then follows, with the aim of understanding what Raman bands in the data cause any separation observed in the projection step. Finally, this information is used to build a classification model, that can make accurate predictions about future unlabelled data.

In the field of Raman spectroscopy and even more generally in chemometrics, PCA is favoured for projection and feature extraction, followed by partial least squares discriminant analysis (PLS-DA) and more recently deep learning models for classification [21, 22, 34]. However, PCA routinely shows poorly defined class boundaries, struggles with large intra-

class variance (such as biological samples) and quickly breaks down for multi-class problems [9]. Furthermore, classification is often handled in isolation to projection and feature extraction, forming a semantic disconnect, and whilst deep learning has shown impressive classification results, these methods offer no insight into the underlying physical and chemical changes.

Our aim is to provide a single method to address each of these stages, connected by a single mathematical principle and improve on the issues found using PCA based approaches. Work by Brereton *et al.* highlighted the use of the self organising map (SOM) applied to nuclear magnetic resonance (NMR) spectroscopy in comparison to PCA, and showed much clearer visualisations. The work was further extended to support feature extraction and classification using SOMs by the introduction of the self organising map discriminant index (SOMDI) [5, 23, 37].

Here, we develop an improved SOMDI based supervised learning method, defined as the self optimising Kohonen index network (SKiNET) to demonstrate effective classification, and illustrate the complete linked workflow from projection to classification by means of a user-friendly web app [2]. This represents a major shift, that follows a growing trend in industry to move from traditional desktop applications to the cloud (including office suites, multimedia editing and computer aided design (CAD)) and yet the advantages of connected scalable applications are seldom leveraged in the scientific community.

The SOM or Kohonen map was first described by Teuvo Kohonen in 1982 as a model inspired by nature and the way that neurons in the visual cortex are spatially organised according to the type of visual stimuli [18]. The SOM defines a 2D map of neurons, typically arranged as a grid of hexagons. Each neuron is assigned a weight vector, which is

initialised randomly and has a length equal to the number of variables in a spectrum. The weight vector effects which neuron will be activated for a given sample and neighbouring neurons will have similar weights. Spatial clustering is therefore observed in the trained map, with spectra that exhibit distinct properties activating different neurons. In order to understand which features in the data cause certain neurons to activate over others, the SOMDI was used [23]. The SOMDI introduces class vectors as labels for each spectrum and corresponding weight vectors for each neuron, without influencing the training process. These allow for the identification of what type of data a given neuron activates, which can be used to inspect the weights across all neurons and extract prominent features belonging to each class.

4.3 Results

Raman spectra were randomly sampled from tissue segments from 11 separate enucleated eyes, by acquiring coarse map scans of 88 spectra per tissue segment. The aqueous humour sitting between the cornea and crystalline lens, consisting mostly of water, was neglected. Fig. 4.2a shows averaged spectra representative of each tissue type, or class to be identified. Individual Raman spectra were kept consciously noisy by using a short acquisition time and limited laser power, to be representative of real world applications, which are limited by both scan time and maximum permissible exposure (MPE) defining eye safe limits [36]. Examples of typical raw spectra (after cosmic ray removal and baseline subtraction) are shown in Fig. 4.2b. Whilst the averaged spectra across each class showed obvious spectral differences, a large degree of variance was seen across each

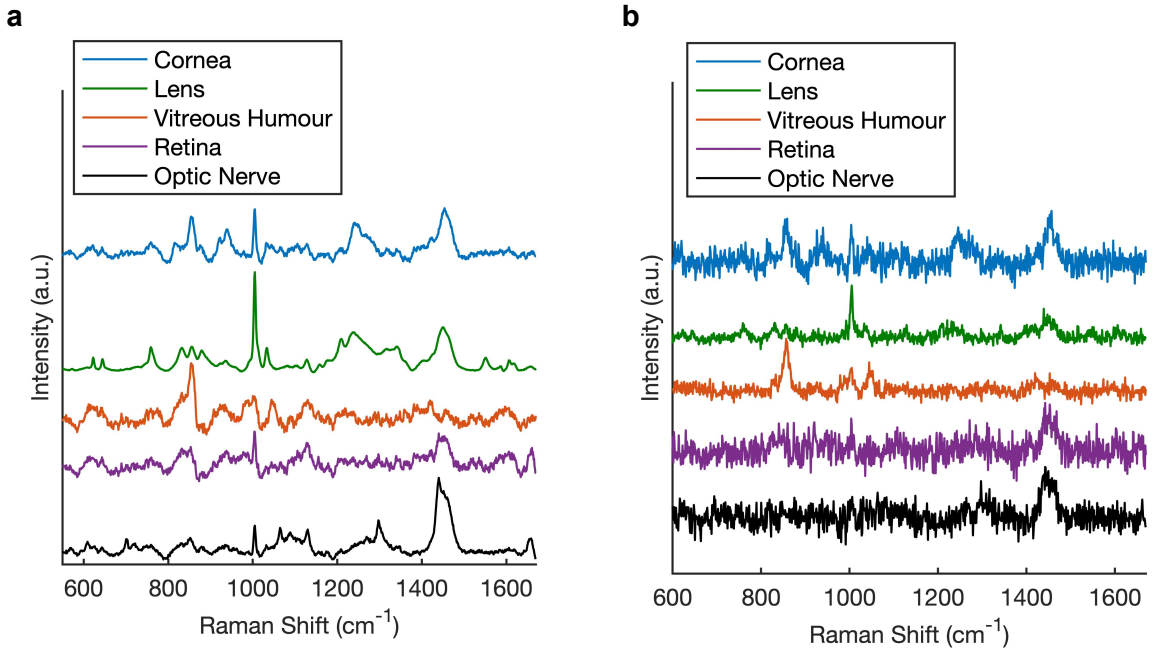

Figure 4.2: Raman Spectra of eye tissue.

a, Averaged Raman spectra from isolated tissue segments of each anatomical layer. **b**, Typical raw spectra for each tissue type used for training and classification.

map scan (Appendix A.1). As neural networks are data hungry algorithms by nature, it was hypothesised that a meaningful model could be trained by using a large enough number of noisy inputs. Initially, a 25 % partition from each class of the 4840 spectra were reserved for test data.

Our results are presented as a typical multivariate analysis workflow of: (1) projection of the hyperspectral data set into 2D space; (2) feature extraction to identify which spectral bands are characteristic of each tissue type and (3) a classification model to automatically identify the origin of an unknown spectrum. In each case, the SOM shows dramatic improvement over PCA based methods, offering better presentation of the data, clearer

insights and greater classification accuracy.

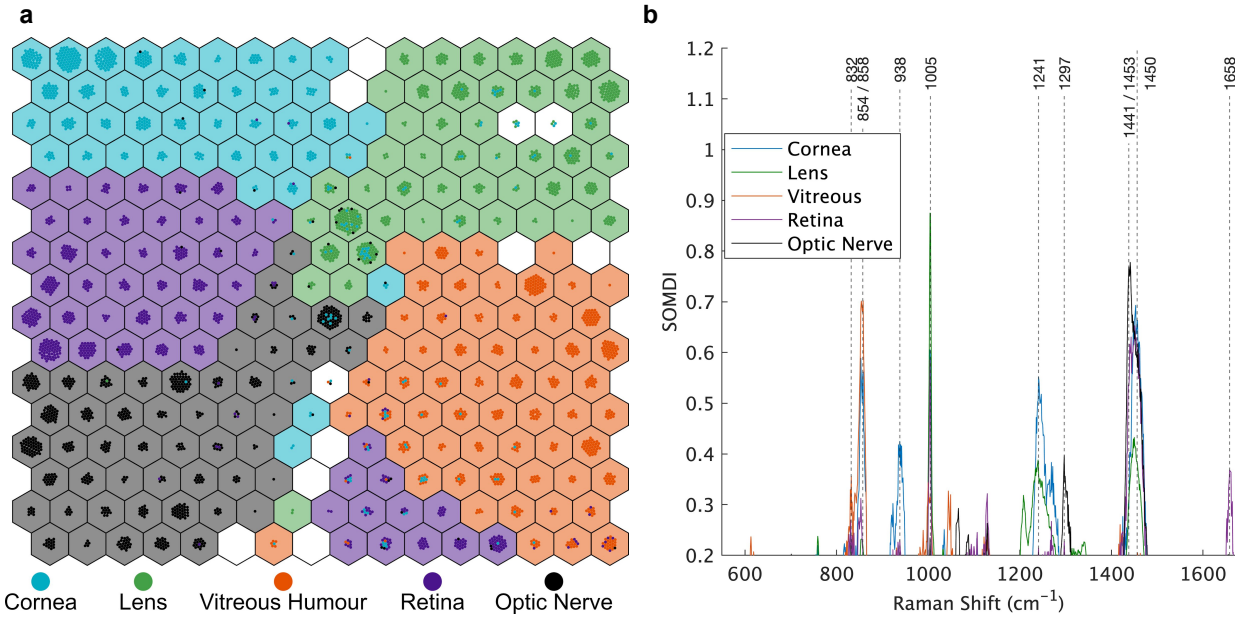

Figure 4.3: Dimensionality reduction and feature extraction of eye tissue spectra using SOMs.

a, SOM trained on spectra across the 5 eye tissue types. **b**, SOMDI showing relative importance of different bands for each class to observed clustering in the SOM.

4.3.1 Data Projection

Fig. 4.3a shows a clear separation of the data from the five tissue classes arranged as a 16x16 SOM, trained on spectra from the five tissue classes. Neurons (hexagons) are coloured according to the modal class they activate, from the training set of Raman spectra. Neurons that have no majority class or activate non of the training data are shown in white. Coloured circles within each neuron represent spectra from the training data that have been activated for that neuron. To aid visualisation, circles have been forced to not overlap in

space using the D3-force library [4], providing an alternative mechanism to display sample frequency and class overlap for each neuron. Note that almost all of the available white space in the figure is used completely. For each class, there is a clearly defined block of neurons, with many of these activating only a single tissue type. An approximately even distribution in the number of neurons required to identify each class is observed, with a slightly higher weighting for the vitreous humour. As a result of the vitreous humour consisting mainly of water and containing very few cells, the additional effort required by the network to isolate the tissue can be observed in the map. This can be considered by analogy to how the brain associates a larger number of neurons to facial features, than for example arms and legs (the cortical homunculus).

The majority of poorly separated samples are located centrally at the boundary between classes and extend down to the bottom edge of the map. Interestingly, in this region, there is a cluster of samples predominately corresponding to the retina, indicating that a number of retina samples are particularly noisy, further corroborated by being spatially located near other neurons that also lack any well defined class. While the SOM is analogous to the PCA scores plot (Appendix A.2a), PCA performs particularly badly when compared against the SOM. However, it should be noted that the level of separation observed by PCA is completely inline with results commonly reported in the literature. Since PCA relies on separation by variance in the data, the class clusters are bound around a central point, as a result of noise or absence or spectral features, causing significant spatial overlap.

4.3.2 Feature Extraction

The SOMDI provides a representation of weights associated with neurons that identify a particular class. A higher SOMDI intensity indicates a greater importance of particular inverse centimetres along the x-axis of a spectrum. Fig. 4.3b shows the SOMDI overlaid for each class, where the most important Raman bands associated with each tissue layer can be easily identified. Despite the level of noise in the original data, well defined peaks are resolved in Fig. 4.3b, which are either more prominent or unique to each class. Strong weights are attributed to the cornea at 938 (C-C stretch) and 1241 cm^{-1} (C-N stretch), which also correspond, with a certain confidence, to the stretching modes of the C-C backbone and amide III modes of collagen.

The crystalline lens of the eye is predominately identified by a very strong SOMDI weight at 1005 cm^{-1} (2,4,6 C radial) and is attributed to phenylalanine, which is abundant in water-soluble proteins present in the lens and directly relates to the tissue's function. The high polarisability of this molecule, which results in a large Raman scattering cross-section, aids in increasing the refractive index of the lens thus, providing fine focusing of light onto the retina. The vitreous humour is more challenging to isolate, with the strongest weights at 854, 858 cm^{-1} overlapping with significant weights for cornea, which have been associated with proline in collagen, along with small distinct weights at 832, 1044 and 1049 cm^{-1}. These bands may be indicative of the difference in collagen type found in the cornea versus the vitreous humour (type I vs. type II respectively) yet, a direct comparison of the two protein types is further required to support this postulation. The interpretation and discrimination of collagen types by Raman spectroscopy is currently an active area of

interest, where SKiNET may also offer additional insight [14, 15].

The remaining two classes of retina and the optic nerve are perhaps the most intriguing, located within the same focal plane, with the optic nerve connecting directly to the brain. An isolated peak at 1658 cm^{-1} (C=O stretch) identifies the retina and is associated with amide I (α-helix) groups in proteins. The detection of light by rods and cones in turn, relies on photo-receptive proteins known as opsins, which have an α-helical secondary structure. In contrast, the optic nerve can be characterised by a strong weight at 1441 (CH2 scissoring, CH3 bending) and 1297 (CH2 deformations) cm^{-1}, strongly associated with lipids and fatty acids. The brain is composed of nearly 60 % fat, with lipids and fatty acids playing important roles in brain function, which here we observe as a clear marker for the distinction between brain and eye tissue via Raman spectroscopy [8]. Furthermore, the optic nerve is devoid of photo-receptive cells and responsible for the blind spot in humans and therefore, the peaks at 1441 and 1658 cm^{-1} act as biologically relevant markers for each [16]. Individual bond assignments were made with reference to Larkin [20], and associations to high level biological structures based on the work by Talari *et al.* and Movasaghi *et al.*, providing databases of Raman bands found in biological tissue [25, 35].

Finally, unlike PCA loadings, which are often used to show similar information, the SOMDI can be interpreted in isolation. Conversely, PCA loadings are only relevant to a direction in PC space, relying on constant reference to the scores plot, which quickly become cumbersome for multi-class problems or where multiple PC scores are considered (Appendix A.2b).

4.3.3 Classification

Automated classification of Raman spectra and assignment to a particular tissue type or disease state is perhaps the most important step for the translation of Raman-based diagnostic techniques to real-world, clinical applications. However, whilst SOMs have historically been used for visual separation of data, experimental results of classification are rare. The most common method is to look-up the modal class of the neuron activated for a test sample, as used to colour neurons in Fig 4.3a. Since the SOMDI automatically provides class labels, the maximum SOMDI weight can also be used to perform class identification of any given neuron. However, both of these methods remain unsupervised learning mechanisms, without optimisation towards the correct answer in the training set. This is in contrast to widely used supervised learning algorithms, such as multi-layer perceptrons (MLP), support vector machines (SVM), PLS-DA and k-nearest neighbours (kNN) [17, 30, 33].

Supervised learning can be introduced to SOMs by allowing the class weights used for the SOMDI to influence the learning process. For large enough label values, this effectively forces the map to cluster, however can result in over-fitting [37]. For our data, no benefit was observed using this method over the modal class on the unsupervised SOM (Appendix A.3). Instead, a concept from learning vector quantisation (LVQ) was applied to the trained map and defined as a self optimising Kohonen index network (SKiNET). A penalty is introduced for spectra (from the training set) that activate neurons identifying a different class. This has a natural tendency to self-optimise, with the identical behaviour to the vanilla SOM when training data activate the correct class. Fig. 4.4a shows the

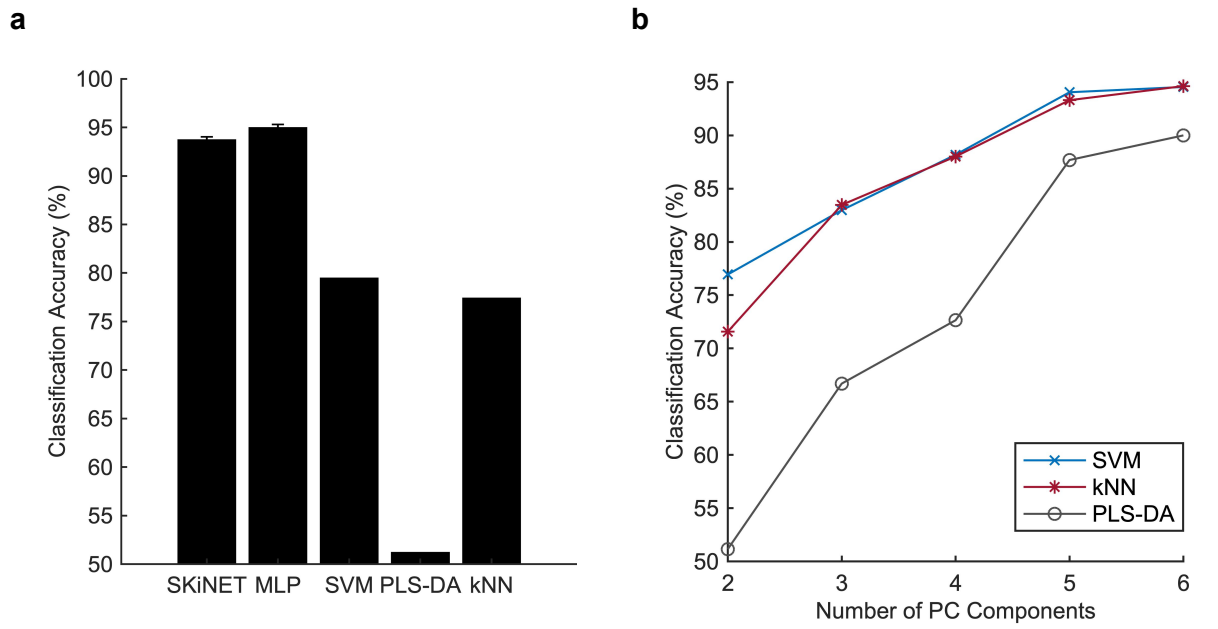

Figure 4.4: Classification performance of SKiNET against current state-of-the-art.

a, Classification accuracy of tissue using SKiNET against current state-of-the-art (multi-layer perceptrons (MLP), support vector machines (SVM), partial least squares discriminant analysis (PLS-DA) and k-nearest neighbours (kNN)). **b**, Effect of number of principal components on classification accuracy for PCA based methods.

classification accuracy across all five tissue types using SKiNET, *vs* current state of the art methods. A 25 % partition of the original data set was randomly assigned as test data and not used for training and optimisation of the network. The remaining 75 % was used to optimise hyper-parameters of each classifier, which were tuned by performing 10-fold stratified cross validation. Most notable is the considerable improvement over PLS-DA, which is perhaps the most widely adopted method in chemometrics [6]. PCA was used as a dimensionality reduction method prior to classification for SVM, PLS-DA and kNN. It should be emphasised that only the first two principal components were kept. Fig 4.4b

shows that by including a larger number of components, each of the classification methods can achieve a similar accuracy. The case of keeping more components for classification than are used for projection and feature extraction is routinely used in the literature. The alternative is to show several pairwise PCA scores plots, which arguably leaves the data in a high dimensional space [11, 21, 34].

However, by implementing SKiNET we are able to achieve a classification accuracy equivalent to keeping 6 components, whilst still being able to fully separate the data in only two spatial dimensions; equivalent to using 2 PCA components. Additionally, SKiNET showed a comparable performance to MLP, whilst providing clear visualisations and feature extraction that MLP and other neural network based methods lack. The confusion matrix (Appendix A.1) provides a breakdown of test samples classified into each class, and highlights the stability of the method across each of the five tissue types.

4.4 Discussion

The use of spectral fingerprints for clinical diagnostics requires two major components: the ability to quickly and accurately distinguish between different states (such as tissue types or diseases) and an understanding of the underlying chemical differences that enable such separation. The former is driven by an obvious need to perform timely diagnostics, but these decisions must be underpinned by biologically relevant changes. These issues are usually treated in isolation by multivariate techniques, with the best classification methods providing no insight into their nature. SKiNET addresses this disconnect, by using a single, simple architecture to provide clear visualisations and a high classification accuracy,

whilst retaining an understanding of the major chemical differences between classes. Furthermore, the SOM removes the need for much of the linear algebra and matrix notation required to fully appreciate PCA. Instead, the SOM can be adequately described using only addition and subtraction.

We reiterate that SOMs can offer a vastly superior spatial separation of chemometric data, that has now been demonstrated for both NMR and Raman spectroscopy. The SOM can be considered mathematically as a non-linear equivalent to PCA, and therefore hints that these data may not in fact be linearly separable, as would normally be assumed from Raman spectroscopy and is a requirement for PCA to be valid [17]. Our assertion is that the inherent heterogeneity combined with spectral overlap could easily lead to this condition for biological samples. Despite the level of overlap and noise present in our raw data, the SOMDI offers a convenient method to quickly isolate important bands and automatically act as a noise filter. By using the SOMDI it was possible to easily identify prominent markers for bulk tissue properties in each of the tissue types considered.

LVQ offers a convenient means of introducing supervised learning into the SOM, however, there are several variations of the LVQ algorithm that have not been explored here. This remains an area for future work, in addition to automatically setting the map parameters such as number of neurons, neighbourhood size, and an adaptive learning rate. Finally, it was shown that SOMDI weights could act as iterative class labels that are present throughout the learning process and change dynamically. As a result, there is scope to explore SKiNET based classification in conjunction with other SOM optimisation methods, that presently rely on a hit count (majority voting), which requires placing all of the training data into the SOM at every learning step where we wish to identify the winning class for

a given neuron [28]. Since the SOMDI provides a constant dynamic neuron identifier, this would allow for scaling to larger training sets using such methods.

In general, SKiNET was seen to offer a huge classification improvement over existing methods, performing particularly better than PLS-DA, which is the current *status quo* in chemometrics. Several of the points stressed here have been mentioned in other publications across different disciplines, but never cohesively. It is therefore of equal importance that the entry point for SKiNET is not to download, buy a software package or compile scripts; but simply visit a website and upload data.

The ability to quickly identify tissue from the noisy spectral response of a short acquisition, as demonstrated here represents an important stepping stone towards the practical applicability of *in-vivo* ophthalmic Raman spectroscopy, allowing for the capture of clean signal in the region of interest only. Filtered signal could then be fed into a second SKiNET model designed to distinguish between specific disease states.

4.5 Methods

4.5.1 Self-optimising Kohonen Index Network (SKiNET)

The SOM is represented by a set of neurons arranged in a (hexagonal) grid. Here, we describe the basic SOM algorithm with SOMDI variables added for feature extraction [18, 23]. We then describe how LVQ is included as an additional step to provide supervised learning, whilst using the SOMDI to identify each neuron class. Variables definitions are shown in Table 4.1 for reference. In each case, the capitalised letter represents the set for

a given variable, e.g., the SOM contains a grid of N neurons.

Variable	Description	Length
i	A single spectrum	1015
j	Spectrum class label vector	5
s	Training sample and label	[i, j]
n	A neuron	
w	Spectrum weight vector	length(i)
c	Class weight vector	length(j)
t	training step	integer

Table 4.1: Definitions of variables used to describe SOM and SKiNET.

Initially, every neuron is assigned weight vectors w (spectrum weight) and c (class weight), which are randomly initialised. The SOM is then trained according to the following algorithm:

1. Select a sample s at random from S
2. Calculate the euclidean distance, d for each n:
   $d = \sqrt{i^2 + w^2}$
3. Define the best matching unit (BMU) as the neuron with minimum d
4. Update weights, w and c of each neuron be similar to the input:
   $scaleFactor = neighbourhood(BMU, t) * learningRate(t)$
   $w = w + scaleFactor * (i - w)$
   $c = c + scaleFactor * (j - c)$

The map is gradually trained by repeating these steps numerous times. The update step applied in step 4 depends on a $neighbourhood$ function which ensures neurons closest to

the best matching unit (BMU) are effected most (according to a Gaussian function), with a decreasing neighbourhood size with each t. Secondly a $learningRate$ influences the update criteria, which linearly decreases with each iteration, t from a fixed initial starting value. To note, while class weights are updated in steps 4, they play no role in step 2, i.e., the spectra alone are responsible for finding the BMU.

The class vectors J have values of 1 for a given index or otherwise 0, e.g., [1, 0, 0 , 0, 0] and [0, 1, 0, 0, 0] representing labels for two of the five classes. As the map is trained, the neuron class vectors C become close to 1 as the neuron activates more of one spectral type and tend towards zero for all other class variables. Fig. 4.5 illustrates how these vectors define class planes that are used to form the SOMDI. Once the map is trained, the class of any given n can be identified by finding the maximum of c.

4.5.1.1 Supervised Learning

A second learning round is then applied, keeping the spatial mapping of neurons, but changing the update criteria to use rules from LVQ:

1. Start with trained SOM
2. Select a sample s at random from S
3. Calculate euclidean distance, for each n
4. Define BMU as the neuron with minimum d
5. Identify BMU and s class labels:

   $class_j = indexOf(max(j))$

$$class_c = indexOf(max(c))$$

6. Update $BMU\ w$ and c:

   if ($class_j$ = $class_c$) then

   $$w = w + scaleFactor * (i - w)$$

   $$c = c + scaleFactor * (j - c)$$

   else

   $$w = w - scaleFactor * (i - w)$$

   $$c = c - scaleFactor * (j - c)$$

where only the update step changes when s lands on an incorrect neuron, to move both the spectrum weights and class weights of the BMU further away (and so making the neuron less likely to activate a similar spectrum in future iterations). During LVQ only the the BMU is updated under this regime and thus, represents only a small perturbation to the network. By analogy, this can be thought of as applying fine details to a painting, after the initial broad brush strokes to block in colours.

The method is described as self-optimising, since when the BMU class matches that of the input, the BMU weights are moved closer to the input as per the original unsupervised SOM algorithm. This allows a natural optimum to be reached, whilst preventing over-fitting. A second consequence of SKiNET, is a greater degree of freedom for each neuron. In the update step, the weight vector for the data and class labels are both updated, allowing for the class definition of a neuron to dynamically change as the map is trained.

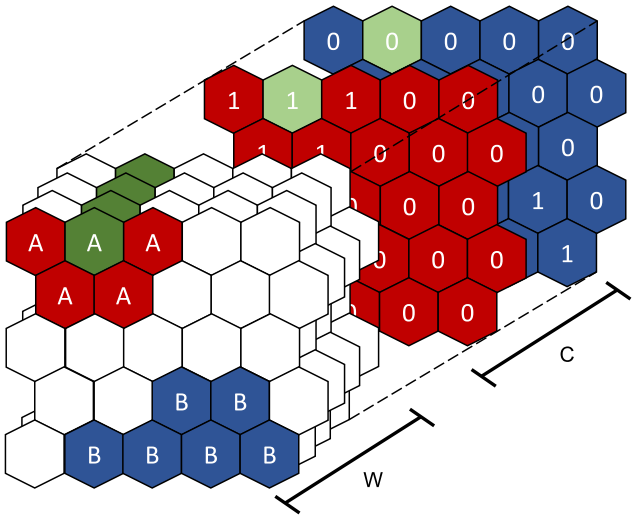

Figure 4.5: Illustration of SOM class planes used for SOMDI.

Illustrative example of SOM for two classes A and B, coloured red and blue, respectively. The weight vectors W and C can be thought of as making up additional planes in the z direction. Class planes are formed having values close to 1 for a given class and values close to 0 otherwise. These are used for classification and identification of the most important planes in W for the SOMDI.

4.5.2 Samples

Tissue samples were retrieved within hours of slaughter from a total of 11 enucleated porcine eyes, provided by Rowley CH Ltd, a local abattoir. Eyes were dissected to isolate small segments of cornea, lens, vitreous humour, retina and optic nerve. Tissue samples were prepared using a protocol suggested by Cui *et al.*, using glass slides covered with aluminium foil as a cost effective substrate, and allowed to air dry for 24 hours [10].

4.5.3 Raman Spectroscopy

An InVia Qontor (Renishaw plc) equipped with a 785 nm laser was used for all measurements. LiveTrack maps over a sample area of 110 x 77 microns were acquired for each sample, with an acquisition time of 5 s for each point location in the map, and laser power of 2 mW, a 50x Leica objective (0.75 NA), 1200 l/mm grating with scans recorded in the range 550-1670 cm^{-1}. A total of 88 scans per tissue sample were recorded (4840 spectra total).

4.5.4 Software and Preprocessing

Baseline subtraction and cosmic ray removal were applied in WiRE 5.1 (Renishaw plc), each sample was independently standardised by mean centering and scaling to unit variance using Scikit-learn in python [29]. The package was then used to define training/test partitions, cross validation folds and define models for each classifier. The SOM based methods were defined in JavaScript by forking an existing open source SOM library [24]. The entire library was heavily refactored to include support for the SKiNET, and is available on Github [1]. For consistency, a wrapper was created around the JavaScript library, to expose the same methods in python, allowing for all models to be benchmarked via the same script.

4.6 References

[1] Banbury, C. [2018*a*], 'An implementation of a Kohonen map in JavaScript extended to provide feature extraction and classification ', `https://github.com/cbanbury/kohonen`.

[2] Banbury, C. [2018*b*], 'Raman toolkit - analysis and data management tool for Raman spectra', `https://github.com/cbanbury/raman-tools`.

[3] Bauer, N. J., Wicksted, J. P., Jongsma, F. H., March, W. F., Hendrikse, F. and Motamedi, M. [1998], 'Noninvasive assessment of the hydration gradient across the cornea using confocal Raman spectroscopy.', *Investigative Ophthalmology & Visual Science* **39**(5), 831–5.

[4] Bostock, M. [2016], 'Force-directed graph layout using velocity Verlet integration.', `https://github.com/d3/d3-force`.

[5] Brereton, R. G. [2012], 'Self organising maps for visualising and modelling', *Chemistry Central Journal* **6**(Suppl 2), 1–15.

[6] Brereton, R. G. and Lloyd, G. R. [2014], 'Partial least squares discriminant analysis: taking the magic away', *Journal of Chemometrics* **28**(4), 213–225.

[7] Butler, H. J., Ashton, L., Bird, B., Cinque, G., Curtis, K., Dorney, J., Esmonde-White, K., Fullwood, N. J., Gardner, B., Martin-Hirsch, P. L., Walsh, M. J., McAinsh, M. R., Stone, N. and Martin, F. L. [2016], 'Using Raman spectroscopy to characterize biological materials', *Nature Protocols* **11**(4), 664–687.

[8] Chang, C.-Y., Ke, D.-S. and Chen, J.-Y. [2009], 'Essential fatty acids and human brain.', *Acta neurologica Taiwanica* **18**(4), 231–41.

[9] Cheriyadat, A. and Bruce, L. [2003], Why principal component analysis is not an appropriate feature extraction method for hyperspectral data, *in* 'IGARSS 2003. 2003 IEEE International Geoscience and Remote Sensing Symposium. Proceedings (IEEE Cat. No.03CH37477)', Vol. 6, IEEE, pp. 3420–3422.

[10] Cui, L., Butler, H. J., Martin-Hirsch, P. L. and Martin, F. L. [2016], 'Aluminium foil as a potential substrate for ATR-FTIR, transflection FTIR or Raman spectrochemical analysis of biological specimens', *Analytical Methods* **8**(3), 481–487.

[11] de Almeida, M. R., Correa, D. N., Rocha, W. F., Scafi, F. J. and Poppi, R. J. [2013], 'Discrimination between authentic and counterfeit banknotes using Raman spectroscopy and PLS-DA with uncertainty estimation', *Microchemical Journal* **109**, 170–177.

[12] Erckens, R., Jongsma, F., Wicksted, J., Hendrikse, F., March, W. and Motamedi, M. [2001], 'Raman spectroscopy in ophthalmology: from experimental tool to applications in vivo.', *Lasers in medical science* **16**(4), 236–52.

[13] Ermakov, I. V., McClane, R. W., Gellermann, W. and Bernstein, P. S. [2001], 'Resonant Raman detection of macular pigment levels in the living human retina', *Optics Letters* **26**(4), 202.

[14] Esmonde-White, K. [2014], 'Raman Spectroscopy of Soft Musculoskeletal Tissues', *Applied Spectroscopy* **68**(11), 1203–1218.

[15] Gamsjaeger, S., Klaushofer, K. and Paschalis, E. P. [2014], 'Raman analysis of proteoglycans simultaneously in bone and cartilage', *Journal of Raman Spectroscopy* **45**(9), 794–800.

[16] Gregory, R. and Cavanagh, P. [2011], 'The Blind Spot', *Scholarpedia* **6**(10), 9618.

[17] Haykin, S. [1999], *Neural networks : a comprehensive foundation*, Prentice Hall.

[18] Kohonen, T. [1982], 'Self-organized formation of topologically correct feature maps', *Biological Cybernetics* **43**(1), 59–69.

[19] Krishnan, R. S. and Shankar, R. K. [1981], 'Raman effect: History of the discovery', *Journal of Raman Spectroscopy* **10**(1), 1–8.

[20] Larkin, P. [2011], 'IR and Raman Spectra-Structure Correlations', *Infrared and Raman Spectroscopy* pp. 73–115.

[21] Li, Y., Huang, W., Pan, J., Ye, Q., Lin, S., Feng, S., Xie, S., Zeng, H. and Chen, R. [2015], 'Rapid detection of nasopharyngeal cancer using Raman spectroscopy and multivariate statistical analysis.', *Molecular and clinical oncology* **3**(2), 375–380.

[22] Liu, J., Osadchy, M., Ashton, L., Foster, M., Solomon, C. J. and Gibson, S. J. [2017], 'Deep convolutional neural networks for Raman spectrum recognition: a unified solution', *Analyst* .

[23] Lloyd, G. R., Wongravee, K., Silwood, C. J., Grootveld, M. and Brereton, R. G. [2009], 'Self Organising Maps for variable selection: Application to human saliva analysed by

nuclear magnetic resonance spectroscopy to investigate the effect of an oral health-care product', *Chemometrics and Intelligent Laboratory Systems* **98**(2), 149–161.

[24] Mondon, N. [2016], 'A basic implementation of a Kohonen map in JavaScript', `https://github.com/seracio/kohonen`.

[25] Movasaghi, Z., Rehman, S. and Rehman, I. U. [2007], 'Raman Spectroscopy of Biological Tissues', *Applied Spectroscopy Reviews* **42**(5), 493–541.

[26] Obana, A., Hiramitsu, T., Gohto, Y., Ohira, A., Mizuno, S., Hirano, T., Bernstein, P. S., Fujii, H., Iseki, K., Tanito, M. and Hotta, Y. [2008], 'Macular carotenoid levels of normal subjects and age-related maculopathy patients in a japanese population', *Ophthalmology* **115**(1), 147–157.

[27] Ozaki, Y., Mizuno, A., Itoh, K., Yoshiura, M., Iwamoto, T. and Iriyama, K. [1983], 'Raman spectroscopic study of age-related structural changes in the lens proteins of an intact mouse lens', *Biochemistry* **22**(26), 6254–6259.

[28] Papadimitriou, S., Mavroudi, S., Vladutu, L., Pavlides, G. and Bezerianos, A. [2002], 'The Supervised Network Self-Organizing Map for Classification of Large Data Sets', *Applied Intelligence* **16**(3), 185–203.

[29] Pedregosa, F., Varoquaux, G., Gramfort, A. and Michel, V. [2011], 'Scikit-learn: Machine Learning in Python', *Journal of Machine Learning Research* **12**, 2825–2830.

[30] Pomerantsev, A. L. and Rodionova, O. Y. [2018], 'Multiclass partial least squares discriminant analysis: Taking the right way-A critical tutorial', *Journal of Chemometrics* **32**(8), e3030.

[31] Rosen, R., Kruger, E., Katz, A. and Alfano, R. [2002], 'Method and system for detection by Raman measurements of bimolecular markers in the vitreous humor'. US Patent 2002/00952.57 A1.

[32] Siebert, F. and Hildebrandt, P. [2008], *Theory of Infrared Absorption and Raman Spectroscopy*, Wiley.

[33] Smola, A. J. and Schölkopf, B. [2004], 'A tutorial on support vector regression', *Statistics and Computing* **14**(3), 199–222.

[34] Surmacki, J. M., Woodhams, B. J., Haslehurst, A., Ponder, B. A. J. and Bohndiek, S. E. [2018], 'Raman micro-spectroscopy for accurate identification of primary human bronchial epithelial cells', *Scientific Reports* **8**(1), 12604.

[35] Talari, A. C. S., Movasaghi, Z., Rehman, S. and Rehman, I. U. [2015], 'Raman Spectroscopy of Biological Tissues', *Applied Spectroscopy Reviews* **50**(1), 46–111.

[36] Tozer, B. A. [1979], 'The calculation of maximum permissible exposure levels for laser radiation', *Journal of Physics E: Scientific Instruments* **12**(10), 922.

[37] Wongravee, K., Lloyd, G. R., Silwood, C. J., Grootveld, M. and Brereton, R. G. [2010], 'Supervised self organizing maps for classification and determination of potentially discriminatory variables: Illustrated by application to nuclear magnetic resonance metabolomic profiling', *Analytical Chemistry* **82**(2), 628–638.

CHAPTER 5

SPECTROSCOPIC DETECTION OF TRAUMATIC BRAIN INJURY SEVERITY AND BIOCHEMISTRY FROM THE RETINA

5.1 Abstract

Traumatic brain injury (TBI) is a major burden on healthcare services worldwide, where scientific and clinical innovation is needed to provide better understanding of biochemical damage to improve both pre-hospital assessment and intensive care monitoring. Here, we present an unconventional concept of using Raman spectroscopy to measure the biochemical response to the retina in an *ex-vivo* murine model of TBI. Through comparison to spectra from the brain and retina following injury, we elicit subtle spectral changes through the use of multivariate analysis, linked to a decrease in cardiolipin and indicating metabolic disruption. The ability to classify injury severity *via* spectra of the retina is demonstrated for severe TBI (82.0 %), moderate TBI (75.1 %) and sham groups (69.4 %). By fundamentally demonstrating that the eye serves as a window to the brain, we lay the groundwork for further exploitation of Raman spectroscopy for indirect, non-invasive assessment of brain chemistry.

5.2 Introduction

TBI, resulting from sudden impact such as assault, sporting injuries or road traffic accidents is a major cause of morbidity and mortality, affecting an estimated 69 million individuals worldwide each year [5]. The initial damage triggers a complex cascade of metabolic, biochemical and inflammatory responses leading to secondary injury that can occur over the following hours, days or months [16]. The Glasgow coma scale (GCS), based on visual assessment of the patient's verbal, visual and motor responses, is the current gold stan-

dard to stratify injury severity and acute clinical evolution in TBI. The GCS defines arbitrary boundaries for injury severity grouped as mild, moderate and severe [23]. Whilst this has real clinical value, minimal mechanistic insight is provided into the pathobiology of damage evolution after injury. Novel technologies which can be applied quickly and non-invasively at the point of care (PoC) for interfacing with the brain and define the chemical signatures of TBI pathobiology are needed. A non-invasive method that can detect and quantify TBI would not only provide a more accurate, objective and timely approach to diagnosis, but may help expand our understanding of injury evolution and enable personalized intervention approaches.

The skull provides a thick protective layer around the brain, which strictly limits the available options for both non-invasive and invasive sampling of brain tissue, especially in pre-hospital settings. However, sitting at the back of the eye exists a small part of the brain covered only by optically clear media; the retina and the optic disc. The optic disc appears as a bright circle in fundus images, and is the route through which visual information captured from the retina is passed to the brain along the optic nerve. Also known as the blind spot, the optic disc is devoid of photoreceptive cells and consists predominantly of white matter. Derived from an out-pouching of the diencephalon as the brain develops and bathed in the cerebrospinal fluid, both the optic nerve and retina are technically part of the central nervous system [17]. The retina and optic nerve have long been known to display physically measurable changes as a result of increased intracranial pressure (ICP), where ICP monitoring is of paramount importance for intensive care monitoring in TBI. Measurements from the eye of such changes have been the target of several studies aiming to develop non-invasive ICP, but to our knowledge no such attempts have been

made to measure the resultant biochemical change [7, 8, 14].

We therefore have hypothesized that a form of optical spectroscopy, which has the potential to be translated into a non-invasive method to probe the posterior segment of the eye (retina and optic nerve), may be able to monitor injury evolution in real time after TBI. Among the optical spectroscopy techniques, Raman spectroscopy offers the richest and most sensitive chemical discrimination. Temporal changes from direct analyses of brain tissue have previously been studied by Surmacki *et al.* [20] using our murine model of TBI. Raman scattering is based on the inelastic interaction between light and a molecule, where the energy exchange from a scattering event causes a change in the vibrational energy level of a molecular bond. Since energy levels of electrons in molecules are quantized, only specific and discrete energy states are allowed. The Raman spectrum therefore defines a chemical fingerprint that is uniquely determined by the underlying molecular constituents [10]. Nevertheless, for biological samples there exists significant redundancy and complexity of spectral bands that makes analysis and interpretation of the data non-trivial. Raman scattering is also an extremely weak effect, and thus, long acquisition times and the use of a high-powered laser focused through an objective are standard requirements for well resolved spectra. The notion of laser exposure to the eye invokes a natural aversion, however every anatomical tissue layer of the eye has been successfully studied using Raman spectroscopy [6]. By adhering to laser safety limits, Obana *et al.* [15] conducted an *in-vivo* study using resonance Raman spectroscopy in humans to assess age-related maculopathy. More recently, Marro *et al.* [13] were able to measure inflammatory changes in retina cell cultures and Stiebing *et al.* [19] have showed how this can be extended to non-resonant Raman spectroscopy, using flat mounted retina samples combined with an

optical pathway mimicking the human eye.

Recently, we developed a machine learning technique based on self organizing maps (SOMs), the self optimizing Kohonen index network (SKiNET) for simultaneously providing rich information and classification from biological samples, even with noisy or poor quality spectra that would result from a lower laser power and short acquisition times [2]. SOMs provide visually intuitive 2D clustering (e.g. according to injury state) of high dimensional data such as Raman spectra, that are otherwise difficult to interpret for large sample and measurement numbers. Whilst SOMs are usually an unsupervised method, SKiNET incorporates supervised learning to additionally provide accurate classification, which could then be used to make diagnostic predictions. Finally, a form of feature extraction using the self organizing map discriminant analysis (SOMDI) allows us to understand which spectral features (and therefore chemical changes) are responsible for the clustering seen in the SOM [12].

Here, Raman spectroscopy combined with SKiNET is applied to investigate whether the retina can reflect the brain microenvironment after injury, in a clinically relevant murine model of focal TBI. Our results show that spectra from the eye can distinguish moderate TBI (mTBI) and severe TBI (sTBI) from a sham group, and show this to be as a result of similar chemical changes to those seen at the point of injury on the brain. Through quantitative and qualitative analysis we suggest the detected changes are largely due to metabolic distress and the release of cardiolipin, consistent with recent work in the field of mass spectrometry [4]. This validation is particularly promising as mass spectrometry provides vastly superior molecular discrimination. However, Raman spectroscopy has the advantage of being a non-destructive technique and as highlighted, there are ongoing

efforts in the field for translation into *in-vivo* measurements, and diagnostics.

5.3 Results and Discussion

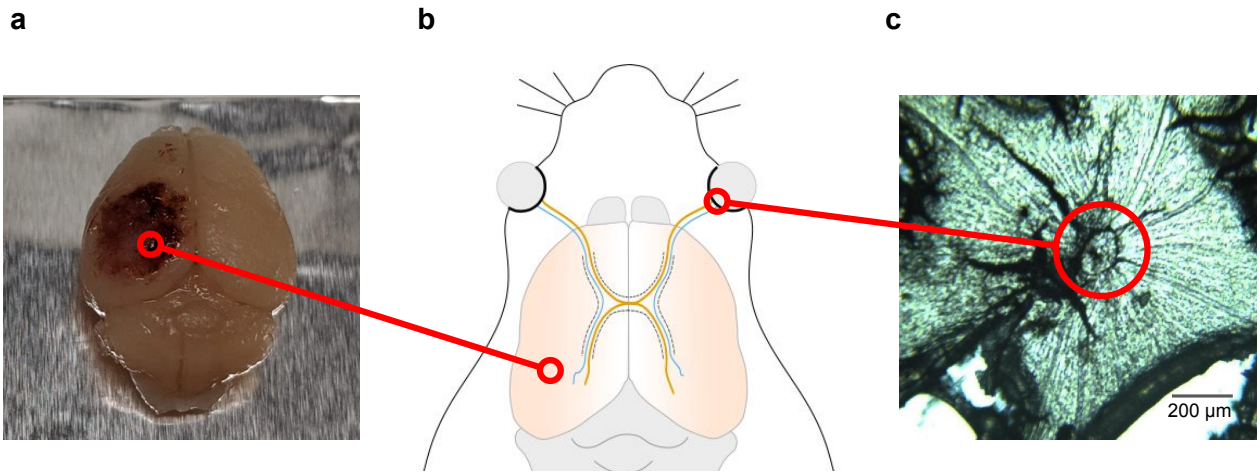

Figure 5.1: Photographs of mouse brain and retina following cortical impact.

a, Photograph of whole brain following sTBI to the left parietotemporal cortex. **b**, Illustration of mouse brain and optic tract, highlighting ipsilateral (blue) and contralateral (orange) projections connecting the brain to the retina. **c**, Example of a bright field microscopy image of a flat mounted retina from the mTBI group.

Experimental TBI was induced by controlled cortical impact in mice (n=6), with the degree of injury (either moderate or severe) being defined by the deformation depth. Tissue samples of postfixed brain (Fig. 5.1a) and eyes were collected 3 days after injury from sham, mTBI and sTBI groups. An illustration of the mouse head is shown in Fig. 5.1b, highlighting the bilateral axon projections that are present between the brain and the retina. Samples from the retinae of both eyes were measured by carefully dissecting each eye and flat mounting the retina onto aluminium slides (Fig. 5.1c). Raman spectra were collected

using identical parameters for brain and retina samples across all injury states. Spectra were collected using surface map scans to follow the tissue topography, with a total of 400 spectra per sample, with a 785 nm excitation (50 mW), 1 s acquisitions and 5 accumulations at each map position. Each Raman map was averaged to give a single spectrum per tissue sample (Appendix B.1, B.2). A complete description of the experimental procedure can be found in the Materials and Methods section.

The averaged Raman spectra from the impact site on the left hemisphere of the brain (contusion core) shows clear changes to the spectral profile (Fig. 5.2a), with noticeable decreases to the bands around 1003, 1266 and 1660 cm^{-1} compared to the sham group for both mTBI and sTBI (Fig. 5.2a). Unsurprisingly, there is a greater change to these bands for sTBI over mTBI, however the sTBI group also shows changes to the bands around 1337 and 1447 cm^{-1}. In comparison to the sham group, TBI samples from the brain appear more noisy, as a result of interference from additional autofluorescence as a consequence of the haemorrhage clearly visible at the impact site (Fig. 5.1a). In one of the mTBI samples, autofluorescence led to the majority of spectra in the map being saturated, and the sample was omitted from the results. The average spectra from retina samples show only slight variations compared to the sham group (Fig. 5.2b), however the changes observed are also predominantly to the bands at 1003, 1266 and 1660 cm^{-1}. To understand whether these slight changes are meaningful, machine learning techniques are required, which is addressed in the multivariate analysis section. For mTBI, the change at 1266 cm^{-1} is the only feature consistent with sTBI in the retina, as well as the observed changes from brain tissue. As with brain tissue, a change at 1337 cm^{-1} is unique to sTBI, but the decrease at 1660 cm^{-1} that was prominent for brain tissue is only seen for sTBI.

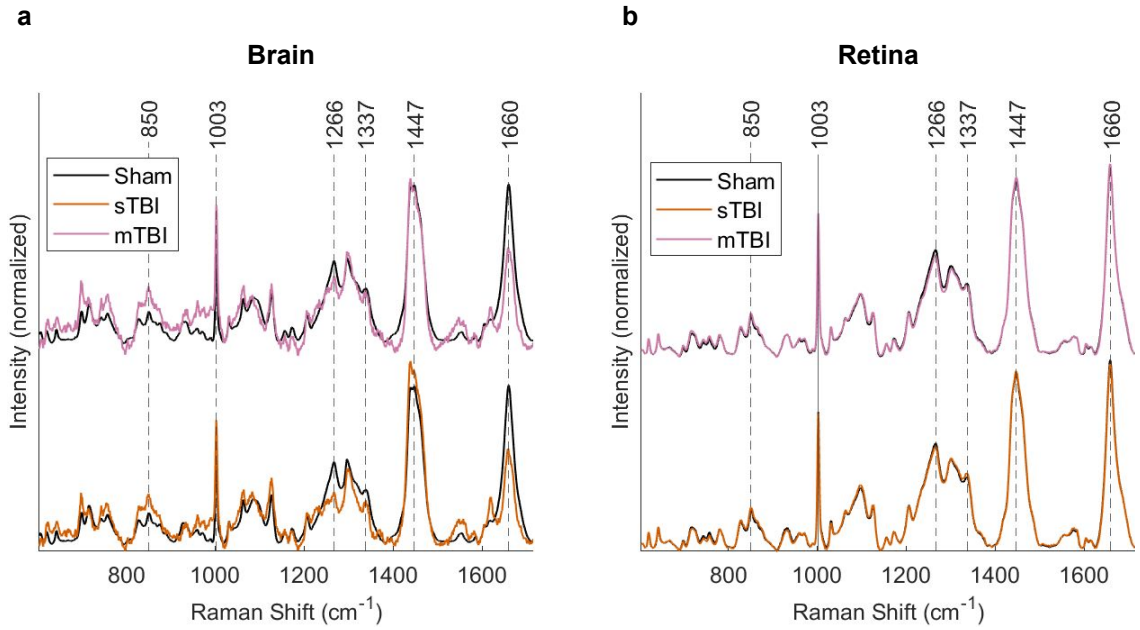

Figure 5.2: Average Raman spectra from brain and retina samples.

a, Average Raman spectra collected in the contusion core for mTBI and sTBI compared to the sham group. **b**, Average Raman spectra collected from flat mounted retina samples (both eyes), showing mTBI and sTBI compared to the sham group. Raman spectra were collected as map measurements of 400 spectra over each sample, using a 785 nm excitation laser (50 mW), 1s acquisitions with 5 accumulations. Map measurements from each sample were averaged to produce a single spectrum per sample (n=6).

The Raman bands labelled in Fig. 5.2a,b are only those that show a noticeable change to both brain and retina tissue. Each band is assigned in terms of the associated chemical vibrational mode, with reference to Larkin [11], along with common biochemical attributions with reference to Talari *et al.* [21] where applicable. From the summary in Table 5.1, it is clear that the most prominent changes are most commonly associated with contributions from both lipids and proteins in the literature [21]. Since the brain contains nearly 60 % fat and the Raman signature for all 12 major and minor brain specific lipids have been well

characterized [3, 9], we can attempt to decompose the changes due to the lipid contribution. This approach was previously performed qualitatively by Surmacki *et al.* [20] on brain tissue using our murine TBI model to study temporal changes with Raman spectroscopy.

Peak (cm^{-1})	Assignment	Attribution
850	C-H wagging	-
1003	**C-C skeletal**	**phenylalanine**
1266	**C-H bending**	**mixed (proteins/lipids)**
1337	C-N stretching, N-H bending	Amide III
1447	$C-H_2$ bending	mixed (proteins/lipids)
1660	**C=C stretching**	**mixed (proteins/lipids)**

Table 5.1: Summary of chemical assignments and biochemical attribution to Raman bands which display a change after TBI. The bands showing the strongest changes in the spectra are highlighted in bold.

Here, we quantitatively assess changes to lipid composition in response to TBI by using non negative least squares non-negative least squares (NNLS) fitting. The raw data for brain specific lipids, provided by Krafft *et al.* [9] was used as NNLS fitting parameters to identify the relative contributions in each tissue sample for sham, mTBI and sTBI. The resultant fitting coefficients for each lipid spectrum are therefore proportional to the lipid concentration measured within each tissue sample. A one-way analysis of variance (ANOVA) shows a statistically significant difference in the contribution (compared to the sham) from cardiolipin (Fig. 5.3a) and cholesterol (Fig. 5.3b), with a decrease in cardiolipin linked to the decrease in the bands at 1266 and 1660 cm^{-1} for TBI, and an increase in cholesterol from the change in the band at 1440 cm^{-1} for both moderate and severe TBI *vs* the sham (Fig. 5.4). However, cholesterol and cardiolipin changes are not affected by the degree of injury (Fig. 5.3a,b).

Cardiolipin is found exclusively in the inner mitochondrial membrane, playing a cru-

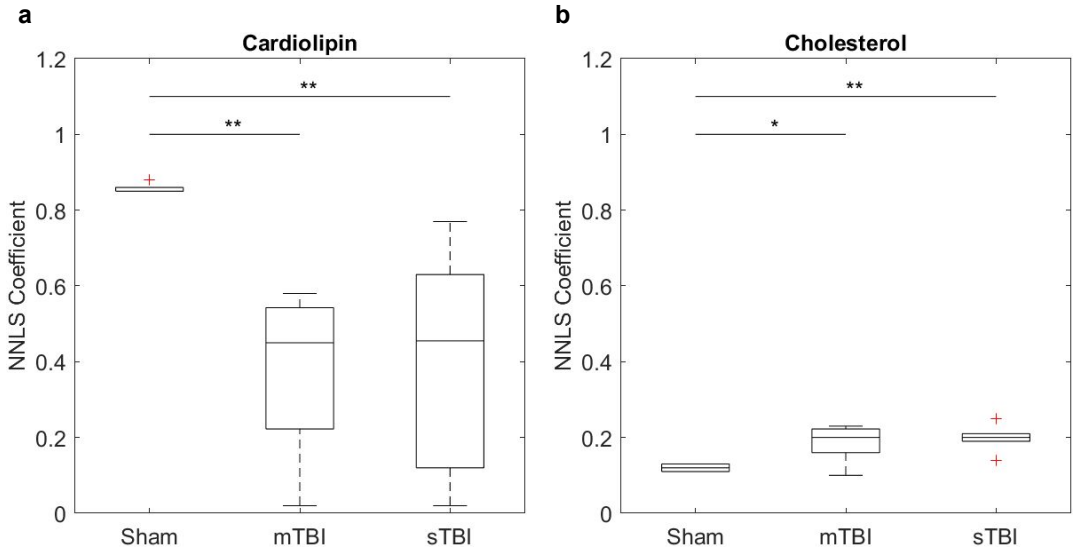

Figure 5.3: Change in contribution from cardiolipin and cholesterol from brain tissue with TBI.

Change in the relative contribution from cardiolipin (**a**) and cholesterol (**b**) for sham, mTBI and sTBI. Boxplots show the NNLS coefficient fitted to the average map spectrum measured from each brain sample at the injury site. A statistically significant difference determined by one-way ANOVA exists in cardiolipin for mTBI ($p = 0.0062$) and sTBI ($p = 0.0074$) compared to the sham. For cholesterol, there is a statistically significant difference between mTBI ($p = 0.0204$) and sTBI ($p = 0.0047$) compared to the sham. There is no statistically significant difference between mTBI and sTBI for either cholesterol or cardiolipin (*$p < 0.05$, **$p < 0.01$).

cial role in cell metabolism and signalling; including apoptosis. A decrease in cardiolipin concentration following cortical impact has recently been shown using mass spectrometry, where both the importance in relation to TBI and opportunity for future therapeutics were highlighted [4]. Furthermore, the release of cardiolipin microparticles following TBI induced cell damage has been show to compromise the blood brain barrier, and so plays a major role in the resulting biochemical cascade and metabolic disruption [26]. Finally these findings are also consistent with earlier studies using Raman spectroscopy to assess TBI

in mice, where the author's concluded a link between the observed spectral changes and apoptosis *via* comparison to immunohistochemistry of the samples [22]. Although these results are encouraging, it should be noted that the spectral bands associated with cardiolipin are also present in several proteins, and so these changes cannot solely be attributed to cardiolipin [18]. The large decrease in fitting coefficient for cardiolipin was accompanied by smaller, but significant increase in cholesterol (Fig. 5.3b). The brain is the most cholesterol rich organ, containing around 20 % of the total amount in the body, which has structural roles in cell membranes and the myelin sheath. An excess of cholesterol is most likely associated with cell debris [25]. Whilst other brain lipids were fitted with non-zero coefficients, no further clear or significant changes were observed in response to TBI (Appendix B.1-B.3).

5.4 Multivariate Analysis Reveals Changes from Retina

We have demonstrated prominent biochemical changes associated with TBI that are detectable from direct Raman analysis of brain tissue, but these changes appear only faintly reflected in the averaged results from the retina. Whilst the average spectra provide an easily digestible format in order to present the data, it forces us to throw away vital information that arises from point-point variation within each sample combined with sample-sample variation. Fortunately, multivariate techniques allow us to capture all of this information and extract the most important spectral features which characterize a group of data, such as an injury state. Recently, we highlighted the value of SOMs in the analysis of Raman spectra from biological samples [2]. The 400 spectra measured across each tissue sample

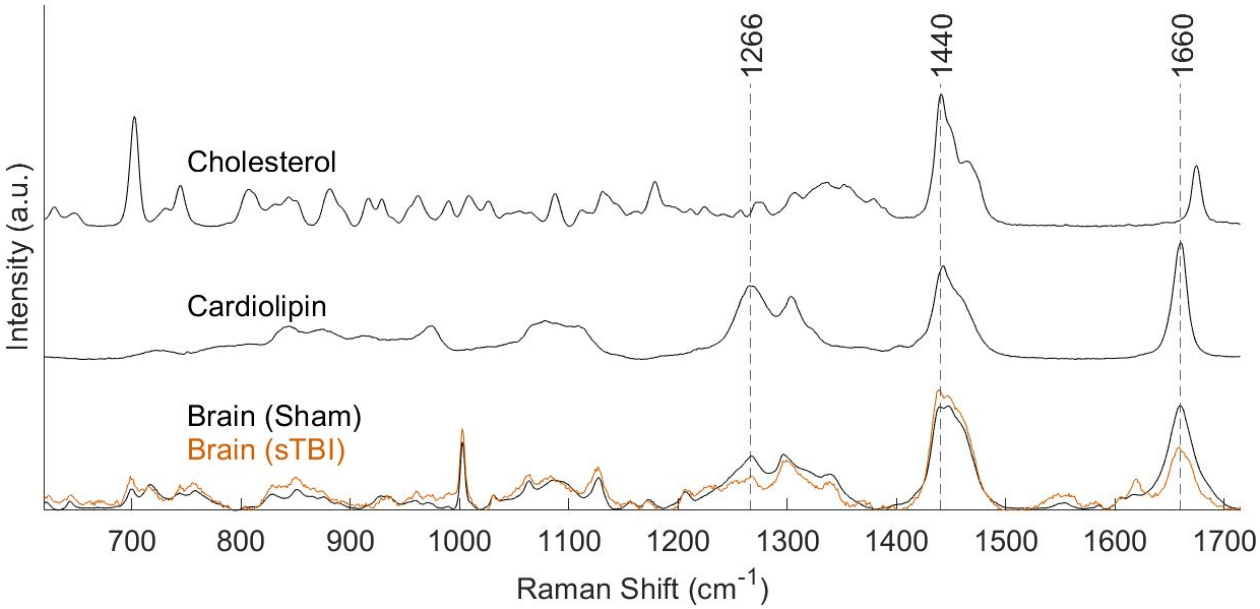

Figure 5.4: Spectra for cholesterol and cardiolipin (using data from Krafft *et al.* [9]) and average spectra for brain tissue from sham and sTBI.

were grouped according to injury state from both eyes (summarized in Table 5.2). 20 % of the data was randomly selected from each group and reserved as test data, leaving the remaining 80 % for training (Table 5.3).

	Spectra Per Tissue Sample	Mice	Eyes	Total
Sham	400	6	2	4800
mTBI	400	6	2	4800
sTBI	400	6	2	4800
				14,400

Table 5.2: Summary of retina spectra used as inputs for multivariate analysis across the three injury states (sham, mTBI and sTBI).

Briefly, a SOM is a type of artificial neural network which is typically visualized as a 2D array of hexagonal neurons, which loosely tries to mimic the visual cortex in the brain;

Injury State	Total	Training Data (80 %)	Test Data (20 %)
Sham	4800	3840	960
mTBI	4800	3840	960
sTBI	4800	3840	960
Total	14,400	11,520	2880

Table 5.3: Breakdown of data across each injury state, and split into training and test data sets.

with neighbouring neurons activating on similar inputs. The training process is performed iteratively by presenting an individual spectrum (ξ) from the training data, and finding the neuron that has previously activated on data most similar to the input, ξ. The winning neuron is then updated to become more likely to activate on data like ξ, along with neighbouring neurons (but to a lesser degree). The result is neurons that are grouped according to particular features, as see in Fig. 5.5a. Each neuron (hexagon) in the SOM is coloured according to the type of data it activates from the training data (sham, mTBI or sTBI), providing immediate visualization of how the data is organized in groups. A clear separation between sham and sTBI groups can be seen in the SOM shown in Fig. 5.5a. To indicate neurons that activate on more than one injury state, colour mixing is used according to the relative proportion of hits from each state. Using the SOMDI [12], it is possible to identify features in the Raman spectrum responsible for the clustering observed in the SOM. For sTBI: increases to the bands around 850, 1098 and 1337 cm^{-1}, coupled to decreases in the bands around 1003, 1266 and 1660 cm^{-1} are observed, relative to the sham group (Fig. 5.5b). These changes largely reflect those observed for sTBI in brain tissue (Fig. 5.2a), including the decrease to the 1266/1660 cm^{-1} bands attributed to cardiolipin. However, minor discrepancies exist between changes to the bands at 1337, and 1447 cm^{-1}. In com-

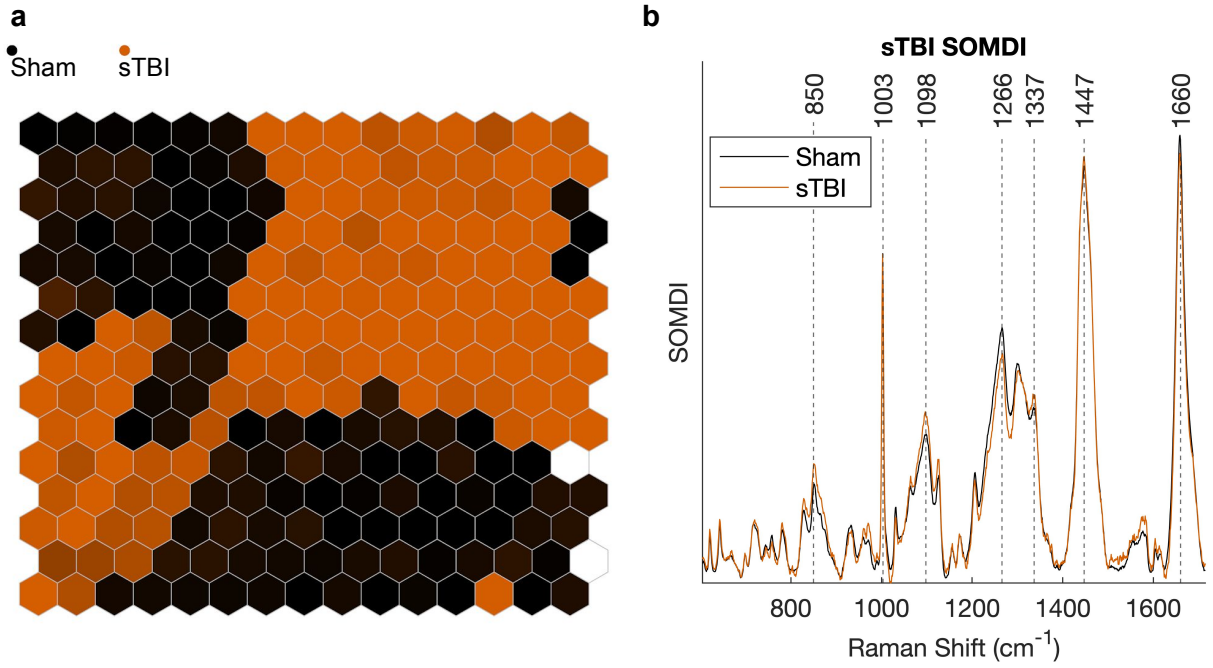

Figure 5.5: Dimensionality reduction and feature extraction of sTBI *vs* sham from spectra of the retina.

a, Clustering of Raman spectra from the retina for sTBI (orange) and sham (black) groups using a SOM. **b**, Features extracted (SOMDI) from SOM shown in **a**, highlighting the Raman bands most influential to neurons in the SOM for sham and sTBI groups.

parison to sTBI, mTBI shows a poorer separation in the SOM (Fig. 5.6a), with a greater proportion of neurons activating on a mixture of mTBI and sham groups, particularly for neurons associated with mTBI. This is seen by mixing of the colors for injury states in the SOM. However, distinct regions are still present for both mTBI and sham groups. The same is true for the SOMDI of mTBI *vs* sham (Fig. 5.6b), with very few spectral regions of similarity between the two groups, indicating a greater degree of heterogeneity. Despite the increased variation, increases to the bands at 850, 1098 coupled to a decrease in the band at 1266 cm^{-1} are still observed for mTBI. The consistency of changes to these three

bands across injury severity and seen both in brain and retina tissue may provide important markers for future studies.

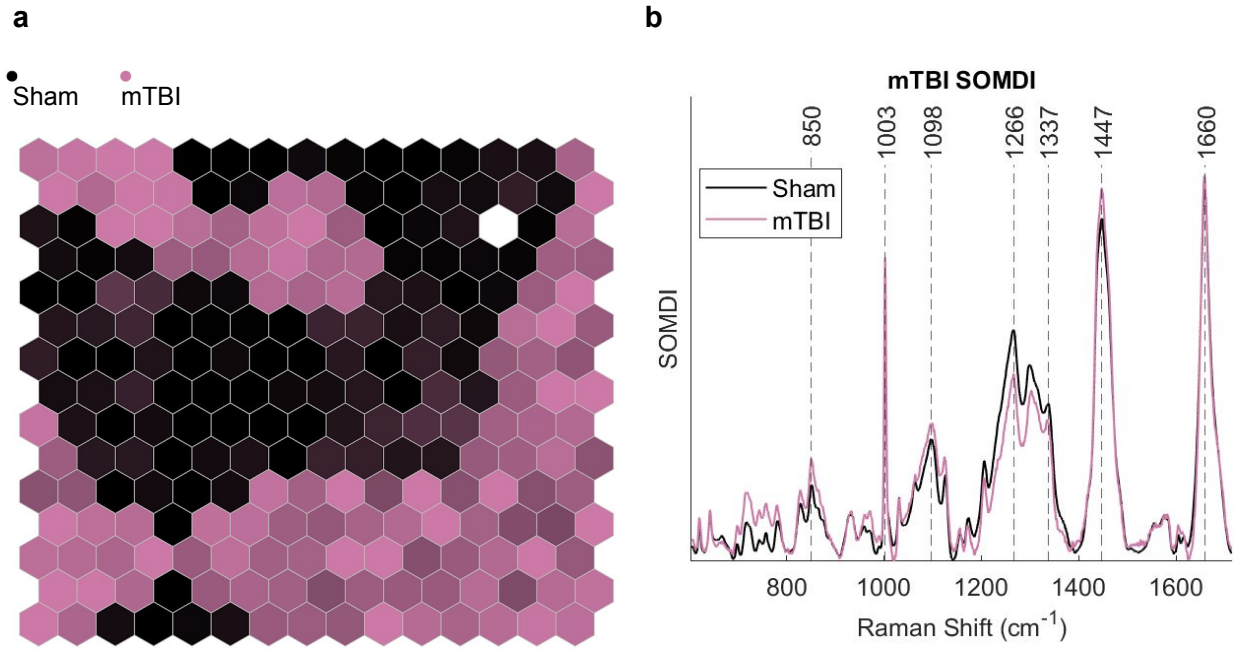

Figure 5.6: Dimensionality reduction and feature extraction of mTBI *vs* sham from spectra of the retina.

a, Clustering of mTBI (purple) and sham (black) Raman spectra from the retina using a SOM. **d**, Features extracted from SOM in **c**, highlighting Raman bands for sham and mTBI groups.

Classification using Raman spectra from the retina is then performed by using SKiNET on the data shown in Table 5.3 to create a predictive model of TBI. Models are optimized by using 10-fold cross validation on the training data to tune: the number of neurons in the SOM; initial learning rate; and training iterations. Following optimization, the trained network is used to predict the previously unused test data, showing a good sensitivity for sTBI (82.0 $\pm$ 1.4 %). A poorer classification accuracy is obtained for sham (69.4 $\pm$ 0.9 %) and mTBI groups (75.1 $\pm$ 0.9 %), with a large proportion of sham data incorrectly

classified as mTBI and *vice versa* (Table 5.4). Similar results are obtained by splitting the data according to ipsilateral (side of injury) and contralateral retinae (Appendix B.4). The classification result may be improved by a much larger training set, however, the modest specificity could be an indicator of the inherent heterogeneity of TBI. Rather than using coarsely defined boundaries of mild, moderate and severe, a study comparing Raman spectroscopy to the total coma score (providing an incremental scale in the range 3-15) may be more appropriate [23], but is outside the current scope.

		Predicted		
		Sham (%)	**mTBI (%)**	**sTBI (%)**
Actual	**Sham (%)**	**69.4**	24.0	6.6
	mTBI (%)	17.9	**75.1**	6.9
	sTBI (%)	7.9	10.0	**82.0**

Table 5.4: Summary of classification accuracy as a confusion matrix for: sham, mTBI and sTBI groups using trained SKiNET against test data. Data shown is the average classification accuracy across 10 SOM initializations, trained using Raman spectra from flat mounted mouse retina (both eyes).

5.5 Conclusions

For the first time, we have shown that Raman spectroscopy can be used to effectively and accurately identify TBI from tissue samples of the retina, coupled to chemical changes from a cortical impact to the brain. Machine learning using the SOMDI and SKiNET has been used to extract the subtle spectral changes present from the retina, and shown these to be in line with the measured changes to brain tissue. Consistent changes to Raman bands were observed both in brain and retina tissue for mTBI and sTBI, when compared

to the sham group. Raman spectroscopy represents a unique opportunity for TBI monitoring throughout the patient journey from pre-hospital assessment, to intensive care and follow up examinations. In demonstrating a fundamental ability to study chemical changes from eye tissue as a result of TBI, we begin to push the boundaries of Raman spectroscopy of the eye beyond purely ophthalmic applications; opening a new window to study neurological changes.

5.6 Methods

5.6.1 Mouse Model of TBI and Tissue Processing

Adult (8 weeks old) C57BL/6J male mice (Envigo RMS srl) were used. No additional procedures were performed on mice except those related to the experiment they were intended for. Procedures involving animals and their care were conducted in conformity with the institutional guidelines at the Istituto di Ricerche Farmacologiche Mario Negri IRCCS, Italy in compliance with national (D.lgs 26/2014; Authorization n. 19/2008-A issued March 6, 2008 by Ministry of Health) and international laws and policies (EEC Council Directive 2010/63/UE; the NIH Guide for the Care and Use of Laboratory Animals, 2011 edition). They were reviewed and approved by the Mario Negri Institute Animal Care and Use Committee that includes ad hoc members for ethical issues, and by the Italian Ministry of Health (Decreto no. D/07/2013-B and 301/2017-PR). Animal facilities meet international standards and are regularly checked by a certified veterinarian who is responsible for health monitoring, animal welfare supervision, experimental protocols and review of procedures.

Mice were anaesthetised by isoflurane inhalation (induction 3%; maintenance 1.5%) in an N_2O/O_2 (70%/30%) mixture and placed in a stereotaxic frame. Rectal temperature was maintained at 37°C. Mice were then subjected to craniectomy followed by induction of controlled cortical impact brain injury as previously described [24]. Briefly, the injury was induced using a 3-mm rigid impactor driven by a pneumatic piston rigidly mounted at an angle of 20° from the vertical plane and applied to the exposed dura mater, between bregma and lambda, over the left parietotemporal cortex (antero-posteriority: -2.5 mm, laterality: -2.5 mm), at an impactor velocity of 5 m/s. The deformation depth was of either 1 mm or 0.5 mm, resulting in a severe (sTBI) or moderate (mTBI) level of injury respectively. The craniotomy was then covered *via* cranioplasty and the scalp sutured. Sham mice received identical anaesthesia and surgery without brain injury. Three days after TBI, mice were deeply anaesthetised with Ketamine Chlorhydrate (20 mg, i.p.) and Medetomidine Chlorhydrate (0.2 mg, i.p.) transcardially perfused with 30 mL of phosphate-buffered saline (PBS) 1% (pH 7.4), followed by 60 mL of paraformaldehyde (PFA) 4% in PBS. The brains and eyes were carefully removed from the skull and post-fixed in 4% PFA in PBS for 24 hours at 4 °C. The post-fixed tissue were then rinsed and stored in normal saline (NaCl 0.9%) at 4°C. Samples we mounted on microscope slides covered with aluminium foil for spectroscopy studies as whole brains. Retina samples were prepared by micro-dissection of eyes in PBS, followed by flat mounting on aluminium slides. Samples were air dried for 1 hour before measurement.

5.6.2 Raman Spectroscopy

An InVia Qontor (Renishaw plc) equipped with a 785 nm laser was used for all measurements. Surface maps over a 20x20 grid, using a step size of 1.5 μm between points were acquired for each sample, with an acquisition time of 1s, 5 accumulations and laser power of 50 mW, a 50x Leica objective (0.75 NA), 1200 l/mm grating with scans recorded in the range 605-1715 cm^{-1}. A total of 400 spectra per tissue sample were recorded. Care was taken to ensure consistent sample preparation between samples and across injury states. All tissue was kept refrigerated in PBS prior to measurement. All Raman spectra were measured on the same day for each tissue type (brain, retina) and within 72 hours of sacrifice. Raman maps were measured in the contusion core for mTBI and sTBI, and the corresponding area in the sham group. Maps measured from the retina of both eyes were taken from an area in close proximity to the optic disc for each mouse. Post processing of spectra was performed in WiRE 5.3 (Renishaw Plc), cosmic rays were removed from each map using the nearest neighbour method, followed by baseline subtraction using the 'intelligent spline' fitting (11 nodes). Finally, the average was taken from each map resulting in a single spectrum per sample. NNLS fitting was performed against each average spectra using lipid data provided by Krafft *et al.* loaded into as components into the analysis tool in WiRE [9]. Multivariate analysis was performed using SKiNET using the accompanying Raman Toolkit web interface to build SOM models using training data and perform predictions against test data [1].

5.7 References

[1] Banbury, C. [2018], 'Raman toolkit - analysis and data management tool for Raman spectra', `https://github.com/cbanbury/raman-tools`.

[2] Banbury, C., Mason, R., Styles, I., Eisenstein, N., Clancy, M., Belli, A., Logan, A. and Goldberg Oppenheimer, P. [2019], 'Development of the self optimising kohonen index network (SKiNET) for Raman spectroscopy based detection of anatomical eye tissue', *Scientific Reports* **9**(1), 10812.

[3] Chang, C., Ke, D. and Chen, J. [2009], 'Essential fatty acids and human brain.', *Acta neurologica Taiwanica* **18**(4), 231–41.

[4] Chao, H., Anthonymuthu, T. S., Kenny, E. M., Amoscato, A. A., Cole, L. K., Hatch, G. M., Ji, J., Kagan, V. E. and Bayır, H. [2018], 'Disentangling oxidation/hydrolysis reactions of brain mitochondrial cardiolipins in pathogenesis of traumatic injury', *JCI Insight* **3**(21).

[5] Dewan, M. C., Rattani, A., Gupta, S., Baticulon, R. E., Hung, Y. C., Punchak, M., Agrawal, A., Adeleye, A. O., Shrime, M. G., Rubiano, A. M., Rosenfeld, J. V. and Park, K. B. [2019], 'Estimating the global incidence of traumatic brain injury', *Journal of Neurosurgery* **130**(4), 1080–1097.

[6] Erckens, R., Jongsma, F., Wicksted, J., Hendrikse, F., March, W. and Motamedi, M. [2001], 'Raman spectroscopy in ophthalmology: From experimental tool to applications in vivo', *Lasers in Medical Science* **16**(4), 236–252.

[7] Geeraerts, T., Duranteau, J. and Benhamou, D. [2008], 'Ocular sonography in patients with raised intracranial pressure: the papilloedema revisited', *Critical Care* **12**(3), 150.

[8] Hayreh, S. S. [1964], 'Pathogenesis of oedema of the optic disc (papilloedema): A preliminary report', *British Journal of Ophthalmology* **48**(10), 522–543.

[9] Krafft, C., Neudert, L., Simat, T. and Salzer, R. [2005], 'Near infrared Raman spectra of human brain lipids', *Spectrochimica Acta Part A: Molecular and Biomolecular Spectroscopy* **61**(7), 1529–1535.

[10] Krishnan, R. S. and Shankar, R. K. [1981], 'Raman effect: History of the discovery', *Journal of Raman Spectroscopy* **10**(1), 1–8.

[11] Larkin, P. [2011], 'IR and Raman Spectra-Structure Correlations', *Infrared and Raman Spectroscopy* pp. 73–115.

[12] Lloyd, G. R., Wongravee, K., Silwood, C. J., Grootveld, M. and Brereton, R. G. [2009], 'Self Organising Maps for variable selection: Application to human saliva analysed by nuclear magnetic resonance spectroscopy to investigate the effect of an oral healthcare product', *Chemometrics and Intelligent Laboratory Systems* **98**(2), 149–161.

[13] Marro, M., Taubes, A., Abernathy, A., Balint, S., Moreno, B., Sanchez-Dalmau, B., Martínez-Lapiscina, E. H., Amat-Roldan, I., Petrov, D. and Villoslada, P. [2014], 'Dynamic molecular monitoring of retina inflammation by in vivo Raman spectroscopy coupled with multivariate analysis', *Journal of Biophotonics* **7**(9), 724–734.

[14] Meyer-Schwickerath, R., Kleinwächter, T., Papenfuß, H. D. and Firsching, R. [1995],

'Central retinal venous outflow pressure', *Graefe's Archive for Clinical and Experimental Ophthalmology* **233**(12), 783–788.

[15] Obana, A., Hiramitsu, T., Gohto, Y., Ohira, A., Mizuno, S., Hirano, T., Bernstein, P. S., Fujii, H., Iseki, K., Tanito, M. and Hotta, Y. [2008], 'Macular carotenoid levels of normal subjects and age-related maculopathy patients in a japanese population', *Ophthalmology* **115**(1), 147–157.

[16] Pearn, M. L., Niesman, I. R., Egawa, J., Sawada, A., Almenar-Queralt, A., Shah, S. B., Duckworth, J. L. and Head, B. P. [2017], 'Pathophysiology associated with traumatic brain injury: Current treatments and potential novel therapeutics'.

[17] Purves, D., Augustine, G. J., Fitzpatrick, D., Katz, L. C., LaMantia, A., McNamara, J. O. and Williams, M. [2001], *Neuroscience*, 2 edn, Sunderland (MA): Sinauer Associates.

[18] Rygula, A., Majzner, K., Marzec, K. M., Kaczor, A., Pilarczyk, M. and Baranska, M. [2013], 'Raman spectroscopy of proteins: a review', *Journal of Raman Spectroscopy* **44**(8), 1061–1076.

[19] Stiebing, C., Schie, I. W., Knorr, F., Schmitt, M., Keijzer, N., Kleemann, R., Jahn, I. J., Jahn, M., Kiliaan, A. J., Ginner, L., Lichtenegger, A., Drexler, W., Leitgeb, R. A. and Popp, J. [2019], 'Nonresonant Raman spectroscopy of isolated human retina samples complying with laser safety regulations for in vivo measurements', *Neurophotonics* **6**(04), 1.

[20] Surmacki, J. M., Ansel-Bollepalli, L., Pischiutta, F., Zanier, E. R., Ercole, A. and Bohndiek, S. E. [2017], 'Label-free monitoring of tissue biochemistry following traumatic brain injury using Raman spectroscopy', *The Analyst* **142**(1), 132–139.

[21] Talari, A. C. S., Movasaghi, Z., Rehman, S. and Rehman, I. U. [2015], 'Raman Spectroscopy of Biological Tissues', *Applied Spectroscopy Reviews* **50**(1), 46–111.

[22] Tay, L., Tremblay, R. G., Hulse, J., Zurakowski, B., Thompson, M. and Bani-Yaghoub, M. [2011], 'Detection of acute brain injury by Raman spectral signature', *The Analyst* **136**(8), 1620.

[23] Teasdale, G., Maas, A., Lecky, F., Manley, G., Stocchetti, N. and Murray, G. [2014], 'The Glasgow coma scale at 40 years: standing the test of time', *The Lancet Neurology* **13**(8), 844–854.

[24] Zanier, E. R., Bertani, I., Sammali, E., Pischiutta, F., Chiaravalloti, M. A., Vegliante, G., Masone, A., Corbelli, A., Smith, D. H., Menon, D. K., Stocchetti, N., Fiordaliso, F., De Simoni, M.-G., Stewart, W. and Chiesa, R. [2018], 'Induction of a transmissible tau pathology by traumatic brain injury', *Brain* .

[25] Zhang, J. and Liu, Q. [2015], 'Cholesterol metabolism and homeostasis in the brain', *Protein & Cell* **6**(4), 254–264.

[26] Zhao, Z., Wang, M., Tian, Y., Hilton, T., Salsbery, B., Zhou, E. Z., Wu, X., Thiagarajan, P., Boilard, E., Li, M., Zhang, J. and Dong, J.-f. [2016], 'Cardiolipin-mediated procoagulant activity of mitochondria contributes to traumatic brain injury–associated coagulopathy in mice', *Blood* **127**(22), 2763–2772.

CHAPTER 6

SIMULTANEOUS FUNDUS PHOTOGRAPHY AND EYE SAFE RAMAN SPECTROSCOPY FOR HANDHELD NEUROLOGICAL POINT-OF-CARE DIAGNOSTICS

6.1 Abstract

Raman spectroscopy offers rich non-invasive chemical information by measuring inelastically scattered light from a laser, making it a target of interest for a number of clinical diagnostic applications. In the field of ophthalmology, several attempts have been made to use Raman spectroscopy to augment existing imaging modalities at every anatomical layer of the eye. The most challenging of these is the retina, sitting at the back of the eye. Recent *ex-vivo* studies of the retina have shown that Raman spectroscopy can identify subtle chemical changes in the presence of disease or injury states that are applicable to both opthalmology and neurology.

However, the inclusion of the optical properties from the eye results in a compound lens effect, which reduces the overall working distance and makes focusing on the retina impossible. Here, we show that using the eye alone to focus a collimated beam onto the retina, high wavenumber Raman bands can be measured, whilst simultaneously performing imaging of the retina (fundus photography). A compact, portable and eye-safe device is shown by incorporating a smartphone fundus camera and Raman spectroscopy in a 3D printed housing, tested on a synthetic tissue phantom that mimicks the optical and spectral characteristics of the undilated eye.

Introduction

Raman spectroscopy has shown potential to provide rapid, real-time and quantitative diagnostic information in a number of clinical settings both *in-vivo*, and *ex-vivo* (e.g. from bio-

logical fluid or tissue biopsies). By measuring subtle changes to inelastically scattered light, Raman spectroscopy is able to accurately measure the chemical composition of samples, identify changes in disease specific biomarkers and provide diagnostic capability [5, 7–9]. A key advantage is the ability to produce portable, even handheld systems that can be used in clinical and surgical settings [17]. Despite the obvious benefit, Raman scattering is a weak effect, and other more prominent optical processes such as fluorescence tend to dominate. Raman scattering occurs at a rate of around one in every million scattering events (five orders of magnitude smaller than Rayleigh scattering). In order to generate a measurable signal, most Raman systems use a focused laser beam to create a high photon flux at the sample. Both the dominance of fluorescence and the need for a high energy density are problematic for studying biological samples, which tend to have a strong autofluorescent signal and are easily damaged by high laser powers. Therefore, the task at the multidisciplinary boundary between academic and clinical work is to maximise the analytical benefit, given the imposed physiological constraints.

Our emphasis is on the development of non-invasive *in-vivo* techniques, which naturally tend to be further limited to the extremities. A few exceptions exist, e.g. using variations such as spatially offset Raman spectroscopy (SORS) to non-invasively study the composition of bone [18]. Perhaps surprisingly, in opthalmology there are a number of attempts to use Raman spectroscopy to identify disease states in the eye [3, 10, 16]. Recent works highlighted the ability to identify malignant tissue in the brain, acting as a surgical guide, but requires direct and invasive access to the brain [5]. In previous work we demonstrated a path towards non-invasive detection of changes to brain chemistry, by using spectra from tissue samples of the retina to identify TBI in a murine model with a

high degree of accuracy and affinity for differing degrees of injury severity [2]. Although the work presented marked an important milestone, the translational step from *ex-vivo* murine tissue to *in-vivo* measurements is far from obvious or trivial. Recent work in the literature has also studied the retina by similar means, using a standard Raman arrangement and flat mounted or cultured retina tissue [12]. However, the major obstacle to in vivo imaging is the use of high magnification, high numerical aperture objective lenses, which are typically required for Raman spectroscopy. Such objectives have a natural incompatibility with imaging the eye posterior, since the eye itself can be considered as a lens with a combined positive power of 60 diopters [19]. The combined eye-microscope optics leads to a compound lens arrangement, which shortens the working distance of the microscope lens (illustrated in Fig. 6.1). Here, we attempt to address this issue by developing a 3D

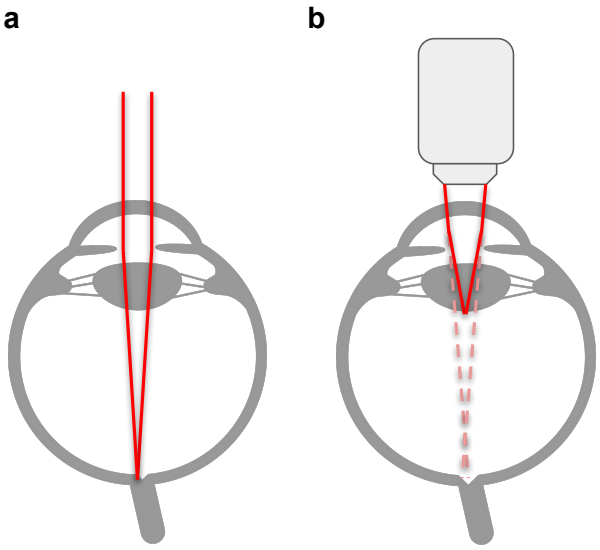

Figure 6.1: Illustration showing the convergence of a collimated beam entering the eye onto the retina (a) and the compound lens effect (b) resulting from the introduction of a microscope objective.

printed eye tissue phantom that mimics both the optical characteristics of the undilated eye and Raman signature from the optic nerve. Combined with a commercially available class I laser, we show that high frequency Raman bands can be safely measured from the retina and highlight the relevance of these spectra to TBI diagnostics as an example application. Stiebing *et al.* [20] have recently demonstrated a similar synthetic model, but considered the dilated pupil; increasing the numerical aperture of the eye. Mydriatic drops can be used to manually dilate pupils, but results in pupil paralysis typically lasting several hours, which is undesirable for rapid TBI diagnostics [14].

The Raman spectrum is commonly divided into distinct frequency regions, with the majority of studies focusing on the fingerprint region between 400 - 1800 cm^{-1}; providing the richest molecular 'fingerprints'. The high frequency bands between 2800 - 3200 cm^{-1} are often used to provide complementary information but contain fewer distinct peaks and provide a more obfuscated picture. Nevertheless, changes to high frequency band profiles have recently been used to provide classification boundaries in their own right between tissue types and disease states for a growing number of cases [11, 15]. This is particularly true for lipid rich fatty substances, which includes brain tissue [13]. Adding to these findings, we show that high wavenumber bands alone can be used to identify TBI from the retina. Using this result, we have then designed a method for eye-safe data acquisition in a realistic synthetic model of the human eye; thereby providing the first tangible path towards non-invasive PoC diagnostics of the brain using Raman spectroscopy. Crucially, our design permits simultaneous Raman spectroscopy and fundus photography by isolating the Raman and white light paths.

Results and Discussion

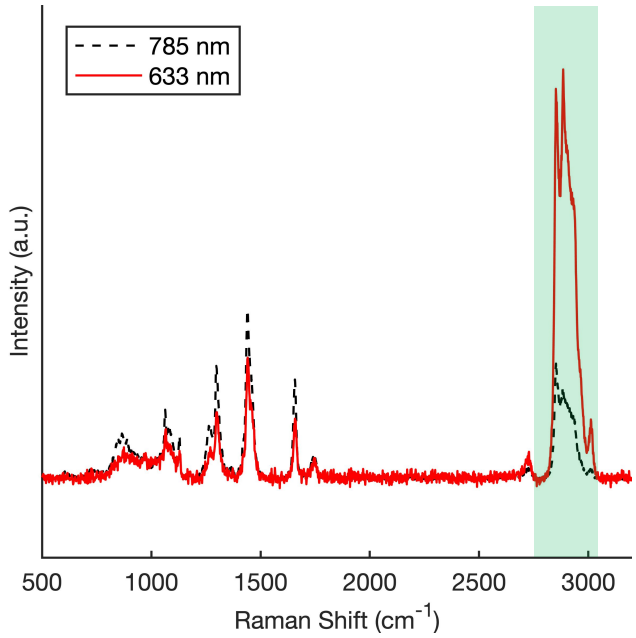

Figure 6.2: Representative Raman spectra of fatty tissue (porcine) covering the fingerprint and high wavenumber regions.

Raman spectra measured using a commercial confocal Raman instrument (Qontor InVia, Renishaw Plc), with excitation wavelengths of 633 nm and 785 nm (1-2 mW). Baseline correction performed in WiRE using intelligent polynomial fitting.

As a result of the fundamental restriction imposed by the optics of the eye shown in Fig. 6.1, we aim to measure Raman spectra from the retina using a collimated beam incident on the cornea, allowing the eye to naturally focus the beam onto the retina. This has previously proven successful *in-vivo*, but limited to identification of age related macular degeneration, by exploiting resonance Raman of macular pigments [6]. Such an effect dramatically enhances the available signal, which helps to mitigate the restricted laser

power and absence of high power optics.

For fatty tissue, such as that found in the brain, we observe an apparent enhancement of high wavenumber bands when using a 633 nm excitation (Fig. 6.2), which normally yields relatively weak bands (e.g. using a 785 nm excitation). Fig. 6.2 shows Raman spectra of fatty tissue measured using an excitation wavelengths of 633 nm and 785 nm, spanning the fingerprint and high frequency regions. In additon to the strong high wavenumber response observed at 633 nm, the high wavenumber bands suffer little intereference from fluorescence, which tends to dominate the fingerprint region. The enhancement effect we observed using a 633 nm laser is not fully understood, but we suggest this may be explained by resonance of the methylene overtone that exists at 619.68 nm [4].

In our previous work, we showed that Raman spectroscopy can be used to detect TBI from the retina in a murine model by using machine learning to separate the data and form a classification model [2]. High wavenumber measurements using an excitation wavelength of 633 nm recorded from these tissue samples are shown for the first time here. These data also display a clear separation between control and TBI groups using the SOM (Fig. 6.3a) [1]. A subtle, but clear change in the ratio of the bands around 2850 and 2930 cm^{-1} can be observed from features extracted using the SOMDI to distinguish between control and TBI samples (Fig. 6.3b). The commercial availability of Conformité Européenne (CE) marked class I lasers, which would guarantee eye safety is low, owing to a lack of demand and a legal responsibility that such devices incur. CE marking indicates conformity with European health and safety regulations, which leaves manufacturers at risk of fines or imprisonment if products are found to be non-compliant. As a result, lasers used in CD drives and even laser pointers are all rated class II or above. Fortunately a

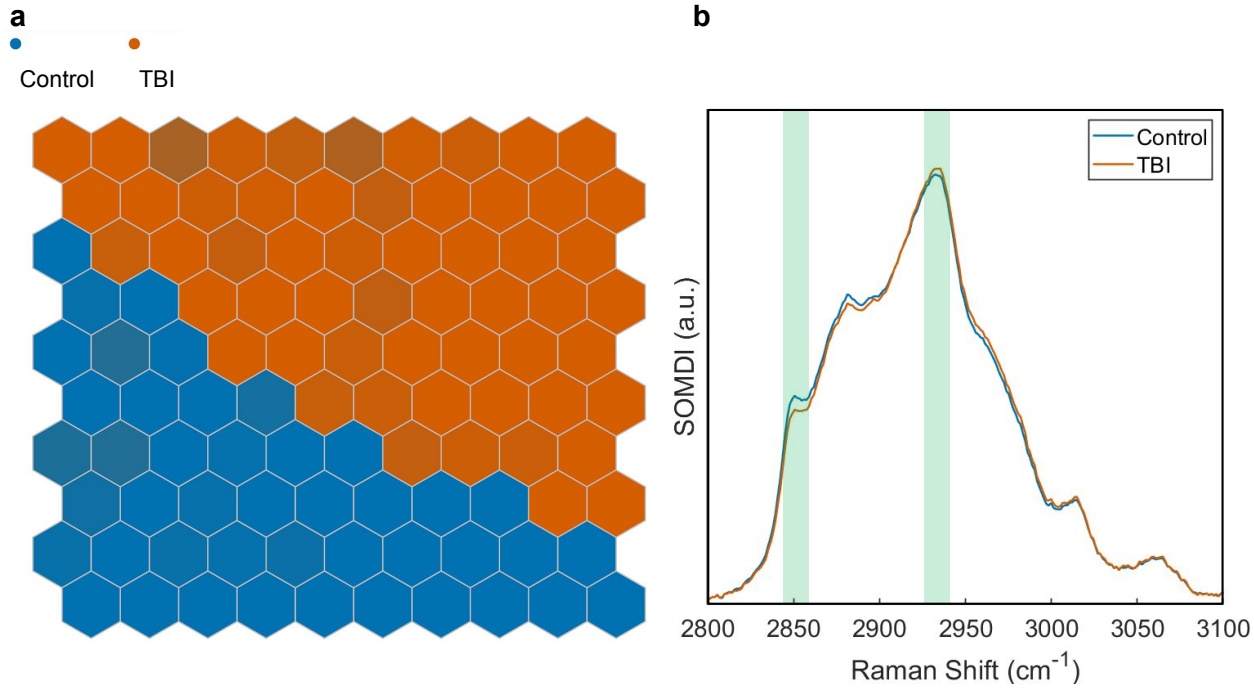

Figure 6.3: a, Spatial clustering of high wavenumber spectra from control and TBI tissue of flat mounted murine retina (n=6) and 400 spectra per sample shown using a SOM. b, Extracted Raman features (SOMDI) for control and TBI groups from the SOM.

635 nm CE marked class I laser is available, advertised for visual fault testing of optical fibres (Kingfisher International). The use of fibre optics allows for further design freedom, allowing for bulky components such as the spectrometer to be kept away from the patient, ensuring a compact imaging system. Silica used in fibre optics normally creates additional interference as this generates its own Raman signal in the fingerprint region. Fortunately, in the high wavenumber region there is no Raman contribution from silica.

We have observed an enhanced response from the high wavenumber region for fatty tissue, shown that these bands alone are capable of detecting the presence of TBI and identified an eye safe laser. In combination with the ability to avoid interference from flu-

orescence and Raman scattering from optical fibres, we therefore have a suitable set of tools to explore the feasibility of detecting high wavenumber Raman bands from the retina.

Simultaneous Raman Spectroscopy and Fundus Photography

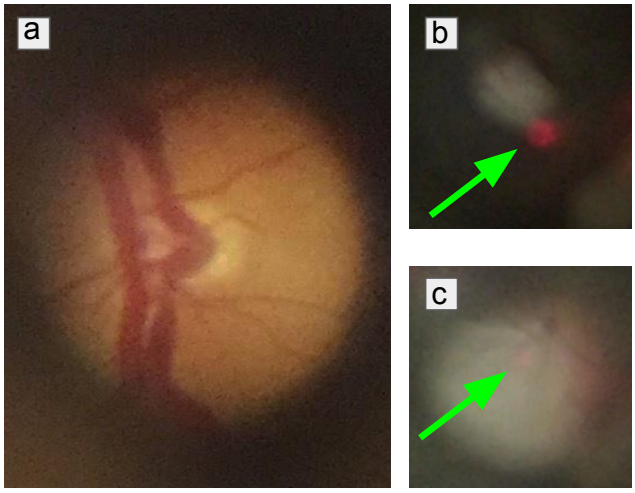

Figure 6.4: Fundus photographs of author's eye and tissue phantom.

a, Fundus photograph of author's eye taken using unmodified D-EYE camera attachment. **b**, fundus photograph (video still) from combined D-EYE and Raman spectroscopy setup, highlighting the laser spot, **c** fundus photograph (video still) focused on the tissue phantom posterior using the combined D-EYE and Raman spectroscopy setup. The laser spot in (i) and (ii) are indicated by an arrow.

In order to measure Raman spectra from the eye posterior a co-aligned imaging system is required to target a region of interest on the retina, such as the optic disc. A D-EYE smartphone fundus camera is used for optical imaging of the retina, which utilises the flash from a smartphone camera for illumination and the phone camera for imaging. The D-EYE is a compact optical module that provides direct illumination and therefore can be used without pupil dilation of the subject. An example fundus image using the D-EYE is

shown in Fig. 6.4a. Fig 6.4b shows that a small amount of laser light is transmitted to the camera through the 625 nm filter, however during fundus imaging (Fig. 6.4c) the laser spot is only faintly visible. A crosshair was drawn onto the phone screen to mark the position of the laser, making targeting straightforward and minimising laser exposure time. A short-

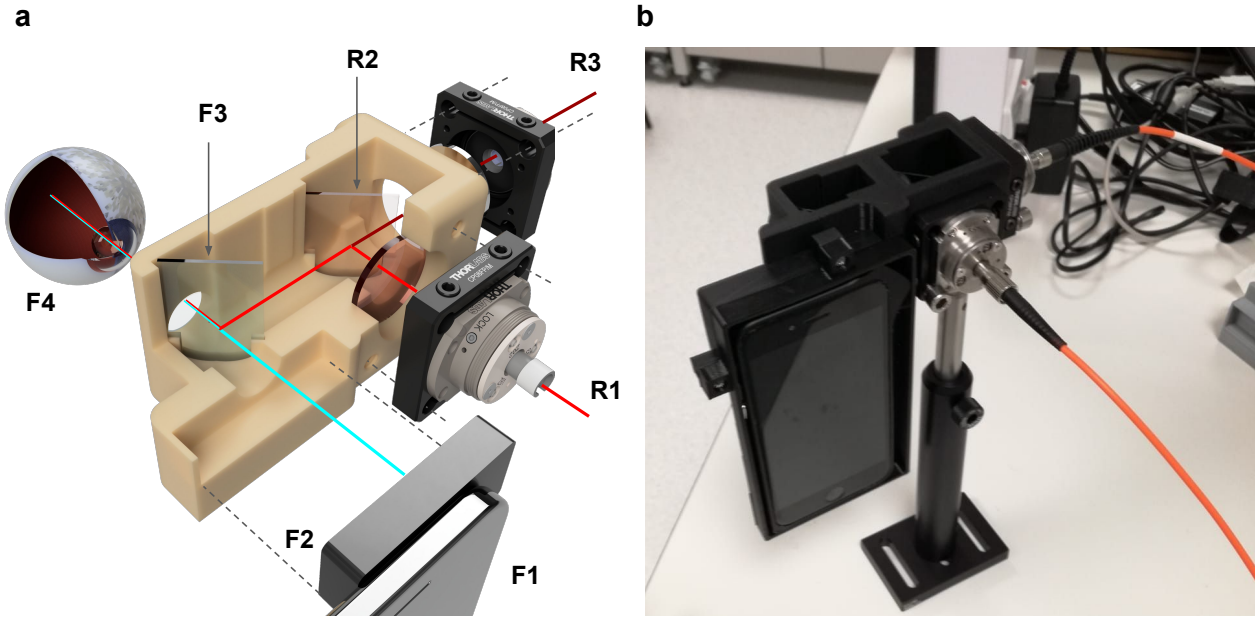

Figure 6.5: Illustration and photograph of combined fundus photography and eye safe Raman spectroscopy optical paths contained within a 3D printed housing.

a, The fundus imaging path consists of a smartphone (F1), D-EYE module (F2), 625 nm short pass filter (F3) and the eye (F4). The Raman spectroscopy path consists primarily of a 635 nm class I laser (0.6 mW) (R1), dichroic beamsplitter (R2) and spectrometer (R3), converging with the imaging path at F3. **b**, Photograph of the completed setup, including smartphone, housing and input/output fibres.

pass 625 nm filter (designed for epifluorescence microscopy) is introduced at an angle of 45 degrees into the optical path between the D-EYE camera and the subject. The cut-off range, edge steepness and efficiency of the filter is such that the majority of the visible

spectrum is transmitted along the path from the camera to the eye and back (> 90 %), whilst rejecting white light from the source at wavelengths > 625 nm that would otherwise interfere with Raman measurements. Wavelengths > 625 nm are efficiently reflected at an angle of 45 degrees (> 98 %), allowing for the introduction of the class I 635 nm laser (0.6 mW) and subsequently Stokes shifted Raman scatter orthogonal to the fundus imaging path.

The combined system is illustrated in Fig. 6.5a showing the 3D printed housing containing the short-pass 625 nm filter (F3). The 635 nm laser is introduced into the housing via a ThorLabs FiberPort, which provides fine control of the beam position and collimation, aiding alignment. The collimated beam is then passed through a 635 nm laser line filter, before being reflected at 45 degrees by a 635 nm dichroic filter (R2) towards F3 and focused onto the retina by the eye. The backscattered Raman light is reflected along the reverse path of F3 towards R2, where the longer wavelength Raman scatter passes through the filter (R2) to a collection FiberPort (R3). Between R2 and R3 sits a 650 nm long pass filter to reject Rayleigh scatter to the detector. R3 is used to focus the beam into a fibre and the spectrum measured using an OceanOptics QE Pro spectrometer tailored for a 638 nm excitation. A photograph of the completed setup is shown in Fig. 6.5b, demonstrating a compact portable and eye safe system for simultaneous fundus photography and detection of high wavenumber Raman bands.

Phantom Eye Model

The device introduced in the previous section relies on the optical power of the eye to focus the Raman laser as shown in Fig. 6.1a. In order to provide a controlled testing environment

with fixed optics, a tissue phantom for the eye was created that mimics the physical dimensions and optical characteristics of the eye, whilst providing a realistic Raman signature of the retina. On average, the human eye has a combined power of 60 diopters, with the majority of focusing being provided by the cornea, and fine adjustment by the crystalline lens [19]. For simplicity a single lens is used to mimic the combined power, restricted by a 4 mm diameter pinhole representing the undilated pupil and housed in a 3D printed case. The tissue characteristics of the retina are then mimicked by a removable sample holder, where a small piece of fatty tissue could be mounted. The sample holder is screwed in place using 3D printed threads, which allows for small focus adjustments to compensate for differences in the thickness of different tissue samples. An exploded view and schematic of the lens (L), housing and sample holder (S) are shown in Fig. 6.6a. The optics of the printed tissue phantom are visually confirmed in Fig. 6.6b, showing a photograph taken using the smartphone without the D-EYE attachment (i), and with the D-EYE attachment (ii), where a target card placed at the position of the retina is only visible through the pupil using the D-EYE fundus camera module. A spectrum measured from the tissue phantom and optical arrangement shown in Fig. 6.5a is shown in Fig. 6.7 (top), where the major bands of the high wavenumber region are clearly resolvable. A representative spectrum from the training dataset used to identify and cluster TBI in the murine model (Fig. 6.3a) is shown in Fig. 6.7 (bottom), where the raw data shown in grey was used in the SOM clustering. This result highlights that whilst the spectra obtainable from a portable system using a class I laser remain noisy, data of this quality can be used to provide meaningful insights with the use of machine learning and a large number of training inputs.

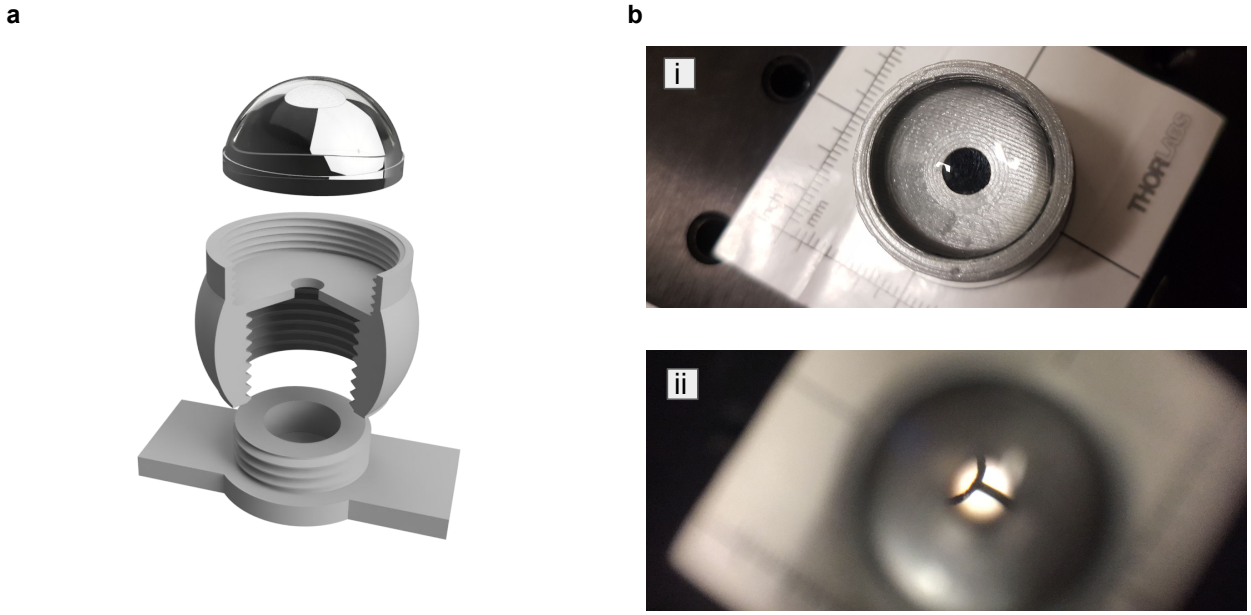

Figure 6.6: 3D printed eye tissue phantom.

a, Exploded view and schematic (inset) of eye tissue phantom, consisting of a single lens to mimic the total power of the eye (L), 4 mm pinhole (P) representing the undilated pupil and screw in sample holder (S). **b**, Photograph of printed tissue phantom (i), Fundus photograph of tissue phantom using D-EYE camera observing target card at eye posterior.

Conclusions

Raman spectroscopy offers a wealth of chemical information that has the potential to offer crucial clinical insight in a growing number of diagnostic and patient monitoring scenarios. By developing an eye safe mechanism that combines fundus photography and Raman spectroscopy for the first time, we start to bridge the gap between potential and reality with the aid of additive manufacturing, smartphone technology, and machine learning. The results presented highlight that Raman spectroscopy of the retina is subject to the natural

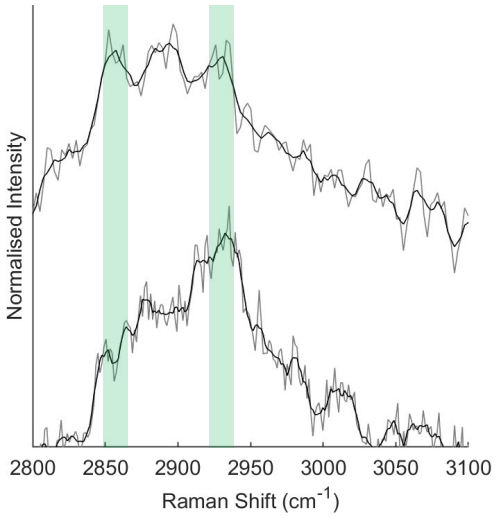

Figure 6.7: High wavenumber spectra from phantom eye model using portable setup (top) and repesentative spectrum from commercial instrument used to form SOM model and distinguish between control and TBI in murine model (bottom).

In each case the raw data is shown in grey, with a smoothed representation shown in black. Smoothing was performed in MATLAB and for visual presentation of the major Raman bands in the high wavenumber region only.

optics and dimensions of the eye, but importantly show how this can be incorporated into the device design.

Whilst we have demonstrated that high wavenumber bands that can be detected from a tissue phantom of the eye can be used to identify TBI, Raman spectroscopy has the potential to be applied to a multitude of neurological and ophthalmic conditions. Importantly, the measurement is made portable and non-invasive, therefore enabling routine point-of-care use and long term patient monitoring. In future, we aim to replace the standalone spectrometer with a compact on-device spectrometer and smartphone readout, allowing for fundus photography and Raman spectroscopy from a single smartphone screen, backed by cloud data processing, storage and machine learning.

Materials and Methods

The combined Raman spectroscopy/fundus photography setup consisted of the following components: iPhone 6 (Apple Inc), D-EYE Smartphone-Based Retinal Imaging System (D-EYE Srl), 625 nm edge BrightLine single-edge shortpass standard epi-fluorescence dichroic beamsplitter, 635 nm BrightLine dichroic beamplitter (Laser 2000 Ltd), 650 nm FEL0650 long pass filter, 635 nm FL0635-10 laser line filter, 2x FiberPort, FC/PC 100 μm 0.22 NA multi-mode input fibre, SMA-SMA 100 μm 0.22 NA multi-mode output fibre (Thor-Labs Inc), 635 nm class I Laser (KI9807A VFL, Kingfisher International), QE Pro Spectrometer optimised for 638 nm (Ocean Optics Inc). The eye tissue phantom consisted of a 3D printed housing encasing an aspheric condenser lens (ACL2018U) with a focal length of 18 mm (ThorLabs Inc). Fatty porcine tissue from bacon was used to simulate the signal from the optic nerve and retina in the phantom. Spectra were acquired using OceanView software (Ocean Optics Inc) and an acquisition time of 30 s and 3 accumulations. CAD designs for 3D printing were made using Autodesk Fusion 360, and printed in polylactic acid (PLA) using an Ultimaker 3 Extended (Ultimaker BV).

Murine Tissue

Raman spectra measured from a clinically relevant murine model of focal TBI (n=6) were acquired using an InVia Qontor (Renish aw plc) equipped with a 633 nm according to the protocol described previously [2]. Surface maps over an area of 2500 μm^2 were acquired for each sample, with an acquisition time of 5s and laser power of 1 mW, a 50x Leica objective (0.75 NA), 1200 l/mm grating with scans recorded in the range 2032-3466 cm^{-1}.

A total of 400 spectra per tissue sample were recorded. Spectra were processed using cosmic ray removal and baseline subtraction in WiRE 5.3 (Renishaw Plc) and exported to text files. SOM analysis was performed using SKiNET [1].

6.2 References

[1] Banbury, C., Mason, R., Styles, I., Eisenstein, N., Clancy, M., Belli, A., Logan, A. and Goldberg Oppenheimer, P. [2019], 'Development of the self optimising kohonen index network (SKiNET) for Raman spectroscopy based detection of anatomical eye tissue', *Scientific Reports* **9**(1), 10812.

[2] Banbury, C., Styles, I., Eisenstein, N., Zanier, E. R., Vegliante, G., Belli, A., Logan, A. and Goldberg Oppenheimer, P. [2020], 'Spectroscopic detection of traumatic brain injury severity and biochemistry from the retina', *Biomedical Optics Express* **11**(11), 6249–6261.

[3] Bauer, N. J., Wicksted, J. P., Jongsma, F. H., March, W. F., Hendrikse, F. and Motamedi, M. [1998], 'Noninvasive assessment of the hydration gradient across the cornea using confocal Raman spectroscopy.', *Investigative Ophthalmology & Visual Science* **39**(5), 831–5.

[4] Cvijin, P., O'Brien, J., Atkinson, G., Wells, W., Lunine, J. and Hunten, D. [1989], 'Methane overtone absorption by intracavity laser spectroscopy', *Chemical Physics Letters* **159**(4), 331–336.

[5] Desroches, J., Jermyn, M., Pinto, M., Picot, F., Tremblay, M.-A., Obaid, S., Marple,

E., Urmey, K., Trudel, D., Soulez, G., Guiot, M.-C., Wilson, B. C., Petrecca, K. and Leblond, F. [2018], 'A new method using Raman spectroscopy for in vivo targeted brain cancer tissue biopsy', *Scientific Reports* **8**(1), 1792.

[6] Ermakov, I. V., McClane, R. W., Gellermann, W. and Bernstein, P. S. [2001], 'Resonant Raman detection of macular pigment levels in the living human retina', *Optics Letters* **26**(4), 202.

[7] Gao, P., Han, B., Du, Y., Zhao, G., Yu, Z., Xu, W., Zheng, C. and Fan, Z. [2017], 'The clinical application of raman spectroscopy for breast cancer detection', *Journal of Spectroscopy* **2017**, 1–10.

[8] Granger, J. H., Granger, M. C., Firpo, M. A., Mulvihill, S. J. and Porter, M. D. [2013], 'Toward development of a surface-enhanced raman scattering (SERS)-based cancer diagnostic immunoassay panel', *Analyst* **138**(2), 410–416.

[9] Höhl, M., Zeilinger, C., Roth, B., Meinhardt-Wollweber, M. and Morgner, U. [2019], 'Multivariate discrimination of heat shock proteins using a fiber optic Raman setup for in situ analysis of human perilymph', *Review of Scientific Instruments* **90**(4), 043110.

[10] Katz, A., Kruger, E. F., Minko, G., Liu, C. H., Rosen, R. B. and Alfano, R. R. [2003], 'Detection of glutamate in the eye by Raman spectroscopy', *Journal of Biomedical Optics* **8**(2), 167.

[11] Koljenović, S., Bakker Schut, T. C., Wolthuis, R., de Jong, B., Santos, L., Caspers, P. J., Kros, J. M. and Puppels, G. J. [2005], 'Tissue characterization using high wave number Raman spectroscopy', *Journal of Biomedical Optics* **10**(3), 031116.

[12] Marro, M., Taubes, A., Abernathy, A., Balint, S., Moreno, B., Sanchez-Dalmau, B., Martínez-Lapiscina, E. H., Amat-Roldan, I., Petrov, D. and Villoslada, P. [2014], 'Dynamic molecular monitoring of retina inflammation by in vivo Raman spectroscopy coupled with multivariate analysis', *Journal of Biophotonics* **7**(9), 724–734.

[13] Minamikawa, T., Harada, Y. and Takamatsu, T. [2015], 'Ex vivo peripheral nerve detection of rats by spontaneous Raman spectroscopy', *Scientific Reports* .

[14] NICE [2020], 'Mydriatics and cycloplegics', `https://bnf.nice.org.uk/treatment-summary/mydriatics-and-cycloplegics.html`.

[15] Nijssen, A., Maquelin, K., Santos, L. F., Caspers, P. J., Bakker Schut, T. C., den Hollander, J. C., Neumann, M. H. A. and Puppels, G. J. [2007], 'Discriminating basal cell carcinoma from perilesional skin using high wave-number raman spectroscopy', *Journal of Biomedical Optics* **12**(3), 034004.

[16] Obana, A., Hiramitsu, T., Gohto, Y., Ohira, A., Mizuno, S., Hirano, T., Bernstein, P. S., Fujii, H., Iseki, K., Tanito, M. and Hotta, Y. [2008], 'Macular carotenoid levels of normal subjects and age-related maculopathy patients in a japanese population', *Ophthalmology* **115**(1), 147–157.

[17] Owens, N. A., Laurentius, L. B., Porter, M. D., Li, Q., Wang, S. and Chatterjee, D. [2018], 'Handheld Raman spectrometer instrumentation for quantitative tuberculosis biomarker detection: A performance assessment for point-of-need infectious disease diagnostics', *Applied Spectroscopy* **72**(7), 1104–1115.

[18] Shu, C., Chen, K., Lynch, M., Maher, J. R., Awad, H. A. and Berger, A. J. [2018], 'Spatially offset raman spectroscopy for in vivo bone strength prediction', *Biomedical Optics Express* **9**(10), 4781.

[19] Smith, G. and Atchison, D. A. [1997], The eye, *in* 'The Eye and Visual Optical Instruments', Cambridge University Press, pp. 291–316.

[20] Stiebing, C., Schie, I. W., Knorr, F., Schmitt, M., Keijzer, N., Kleemann, R., Jahn, I. J., Jahn, M., Kiliaan, A. J., Ginner, L., Lichtenegger, A., Drexler, W., Leitgeb, R. A. and Popp, J. [2019], 'Nonresonant Raman spectroscopy of isolated human retina samples complying with laser safety regulations for in vivo measurements', *Neurophotonics* **6**(04), 1.

CHAPTER 7

SUMMARY AND FUTURE WORK

7.1 Summary

The work in this thesis explored the blue sky concept of measuring changes to brain chemistry non-invasively *via* the eye, imposing strict constraints that are highly unfavourable for Raman spectroscopy. In the absence of SERS, we have shown that machine learning methods can make meaningful insights from extremely noisy spectra. In Chapter 4, computational tools were developed to bridge the disconnect between multivariate analysis in academia and the classification performance offered by ANNs, due to the current resurgence in artificial intelligence. Combining the aspects of data projection, feature extraction and classification into one pipeline rooted in a single mathematical principle, provides a streamlined process for data analysis. By leveraging modern web technologies, data analysis can be performed remotely on any device that has a web browser, and designed to be user friendly to spectroscopists and clinicians, rather than statisticians [2]. A common criticism of ANNs and JavaScript is that they take a long time to train, and that JavaScript is by no means an efficient language. However, the interface provided by commercial PCA tools is so cumbersome that SKiNET can create projects, upload data and train SOMs, whilst the former is still loading the data. It is therefore naive to consider a system based on the performance of the chosen language and hardware alone.

Chapter 5 shows the first evidence that Raman spectra of the retina can be used to identify TBI. Through the application of SKiNET, we reveal the changes to the spectra responsible for the spatial clustering and classification results to be in-line with those observed from Raman spectra of the brain. Furthermore, our findings were in keeping with prior work in the literature for TBI brain tissue, in both the fields of Raman spectroscopy

and mass spectrometry [5, 11, 12]. Whilst these results are extremely encouraging, the sample numbers were limited (as part of the 3R's and financially) and we did not study the case of mild TBI.

One possible solution for addressing the issue of sample numbers, would be to have a method for direct *in-vivo* measurements of spectra from the retina and optic nerve, which is eye safe. Chapter 6 demonstrates a possible pathway for translation, as a handheld smartphone device capable of both fundus photography and high wavenumber Raman spectroscopy simultaneously. The key design elements that allowed for this were the D-EYE smartphone camera (modified to allow additional optics to be placed between the lens and patient), and 625 nm filter used to efficiently separate the imaging and Raman light paths. A limitation of the existing design is that only high wavenumber bands can be measured. Although these have shown promise as diagnostic markers for a number of cases, the specificity in multi-disease setting is unknown [3, 6, 8]. That said, the approaches used clinically today and many of the proposed methods (such as S100-B biomarker assays) suffer the same lack of specificity [1].

For now, the GCS remains the only ground truth for clinical and academic understanding of TBI that can span the entire patient journey as well as injury severity. Non-invasive *in-vivo* Raman spectroscopy may represent the first opportunity for a real alternative, whilst simultaneously offering greater mechanistic insight to further our understanding of the underlying pathobiology of TBI.

7.2 Future Work

For the immediate future, there is a need to validate our findings through internal and external references. Internal references refer to a method of direct analysis of brain tissue *in-vivo* in humans in the context of TBI. We have performed preliminary work for incorporating Raman spectroscopy into an existing standard of care for invasive monitoring in intensive care following TBI, *via* an intracranial bolt [10]. This approach reduces the barrier to entry for ethical approval and allows ground truth assessment with respect to the GCS and ICP. External referencing refers to validation of the biochemical attributions made by a means other than Raman spectroscopy. Since it is possible to measure the optic nerve sheath diameter using MRI [7], it may also be feasible to measure chemical information from the optic nerve sheath using MRS. Chemical species detected by MRS such as NAA could then be used as reference compounds in a fitting library for complementary Raman spectra. However, this requires further development of the device demonstrated in chapter 6, and ethical approval for use *in-vivo*. A drawback of the current design is the apparent intensity of the class I laser as perceived by the patient. A more appropriate approach may be to explore laser wavelengths outside the visible range (e.g. 1064 nm), however this is introduces a new set of challenges. Most notably, there is a much higher demand for optics in the visible over the near-infrared, and so the corresponding filters and detectors tend to lag behind in terms of efficiency. A counter argument to this statement is that in the near-infrared there is much more room for future innovation. Given the experience in lithography and metamaterials within our research group, there may be scope to address existing shortcomings through the development of in-house filters and sensors .

Equally important, given the label free nature of Raman spectroscopy is to show whether diagnostic capabilities of existing studies hold true under multi-disease settings. Since much of the work in the literature makes reference to cellular processes involved in inflammation and apoptosis, which are not disease specific, it is important that this is addressed *in-vitro* and *ex-vivo* [9, 12]. Failure to do so could result in a critical barrier as applications are translated from academic to clinical domains.

More generally, the field of Raman spectroscopy remains immature in comparison to techniques such as mass spectrometry. It is somewhat perplexing that assignments of Raman bands and identification of spectra are still made manually. These are tasks which are far better served by computational methods, and should be automated. Unfortunately, what few databases do exist are far from exhaustive, yet come at a high premium as proprietary offerings from device manufacturers. Ultimately, the only way to address this fundamental shortcoming is through open collaboration.

Imagine that instead of Raman measurements running on offline systems, which frequently crash, are seldom updated and often require deprecated software, Raman spectroscopy to be conducted through cloud systems and behave more like a Google search. Since curation of data is an uninteresting task, by far the best way to build large and accurate databases quickly is through the wisdom of crowds [4]. Such a platform could easily be made independent of device manufacturers, with leading device manufacturers starting to offer programmatic interfaces for exactly this purpose.

Clearly, before Raman spectroscopy can become a disruptive and successful clinical technology, there are many scientific and engineering obstacles which need to be addressed. Overcoming these challenges remains multidisciplinary in nature, at the precipice

between scientific and commercial domains.

7.3 References

[1] Anderson, R. E., Hansson, L.-O., Nilsson, O., Dijlai-Merzoug, R. and Settergren, G. [2001], 'High serum S100B levels for trauma patients without head injuries', *Neurosurgery* **48**(6), 1255–1260.

[2] Banbury, C. [2018], 'Raman toolkit - analysis and data management tool for Raman spectra', `https://github.com/cbanbury/raman-tools`.

[3] Bauer, N. J., Wicksted, J. P., Jongsma, F. H., March, W. F., Hendrikse, F. and Motamedi, M. [1998], 'Noninvasive assessment of the hydration gradient across the cornea using confocal Raman spectroscopy.', *Investigative Ophthalmology & Visual Science* **39**(5), 831–5.

[4] Cao, Y. and Zhou, X. [2013], Harnessing the wisdom of crowds for corpus annotation through CAPTCHA, *in* 'Lecture Notes in Computer Science (including subseries Lecture Notes in Artificial Intelligence and Lecture Notes in Bioinformatics)', Vol. 7808 LNCS, Springer, Berlin, Heidelberg, pp. 638–645.

[5] Chao, H., Anthonymuthu, T. S., Kenny, E. M., Amoscato, A. A., Cole, L. K., Hatch, G. M., Ji, J., Kagan, V. E. and Bayır, H. [2018], 'Disentangling oxidation/hydrolysis reactions of brain mitochondrial cardiolipins in pathogenesis of traumatic injury', *JCI Insight* **3**(21).

[6] Desroches, J., Jermyn, M., Pinto, M., Picot, F., Tremblay, M.-A., Obaid, S., Marple, E., Urmey, K., Trudel, D., Soulez, G., Guiot, M.-C., Wilson, B. C., Petrecca, K. and Leblond, F. [2018], 'A new method using Raman spectroscopy for in vivo targeted brain cancer tissue biopsy', *Scientific Reports* **8**(1), 1792.

[7] Kim, D. H., Jun, J.-S. and Kim, R. [2018], 'Measurement of the optic nerve sheath diameter with magnetic resonance imaging and its association with eyeball diameter in healthy adults', *Journal of Clinical Neurology* **14**(3), 345.

[8] Koljenović, S., Bakker Schut, T. C., Wolthuis, R., de Jong, B., Santos, L., Caspers, P. J., Kros, J. M. and Puppels, G. J. [2005], 'Tissue characterization using high wave number Raman spectroscopy', *Journal of Biomedical Optics* **10**(3), 031116.

[9] Marro, M., Taubes, A., Abernathy, A., Balint, S., Moreno, B., Sanchez-Dalmau, B., Martínez-Lapiscina, E. H., Amat-Roldan, I., Petrov, D. and Villoslada, P. [2014], 'Dynamic molecular monitoring of retina inflammation by in vivo Raman spectroscopy coupled with multivariate analysis', *Journal of Biophotonics* **7**(9), 724–734.

[10] Mowbray, M., Banbury, C., Rickard, J. J. S., Davies, D. J. and P., G. [2020], Development of an advanced medical probe-device for intracranial monitoring of traumatic brain injury via raman spectroscopy (unpublished).

[11] Surmacki, J. M., Ansel-Bollepalli, L., Pischiutta, F., Zanier, E. R., Ercole, A. and Bohndiek, S. E. [2017], 'Label-free monitoring of tissue biochemistry following traumatic brain injury using Raman spectroscopy', *The Analyst* **142**(1), 132–139.

[12] Tay, L., Tremblay, R. G., Hulse, J., Zurakowski, B., Thompson, M. and Bani-Yaghoub, M. [2011], 'Detection of acute brain injury by Raman spectral signature', *The Analyst* **136**(8), 1620.

Appendices

APPENDIX A

SUPPORTING INFORMATION FOR CHAPTER 4

	Cornea	Lens	Vitreous Humour	Retina	Optic Nerve
Cornea	88.0	2.1	4.7	3.3	2.8
Lens	0.5	99.8	0.5	0	0.1
Vitreous Humour	1.0	0.1	96.5	2.7	0.5
Retina	1.0	0.2	2.3	95.7	1.7
Optic Nerve	4.6	0.71	0.8	2.2	92.5

Table A.1: Confusion matrix showing average percentage for each class from the 1210 test spectra.

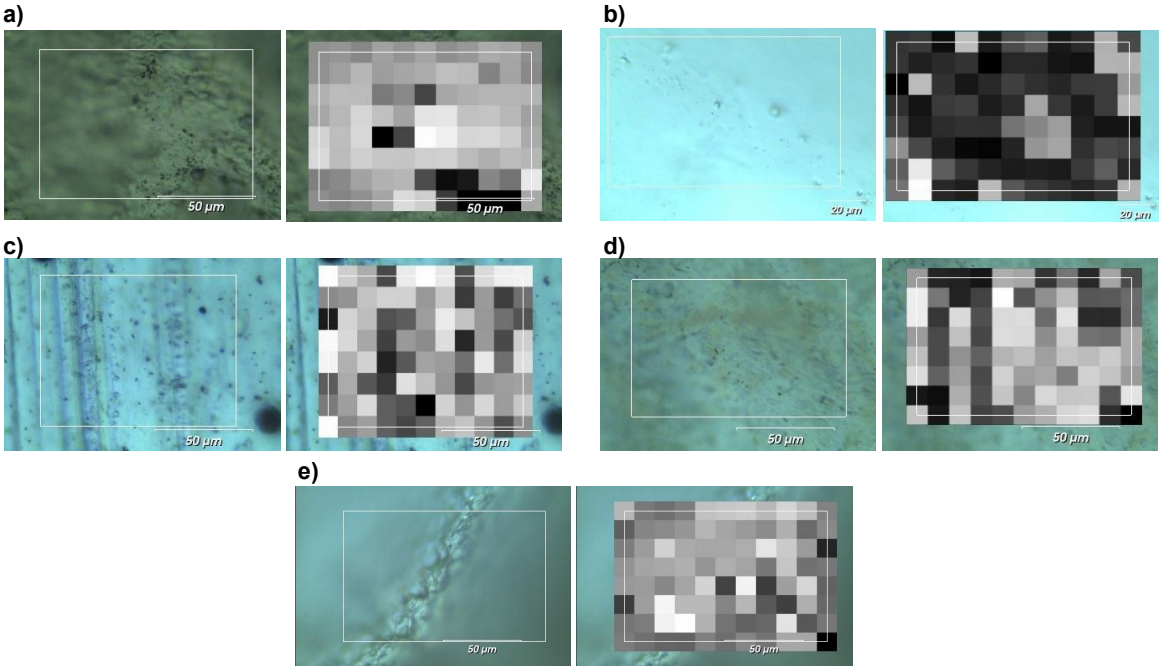

Figure A.1: Paired examples of bright field optical microscope images (left) and PCA scores across map scan (right) for each tissue type: a, cornea, b, lens, c, vitreous humour, d, retina and e, optic nerve.

a)

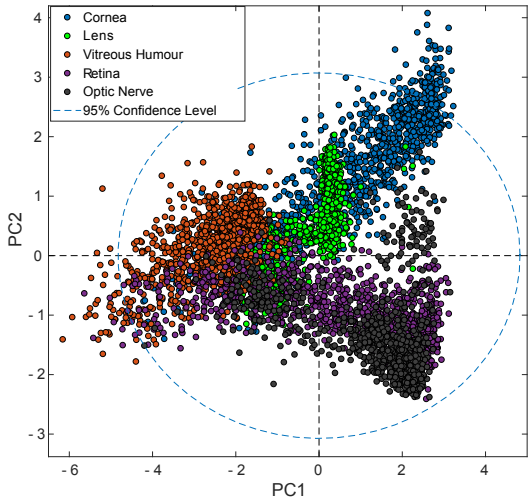

b)

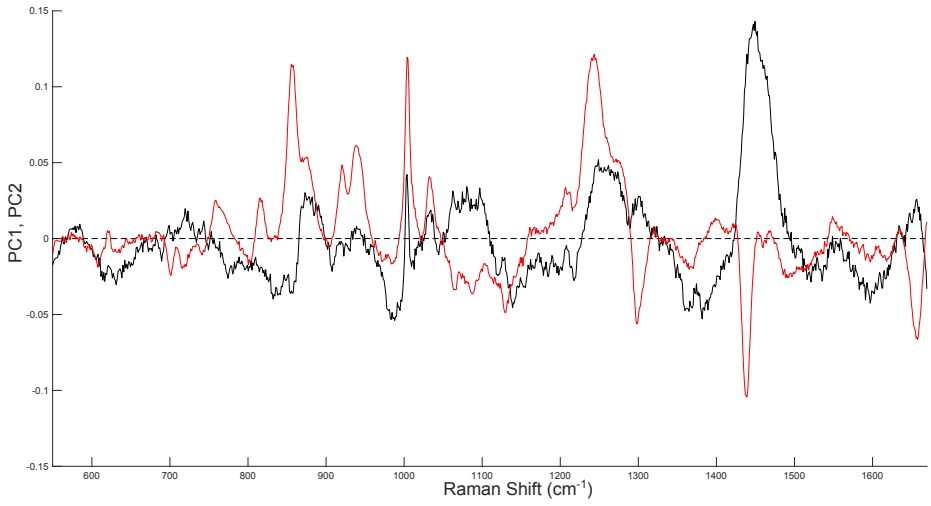

Figure A.2: a, Scores plot for the first two principal components showing poor spatial separation of classes. b, Loadings for PC1 and PC2.

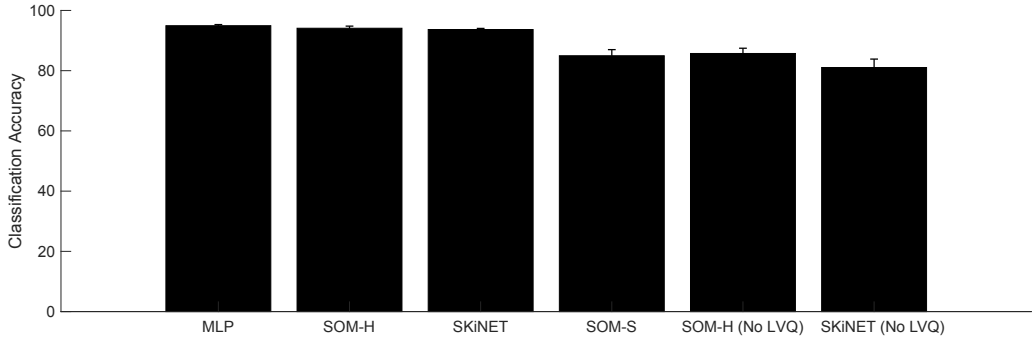

Figure A.3: Comparison of classification accuracy for different approaches to SOM based classification. SOM-H refers to using the hit count for class identification, SOM-S uses supervised SOMs with an optimal scaling value.

APPENDIX B

SUPPORTING INFORMATION FOR CHAPTER 5

Lipid	#07	#08	#09	#64	#65	#69	Average
Cardiolipin	0.88	0.85	0.86	0.86	0.85	0.86	0.86
Cholesteryl ester	0	0	0	0	0	0	0
Cholesterol	0.11	0.12	0.13	0.11	0.13	0.12	0.12
Cytochrome C	0.11	0.12	0.15	0.12	0.11	0.11	0.12
Galactocerebroside	0	0	0	0	0	0	0
Ganglioside	0	0	0	0	0	0	0
Sphyingomyelin	1.15	1.24	0.87	1.38	1.39	1.41	1.24
Phosphatidylcholine	0	0	0	0	0	0	0
Phosphatidylserine	0	0	0	0	0	0	0
Phosphatidylinositol	0	0	0	0	0	0	0
Phosphatidylethanolamine	0	0	0	0	0	0	0
Sulfatide	0	0	0	0	0	0	0
Triacylglyceride	0.05	0.06	0.06	0.03	0.03	0.03	0.04

Table B.1: Decomposition of contribution from brain lipids in average Raman spectra of brain samples from contusion core for sham group using NNLS fitting.

Lipid	#04	#05	#06	#66	#67	Average
Cardiolipin	0.29	0.58	0.53	0.02	0.45	0.37
Cholesteryl ester	0	0	0	0	0	0
Cholesterol	0.2	0.18	0.23	0.1	0.22	0.18
Cytochrome C	0.48	0.22	0.02	0.24	0.12	0.22
Galactocerebroside	0	0	0	0	0	0
Ganglioside	0	0	0	0	0	0
Sphyingomyelin	0	1.48	2.6	0	1.02	1.02
Phosphatidylcholine	0.78	0	0	0.2	0.64	0.32
Phosphatidylserine	0	0	0	0	0	0
Phosphatidylinositol	0	0	0	1.33	0	0.27
Phosphatidylethanolamine	0.01	0	0	0	0.04	0.01
Sulfatide	0	0	0.32	0	0	0.06
Triacylglyceride	0.02	0.05	0.06	0	0.06	0.04

Table B.2: Decomposition of contribution from brain lipids in average Raman spectra of brain samples from contusion core for mTBI group using NNLS fitting. Lipids that have non-zero fitting coefficients in the sham group are highlighted in bold.

Lipid	#01	#02	#03	#61	#62	#63	Average
Cardiolipin	0.02	0.63	0.58	0.33	0.12	0.77	0.41
Cholesteryl ester	0	0	0	0	0.02	0	0.00
Cholesterol	0.19	0.2	0.21	0.2	0.25	0.14	0.20
Cytochrome C	0.4	0.01	0.21	0.34	0	0	0.16
Galactocerebroside	0	0	0	0	0	0	0
Ganglioside	0	0	0	0	0.22	0	0.04
Sphyingomyelin	0	2.6	1.22	2.02	0.42	2.22	1.41
Phosphatidylcholine	0.94	0	0	0	1.1	0	0.34
Phosphatidylserine	0	0	0.16	0	0	0	0.03
Phosphatidylinositol	0.28 0	0	0	0	0	0.05	
Phosphatidylethanolamine	0	0	0	0	0	0	0
Sulfatide	0	0.13	0	0	0	0	0.02
Triacylglyceride	0.11	0.07	0.03	0.09	0.18	0.08	0.09

Table B.3: Decomposition of contribution from brain lipids in average Raman spectra of brain samples from contusion core for sTBI group using NNLS fitting. Lipids that have non-zero fitting coefficients in the sham group are highlighted in bold.

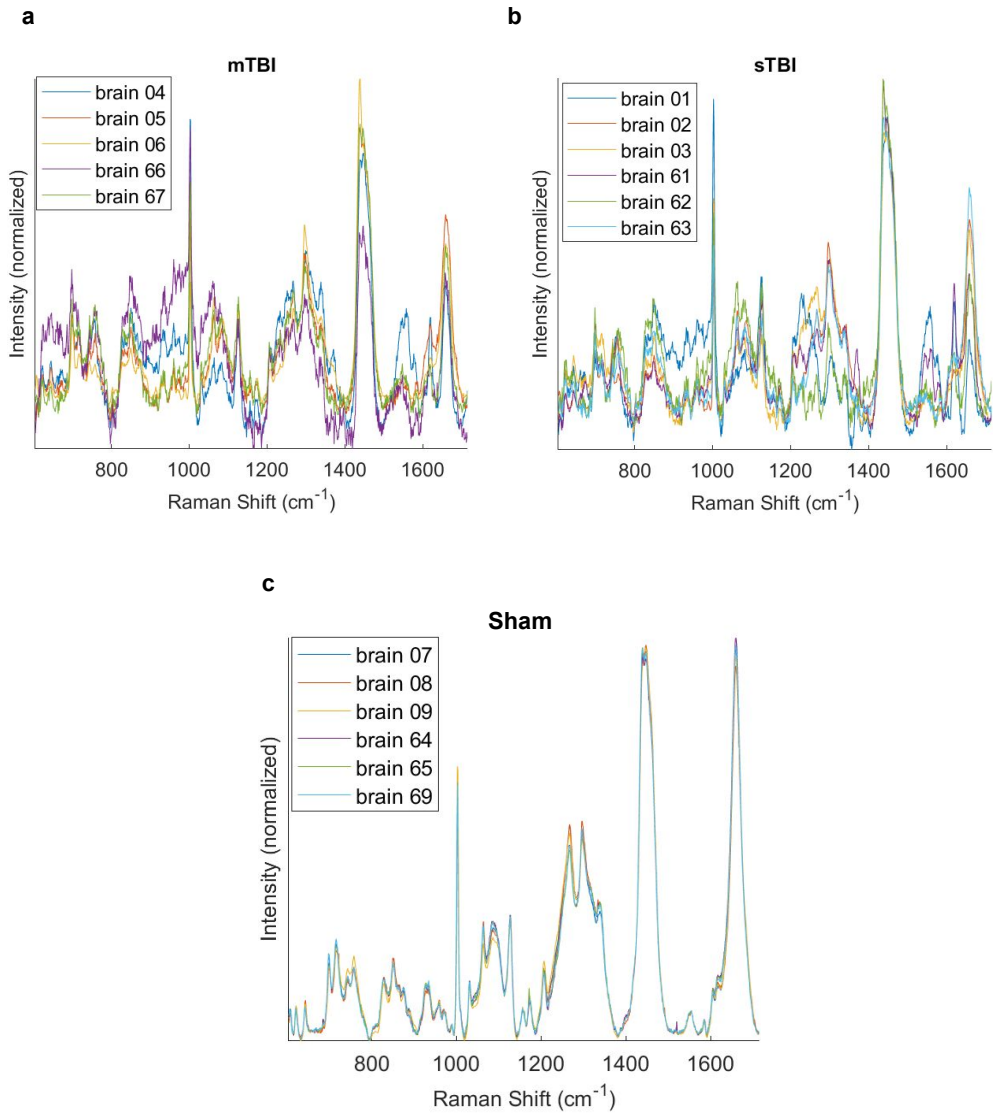

Figure B.1: Raman spectra collected from the injury site on left hemisphere of brain (n=6) for mTBI (a), sTBI (b), and sham (c) groups. Data for each tissue sample were collected as a Raman surface map (400 points) following the surface topography. Raman maps were averaged to give a single spectrum per sample, followed by baseline subtraction using an intelligent spline fit.

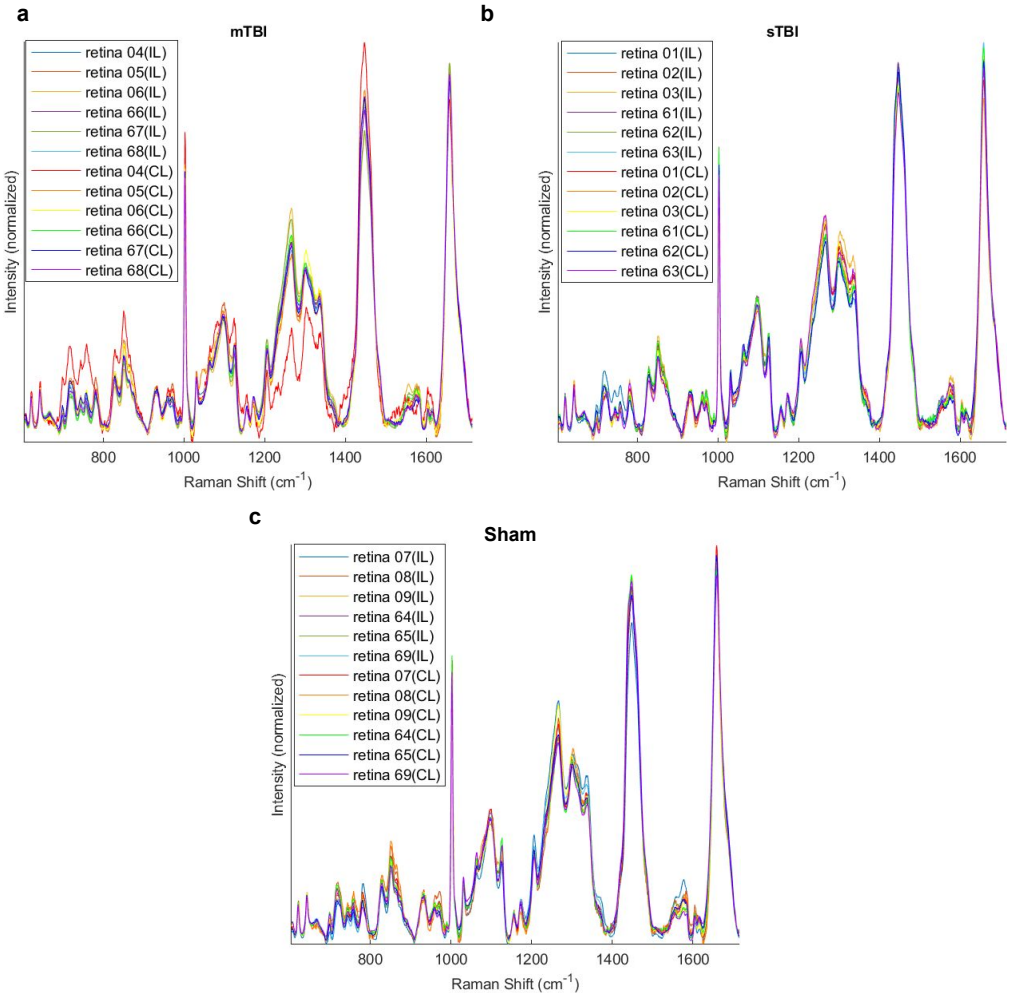

Figure B.2: Raman spectra collected from ipsilateral (IL) and contralateral (CL) flat mounted retina (n=6) for mTBI (a), sTBI (b), and sham (c) groups. Data for each tissue sample were collected as a Raman surface map (400 points) following the surface topography. Raman maps were averaged to give a single spectrum per sample, followed by baseline subtraction using an intelligent spline fit.

Model	Sham (%)	mTBI (%)	sTBI (%)
Bilateral	69.4 ($\pm$ 0.9)	75.1 ($\pm$ 0.9)	82.0 ($\pm$ 1.4)
Ipsilateral	81.5 ($\pm$ 0.8)	76.7 ($\pm$ 1.9)	86.2 ($\pm$ 1.4)
Contralateral	76.6 ($\pm$ 1.6)	76.6 ($\pm$ 1.2)	88.7 ($\pm$ 0.9)

Table B.4: Classification accuracy of TBI using Raman spectra of retina, modeled using data from both eyes (bilateral), eyes from the side of injury only (ipsilateral) and contralateral eyes. Results show the average over 10 SOM initializations and standard deviation in brackets.

APPENDIX C

TUNEABLE METAMATERIAL-LIKE PLATFORMS FOR SURFACE-ENHANCED RAMAN SCATTERING VIA THREE-DIMENSIONAL BLOCK CO-POLYMER-BASED NANOARCHITECTURES

ACS APPLIED MATERIALS & INTERFACES

Research Article

Cite This: ACS Appl. Mater. Interfaces 2019, 11, 14437−14444

www.acsami.org

Tuneable Metamaterial-like Platforms for Surface-Enhanced Raman Scattering via Three-Dimensional Block Co-polymer-Based Nanoarchitectures

Carl Banbury,[†] Jonathan James Stanley Rickard,[†,‡] Sumeet Mahajan,[§] and Pola Goldberg Oppenheimer*[,†]

[†]School of Chemical Engineering, College of Engineering and Physical Sciences, University of Birmingham, Birmingham B15 2TT, U.K.

[‡]Department of Physics, Cavendish Laboratory, University of Cambridge, JJ Thomson Avenue, Cambridge CB3 0HE, U.K.

[§]Department of Chemistry and the Institute for Life Sciences, University of Southampton, University Road, Southampton SO17 1BJ, U.K.

Supporting Information

ABSTRACT: Surface-enhanced Raman spectroscopy (SERS) pushes past the boundaries and inherent weaknesses of Raman spectroscopy, with a great potential for a broad range of applications particularly, for sensing. Yet, current real world applications are limited due to poor reproducibility, low-throughput, and stability issues. Here, we present the design and fabrication of self-assembly guided structures based on adjustable block co-polymer (BCP) nanomorphologies and demonstrate reproducible SERS enhancement across large areas. Golden three-dimensional (3D) nanostructured morphologies with controllable dimensions and morphologies exhibit high chemical stability, enhanced plasmonic properties and are highly suitable for SERS substrates due to the strong enhancement of the electromagnetic field. Adjustable, free standing porous nanostructures, continuous in 3D space are achieved by removal of selected BCP constituents. Four BCP morphologies and the corresponding achievable enhancement factors are investigated at 633 and 785 nm excitation wavelengths. The choice of excitation laser is shown to greatly affect the observed signal enhancement, highlighting the sensitivity of the technique to the underlying surface architecture and length scales. By using BCP assemblies, it is possible to reliably tune these parameters to match specific applications, thus bridging the gap toward the realization of applied metamaterials. The fabricated SERS platforms via three-dimensional block co-polymer-based nanoarchitectures provide a recipe for intelligent engineering and design of optimized SERS-active substrates for utilization in the Raman spectroscopy-based devices toward enabling the next-generation technologies fulfilling a multitude of criteria.

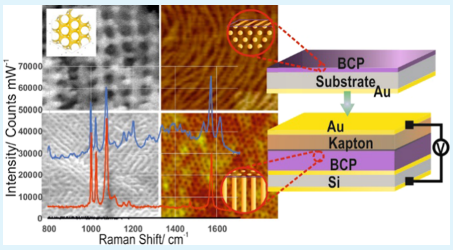

KEYWORDS: *surface-enhanced Raman spectroscopy (SERS), block-co-polymer nanomorphologies, tuneable golden 3D nanostructures*

INTRODUCTION

Block co-polymer (BCP) nanoarchitectures have been emerging as straightforward and high-throughput platforms for designing and fabricating a range of large-area nanostructures with controllable dimensions, composition, and spatial arrangement. Considerable research has been directed toward fabricating and exploiting the self-assembled BCP microphases for their potential implementation into a variety of functional applications, including additives to enable enhanced toughness of plastics and polymer blend composites, guiding the synthesis of nanoparticles[1] acting as capsules for drug delivery,[2] platforms for organic photovolatics, electronics, data storage, and sensors.[3−6] Surface-enhanced Raman spectroscopy (SERS) has been concurrently, a topic of extensive scientific investigations in particular, because of its high-sensitivity and specificity for tracing molecular fingerprints, aided by optically excited localized surface plasmon resonances (LSPRs), yielding intense local electric fields on metal micro to nanostructures.[7−9] A significant SERS enhancement can be achieved via the coupling of the excitations of surface fields to adsorbed or proximal molecules.[10−12] The substrate on which SERS[10,13−21] is performed is often the crucial factor for successful signal enhancement. However, consistent and controllable fabrication of SERS-active, sensitive and adjustable surfaces still remains

Received: January 8, 2019
Accepted: March 18, 2019
Published: March 18, 2019

challenging. SERS substrates are often limited by instability and lack of tuneability. Since every flaw in the substrate has a direct and considerable impact on the ultimate signal, SERS still requires development of methods for designing, fabricating, and controlling the surface architecture. Many studies exploit nanoparticle-based systems for SERS enhancement and consequently, their reproducibility, stability, and practical applications remain debatable.[22−25] The vast majority of top-down synthetic routes to generate nanostructures are based on conventional patterning techniques and are typically expensive, complex and often require precise integration of multistep processes while exhibiting a limited scalability, highlighting the need for more reliable and straightforward lithographic methods to develop efficient access to adjustable three-dimensionally (3D) isotropic nanostructures. This has driven extensive efforts to explore novel processes for the fabrication of highly ordered 3D structures with sub-micrometer periodicities, signposting BCP self-assembly as an alternative bottom-up lithographic method, enabling specific orientations from chosen materials on supporting substrates, as a platform for a next generation of miniaturized devices. However, the utilization of self-assembled BCPs for plasmonics, including SERS, has only recently begun to gain traction[9,26,27] but still remains predominantly underexplored. Recently, Zhang et al. reported the use of BCP cylinders integrated with silver nanoparticles for enhancing Raman signals,[28] although for practical SERS applications, gold, being more inert and stable, is more suitable than silver. Furthermore, none of the studies has paid attention to the optimization and tuning possibilities, which can be accessed via the range of morphologies of BCP-based substrates for advanced SERS applications. Careful control, understanding, and subsequent intelligent engineering can, therefore, further enable the tailoring of bottom-up BCP morphologies for the generation of "hot-spots"; to take full advantage of the synergistic functions of the resulting BCP-based SERS architectures.

Here, we demonstrate a range of gold SERS-active 3D nanostructures fabricated from block co-polymer self-assembled materials and study their corresponding SERS enhancement and optical properties. Through tailoring the BCP synthesis and tuning the self-assembly, combined with guidance and fabrication of nanomorphologies with characteristic length scales, patterning method and laser frequencies, flexible 3D architectures are fabricated, which are difficult to achieve in another fashion. The fabricated 3D gold SERS substrates are based on block-co-polymer microdomain morphologies and comprised of planar (lamellar) structures, cylindrical (both parallel and perpendicular to the supporting substrates), and gyroid (double and free-standing) morphologies. Selective degradation of the self-assembled phase-separated BCP components, plated with a plasmon-active metal (gold) effectively enhances the electromagnetic field, yielding high SERS signals. Consequently, we have designed nanostructured substrates with varying, laser-matching SERS enhancements, which are known to exhibit different Raman signal augmentation at different excitation wavelengths. Characterization of the photonic properties of 3D BCP-based nano-morphologies revealed that these composite nanostructures behave like new metals with distinct optical characteristics, with a plasma edge shifted to longer wavelengths and a transparency that is greatly increased compared to naturally occurring bulk metal.[29] Substrates with tuneable (controllable) surface plasmon resonances of the nanostructures matching the excitation lasers are essential for gaining the highest enhancements. Broad surface plasmon resonances are needed, especially with red and near-infrared excitation lasers so that high electric fields at both the excitation and Raman scattered wavelengths can be available, to allow for the highest enhancements to be obtained.[30] The obtainable optical properties can be further tuned immensely by variation of the unit cell size, the fill fraction, choice of the BCP morphology, and the plasmonic metal used for filling into the template, building upon the various approaches developed to tune the size, shape, and spacing of BCP domains and the nanostructures derived from them.[31−35] The architectures fabricated here can provide low-cost, simple, large-active-area substrates, with broad plasmon resonances which open a window for a range of SERS active, easily switchable structures to accommodate various applications toward developing novel, adjustable photonic metamaterials and miniaturized devices.

RESULTS AND DISCUSSION

The phase diagram in Figure 1 demonstrates the designed and fabricated BCP assemblies containing a range of nano-

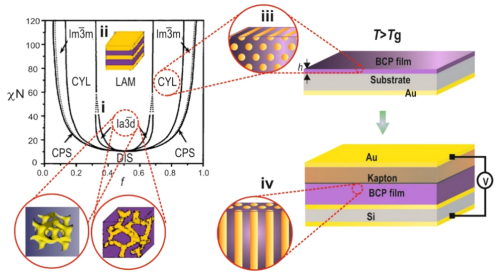

Figure 1. Schematic representation of the fabrication of four morphologies for SERS substrates from the available self-assembled range of BCPs. (i) Three-dimensional gyroid nanostructures comprised of three rotated arms at the 3-fold junction with each arm attached to another set. (ii) Tuning the volume fractions of the blocks yields lamellae and cylinder morphologies. (iii, iv) Fabrication of mixed (hexagonal and lying) cylinder arrays and those perpendicular to the substrate (iv) via annealing of poly(ferrocenylsilane)-*block*-polylactide (PFS-*b*-PLA) film above the glass transition temperature, T_g in a capacitor like set-up with an applied E_f of 155 ± 15 V/μm, which are solidified by quenching to room temperature. Mixed morphology comprised of a combination of parallel and perpendicular to the substrate cylinders can be generated in-between (iii) and (iv) by controlling the strength of the applied electric field.

structured morphologies, including the double gyroid (DG), free-standing gyroid (FSG), mixed combination of parallel and perpendicular to the substrate, (MCYL), hexagonal cylinder domains and only perpendicular cylinders (CYL), accordingly. In the bulk, various morphologies that depend on the relative volume fraction of one block relative to the other produce complex nanostructures due to the microphase separation of the BCPs on the molecular scale resulting in a spontaneous formation of a broad spectrum of ordered nanostructures. The evolving nanomorphologies from the BCP melt are determined by the competition of entropy and the enthalpy between the

DOI: 10.1021/acsami.9b00420
ACS Appl. Mater. Interfaces 2019, 11, 14437−14444

two blocks and eventually result in the minimization of the system's energy, yielding the most favorable configurations.

BCP phase morphology typically evolves at the length scale of tens of nanometers and can be controlled by the volume fractions of the constituent blocks, whereas the total number of monomers N in the BCP chain determines the dimensions of the nanostructure. Lamellar morphology typically results from the alternating symmetric BCP layers, whereas higher levels of one constituting block volume fraction yield asymmetric morphologies comprised of one component forming the minority phase and the other, the matrix phase and finally, with the bicontinuous gyroids (Figure 1i) formed between the lamellae (Figure 1ii) and the hexagonally packed cylinders, oriented parallel to the substrate. BCP self-assembly of random-coil polymers is a highly efficient process and on supporting surfaces, many of the co-polymer morphologies exist naturally in a thin film or layer geometries. However, the interactions of the blocks with the surface typically result in an orientation of the microdomains parallel to the substrate, (Figure 1iii) limiting the successful replication of "lying" cylinders due to the collapse of the structure following the removal of the matrix during the templating process.

Well-defined nanostructures with long-range positional tuning and a high-degree of alignment can be achieved by controlling the hydrodynamic flow and the strength of applied field in a microcapacitor device. Therefore, an experimental set-up for exposing BCP films to an electric field, without a gap, was assembled to perpendicularly align the cylinders lying parallel to the supporting substrate inside the BCP thin film. Application of an external electric field, E_f, enables control of the degree of alignment of the hexagonally ordered cylinders, between lying to perpendicular orientations as well as (between Figure 1iii to iv, accordingly) mixed cylinders morphologies, i.e., MCYL. Annealing above the glass transition temperature of the thin BCP film, without applying an external electric field, results in cylinders which predominantly remain oriented parallel to the substrate with distinctive areas of a terraced-like morphology (Figure 1iii) due to the reorganization of the highly mobile chains in the BCP melt.

Polystyrene-*b*-poly(D,L-lactide) (PS-*b*-PLLA) block-co-polymer was used to synthesize the double gyroid nanostructure comprising two interpenetrating, three-dimensional and continuous networks containing 39% fill fraction (Figure 2a). Selective degradation of the minor phase, while preserving the majority one in a phase-separated block co-polymer morphology, by ultraviolet (UV) ozone etching and via a subtle hydrolytic-degradation, yielded a free-standing gyroid template (Figure 2b), which was subsequently coated with inorganic material such as gold (Figure 3). Thin films (50−400 nm) of poly(ferrocenylsilane)-*block*-polylactide (PFS-*b*-PLA), spin-coated onto a p-doped silicon wafer (covered with a 50 nm gold layer on their backside) or on the fluorine-doped tin oxide (FTO) glass, formed a cylindrical microphase morphology with an ordered block co-polymer containing cylinders of PLA in a matrix of PFS, lying in the plane of the film (Figure 2c). Cylinder orientation parallel to the film's surface is typically thermodynamically preferred because of the differing surface energies of the two blocks at one or both interfaces. The electric field-guided surface morphology of co-polymer cylinders annealed above the glass transition temperature in the capacitor sandwich with an applied voltage of 3−4 kV yielding vertically aligned cylindrical nanodomains parallel to the axis of the electric field lines, (Figure 2d) due to the

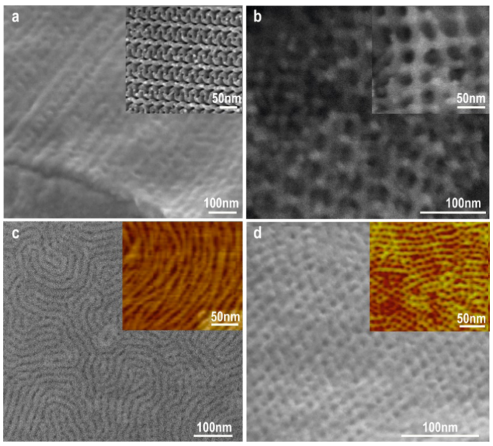

Figure 2. Scanning electron microscopy (SEM) and atomic force microscopy (AFM) characterization of the BCP-based nanomorphologies. Tilted (a) and a top-view (a, inset) images of the initially fabricated DG morphology and (b) FSG nanostructures after the selective removal of the minor phase yielding matrix with interconnected networks as a template for further nucleation and growth of inorganic material. (c) As-spun thin BCP film reveals microphase morphology of lying cylinders (inset) which are then reorganized into vertical cylinders (d) mixed with areas of lying cylinders (MCYL) (d, inset) after the electric field application and annealing in a controlled manner.

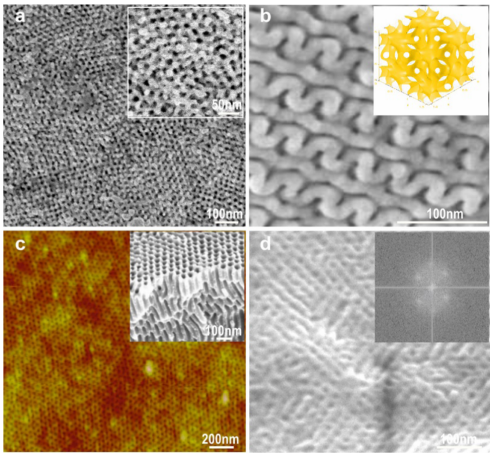

Figure 3. Gold-plated three-dimensional nanomorphologies. Low-angle backscattered scanning electron microscopy (LAB-SEM) images of Au-plated and -sputtered nanostructures of (a) FSG with a unit cell of 20 nm and fill fraction of 21% and (b) DG with the corresponding MATLAB-generated simulations of the nanostructure's cell-unit (inset). (c) AFM height image of aligned cylinders continuously spanning the two electrodes with cross-sectional SEM (c, inset) revealing voids left by removal of the minor phase and subsequently gold plated and sputtered. (d) Surface SEM of the Au-replicated mixed cylindrical morphology after UV ozone etching of PFS matrix with the FFT of the image (inset).

DOI: 10.1021/acsami.9b00420
ACS Appl. Mater. Interfaces 2019, 11, 14437−14444

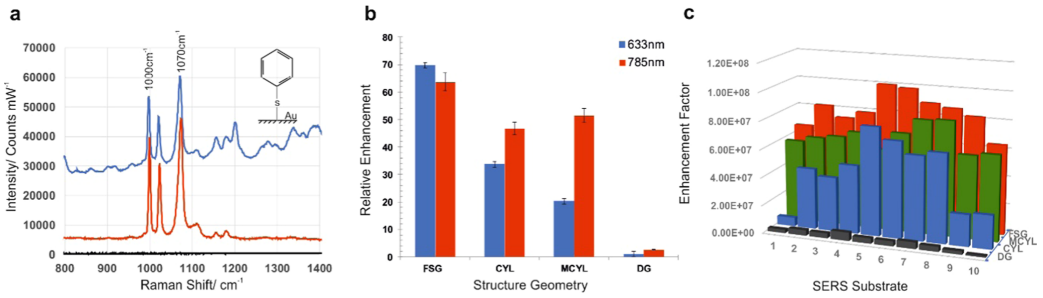

Figure 4. BCP-based SERS substrates. (a) Representative SERS spectra of benzenethiol (inset) recorded from substrates excited with a 633 nm (blue) and 785 lasers (red) with typical Raman bands at 1000 and 1070 cm^{-1} of the aromatic ring deformation vibrations. (b) Relative SERS enhancement of the 1070 cm^{-1} peak with the highest signal enhancement obtained for the FSG with 633 nm followed by MCYL with 785 nm. (c) The average SERS enhancement factors (EFs) of the 3D SERS-active nanomorphologies across 10 areas on each substrate indicate uniform properties across the structured area with EFs of the order of 10^{7-8} for FSG and MCYL and only 10^{5-6} for the DG nanostructures.

fluctuations of the cylinders around their equilibrium positions and reorganization of the annealed microphase morphology toward a higher lateral symmetry. In the assembled micro-capacitor-device geometry, the electric field results in an aligning torque on the BCP cylindrical morphology and enables control and manipulation of the degree and proportion of the alignment yielding the mixed nanomorphology of MCYL (Figures 2d, inset and 3d).[36,37]

Subsequently, a range of gold-plated nanostructures based on branched 3D organic/inorganic nanohybrids was fabricated. Au-plated DG (Figure 3b) and FSG (Figure 3a) interconnected nanonetworks were generated via selective degradation of the PLLA phase and plating with gold (200 ± 30 nm) via electrodeposition or sputtering (see Supporting Information, S1), followed by the UV irradiation, at a wavelength of 254 nm, removing the sacrificial organic layer. Hydrolytic removal of the PLA phase in the cylindrical morphologies and the subsequent electroplating of gold nanolayer, provided topographic cylindrical features, visible in the AFM height and cross-sectional low-angle backscattered scanning electron microscopy (LAB-SEM) images, (Figure 3c and inset) revealing vertically organized cylindrical phase morphologies. Absence or existence of a characteristic frequency in the two-dimensional fast Fourier transform (2D-FFT) power spectrum further helps to identify the lack or existence of the corresponding periodical structural patterns. The lower symmetry of the 2D-FFT power spectrum, corresponding to the experimentally obtained SEM image, pattern in the inset of Figure 3d is indicative of the shorter-range packing in the case of the mixed cylindrical nanomorphologies with a proportion of horizontal and vertical cylinders (Figure 3d).

SERS performance of the four fabricated nanostructures was evaluated through adsorbing a monolayer of benzenethiol, as a Raman probe, from a 10 μM ethanolic solution on each gold nanosurface (Figure 4a) at excitation wavelengths of 633 and 785 nm as well as using rhodamine 6G (R6G) as a Raman active molecule (see Supporting Information, S3).[17,38,39] Notably, SERS spectra of benzenethiol exhibit a difference in intensity of the Raman bands at different excitation wavelengths. Although strong Raman bands at 1000, 1027, and 1070 cm^{-1}, corresponding to the aromatic ring breathing modes, in-plane C−H deformation and rocking vibrations of benzene are observed under excitation of both 633 and 785 nm, at the shorter laser wavelength of 633 nm additional Raman bands, above 1300 cm^{-1} are also enhanced. The absolute enhancement factor (EF) (Figure 4b) for the FSG-based SERS substrate was found to be 6.1×10^7 and 6.7×10^7 at 785 and 633 nm, respectively. For the other three nanostructures of CYL, MCYL and DG, the EF was consistently higher at 785 nm excitation laser with 38% increase in enhancement for the CYL (EF = 4.5×10^7 and 3.2×10^7 at 785 and 633 nm, respectively) and 61% for the MCYL (EF = 5.0×10^7 and 1.9×10^7 at 785 and 633 nm, respectively) in comparison to excitation with a 633 nm laser. The smallest enhancement was observed for the DG based SERS nanostructures with EF of 2.6×10^6 at 785 nm and 9.6×10^5 at 633 nm. The substrates exhibited a good SERS signal reproducibility which was established by examining random areas (n = 10) across each surface under identical experimental conditions using benzenethiol monolayer as the SERS probe, yielding similar relative peak intensities. Uniform and consistent SERS signals were detected from different locations across each sample area as well as across several substrates under identical experimental conditions, with the correlated SERS based enhancement factor calculation, (see Supporting Information, S2) demonstrating that the values are narrowly distributed around the average of $(8.2 \pm 1.2) \times 10^7$, $(4.5 \pm 2.3) \times 10^7$, $6.6 \times 10^7 \pm 8.9 \times 10^6$ and $(3.5 \pm 1.3) \times 10^6$ for FSG, CYL, MCYL and DG, accordingly (Figure 4c). Based on the 0.95 confidence interval data, we therefore expect the difference in enhancement factor as measured between the different areas to lie between (5.8×10^7, 1.1×10^8), (4.6×10^7, 9.0×10^7), (4.9×10^7, 8.4×10^7) and (7.8×10^5, 6.1×10^6) for FSG, CYL, MCYL and DG, respectively. Importantly, all the EFs are on the same order of magnitude of $\times 10^7$ (for FSG, MCYL and CYL) and $\times 10^6$ (for DG) with the small variation in the pre-factor values, with the largest difference in the SERS EFs of less than 7-fold for the DG and less than 2-fold for both the for the MCYL and the FSG (Figure S2), indicating good signal reproducibility in agreement with the typical SERS platforms, considered highly similar even when showing a nearly 1 order of magnitude difference.[40] The EF achieved with these morphologies is of similar or higher magnitude to the commercially available SERS substrates such as for instance, Mesophotincs,[41] ST Japan,[42] Stellnet Inc.[43] as well as to the conventional surfaces reported in literature.[4,44,45]

Interestingly, only for the FSG nanostructure, the relative SERS enhancement of benzenthiol molecules was found to be

DOI: 10.1021/acsami.9b00420
ACS Appl. Mater. Interfaces 2019, 11, 14437−14444

both the highest as well as greater while using the 633 nm laser versus the 785 nm, in comparison to the rest of the nanoarchitectures, for which the 785 nm yielded higher enhancement of the signal relative to the 633 nm. Furthermore, the MCYL SERS surface demonstrated the biggest increase in enhancement using the 785 nm excitation laser versus the 633 nm, greatly exceeding the DG nanostructure, which showed the lowest EF amongst the fabricated substrates (1.9×10^7 compared to 9.6×10^5) (Figure 4b). This can be explained by the fact that SERS enhancement effect is dependent on the wavelength and mainly arises from the LSPRs of the nanoarchitectures and therefore, a particular SERS substrate will exhibit highest enhancement at a certain excitation wavelength. These results indicate that the FSG is the optimal nanostructure to be exploited with the 633 nm excitation laser to yield the highest enhancement. However, since BCP morphologies that are bicontinuous in all three spatial dimensions are still rare and difficult to manufacture in particular, over large areas, the MCYL morphology presents itself as a particularly promising and viable candidate as a strong SERS enhancing substrate with a 785 nm laser. Since the shape of the nano-morphology plays an important role in SERS, and the electromagnetic enhancement is strongly dependent on the surface morphology and precise shape of the features at the metal surface, the optimal SERS enhancement requires a delicate balance between the excited and scattered wavelengths with the plasmon peak of the metal nanostructure. A plasmon which can be excited at the scattered wavelength out-couples the Raman scattered radiation more efficiently. This is important especially in the near-infrared, where the laser excitation and the Raman scattered radiation can be significantly different in terms of wavelength and hence, excitation or existence of plasmonic absorption at one of these is not sufficient for obtaining the highest SERS enhancements. We show that the enhancement factors in SERS are dependent on the excitation wavelength for the same SERS probe molecule even for the same nanostructure. While thiols, such as mercaptobenzoic acid, bind covalently to the gold surface, there has not been any report of contribution of chemical enhancement mechanism in studies using 633 or 785 nm excitation wavelengths[46] except when using semiconductors as substrates.[47] Hence, we can conclude that in this case the electromagnetic enhancement mechanism is the primary reason for the enhancements of 10^5–10^8 observed for the various structures.

While the SERS activity of the plasmonic BCP-morphologies is promising for detection applications due to uniform and high EFs the optical properties of these metamaterials themselves are interesting. New optical properties emerge, different to bulk gold in these metamaterial-like nanostructures. Figure 5 shows the transmittance spectra recorded with unpolarized light in the visible range on each gold-plated nanostructure sample (Figure 5, inset). The spectra are normalized relative to the transmission from a smooth gold film on the same supporting substrate.

For the gold infiltrated nanomorphologies there is a distinct change in the position of the extinction wavelength maximum. For the FSG, a characteristic extinction peak in the transmission is observed around 600 nm, which shifts progressively to higher energy of 485 nm for CYL, 520 nm for MCYL and 540 nm for the DG. The MCYL extinction maximum at 520 nm absorption max is also observed for

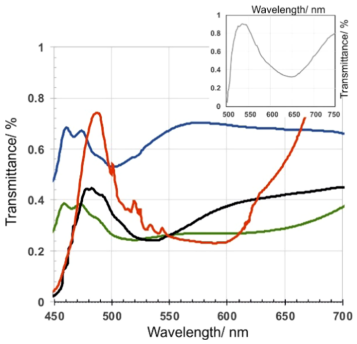

Figure 5. Optical properties of gold-plated nanostructures. Spectroscopic characterization of the optical behavior for transmission configuration with unpolarized incident light for each BCP-based nanomorphology (red: FSG, green: MCYL, blue: CYL and black: DG) with characteristic extinction peaks compared to a gold layer of similar thickness. The blue shift is consistent with what predicted and measured for metamaterials and porous gold and is due to a reduction in the average electron density of the nanostructure and an increase in the self-inductance of the interconnected network of gold.

nanoparticles (20 nm particles) while for bulk gold it is further blue-shifted to 500 nm or below and is related to inter-band transitions, here it is additionally attributable to multi-domain structure as the plasma frequency is inherently modified by the nano-structuring and corresponding air-filling fraction.[48] For single gyroid metamaterials fabricated in gold, properties such as enhanced transmission have been previously observed due to their sub-wavelength architectures and the arising plasmon resonances.[29] The transmission spectrum in Figure 5 of FSG nanostructure is qualitatively similar to that shown for single gyroids previously. The difference in the maximum extinction wavelength at 600 nm compared to the one reported by Salvatore et al.[29] is attributed to the 20 nm unit cell size in the fabricated structures. For DG structures, very low transmission is observed. This is not unsurprising as Hur et al. have previously predicted a different mechanism of propagation of surface plasmons in double gyroid metamaterials.[49] The existence of two interpenetrating continuous plasmon metal networks induces local capacitance and alters the surface plasmon propagation. Thus, losses can be higher and also significantly dependent on each of the interpenetrating structures, e.g., their relative fill-fraction or size of struts. The filling fraction of double gyroid (DG) is higher at 39% than the single gyroid (free standing gyroid; FSG) at 21%. As mentioned by Salvatore et al.[29] and further described by Farah et al.[50] that the reflectivity spectra depend on the structural motifs such as the size of the struts and tune with fill fraction, gyroid pitch and dielectric filling. In our results shown in Figure 5, there is a blue shift of the transmittance-dip between the DG and FSG spectra consistent with the decrease in the filling-fraction. Moreover, the polarization of domains with respect to the incident light can also yield a blue shift of spectra of metamaterials as shown by Vignolini et al.[51] although in our case, we do not expect such differences between FSG and DG films. On the other hand, comparing the spectra for the cylindrical structures we find that the mixed cylinders show two broad peaks while the aligned cylinders show only one peak. This is attributed to the alignment of the

DOI: 10.1021/acsami.9b00420
ACS Appl. Mater. Interfaces 2019, 11, 14437−14444

cylinders with respect to the polarization of the incident (unpolarized) light. In the case of the MCYL the alignment of the cylinders is both perpendicular and parallel to the surface while in the CYL, the cylinders are predominantly perpendicular to the surface. Although an analytical model to predict the extinction peaks is beyond the scope of the current work, we speculate that the broader peak at >600 nm is due to the cylinders parallel to surface (longitudinal mode: along the length) while the peak at ∼500 nm is due to the cylinders perpendicular to the surface (transverse mode). To note, that while the SERS enhancements of the substrates and the optical properties are related, the optical properties of metamaterials, even though fabricated from plasmonic materials, are dominated by those due to their intrinsic structure. Plasmon length scales are of the order of ∼100 nm, while metamaterials such those demonstrated here have <10 nm length scales. The SERS enhancements which are observed in our case provide clear evidence that plasmons are excited in these metamaterials. However, the optical transmission spectra indicate that the optical properties are more than due to plasmonic absorption only with the understanding of the extraordinary optical properties of novel plasmonic metamaterials being an area of active, ongoing research.[52]

CONCLUSIONS

The guided self-assembly of the BCP blocks offers a unique platform for structuring materials with tuneable sizes on the nanoscale thus, offering a great variability of structural features by the independent control of experimental parameters in a robust manner, generating high-fidelity consistent nano-architectures across large substrate areas and subsequently, enabling reliable manufacture of substrates with high SERS enhancements. The optical properties of these nanomaterials are found to be distinguished primarily by the morphology, length scale and periodicity on which the constituent materials are structured. The tuning of plasmon resonances can further be accomplished by controlling the dimensions (size and periods) of the microphase-separated nanostructures, through alteration of the molecular weight and composition which in turn, will allow the design of SERS substrates that generate strong localized electromagnetic fields at optical wavelengths that are required for the optimum SERS excitation by different laser sources thus, harnessing such inherently precise self-assembly behavior of BCPs towards the realization of 3D metamaterials. Dimensional control of the nano-morphologies combined with theoretical modeling could further improve the BCP-based SERS substrates and the enhancements that can be obtained from them and is currently underway. Finally, establishing of such a technique might also provide the missing-link towards the realization of applied metamaterials, heralding a new era for developing novel types of optical materials from BCP self-assembly and their integration into composite functional devices.

EXPERIMENTAL SECTION

Sample Preparation. The samples were prepared using the PFS-*b*-PLA and PS-*b*-PLLA block-copolymers (volume fraction, f = 39%) with thin films spin-coated from a 5−10 wt/wt %, from toluene, onto Au-plated p-doped silicon wafers or transparent FTO glass substrates. The minority component was subsequently removed either by UV etching (15 min at 254 nm) or exposure to plasma system (10 min, O_2 plasma) under controlled low pressure conditions. In order to release the BCP film prior or post degradation and for imaging purposes, the underlying gold layer was removed via etching in 80:1 bromine to methanol solution. The resulting nanostructures were plated via electrodeposition with Au with an initial nucleation step between 0.0 and −1.2 V at a scan rate of 50 mV/s (average of three cyclic voltammetry scans) followed by the deposition step (100 s, −0.8 V) up to a thickness in ranges between 200 and 300 nm.[53] A reaction kinetics-controlled region (from −0.2 to −0.75 V) was followed by a mass transport-controlled region (from −0.8 to −1 V), featuring a cathodic peak characteristic of diffusion-controlled electroplating processes. As the electroplating process was used to obtain nanometer Au layers, the gold growth rate was slow enough to enable careful control over the deposition process, generally achieved in the kinetics-controlled region, where the applied over-potential with respect to the open circuit potential value is small and therefore, acts as the gold deposition driving force. Plating at E = −0.8 V, the electrochemically-driven Au^{3+} reduction occurred at the working electrode with a high deposition rate, leading to the formation of a large number of initial nuclei which ultimately grow to overlap and form a full layer with an average representative thickness of 200 nm (at 100 s deposition time).[54] The nanostructures were alternatively (or additionally) covered with a thin Au film using an Emitech sputter-coater with a direct current Ar plasma (gold target purity 99.999%, Kurt J. Lesker Company) with two cycles of 10 s at 55 mA were carried out.

Alignment of BCP Using an Electric Field. BCP thin film was spin-coated onto a supporting conductive substrate, serving as a bottom electrode, of either silicon with a nanometre gold layer evaporated on the back side of it or FTO glass with a thin layer of silver paste around the edge of the substrate. A capacitor-like device was subsequently assembled with vertical electric field applied across it (a constant high-voltage of 4 kV was applied across the assembled capacitor device), while the BCP film was annealed above the glass transition temperature of both constituent blocks ($T_{g(PFS)}$ = 103 °C and $T_{g(PLA)}$ = 57 °C). The opposing electrode was a 20 μm thick sheet of Kapton with a 50 nm evaporated gold layer on the bottom side along with a thin layer of 2 μm of poly(dimethylsiloxane) (Sylgard 184, Dow-Corning) spin-coated on front of it to establish a conformal contact with the BCP film.

Atomic Force Microscopy. NanoScope IV Multimode and Dimension 3100 (Digital Instruments, Santa Barbara, CA) atomic force microscope were used to thoroughly characterize the surfaces' topography. The AFM measurements were performed using tapping mode via an intermittent contact of the tip with the sample, in ambient conditions. NSG 20 cantilevers with a resonance frequency of 260 kHz and a stiffness of 28 N/m were used. Height and phase images were analyzed with the Nanoscope software (Digital Instruments). To improve contrast, patterns were exposed to UV-light and rinsed in cyclohexane to remove some of the PS phase.

Scanning Electron Microscopy. Samples for SEM imaging were prepared by placing a post-experiment, disassembled substrate with the generated patterns on an inclined or cross-sectional holder to enable the imaging of the top and cross-sectional views. Scanning electron micrographs were acquired using a thermally assisted field emission scanning electron microscope (LEO VP 1530 and FEI Magellan and Helios) with a lateral resolution of 1−5 nm. A LEO ULTRA 55 SEM instrument including a Schottky emitter (ZrO/W cathode) was also used for imaging the samples with a typical acceleration voltage of 2−5 kV equipped with the energy dispersive X-ray spectroscopy. Scanning transmission electron microscope (STEM) images were obtained using Hitachi s5500 with a cold field-emission source and lens detector with 4 Å resolution, allowing adjustable acceptance angle STEM imaging. Low-angle backscattered electron imaging mode was used to contrast the as-spun and those gold replicated samples, providing the atomic number contrast. The power spectrum results of BCP nanostructure images were obtained with the image analysis program (ImageJ) applying a 2D-FFT algorithm.

SERS Measurements. SERS measurements were carried out using micro Raman spectroscopy system with InVia Qontor spectrometer for confocal Raman (Renishaw Plc.) equipped with

DOI: 10.1021/acsami.9b00420
ACS Appl. Mater. Interfaces 2019, 11, 14437−14444

514, 633 and 785 nm lasers which was adjusted for optimal throughput, fluorescence control and sensitivity. Benzenethiol was adsorbed onto the gold surface by soaking in a 10 μm solution in ethanol for 30 min. The samples were then rinsed with ethanol and left to dry in air for 15 min before measurement. The spectra were typically acquired at 10 s exposure time and a laser power of 1−3 mW to avoid photochemical effects in the SERS spectra, sample damage or degradation. SERS maps were generated in a Streamline mode scan with 10 s exposure time and 50 mW power at 633 and 785 nm. A 50× objective with a numerical aperture of 0.75 was used for SERS measurements over a range of 500−1600 cm^{-1} relative to the excitation Raman shift. Optical measurements were carried out with a specially adapted research grade microscope (Leica DM 2700 M) equipped with incoherent white light source, allowing confocal measurements with 2.5 μm depth resolution. The spectra were normalized with respect to those recorded on flat gold or gold covered flat copolymer film surfaces. An intelligent fitting filter was applied for baseline subtraction. After excluding regions with peaks, the baseline was fitted to all the remaining points in each spectrum and a polynomial order of 8 with the noise tolerance of 1.50 was applied.

Optical Characterization. Leica DM200 optical polarizing microscope was used to investigate the optical texture of the samples. The optical transmission characterization of the samples was evaluated in terms of variations of the intensity of transmitted light using unpolarized incident light and the attached spectrometer (Horiba). The microscope xenon lamp acted as an illumination source for the spectroscopic measurements. 100 um optical fiber (ThorLabs) in the focal plane of 20× microscope objective working distance has served as pinhole for the signal collection. Motorized MicroHR Imaging Spectrometer with solid state UV coated silicon over indium gallium arsenide detector for 200−1700 nm and the SynerJY for Windows software were used for data acquisition and analysis.

■ ASSOCIATED CONTENT

Supporting Information

The Supporting Information is available free of charge on the ACS Publications website at DOI: 10.1021/acsami.9b00420.

Thickness characterization of the electrodeposited gold, SERS performance of the BCP-based nanomorphologies using R6G as Raman probe, overview and calculation of the enhancement factor reproducibility (PDF)

■ AUTHOR INFORMATION

Corresponding Author

*E-mail: GoldberP@bham.ac.uk.

ORCID

Sumeet Mahajan: 0000-0001-8923-6666

Pola Goldberg Oppenheimer: 0000-0002-8440-4808

Notes

The authors declare no competing financial interest.

■ ACKNOWLEDGMENTS

We acknowledge funding from the Wellcome Trust (174ISSFPP) and the Royal Academy of Engineering (RF1415/14/28). P.G.O. is a Royal Academy of Engineering Research (RAEng) Fellowship holder. C.B. gratefully acknowledges funding from EPSRC through a studentship from the Sci-Phy-4-Health Centre for Doctoral Training (EP/L016346/1).

■ REFERENCES

(1) Ray, D.; Aswal, V. K.; Kohlbrecher, J. Synthesis and Characterization of High Concentration Block Copolymer-Mediated Gold Nanoparticles. *Langmuir* **2011**, *27*, 4048−4056.

(2) Adams, M. L.; Lavasanifar, A.; Kwon, G. S. Amphiphilic Bock Copolymers for Drug Delivery. *J. Pharm. Sci.* **2003**, *92*, 1343−1355.

(3) Darling, S. B. Block Copolymers for Photovoltaics. *Energy Environ. Sci.* **2009**, *2*, 1266−1273.

(4) Goldberg-Oppenheimer, P.; Kabra, D.; Vignolini, S.; Hüttner, S.; Sommer, M.; Neumann, K.; Thelakkat, M.; Steiner, U. Hierarchical Orientation of Crystallinity by Block-Copolymer Patterning and Alignment in an Electric Field. *Chem. Mater.* **2013**, *25*, 1063−1070.

(5) Park, T. H.; Yu, S.; Cho, S. H.; Kang, H. S.; Kim, Y.; Kim, M. J.; Eoh, H.; Park, C.; Jeong, B.; Lee, S. W.; Ryu, D. Y.; Huh, J.; Park, C. Block Copolymer Structural Color Strain Sensor. *NPG Asia Mater.* **2018**, DOI: 10.1038/s41427-018-0036-3.

(6) Segalman, R. A.; McCulloch, B.; Kirmayer, S.; Urban, J. J. Block Copolymers for Organic Optoelectronics. *Macromolecules* **2009**, *42*, 9205−9216.

(7) Bezares, F. J.; Caldwell, J. D.; Glembocki, O.; Rendell, R. W.; Feygelson, M.; Ukaegbu, M.; Kasica, R.; Shirey, L.; Bassim, N. D.; Hosten, C. The Role of Propagating and Localized Surface Plasmons for SERS Enhancement in Periodic Nanostructures. *Plasmonics* **2012**, *7*, 143−150.

(8) Caldwell, J. D.; Glembocki, O.; Bezares, F. J.; Bassim, N. D.; Rendell, R. W.; Feygelson, M.; Ukaegbu, M.; Kasica, R.; Shirey, L.; Hosten, C. Plasmonic Nanopillar Arrays for Large-Area, High-Enhancement Surface-Enhanced Raman Scattering Sensors. *ACS Nano* **2011**, *5*, 4046−4055.

(9) Hu, W.; Zou, S. Proposed Substrates for Reproducible Surface-Enhanced Raman Scattering Detection. *J. Phys. Chem. C* **2011**, *115*, 4523−4532.

(10) Barnes, W. L.; Dereux, A.; Ebbesen, T. W. Surface Plasmon Subwavelength Optics. *Nature* **2003**, *424*, 824.

(11) Kneipp, K.; Wang, Y.; Kneipp, H.; Perelman, L. T.; Itzkan, I.; Dasari, R. R.; Feld, M. S. Single Molecule Detection Using Surface-Enhanced Raman Scattering (SERS). *Phys. Rev. Lett.* **1997**, *78*, 1667−1670.

(12) Nie, S.; Emory, S. R. Probing Single Molecules and Single Nanoparticles by Surface-Enhanced Raman Scattering. *Science* **1997**, *275*, 1102−1106.

(13) Kho, K.; Qing, Z. M.; Shen, Z. X.; Ahmad, I. B.; Lim, S. C.; Mhaisalkar, S.; White, T.; Watt, F.; Soo, K. C.; Olivo, M. Polymer-Based Microfluidics with Surface-Enhanced Raman-Spectroscopy-Active Periodic Metal Nanostructures for Biofluid Analysis. *J. Biomed. Opt.* **2008**, *13*, No. 054026.

(14) Mahajan, S.; Cole, R. M.; Soares, B. F.; Pelfrey, S. H.; Russell, A. E.; Baumberg, J. J.; Bartlett, P. N. Relating SERS Intensity to Specific Plasmon Modes on Sphere Segment Void Surfaces. *J. Phys. Chem. C* **2009**, *113*, 9284−9289.

(15) Ozbay, E. Plasmonics: Merging Photonics and Electronics at Nanoscale Dimensions. *Science* **2006**, *311*, 189−193.

(16) Pennathur, S.; Fygenson, D. Improving Fluorescence Detection in Lab on Chip Devices. *Lab Chip* **2008**, *8*, 649−652.

(17) Goldberg-Oppenheimer, P.; Mahajan, S.; Steiner, U. Hierarchical Electrohydrodynamic Structures for Surface-Enhanced Raman Scattering. *Adv. Mater.* **2012**, *24*, OP175−OP180.

(18) Rebbecchi, T. A.; Chen, Y. Template-based Fabrication of Nanoporous Metals. *J. Mater. Res.* **2018**, *33*, 2−15.

(19) Bartlett, P. N.; Baumberg, J. J.; Birkin, P. R.; Ghanem, M. A.; Netti, M. C. Highly Ordered Macroporous Gold and Platinum Films Formed by Electrochemical Deposition through Templates Assembled from Submicron Diameter Monodisperse Polystyrene Spheres. *Chem. Mater.* **2002**, *14*, 2199−2208.

(20) Ngo, Y. H.; Li, D.; Simon, G. P.; Garnier, G. Gold Nanoparticle−Paper as a Three-Dimensional Surface Enhanced Raman Scattering Substrate. *Langmuir* **2012**, *28*, 8782−8790.

(21) Santoro, G.; Yu, S.; Schwartzkopf, M.; Zhang, P.; Vayalil, S. K.; Risch, J. F. H.; Rübhausen, M. A.; Hernández, M.; Domingo, C.;

Roth, S. V. Silver Substrates for Surface Enhanced Raman Scattering: Correlation Between Nanostructure and Raman Scattering Enhancement. *Appl. Phys. Lett.* **2014**, *104*, No. 243107.
(22) Lim, C.; Hong, J.; Chung, B. G.; deMello, A. J.; Choo, J. Optofluidic platforms Based on Surface-Enhanced Raman Scattering. *Analyst* **2010**, *135*, 837−844.
(23) Piorek, B. D.; Lee, S. J.; Santiago, J. G.; Moskovits, M.; Banerjee, S.; Meinhart, C. D. Free-Surface Microfluidic Control of Surface-Enhanced Raman Spectroscopy for the Optimized Detection of Airborne Molecules. *Proc. Natl. Acad. Sci. U.S.A.* **2007**, *104*, 18898−18901.
(24) Qian, X.; Zhou, X.; Nie, S. Surface-Enhanced Raman Nanoparticle Beacons Based on Bioconjugated Gold Nanocrystals and Long Range Plasmonic Coupling. *J. Am. Chem. Soc.* **2008**, *130*, 14934−14935.
(25) Ackermann, L.; Andreas, A.; Robert, B. Catalytic Arylation Reactions by C-H Bond Activation with Aryl Tosylates. *Angew. Chem., Int. Ed.* **2006**, *45*, 2619−2622.
(26) Hsueh, H.-Y.; Hung-Ying, C.; Yu-Chueh, H.; Yi-Chun, L.; Shangjr, G.; Rong-Ming, H. Well-Defined Multibranched Gold with Surface Plasmon Resonance in Near-Infrared Region from Seeding Growth Approach Using Gyroid Block Copolymer Template. *Adv. Mater.* **2013**, *25*, 1780−1786.
(27) Wang, Y.; Becker, M.; Wang, L.; Liu, J.; Scholz, R.; Peng, J.; Gösele, U.; Christiansen, S.; Kim, D. H.; Steinhart, M. Nanostructured Gold Films for SERS by Block Copolymer-Templated Galvanic Displacement Reactions. *Nano Lett.* **2009**, *9*, 2384−2389.
(28) Zhang, X.; Lee, W.; Lee, S. Y.; Gao, Z.; Rabin, O.; Briber, R. In *Silver Based SERS Substrates Fabricated from Block Copolymer Thin Film*, APS March Meeting, 2013; p 34006.
(29) Salvatore, S.; Demetriadou, A.; Vignolini, S.; Oh, S. S.; Wuestner, S.; Yufa, N. A.; Stefik, M.; Weisner, U.; Baumberg, J. J.; Hess, O.; Steiner, U. Tunable 3D Extended Self-Assembled Gold Metamaterials with Enhanced Light Transmission. *Adv. Mater.* **2013**, *25*, 2713−2716.
(30) Mahajan, S.; Baumberg, J. J.; Russell, A. E.; Bartlett, P. N. Reproducible SERRS from Structured Gold Surfaces. *Phys. Chem. Chem. Phys.* **2007**, *9*, 6016−6020.
(31) Vriezekolk, E. J.; de Weerd, E.; de Vos, W. M.; Nijmeijer, K. Control of Pore Size and Pore Uniformity in Films Based on Self-Assembling Block Copolymers. *J. Polym. Sci., Part B: Polym. Phys.* **2014**, *52*, 1568−1579.
(32) Radjabian, M.; Abetz, V. Tailored Pore Sizes in Integral Asymmetric Membranes Formed by Blends of Block Copolymers. *Adv. Mater.* **2015**, *27*, 352−355.
(33) Gu, Y.; Wiesner, U. Tailoring Pore Size of Graded Mesoporous Block Copolymer Membranes: Moving from Ultrafiltration toward Nanofiltration. *Macromolecules* **2015**, *48*, 6153−6159.
(34) Guo, T.; Gao, J.; Xu, M.; Ju, Y.; Li, J.; Xue, H. Hierarchically Porous Organic Materials Derived From Copolymers: Preparation and Electrochemical Applications. *Polym. Rev.* **2018**, 1−38.
(35) Dorin, R. M.; Phillip, W. A.; Sai, H.; Werner, J.; Elimelech, M.; Wiesner, U. Designing Block Copolymer Architectures for Targeted Membrane Performance. *Polymer* **2014**, *55*, 347−353.
(36) Crossland, E. J. W.; Kamperman, M.; Nedelcu, M.; Ducati, C.; Wiesner, U.; Smilgies, D. M.; Toombes, G. E. S.; Hillmyer, M. A.; Ludwigs, S.; Steiner, U.; Snaith, H. J. A Bicontinuous Double Gyroid Hybrid Solar Cell. *Nano Lett.* **2009**, *9*, 2807−2812.
(37) Goldberg-Oppenheimer, P.; Eder, D.; Steiner, U. Carbon Nanotube Alignment *via* Electrohydrodynamic Patterning of Nanocomposites. *Adv. Funct. Mater.* **2011**, *21*, 1895−1901.
(38) Biggs, K. B.; Camden, J. P.; Anker, J. N.; Duyne, R. P. V. Surface-Enhanced Raman Spectroscopy of Benzenethiol Adsorbed from the Gas Phase onto Silver Film over Nanosphere Surfaces: Determination of the Sticking Probability and Detection Limit Time. *J. Phys. Chem. A* **2009**, *113*, 4581−4586.
(39) Tian, F.; Bonnier, F.; Casey, A.; Shanahan, A. E.; Byrne, H. J. Surface enhanced Raman scattering with gold nanoparticles: effect of particle shape. *Anal. Methods* **2014**, *6*, 9116−9123.
(40) Ansar, S. M.; Li, X.; Zou, S.; Zhang, D. Quantitative Comparison of Raman Activities, SERS Activities, and SERS Enhancement Factors of Organothiols: Implication to Chemical Enhancement. *J. Phys. Chem. Lett.* **2012**, *3*, 560−565.
(41) Mesophotonics. http://www.mesophotonics.com/products/klarite.html.
(42) Japan, S.T.. http://www.stjapan.de/en/shop/accessories-for-spectroscopy-microanalysis/raman-sers-substrate/).
(43) StellarNet, Inc.. https://www.stellarnet.us/spectrometers-accessories/sers-substrates/.
(44) Srichan, C.; Ekpanyapong, M.; Horprathum, M.; Eiamchai, P.; Nuntawong, N.; Phokharatkul, D.; Danvirutai, P.; Bohez, E.; Wisitsoraat, A.; Tuantranont, A. Highly-Sensitive Surface-Enhanced Raman Spectroscopy (SERS)-based Chemical Sensor using 3D Graphene Foam Decorated with Silver Nanoparticles as SERS substrate. *Sci. Rep.* **2016**, *6*, No. 23733.
(45) Schmidt, M. S.; Hübner, J.; Boisen, A. Large Area Fabrication of Leaning Silicon Nanopillars for Surface Enhanced Raman Spectroscopy. *Adv. Mater.* **2012**, *24*, OP11−OP18.
(46) Michota, A.; Bukowska, J. Surface-Enhanced Raman Scattering (SERS) of 4-Mercaptobenzoic Acid on Silver and Gold Substrates. *J. Raman Spectrosc.* **2003**, *34*, 21−25.
(47) Zhang, X.; Yu, Z.; Ji, W.; Sui, H.; Cong, Q.; Wang, X.; Zhao, B. Charge-Transfer Effect on Surface-Enhanced Raman Scattering (SERS) in an Ordered Ag NPs/4-Mercaptobenzoic Acid/TiO2 System. *J. Phys. Chem. C* **2015**, *119*, 22439−22444.
(48) Dolan, J. A.; Saba, M.; Dehmel, R.; Gunkel, I.; Gu, Y.; Wiesner, U.; Hess, O.; Wilkinson, T. D.; Baumberg, J. J.; Steiner, U.; Wilts, B. D. Gyroid Optical Metamaterials: Calculating the Effective Permittivity of Multidomain Samples. *ACS Photonics* **2016**, *3*, 1888−1896.
(49) Hur, K.; Fracescato, Y.; Giannini, V.; Maier, S.; Hennig, R. G.; Weisner, U. Three-Dimensionally Isotropic Negative Refractive Index Materials from Block Copolymer Self-Assembled Chiral Gyroid Networks. *Angew. Chem., Int. Ed.* **2011**, *50*, 11985−11989.
(50) Farah, P.; Demetriadou, A.; Salvatore, S.; Vignolini, S.; Stefik, M.; Wiesner, U.; Hess, O.; Steiner, U.; Valev, V.; Baumberg, J. Ultrafast Non-linear Response of Gold Gyroid 3D Metamaterials. *Phys. Rev. Appl.* **2014**, *2*, No. 044002.
(51) Vignolini, S.; Yufa, N. A.; Cunha, P. S.; Guldin, S.; Rushkin, I.; Stefik, M.; Hur, K.; Wiesner, U.; Baumberg, J. J.; Steiner, U. A 3D Optical Metamaterial Made by Self-Assembly. *Adv. Mater.* **2012**, *24*, OP23−OP27.
(52) Hess, O.; Pendry, J. B.; Maier, S. A.; Oulton, R. F.; Hamm, J. M.; Tsakmakidis, K. L. Active Nanoplasmonic Metamaterials. *Nat. Mater.* **2012**, *11*, 573−584.
(53) Tucker, R. E. *Universal Metal Finishing Guidebook*; Elsevier: New York, 2014.
(54) Estrine, E. C.; Riemer, S.; Venkatasamy, V.; Stadler, B.; Tabakovic, I. Mechanism and Stability Study of Gold Electrodeposition from Thiosulfate-Sulfite Solution. *J. Electrochem. Soc.* **2014**, *161*, 687−696.

DOI: 10.1021/acsami.9b00420
ACS Appl. Mater. Interfaces 2019, 11, 14437−14444

-Supporting Information-

Tuneable Metamaterial-like Platforms for Surface Enhanced Raman Scattering *via* Three-Dimensional Block Copolymer Based Nanoarchitectures

Carl Banbury[1], Jonathan James Stanley Rickard[1,2], Sumeet Mahajan[3] and Pola Goldberg Oppenheimer[1,*]

[1] *School of Chemical Engineering, College of Engineering and Physical Sciences, University of Birmingham, Birmingham, B15 2TT, UK*
[2] *Department of Physics, Cavendish Laboratory, University of Cambridge, JJ Thomson Avenue, Cambridge, CB3 0HE, UK*
[3] *Department of Chemistry and the Institute for Life sciences, University of Southampton, University Road, Southampton, SO17 1BJ, UK*

[*] E-mail: GoldberP@bham.ac.uk

S1: Depth/Thickness Characterisation of the Electrdeposited Gold

Using the electrodeposition, thicknesses ranging from fractions of a template layer to several template layers can be obtained by adjusting the deposition time. At our experimental conditions, with the nucleation step consisting of 3 CV scans at a scan rate of 50mVs^{-1} and a deposition step at a fixed potential of -0.8V (*vs.* SCE, where maximum deposition efficiency occurs) for 100s (reaction kinetics-controlled region followed by a mass transport-controlled region, featuring a cathodic peak characteristic of diffusion-controlled electroplating processes) is known to yield a final thickness of 200±30nm. [Estrine, E.C. *et* al. *J. Electrochem. Chem.* **2014**, 161, D687; Universal Metal Finishing Guidebook. *Elsevier*, **2013**]

Based on the Faraday-Couloumb's Law, [Randles, J.E.B. *Trans. Faraday Soc.* **1948**, 327] the coating thickness can be stabilized for each metal by time and, under constant circumstances with constant current density (I), thickness rate of the coating (dX) develops related to time which is described through Equation [1]:

$$\frac{dx}{dt} = \frac{M_w I \varphi}{\rho A z F} \qquad [1]$$

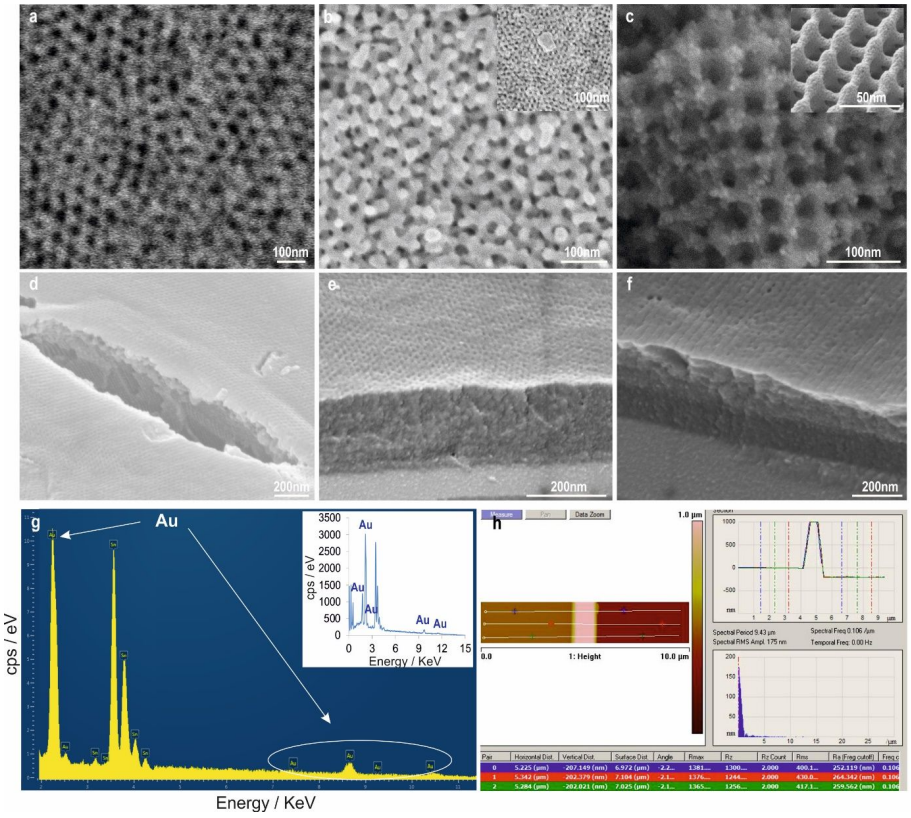

Supplementary Figure S1. (a). Low-angle back-scattered top-view SEM images of non-plated (a) *versus* the Au replicated (b-c) gyroid morphologies and the cross-sectional LAB-SEM profile images of gyroid and cylinder morphologies (d-f), electrochemically filled to depths of 200-230nm, with occasional overgrowth (above the thickness of the nano-morphology) appearing as florets of gold in several areas (b, inset) and the remaining polymer matrix was removed by exposing the material to 254nm UV etching. (g). EDX profile analysis reveals dominant Au peaks (highlighted with arrows) and given it interaction volume (at 5keV electron beam penetration depth is ~500nm), it also relevels occasional peaks of indium from the undelaying

ITO glass. (h). AFM height (left hand-side) and the corresponding cross-sectional depth profiles (right-hand side) of as-plated Au nanolayer (no BCP structure) highlighting 3 random locations on the substrate with an average heights of 203nm at set plating conditions. The AFM height images were acquired by plating the Au layer (left hand-side of the AFM height image) and subsequently, scalpel removal of the deposited gold, revealing bare substrate (right hand-side of the AFM height image) and creating the 'step-profile' enabling the characterisation of the depth profiles.

where, M_w is the molar weight of materials, (φ) current efficiency, ρ density of the sheeted layer, A deposited space, z the number of transferred electrons, and F is Faraday constant. Therefore, thickness (x) = [$It M_w \varphi$]/[96485ρAz]. Hence, at the current efficiency of 100% with the current density of 2mA/cm^2 at 0.8V *vs.* SCE at our experimental conditions, the plating rate is 120nm/min. Therefore, the calculated gold plated thickness is 200nm (for 100s). [Estrine, E.C. *et* al. *Journal of Electrochemical Chemistry* **2014**, 161, D687] and the deposited thickness can be altered from several single layers up to hundreds micrometres.

S2: Enhancement Factor Reproducibility

The reproducibility of the enhancement factor was obtained from 10 random areas for each of the four morphologies with the corresponding confidence intervals.

a

	Area on Substrate	Average Intensity / Counts mW^{-1}	Enhancement Factor	Relative Enhancement
FSG	1	35136.0	6.59E+07	1.03084
	2	43664.9	8.19E+07	1.28106
	3	39405.0	7.39E+07	1.15608
	4	42139.3	7.90E+07	1.23630
	5	53449.3	1.00E+08	1.54261
	6	52579.8	9.86E+07	1.54261
	7	47614.1	8.93E+07	1.39693
	8	46284.5	8.68E+07	1.35792
	9	43803.5	8.21E+07	1.28513
	10	34084.9	6.39E+07	1.00000
	Average		**8.22E+07**	
	STDEV		**1.22E+07**	

b

MCYL	1	30999.3	5.81E+07	1.00711
	2	32972.2	6.18E+07	1.10859
	3	34123.0	6.40E+07	1.10859
	4	36445.7	6.83E+07	1.18405
	5	30780.6	5.77E+07	1.00000
	6	37537.5	7.04E+07	1.21952
	7	43235.8	8.11E+07	1.40464
	8	43746.9	8.20E+07	1.42125
	9	31598.5	5.92E+07	1.02657
	10	32665.3	6.12E+07	1.06123
	Average		**6.64E+07**	
	STDEV		**8.99E+06**	

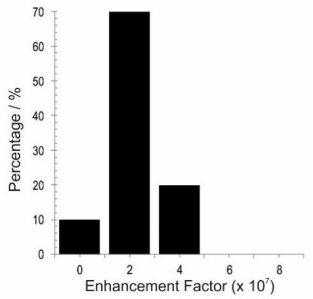

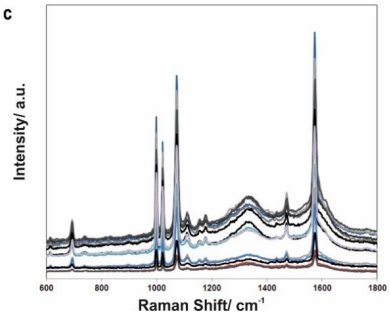

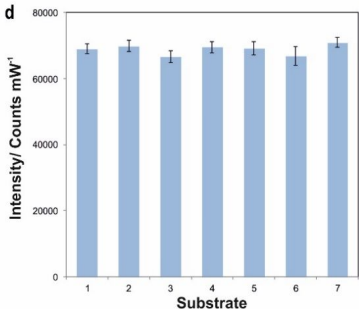

Supplementary Figure S2. Calculation of the Enhancement Factor and Reproducibility (a-b, left) and the corresponding narrowly distributed EF values (all around x10^7) for the FSG (a, right) and MCYL (b, right) morphologies. (c). Three different

substrates at 4-7 locations, under identical experimental conditions using BT monolayer as a standard probe analyte, yielded reproducible relative SERS intensities with variations of less than 9% in relative STDEV and less than 5.5% in terms of the relative peak intensities. (d). SERS signal of the peaks at 1070cm^{-1} of BT from 7 randomly selected positions on the substrates.

The limits of agreement and a range within which we expect 95% of future differences in measurements between each two substrates to lie, are calculated by first, establishing the mean and the STDEV for 10 areas across each substrate and subsequently, for the normally distributed data, the confidence interval limits for the EF values were calculated according to the: mean difference -1.96×STDEV (differences) and mean difference + 1.96×STDEV (differences). The EF values are narrowly distributed around the average of $8.2\times10^7 \pm 1.2\times10^7$, $4.5\times10^7 \pm 2.3\times10^7$, $6.6\times10^7 \pm 8.9\times10^6$ and $3.5\times10^6 \pm 1.3\times10^6$ for FSG (**Fig. S2, a; left hand-side**), CYL, MCYL (**Fig.S2, b; left hand-side**) and DG, accordingly.

The enhancement factors of the FSG-SERS substrates (**Fig.S2, a; right hand-side**) and MCYL-SERS substrates (**Fig.S2, b; right hand-side**) (n=10) show a narrow distribution with an average enhancement on the scale of (6-9) x10^7 (excluding one single area). Importantly, all EFs are on the same order of magnitude of x10^7 (for FSG, MCYL and CYL) and x10^6 (for DG) with the small variation in the pre-factor values. This confirms high-signal reproducibility over large areas in particular, as SERS EFs are typically considered very similar even when they show a nearly 1 order of magnitude difference [*e.g.,* Ansar, S.M. *et* al. *Phys. Chem. Lett.* **2012**, 3, 560]. SERS spectra of benzenethiol (**Fig.S2, c**) and intensities of the peaks at 1070cm^{-1} (**Fig.S2, d**) on 7 MCYL substrates across several random locations on each, with a 785nm laser and a 10s integration time, demonstrate reliable signal and substrate reproducibility. Repeatable SERS response was obtained from the surfaces with relative standard deviation values of less than 8.7% in the framework of one sample (error bars) and between the different samples (height of the bars).

S3: SERS Performance of the BCP-based Nanomorphologies Using R6G as Raman Probe

SERS performance of the four fabricated nanostructures was also evaluated with of 10μM R6G (P_{laser} = 3mW, t =10s) on each gold nanosurface (**Fig. S3, a**) at excitation wavelengths of 633 (grey) and 785nm (black).

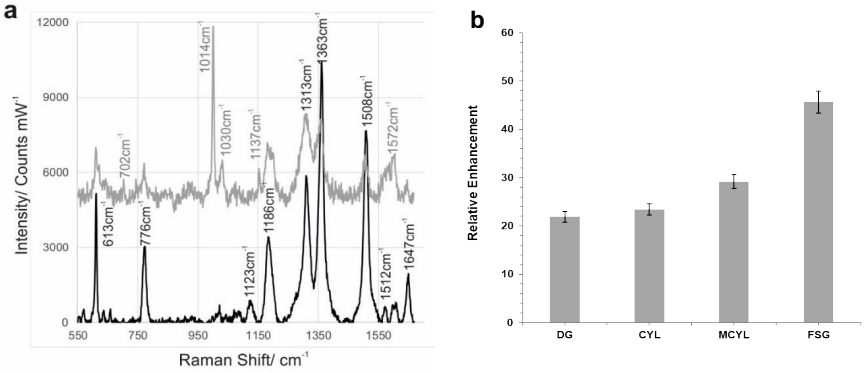

Supplementary Figure S3. (a). Representative SERS spectra of R6G recorded from substrates excited with a 633nm (grey) and 785 lasers (black) with typical Raman bands at 1363 and 1508cm^{-1} of the aromatic C-C stretching. (b). Relative SERS enhancement of the 1363cm^{-1} peak with the highest signal enhancement obtained for the FSG with 785nm followed by MCYL.

The marked peaks correspond to the Raman lines for R6G. SERS spectra exhibit difference in intensity and in certain enhanced Raman peaks at each excitation wavelength. While strong representative Raman bands at 613, 776, 1313, 1363 and 1508cm^{-1}, corresponding to the C-C-C in-plane ring bending, C-H out-of-plane bending and the aromatic C-C stretching, accordingly, are observed under excitation of both 633 and 785nm, at the shorter laser wavelength of 633nm additional Raman bands, of 1014, 1030, 1137 and 1572cm^{-1} are also enhanced, while the 1123 cm^{-1} (C-H in-plane bending) and 1647cm^{-1} (aromatic C-C stretching) peaks are further enhanced at 785nm excitation laser only. The absolute enhancement factor (EF) for all four nano-morphologies was found to be on the order of 10^7 with the FSG, followed by the MCYL, outperforming all the other nanostructures at 785nm, similarly to the case of BT (**Fig. S3, b**).

APPENDIX D

DEVELOPMENT OF THE SELF OPTIMISING KOHONEN INDEX NETWORK (SKINET) FOR RAMAN SPECTROSCOPY BASED DETECTION OF ANATOMICAL EYE TISSUE

SCIENTIFIC REPORTS

OPEN

Development of the Self Optimising Kohonen Index Network (SKiNET) for Raman Spectroscopy Based Detection of Anatomical Eye Tissue

Received: 28 March 2019
Accepted: 8 July 2019
Published online: 25 July 2019

Carl Banbury[1], Richard Mason[2], Iain Styles[3], Neil Eisenstein[1], Michael Clancy[1], Antonio Belli[4], Ann Logan[4] & Pola Goldberg Oppenheimer[1]

Raman spectroscopy shows promise as a tool for timely diagnostics via *in-vivo* spectroscopy of the eye, for a number of ophthalmic diseases. By measuring the inelastic scattering of light, Raman spectroscopy is able to reveal detailed chemical characteristics, but is an inherently weak effect resulting in noisy complex signal, which is often difficult to analyse. Here, we embraced that noise to develop the self-optimising Kohonen index network (SKiNET), and provide a generic framework for multivariate analysis that simultaneously provides dimensionality reduction, feature extraction and multi-class classification as part of a seamless interface. The method was tested by classification of anatomical *ex-vivo* eye tissue segments from porcine eyes, yielding an accuracy >93% across 5 tissue types. Unlike traditional packages, the method performs data analysis directly in the web browser through modern web and cloud technologies as an open source extendable web app. The unprecedented accuracy and clarity of the SKiNET methodology has the potential to revolutionise the use of Raman spectroscopy for *in-vivo* applications.

Raman spectroscopy is a non-invasive technique for immediate detection and analyses of the biochemical composition of analytes by measurement of the inelastic scattering of light. A schematic showing a typical experimental arrangement is shown in Fig. 1a, where longer wavelength inelastically scattered light from the sample is directed to a spectrometer via a beamsplitter. It is one of most sensitive optical spectroscopy methods yet can be packaged as a hand-held device[1,2]. Therefore, there is a considerable interest in applying Raman spectroscopy for the point-of-care detection of clinical biomarkers. Ophthalmic applications have received particular interest, as the optically clear nature of the eye provides a convenient route for *in-vivo* measurements[3–8].

The eye consists of a number of anatomical layers (Fig. 1b), each with their own specific functions, which are biologically and chemically distinct. Despite studies highlighting the potential for early diagnostics of diseases that target a specific tissue type, there is currently no direct comparison of Raman spectra from each anatomical tissue layer. Whilst Raman spectroscopy offers excellent chemical specificity, biological samples form complex permutations built from only a few amino acid building blocks, resulting in considerable spectral overlap and complex data analysis[9]. The problem is further compounded by poor signal to noise as a result of the Raman effect being relatively weak. Particularly for diagnostic applications, it is crucial to be able to accurately identify and understand the signal originating from different parts of the eye. In addition to eye tissue, the optic nerve was included as an additional class, as this represents a particularly interesting target for applications beyond ophthalmology. Forming part of the central nervous system, the optic nerve is technically part of the brain and lies at the same focal plane as the retina. The ability to spectrally isolate and characterise the optic nerve from the rest of the eye would lay foundations for further diagnostic possibilities of major neurological diseases including for instance: traumatic brain injury, multiple sclerosis or Alzheimer's disease.

The analysis of such datasets is often conducted as a workflow of three stages: projection, feature extraction and classification. The initial step (projection) aims to show spatial separation of data from spectra according to

[1]Chemical Engineering, University of Birmingham, Birmingham, UK. [2]Physics and Astronomy, University of Birmingham, Birmingham, UK. [3]Computer Science, University of Birmingham, Birmingham, UK. [4]Institute of Inflammation and Ageing, University of Birmingham, Birmingham, UK. Correspondence and requests for materials should be addressed to P.G.O. (email: P.GoldbergOppenheimer@bham.ac.uk)

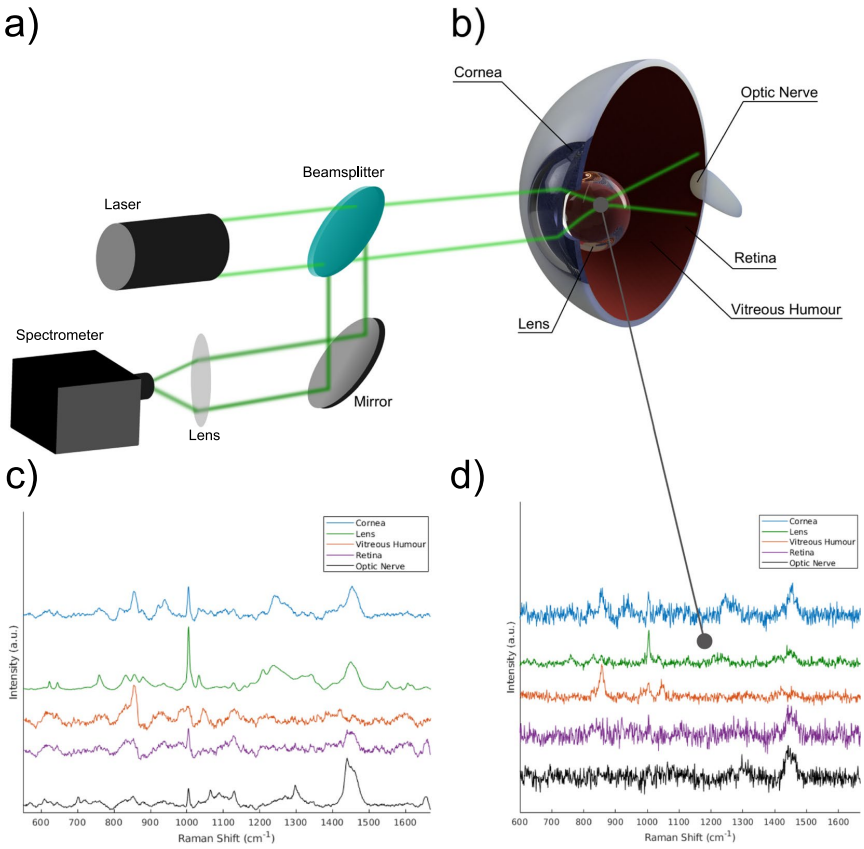

Figure 1. (**a**) Schematic of a typical Raman setup. Light from a laser is focused into the eye. Backscattered light is then directed via a beamsplitter to a spectrometer. (**b**) Schematic of the eye. (**c**) Averaged Raman spectra from isolated tissue segments of each anatomical layer. (**d**) Typical raw spectra for each tissue type used for training and classification.

different types or classes in two or three dimensions. Feature extraction then follows, with the aim of understanding what Raman bands in the data cause any separation observed in the projection step. Finally, this information is used to build a classification model, that can make accurate predictions about future unlabelled data.

In the field of Raman spectroscopy and even more generally in chemometrics, principal component analysis (PCA) is favoured for projection and feature extraction, followed by partial least squares discriminant analysis (PLS-DA) and more recently deep learning models for classification[10–12]. However, PCA routinely shows poorly defined class boundaries, struggles with large intra-class variance (such as biological samples) and quickly breaks down for multi-class problems[13]. Furthermore, classification is often handled in isolation to projection and feature extraction, forming an semantic disconnect, and whilst deep learning has shown impressive classification results, these methods offer no insight into the underlying physical and chemical changes.

Our aim is to provide a single method to address each of these stages, connected by a single mathematical principle and improve on the issues found using PCA based approaches. Work by Brereton *et al.* highlighted the use of self organising maps (SOMs) applied to nuclear magnetic resonance spectroscopy in comparison to PCA, and showed much clearer visualisations. The work was further extended to support feature extraction and classification using SOMs by the introduction of the self organising map discriminant index (SOMDI)[14–16].

Here, we develop an improved SOMDI based supervised learning method, defined as the self-optimising Kohonen index network (SKiNET) to demonstrate effective classification, and illustrate the complete linked workflow from projection to classification by means of a user-friendly web app[17]. This represents a major shift, that follows a growing trend in industry to move from traditional desktop applications to the cloud (including office suites, multimedia editing and computer aided design (CAD)) and yet the advantages of connected scalable applications are seldom leveraged in the scientific community.

The SOM or Kohonen map was first described by Teuvo Kohonen in 1982 as a model inspired by nature and the way that neurons in the visual cortex are spatially organised according to the type of visual stimuli[18]. The SOM defines a 2D map of neurons, typically arranged as a grid of hexagons. Each neuron is assigned a weight vector, which is initialised randomly and has a length equal to the number of variables in a spectrum. The weight vector effects which neuron will be activated for a given sample and neighbouring neurons will have similar weights. Spatial clustering is therefore observed in the trained map, with spectra that exhibit distinct properties activating different neurons. In order to understand which features in the data cause certain neurons to activate over others, the self organising map discriminant index (SOMDI) was used[15]. The SOMDI introduces class vectors as labels for each spectrum and corresponding weight vectors for each neuron, without influencing the training process. These allow for the identification of what type of data a given neuron activates, which can be used to inspect the weights across all neurons and extract prominent features belonging to each class.

Results

Raman spectra were randomly sampled from tissue segments from 11 separate enucleated eyes, by acquiring coarse map scans of 88 spectra per tissue segment. The aqueous humour sitting between the cornea and crystalline lens, consisting mostly of water, was neglected. Figure 1c shows averaged spectra representative of each tissue type, or class to be identified. Individual Raman spectra were kept consciously noisy by using a short acquisition time and limited laser power, to be representative of real world applications, which are limited by both scan time and maximum permissible exposure (MPE) defining eye safe limits[19]. Examples of typical raw spectra (after cosmic ray removal and baseline subtraction) are shown in Fig. 1d. Whilst the averaged spectra across each class showed obvious spectral differences, a large degree of variance was seen across each map scan (Supplementary Information, Fig. S1). As neural networks are data hungry algorithms by nature, it was hypothesised that a meaningful model could be trained by using a large enough number of noisy inputs. Initially, a 25% partition from each class of the 4840 spectra were reserved for test data.

Our results are presented as a typical mutlivariate analysis workflow of: (1) projection of the hyperspectral data set into 2D space; (2) feature extraction to identify which spectral bands are characteristic of each tissue type and (3) a classification model to automatically identify the origin of an unknown spectrum. In each case, the SOM shows dramatic improvement over PCA based methods, offering better presentation of the data, clearer insights and greater classification accuracy.

Data projection. Figure 2a shows a clear separation of the data from the five tissue classes arranged as a 16×16 SOM, trained on spectra from the five tissue classes. Neurons (hexagons) are coloured according to the modal class they activate, from the training set of Raman spectra. Neurons that have no majority class or activate non of the training data are shown in white. Coloured circles within each neuron represent spectra from the training data that have been activated for that neuron. To aid visualisation, circles have been forced to not overlap in space using the D3-force library[20], providing an alternative mechanism to display sample frequency and class overlap for each neuron. Note that almost all of the available white space in the figure is used completely. For each class, there is a clearly defined block of neurons, with many of these activating only a single tissue type. An approximately even distribution in the number of neurons required to identify each class is observed, with a slightly higher weighting for the vitreous humour. As a result of the vitreous humour consisting mainly of water and containing very few cells, the additional effort required by the network to isolate the tissue can be observed in the map. This can be considered by analogy to how the brain associates a larger number of neurons to facial features, than for example arms and legs (the cortical homunculus).

The majority of poorly separated samples are located centrally at the boundary between classes and extend down to the bottom edge of the map. Interestingly, in this region, there is a cluster of samples predominately corresponding to the retina, indicating that a number of retina samples are particularly noisy, further corroborated by being spatially located near other neurons that also lack any well defined class. While the SOM is analogous to the PCA scores plot (Supplementary Information, Fig. S2a), PCA performs particularly badly when compared against the SOM. However, it should be noted that the level of separation observed by PCA is completely inline with results commonly reported in the literature. Since PCA relies on separation by variance in the data, the class clusters are bound around a central point, as a result of noise or absence or spectral features, causing significant spatial overlap.

Feature extraction. The SOMDI provides a representation of weights associated with neurons that identify a particular class. A higher SOMDI intensity indicates a greater importance of particular inverse centimetres along the x-axis of a spectrum. Figure 2b shows the SOMDI overlaid for each class, where the most important Raman bands associated with each tissue layer can be easily identified. Despite the level of noise in the original data, well defined peaks are resolved in Fig. 2b, which are either more prominent or unique to each class. Strong weights are attributed to the cornea at 938 (C-C stretch) and 1241 cm^{-1} (C-N stretch), which also correspond, with a certain confidence, to the stretching modes of the C-C backbone and amide III modes of collagen.

The crystalline lens of the eye is predominately identified by a very strong SOMDI weight at 1005 cm^{-1} (2,4,6C radial) and is attributed to phenylalanine, which is abundant in water-soluble proteins present in the lens and directly relates to the tissue's function. The high polarizability of this molecule, which results in a large Raman scattering cross-section, aids in increasing the refractive index of the lens thus, providing fine focusing of light onto the retina. The vitreous humour is more challenging to isolate, with the strongest weights at 854, 858 cm^{-1} overlapping with significant weights for cornea, which have been associated with proline in collagen, along with small distinct weights at 832, 1044 and 1049 cm^{-1}. These bands may be indicative of the difference in collagen type found in the cornea versus the vitreous humour (type I vs. type II respectively) yet, a direct comparison of the two protein types is further required to support this postulation. The interpretation and discrimination of

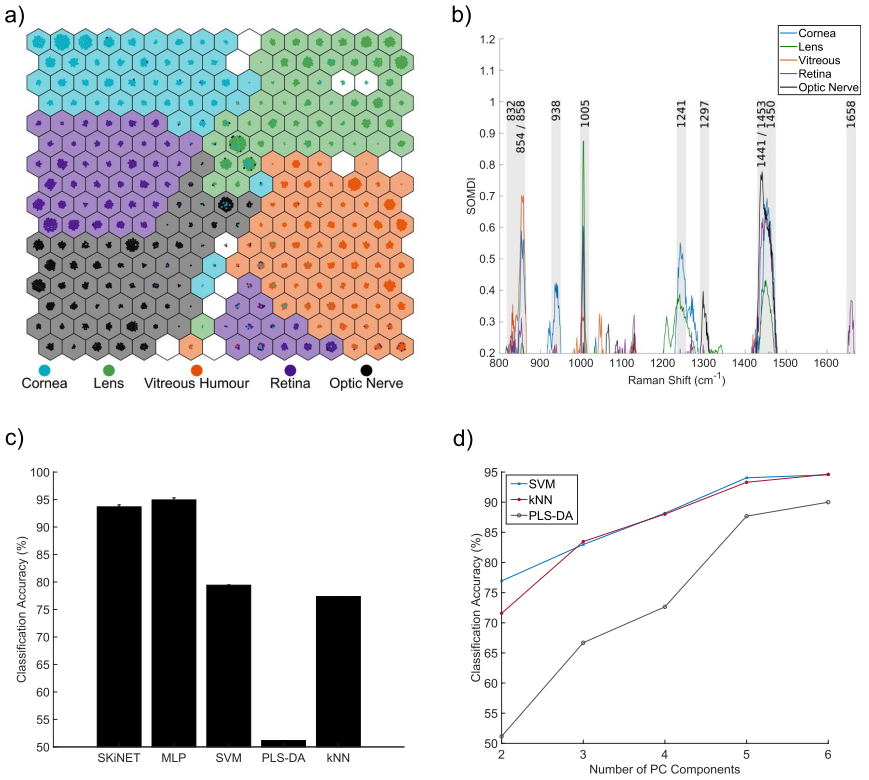

Figure 2. (**a**) SOM trained on spectra across the 5 eye tissue types. (**b**) SOMDI showing relative importance of different bands for each class to observed clustering in the SOM. (**c**) Classification accuracy of tissue using SKiNET against current state-of-the-art (multi-layer perceptrons (MLP), support vector machines (SVM), partial least squares discriminant analysis (PLS-DA) and k-nearest neighbours (kNN)). (**d**) Effect of number of principal components on classification accuracy for PCA based methods.

collagen types by Raman spectroscopy is currently an active area of interest, where SkiNET may also offer additional insight[21,22].

The remaining two classes of retina and the optic nerve are perhaps the most intriguing, located within the same focal plane, with the optic nerve connecting directly to the brain. An isolated peak at 1658 cm^{-1} (C=O stretch) identifies the retina and is associated with amide I (α-helix) groups in proteins. The detection of light by rods and cones in turn, relies on photo-receptive proteins known as opsins, which have an α-helical secondary structure. In contrast, the optic nerve can be characterised by a strong weight at 1441 (CH2 scissoring, CH3 bending) and 1297 (CH2 deformations) cm^{-1}, strongly associated with lipids and fatty acids. The brain is composed of nearly 60% fat, with lipids and fatty acids playing important roles in brain function, which here we observe as a clear marker for the distinction between brain and eye tissue via Raman spectroscopy[23]. Furthermore, the optic nerve is devoid of photo-receptive cells and responsible for the blind spot in humans and therefore, the peaks at 1441 and 1658 cm^{-1} act as biologically relevant markers for each[24]. Individual bond assignments were made with reference to Larkin[25], and associations to high level biological structures based on the work by Talari *et al.* and Movasaghi *et al.*, providing databases of Raman bands found in biological tissue[26,27].

Finally, unlike PCA loadings, which are often used to show similar information, the SOMDI can be interpreted in isolation. Conversely, PCA loadings are only relevant to a direction in PC space, relying on constant reference to the scores plot, which quickly become cumbersome for multi-class problems or where multiple PC scores are considered (Supplementary Information, Fig. S2b).

Classification. Automated classification of Raman spectra and assignment to a particular tissue type or disease state is perhaps the most important step for the translation of Raman-based diagnostic techniques to real-world, clinical applications. However, whilst SOMs have historically been used for visual separation of data, experimental results of classification are rare. The most common method is to look-up the modal class of the neuron activated for a test sample, as used to colour neurons in Fig. 2a. Since the SOMDI automatically provides class labels, the maximum SOMDI weight can also be used to perform class identification of any given neuron.

However, both of these methods remain unsupervised learning mechanisms, without optimisation towards the correct answer in the training set. This is in contrast to widely used supervised learning algorithms, such as multi-layer perceptrons (MLP), support vector machines (SVM), partial least squares discriminant analysis (PLS-DA) and k-nearest neighbours (kNN)[28–30].

Supervised learning can be introduced to SOMs by allowing the class weights used for the SOMDI to influence the learning process. For large enough label values, this effectively forces the map to cluster, however can result in over-fitting[16]. For our data, no benefit was observed using this method over the modal class on the unsupervised SOM (Supplementary Information, Fig. S3). Instead, a concept from learning vector quantisation (LVQ) was applied to the trained map and defined as a self-optimising Kohonen index network (SKiNET). A penalty is introduced for spectra (from the training set) that activate neurons identifying a different class. This has a natural tendency to self-optimise, with the identical behaviour to the vanilla SOM when training data activate the correct class.

Figure 2c shows the classification accuracy across all five tissue types using SKiNET, vs. current state-of-the-art methods. A 25% partition of the original data set was randomly assigned as test data and not used for training and optimisation of the network. The remaining 75% was used to optimise hyper-parameters of each classifier, which were tuned by performing 10-fold stratified cross validation. Most notable is the considerable improvement over PLS-DA, which is perhaps the most widely adopted method in chemometrics[31]. PCA was used as a dimensionality reduction method prior to classification for SVM, PLS-DA and kNN. It should be emphasised that only the first two principal components were kept. Figure 2d shows that by including a larger number of components, each of the classification methods can achieve a similar accuracy. The case of keeping more components for classification than are used for projection and feature extraction is routinely used in the literature. The alternative is to show several pairwise PCA scores plots, which arguably leaves the data in a high dimensional space[10,11,32].

However, by implementing SKiNET we are able to achieve a classification accuracy equivalent to keeping 6 components, whilst still being able to fully separate the data in only two spatial dimensions; equivalent to using 2 PCA components. Additionally, SKiNET showed a comparable performance to multi-layered perceptrons (MLP), whilst providing clear visualisations and feature extraction that MLPs and other neural network based methods lack. The confusion matrix (Supplementary Information, Table. S1) provides a breakdown of test samples classified into each class, and highlights the stability of the method across each of the five tissue types.

Discussion

The use of spectral fingerprints for clinical diagnostics requires two major components: the ability to quickly and accurately distinguish between different states (such as tissue types or diseases) and an understanding of the underlying chemical differences that enable such separation. The former is driven by an obvious need to perform timely diagnostics, but these decisions must be underpinned by biologically relevant changes. These issues are usually treated in isolation by multivariate techniques, with the best classification methods providing no insight into their nature. SKiNET addresses this disconnect, by using a single, simple architecture to provide clear visualisations and a high classification accuracy, whilst retaining an understanding of the major chemical differences between classes. Furthermore, the SOM removes the need for much of the linear algebra and matrix notation required to fully appreciate PCA. Instead, the SOM can be adequately described using only addition and subtraction.

We reiterate that SOMs can offer a vastly superior spatial separation of chemometric data, that has now been demonstrated for both NMR and Raman spectroscopy. The SOM can be considered mathematically as a non-linear equivalent to PCA, and therefore hints that these data may not in fact be linearly separable, as would normally be assumed from Raman spectroscopy and is a requirement for PCA to be valid[30]. Our assertion is that the inherent heterogeneity combined with spectral overlap could easily lead to this condition for biological samples. Despite the level of overlap and noise present in our raw data, the SOMDI offers a convenient method to quickly isolate important bands and automatically act as a noise filter. By using the SOMDI it was possible to easily identify prominent markers for bulk tissue properties in each of the tissue types considered.

LVQ offers a convenient means of introducing supervised learning into the SOM, however there are several variations of the LVQ algorithm that have not been explored here. This remains an area for future work, in addition to automatically setting the map parameters such as number of neurons, neighbourhood size, and an adaptive learning rate. Finally, it was shown that SOMDI weights could act as iterative class labels that are present throughout the learning process and change dynamically. As a result, there is scope to explore SKiNET based classification in conjunction with other SOM optimisation methods, that presently rely on a hit count (majority voting), which requires placing all of the training data into the SOM at every learning step where we wish to identify the winning class for a given neuron[33]. Since the SOMDI provides a constant dynamic neuron identifier, this would allow for scaling to larger training sets using such methods.

In general, SKiNET was seen to offer a huge classification improvement over existing methods, performing particularly better than PLS-DA, which is the current *status quo* in chemometrics. Several of the points stressed here have been mentioned in other publications across different disciplines, but never cohesively. It is therefore of equal importance that the entry point for SKiNET is not to download, buy a software package or compile scripts; but simply visit a website and upload data.

The ability to quickly identify tissue from the noisy spectral response of a short acquisition, as demonstrated here represents an important stepping stone towards the practical applicability of *in-vivo* ophthalmic Raman spectroscopy, allowing for the capture of clean signal in the region of interest only. Filtered signal could then be fed into a second SKiNET model designed to distinguish between specific disease states.

Variable	Description	Length
i	A single spectrum	1015
j	Spectrum class label vector	5
s	Training sample and label	$[i, j]$
n	A neuron	
w	Spectrum weight vector	length(i)
c	Class weight vector	length(j)
t	Training step	integer

Table 1. Definitions of variables used to describe SOM and SKiNET.

Methods

Self-optimising kohonen index network (SKiNET). The SOM is represented by a set of neurons arranged in a (hexagonal) grid. Here, we describe the basic SOM algorithm with SOMDI variables added for feature extraction[15,18]. We then describe how LVQ is included as an additional step to provide supervised learning, whilst using the SOMDI to identify each neuron class. Variables definitions are shown in Table 1 for reference. In each case, the capitalised letter represents the set for a given variable, e.g., the SOM contains a grid of N neurons.

Initially, every neuron is assigned weight vectors w (spectrum weight) and c (class weight), which are randomly initialised. The SOM is then trained according to the following algorithm:

1. Select a sample s at random from S
2. Calculate the euclidean distance, d for each n:

$$d = \sqrt{i^2 + w^2}$$

3. Define the best matching unit (BMU) as the neuron with minimum d
4. Update weights, w and c of each neuron be similar to the input:

$$scaleFactor = neighbourhood(BMU, t) * learningRate(t)$$

$$w = w + scaleFactor * (i - w)$$

$$c = c + scaleFactor * (j - c)$$

The map is gradually trained by repeating these steps numerous times. The update step applied in step 4 depends on a *neighbourhood* function which ensures neurons closest to the BMU are effected most (according to a Gaussian function), with a decreasing neighbourhood size with each t. Secondly a *learningRate* influences the update criteria, which linearly decreases with each iteration, t from a fixed initial starting value. To note, while class weights are updated in steps 4, they play no role in step 2, i.e., the spectra alone are responsible for finding the BMU.

The class vectors J have values of 1 for a given index or otherwise 0, e.g.,[1, 0, 0, 0, 0] and [0, 1, 0, 0, 0] representing labels for two of the five classes. As the map is trained, the neuron class vectors C become close to 1 as the neuron activates more of one spectral type and tend towards zero for all other class variables. Figure 3 illustrates how these vectors define class planes that are used to form the SOMDI. Once the map is trained, the class of any given n can be identified by finding the maximum of c.

Supervised learning. A second learning round is then applied, keeping the spatial mapping of neurons, but changing the update criteria to use rules from LVQ:

1. Start with trained SOM
2. Select a sample s at random from S
3. Calculate euclidean distance, for each n
4. Define BMU as the neuron with minimum d
5. Identify BMU and s class labels:

$$class_j = indexOf(max(j))$$

$$class_c = indexOf(max(c))$$

6. Update BMU w and c:

if ($class_j = class_c$) then

$$w = w + scaleFactor * (i - w)$$

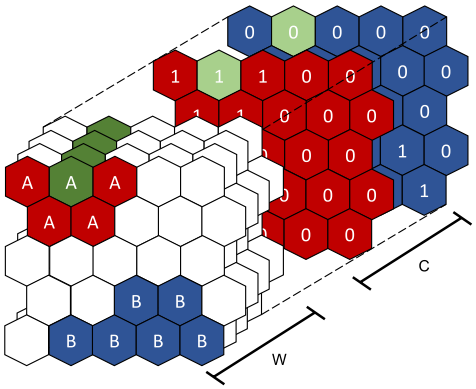

Figure 3. Illustrative example of SOM for two classes A and B, coloured red and blue, respectively. The weight vectors *W* and *C* can be thought of as making up additional planes in the z direction. Class planes are formed having values close to 1 for a given class and values close to 0 otherwise. These are used for classification and identification of the most important planes in *W* for the SOMDI.

$$c = c + scaleFactor * (j - c)$$

else

$$w = w - scaleFactor * (i - w)$$

$$c = c - scaleFactor * (j - c)$$

where only the update step changes when *s* lands on an incorrect neuron, to move both the spectrum weights and class weights of the BMU further away (and so making the neuron less likely to activate a similar spectrum in future iterations). During LVQ only the the BMU is updated under this regime and thus, represents only a small perturbation to the network. By analogy, this can be thought of as applying fine details to a painting, after the initial broad brush strokes to block in colours.

The method is described as self-optimising, since when the BMU class matches that of the input, the BMU weights are moved closer to the input as per the original unsupervised SOM algorithm. This allows a natural optimum to be reached, whilst preventing over-fitting. A second consequence of SKiNET, is a greater degree of freedom for each neuron. In the update step, the weight vector for the data and class labels are both updated, allowing for the class definition of a neuron to dynamically change as the map is trained.

Samples. Tissue samples were retrieved within hours of slaughter from a total of 11 enucleated porcine eyes, provided by Rowley CH Ltd, a local abattoir. Eyes were dissected to isolate small segments of cornea, lens, vitreous humour, retina and optic nerve. Tissue samples were prepared using a protocol suggested by Cui *et al.*, using glass slides covered with aluminium foil as a cost effective substrate, and allowed to air dry for 24 hours[34].

Raman spectroscopy. An InVia Qontor (Renishaw plc) equipped with a 785 nm laser was used for all measurements. LiveTrack maps over a sample area of 110 × 77 microns were acquired for each sample, with an acquisition time of 5 s for each point location in the map, and laser power of 2 mW, a 50 × Leica objective (0.75 NA), 1200 l/mm grating with scans recorded in the range 550–1670 cm^{-1}. A total of 88 scans per tissue sample were recorded (4840 spectra total).

Software and preprocessing. Baseline subtraction and cosmic ray removal were applied in WiRE 5.1 (Renishaw plc), each sample was independently standardised by mean centering and scaling to unit variance using Scikit-learn in python[35]. The package was then used to define training/test partitions, cross validation folds and define models for each classifier. The SOM based methods were defined in JavaScript by forking an existing open source SOM library[36]. The entire library was heavily refactored to include support for SKiNET, and is available on Github[37]. For consistency, a wrapper was created around the JavaScript library, to expose the same methods in python, allowing for all models to be benchmarked via the same script.

Code and Data Availability

For SOM and SOM based classification, the code was implemented in JavaScript, chosen for it's ubiquity on almost every modern device. This allowed for the creation of simple, user friendly web interface that can be easily accessed from any location, without any need to install or compile a single line of code. The lack of easily accessible tools has previously been cited as a reason for poor adoption of such methods as seen in chemometrics. We are aiming to address this gap by providing both a library and web app available as open source tools[17,37]. All Raman spectra used in the analysis presented are available in electronic form from the corresponding author upon request.

References

1. Krishnan, R. S. & Shankar, R. K. Raman effect: History of the discovery. *Journal of Raman Spectroscopy* **10**, 1–8 (1981).
2. Siebert, F. & Hildebrandt, P. *Theory of Infrared Absorption and Raman Spectroscopy* (Wiley-VCH Verlag GmbH, 2008).
3. Bauer, N. J. *et al*. Noninvasive assessment of the hydration gradient across the cornea using confocal Raman spectroscopy. *Investigative ophthalmology & visual science* **39**, 831–5 (1998).
4. Ozaki, Y. *et al*. Raman spectroscopic study of age-related structural changes in the lens proteins of an intact mouse lens. *Biochemistry* **22**, 6254–6259 (1983).
5. Rosen, R., Kruger, E., Katz, A. & Alfano, R. Method and system for detection by Raman measurements of bimolecular markers in the vitreous humor. US Patent 2002/00952.57 A1 (2002).
6. Ermakov, I. V., McClane, R. W., Gellermann, W. & Bernstein, P. S. Resonant Raman detection of macular pigment levels in the living human retina. *Optics Letters* **26**, 202 (2001).
7. Obana, A. *et al*. Macular Carotenoid Levels of Normal Subjects and Age-Related Maculopathy. *Ophthalmology* **115**, 2–12 (2008).
8. Erckens, R. J. *et al*. Raman spectroscopy in ophthalmology: from experimental tool to applications *in vivo*. *Lasers in medical science* **16**, 236–52 (2001).
9. Butler, H. J. *et al*. Using Raman spectroscopy to characterize biological materials. *Nature Protocols* **11**, 664–687 (2016).
10. Surmacki, J. M. *et al*. Raman micro-spectroscopy for accurate identification of primary human bronchial epithelial cells. *Scientific Reports* **8**, 12604 (2018).
11. Li, Y. *et al*. Rapid detection of nasopharyngeal cancer using Raman spectroscopy and multivariate statistical analysis. *Molecular and clinical oncology* **3**, 375–380 (2015).
12. Liu, J. *et al*. Deep convolutional neural networks for Raman spectrum recognition: a unified solution. *Analyst* (2017).
13. Cheriyadat, A. & Bruce, L. Why principal component analysis is not an appropriate feature extraction method for hyperspectral data. In *IGARSS 2003. 2003 IEEE International Geoscience and Remote Sensing Symposium. Proceedings (IEEE Cat. No.03CH37477)*, vol. 6, 3420–3422 (IEEE, 2003).
14. Brereton, R. G. Self organising maps for visualising and modelling. *Chemistry Central Journal* **6**, 1–15 (2012).
15. Lloyd, G. R., Wongravee, K., Silwood, C. J., Grootveld, M. & Brereton, R. G. Self Organising Maps for variable selection: Application to human saliva analysed by nuclear magnetic resonance spectroscopy to investigate the effect of an oral healthcare product. *Chemometrics and Intelligent Laboratory Systems* **98**, 149–161 (2009).
16. Wongravee, K., Lloyd, G. R., Silwood, C. J., Grootveld, M. & Brereton, R. G. Supervised Self Organizing Maps for Classification and Determination of Potentially Discriminatory Variables: Illustrated by Application to Nuclear Magnetic Resonance Metabolomic Profiling. *Analytical Chemistry* **82**, 628–638 (2010).
17. Banbury, C. Raman Toolkit - Analysis and Data Management Tool for Raman Spectra, https://github.com/cbanbury/raman-tools (2018).
18. Kohonen, T. Self-organized formation of topologically correct feature maps. *Biological Cybernetics* **43**, 59–69 (1982).
19. Tozer, B. A. The calculation of maximum permissible exposure levels for laser radiation. *Journal of Physics E: Scientific Instruments* **12**, 922 (1979).
20. Bostock, M. Force-directed graph layout using velocity Verlet integration, https://github.com/d3/d3-force (2016).
21. Esmonde-White, K. Raman Spectroscopy of Soft Musculoskeletal Tissues. *Applied Spectroscopy* **68**, 1203–1218 (2014).
22. Gamsjaeger, S., Klaushofer, K. & Paschalis, E. P. Raman analysis of proteoglycans simultaneously in bone and cartilage. *Journal of Raman Spectroscopy* **45**, 794–800 (2014).
23. Chang, C.-Y. *et al*. Essential fatty acids and human brain. *Acta neurologica Taiwanica* **18**, 231–41 (2009).
24. Gregory, R. & Cavanagh, P. The Blind Spot. *Scholarpedia* **6**, 9618 (2011).
25. Larkin, P. IR and Raman Spectra-Structure Correlations. *Infrared and Raman Spectroscopy* 73–115 (2011).
26. Talari, A. C. S., Movasaghi, Z., Rehman, S. & Rehman, I. U. Raman Spectroscopy of Biological Tissues. *Applied Spectroscopy Reviews* **50**, 46–111 (2015).
27. Movasaghi, Z., Rehman, S. & Rehman, I. U. Raman Spectroscopy of Biological Tissues. *Applied Spectroscopy Reviews* **42**, 493–541 (2007).
28. Smola, A. J. & Schölkopf, B. A tutorial on support vector regression. *Statistics and Computing* **14**, 199–222 (2004).
29. Pomerantsev, A. L. & Rodionova, O. Y. Multiclass partial least squares discriminant analysis: Taking the right way-A critical tutorial. *Journal of Chemometrics* **32**, e3030 (2018).
30. Haykin, S. *Neural networks: a comprehensive foundation* (Prentice Hall, 1999).
31. Brereton, R. G. & Lloyd, G. R. Partial least squares discriminant analysis: taking the magic away. *Journal of Chemometrics* **28**, 213–225 (2014).
32. de Almeida, M. R., Correa, D. N., Rocha, W. F., Scafi, F. J. & Poppi, R. J. Discrimination between authentic and counterfeit banknotes using Raman spectroscopy and PLS-DA with uncertainty estimation. *Microchemical Journal* **109**, 170–177 (2013).
33. Papadimitriou, S., Mavroudi, S., Vladutu, L., Pavlides, G. & Bezerianos, A. The Supervised Network Self-Organizing Map for Classification of Large Data Sets. *Applied Intelligence* **16**, 185–203 (2002).
34. Cui, L., Butler, H. J., Martin-Hirsch, P. L. & Martin, F. L. Aluminium foil as a potential substrate for ATR-FTIR, transflection FTIR or Raman spectrochemical analysis of biological specimens. *Analytical. Methods* **8**, 481–487 (2016).
35. Pedregosa, F., Varoquaux, G., Gramfort, A. & Michel, V. Scikit-learn: Machine Learning in Python. *Journal of Machine Learning Research* **12**, 2825–2830 (2011).
36. Mondon, N. A basic implementation of a Kohonen map in JavaScript, https://github.com/seracio/kohonen (2016).
37. Banbury, C. An implementation of a Kohonen map in JavaScript extended to provide feature extraction and classification, https://github.com/cbanbury/kohonen (2018).

Acknowledgements

C. Banbury gratefully acknowledges funding from EPSRC through a studentship from the Sci-Phy-4-Health Centre for Doctoral Training (EP/L016346/1). PGO is a Royal Academy of Engineering Research (RAEng) Fellowship holder and would like to acknowledge the support for this research (RF1415/14/28).

Author Contributions

C.B., N.E. and P.G.O. conceptualised the study. A.B. and A.L. provided expertise in tissue handling, sample preparation and characterisation. R.M., M.C. and I.S. guided testing and validation of the method. C.B. conducted experimental work, data analysis and wrote the paper. P.G.O., N.E. and I.S. have provided further insightful inputs into the paper.

Additional Information

Supplementary information accompanies this paper at https://doi.org/10.1038/s41598-019-47205-5.

Competing Interests: The authors declare no competing interests.

Publisher's note: Springer Nature remains neutral with regard to jurisdictional claims in published maps and institutional affiliations.

Development of the Self Optimising Kohonen Index Network (SKiNET) for Raman Spectroscopy Based Detection of Anatomical Eye Tissue

Carl Banbury[1] Richard Mason[2] Iain Styles[3] Neil Eisenstein[1]
Michael Clancy[1] Antonio Belli[4] Ann Logan[4]

[†]Pola Goldberg Oppenheimer[1]

[1]*Chemical Engineering, University of Birmingham* [2]*Physics and Astronomy, University of Birmingham*
[3]*Computer Science, University of Birmingham* [4]*Institute of Inflammation and Ageing, University of Birmingham*

Supplementary Information

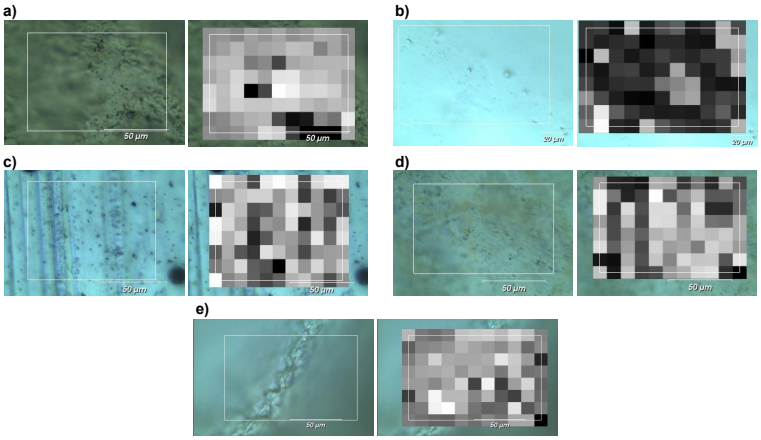

Figure S1: Paired examples of bright field optical microscope images (left) and PCA scores across map scan (right) for each tissue type: **a**, cornea, **b**, lens, **c**, vitreous humour, **d**, retina and **e**, optic nerve.

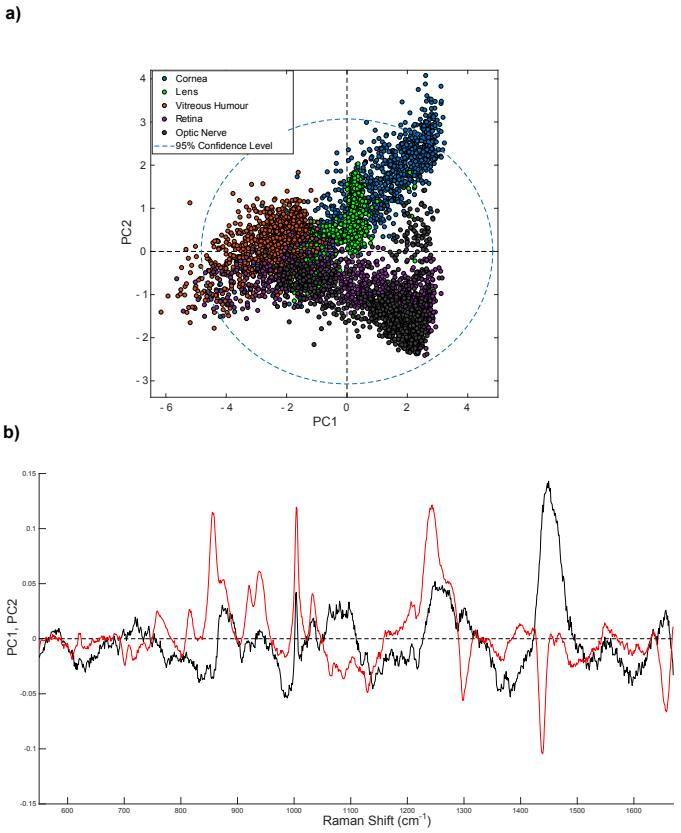

Figure S2: **a**, Scores plot for the first two principal components showing poor spatial separation of classes. **b**, Loadings for PC1 and PC2.

	Cornea	Lens	Vitreous Humour	Retina	Optic Nerve
Cornea	88.0	2.1	4.7	3.3	2.8
Lens	0.5	99.8	0.5	0	0.1
Vitreous Humour	1.0	0.1	96.5	2.7	0.5
Retina	1.0	0.2	2.3	95.7	1.7
Optic Nerve	4.6	0.71	0.8	2.2	92.5

Table S1: Confusion matrix showing average percentage for each class from the 1210 test spectra.

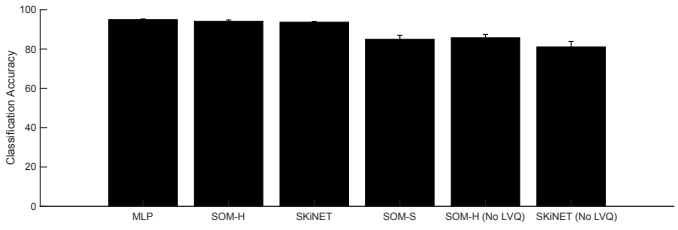

Figure S3: Comparison of classification accuracy for different approaches to SOM based classification. SOM-H referrs to using the hit count for class identification, SOM-S uses supervised SOMs as described here [16]

APPENDIX E

SPECTROSCOPIC DETECTION OF TRAUMATIC BRAIN INJURY SEVERITY AND BIOCHEMISTRY FROM THE RETINA

Research Article Vol. 11, No. 11 / 1 November 2020 / Biomedical Optics Express 6249
Biomedical Optics EXPRESS

Spectroscopic detection of traumatic brain injury severity and biochemistry from the retina

CARL BANBURY,[1] IAIN STYLES,[2] NEIL EISENSTEIN,[1] ELISA R. ZANIER,[3] GLORIA VEGLIANTE,[3] ANTONIO BELLI,[4] ANN LOGAN,[4] AND POLA GOLDBERG OPPENHEIMER[1,*]

[1]School of Chemical Engineering, The University of Birmingham, Edgbaston, Birmingham, B15 2TT, UK
[2]Computer Science, The University of Birmingham, Edgbaston, Birmingham, B15 2TT, UK
[3]Department of Neuroscience, Istituto di Ricerche Farmacologiche Mario Negri IRCCS, Milan, Italy
[4]Institute of Inflammation and Ageing, The University of Birmingham, Edgbaston, Birmingham, B15 2TT, UK
[*]P.GoldbergOppenheimer@bham.ac.uk
https://anmsa.com

Abstract: Traumatic brain injury (TBI) is a major burden on healthcare services worldwide, where scientific and clinical innovation is needed to provide better understanding of biochemical damage to improve both pre-hospital assessment and intensive care monitoring. Here, we present an unconventional concept of using Raman spectroscopy to measure the biochemical response to the retina in an *ex-vivo* murine model of TBI. Through comparison to spectra from the brain and retina following injury, we elicit subtle spectral changes through the use of multivariate analysis, linked to a decrease in cardiolipin and indicating metabolic disruption. The ability to classify injury severity via spectra of the retina is demonstrated for severe TBI (82.0 %), moderate TBI (75.1 %) and sham groups (69.4 %). By showing that optical spectroscopy can be used to explore the eye as the window to the brain, we lay the groundwork for further exploitation of Raman spectroscopy for indirect, non-invasive assessment of brain chemistry.

1. Introduction

Traumatic brain injury (TBI), resulting from sudden impact such as assault, sporting injuries or road traffic accidents is a major cause of morbidity and mortality, affecting an estimated 69 million individuals worldwide each year [1]. The initial damage triggers a complex cascade of metabolic, biochemical and inflammatory responses leading to secondary injury that can occur over the following hours, days or months [2]. The Glasgow coma scale (GCS), based on visual assessment of the patient's verbal, visual and motor responses, is the current gold standard to stratify injury severity and acute clinical evolution in TBI. The GCS defines arbitrary boundaries for injury severity grouped as mild, moderate and severe [3]. Whilst this has real clinical value, minimal mechanistic insight is provided into the pathobiology of damage evolution after injury. Novel technologies which can be applied quickly and non-invasively at the point of care (PoC) for interfacing with the brain and define the chemical signatures of TBI pathobiology are needed. A non-invasive method that can detect and quantify TBI would not only provide a more accurate, objective and timely approach to diagnosis, but may help expand our understanding of injury evolution and enable personalized intervention approaches.

The skull provides a thick protective layer around the brain, which strictly limits the available options for both non-invasive and invasive sampling of brain tissue, especially in pre-hospital settings. However, sitting at the back of the eye exists a small part of the brain covered only by optically clear media; the retina and the optic disc. The optic disc appears as a bright circle in

#399473 https://doi.org/10.1364/BOE.399473
Journal © 2020 Received 4 Jun 2020; revised 19 Aug 2020; accepted 15 Sep 2020; published 8 Oct 2020

Biomedical Optics EXPRESS

fundus images, and is the route through which visual information captured from the retina is passed to the brain along the optic nerve. Also known as the blind spot, the optic disc is devoid of photoreceptive cells and consists predominantly of white matter. Derived from an out-pouching of the diencephalon as the brain develops and bathed in the cerebrospinal fluid, both the optic nerve and retina are technically part of the central nervous system [4]. The retina and optic nerve have long been known to display physically measurable changes as a result of increased intracranial pressure (ICP), where ICP monitoring is of paramount importance for intensive care monitoring in TBI. Measurements from the eye of such changes have been the target of several studies aiming to develop non-invasive ICP, but to our knowledge no such attempts have been made to measure the resultant biochemical change [5–7].

We therefore have hypothesized that a form of optical spectroscopy, which has the potential to be translated into a non-invasive method to probe the posterior segment of the eye (retina and optic nerve), may be able to monitor injury evolution in real time after TBI. Among the optical spectroscopy techniques, Raman spectroscopy offers the richest and most sensitive chemical discrimination. Temporal changes from direct analyses of brain tissue have previously been studied by Surmacki *et al.* [8] using our murine model of TBI. Raman scattering is based on the inelastic interaction between light and a molecule, where the energy exchange from a scattering event causes a change in the vibrational energy level of a molecular bond. Since energy levels of electrons in molecules are quantized, only specific and discrete energy states are allowed. The Raman spectrum therefore defines a chemical fingerprint that is uniquely determined by the underlying molecular constituents [9]. Nevertheless, for biological samples there exists significant redundancy and complexity of spectral bands that makes analysis and interpretation of the data non-trivial. Raman scattering is also an extremely weak effect, and thus, long acquisition times and the use of a high-powered laser focused through an objective are standard requirements for well resolved spectra. The notion of laser exposure to the eye invokes a natural aversion, however every anatomical tissue layer of the eye has been successfully studied using Raman spectroscopy [10]. By adhering to laser safety limits, Obana *et al.* [11] conducted an *in-vivo* study using resonance Raman spectroscopy in humans to assess age-related maculopathy. More recently, Marro *et al.* [12] were able to measure inflammatory changes in retina cell cultures and Stiebing *et al.* [13] have showed how this can be extended to non-resonant Raman spectroscopy, using flat mounted retina samples combined with an optical pathway mimicking the human eye.

Recently, we developed a machine learning technique based on self organizing maps (SOM)s, the self optimizing Kohonen index network (SKiNET) for simultaneously providing rich information and classification from biological samples, even with noisy or poor quality spectra that would result from a lower laser power and short acquisition times [14]. SOMs provide visually intuitive 2D clustering (e.g. according to injury state) of high dimensional data such as Raman spectra, that are otherwise difficult to interpret for large sample and measurement numbers. Whilst SOMs are usually an unsupervised method, SKiNET incorporates supervised learning to additionally provide accurate classification, which could then be used to make diagnostic predictions. Finally, a form of feature extraction using the self organizing map discriminant index (SOMDI) allows us to understand which spectral features (and therefore chemical changes) are responsible for the clustering seen in the SOM [15].

Here, Raman spectroscopy combined with SKiNET is applied to investigate whether the retina can reflect the brain microenvironment after injury, in a clinically relevant murine model of focal TBI. Our results show that spectra from the eye can distinguish moderate TBI (mTBI) and severe TBI (sTBI) from a sham group, and show this to be as a result of similar chemical changes to those seen at the point of injury on the brain. Through quantitative and qualitative analysis we suggest the detected changes are largely due to metabolic distress and the release of cardiolipin, consistent with recent work in the field of mass spectrometry [16]. This validation is particularly promising as mass spectrometry provides vastly superior molecular discrimination. However,

Biomedical Optics EXPRESS

Raman spectroscopy has the advantage of being a non-destructive technique and as highlighted, there are ongoing efforts in the field for translation into *in-vivo* measurements, and diagnostics.

2. Methods

2.1. Mouse model of TBI and tissue processing

Adult (8 weeks old) C57BL/6J male mice (Envigo RMS srl) were used. No additional procedures were performed on mice except those related to the experiment they were intended for. Procedures involving animals and their care were conducted in conformity with the institutional guidelines at the Istituto di Ricerche Farmacologiche Mario Negri IRCCS, Italy in compliance with national (D.lgs 26/2014; Authorization n. 19/2008-A issued March 6, 2008 by Ministry of Health) and international laws and policies (EEC Council Directive 2010/63/UE; the NIH Guide for the Care and Use of Laboratory Animals, 2011 edition). They were reviewed and approved by the Mario Negri Institute Animal Care and Use Committee that includes ad hoc members for ethical issues, and by the Italian Ministry of Health (Decreto no. D/07/2013-B and 301/2017-PR). Animal facilities meet international standards and are regularly checked by a certified veterinarian who is responsible for health monitoring, animal welfare supervision, experimental protocols and review of procedures. Mice were anesthetized by isoflurane inhalation (induction 3%; maintenance 1.5%) in an N_2O/O_2 (70%/30%) mixture and placed in a stereotaxic frame. Rectal temperature was maintained at 37 °C. Mice were then subjected to craniectomy followed by induction of controlled cortical impact brain injury as previously described [17]. Briefly, the injury was induced using a 3-mm rigid impactor driven by a pneumatic piston rigidly mounted at an angle of 20° from the vertical plane and applied to the exposed dura mater, between bregma and lambda, over the left parietotemporal cortex (antero-posteriority: −2.5 mm, laterality: −2.5 mm), at an impactor velocity of 5 m/s. The deformation depth was of either 1 mm or 0.5 mm, resulting in a severe (sTBI) or moderate (mTBI) level of injury respectively. The craniotomy was then covered *via* cranioplasty and the scalp sutured. Sham mice received identical anesthesia and surgery without brain injury. Three days after TBI, mice were deeply anesthetized with Ketamine Chlorhydrate (150 mg/kg, i.p.) and Medetomidine Chlorhydrate (0.2 mg/kg, i.p.) transcardially perfused with 30 mL of phosphate-buffered saline (PBS) 1% (pH 7.4), followed by 60 mL of paraformaldehyde (PFA) 4% in PBS. The brains and eyes were carefully removed from the skull and post-fixed in 4% PFA in PBS for 24 hours at 4 °C. The post-fixed tissue were then rinsed and stored in normal saline (NaCl 0.9%) at 4 °C. Samples we mounted on microscope slides covered with aluminum foil for spectroscopy studies as whole brains. Retina samples were prepared by micro-dissection of eyes in PBS, followed by flat mounting on aluminum slides. Samples were air dried for 1 hour before measurement.

2.2. Raman spectroscopy

An InVia Qontor (Renishaw plc) equipped with a 785 nm laser was used for all measurements. Raman maps over a 20x20 grid (400 spectra), using a step size of 1.5 µm between points were acquired for each sample. The surface map feature in the instrument software (WiRE (Renishaw plc)) was used to follow the topography of the sample, by uniformly measuring 9 position coordinates (x,y,z) and interpolating over the map area. At each position, a spectrum was recorded using a laser power of 50 mW, focused through a 50x Leica objective (0.75 NA) over 5 s (1 s acquisition, 5 accumulations). Spectra were measured in the range 605-1715 cm^{-1} using a 1200 l/mm grating. Instrument calibration was performed using the internal silicon reference built into the InVia system. Care was taken to ensure consistent sample preparation between samples and across injury states. All tissue was kept refrigerated in PBS prior to measurement. All Raman spectra were measured on the same day for each tissue type (brain, retina) and within 72 hours of sacrifice. Raman maps were measured in the contusion core for mTBI and sTBI, and

Biomedical Optics EXPRESS

the corresponding area in the sham group. Maps measured from the retina of both eyes were taken from an area in close proximity to the optic disc for each mouse. Post processing of spectra was performed in WiRE 5.3 (Renishaw Plc), cosmic rays were removed from each map using the nearest neighbor method, followed by baseline subtraction using the 'intelligent spline' fitting (11 nodes). Finally, the average was taken from each map resulting in a single spectrum per sample.

2.3. Analysis of retina tissue

The 400 spectra measured across each tissue sample were grouped according to injury state from both eyes (summarized in Table 1). 20 % of the data was randomly selected from each group and reserved as test data, leaving the remaining 80 % for training (Table 2). Analysis of the training data was performed using SKiNET [18], by randomly passing samples from the training data into the SOM over a number of iterations. SKiNET models were optimized by performing 10 fold cross validation on the the training data, and tuning the number of neurons, initial learning rate and number of training steps. The final model used a 20x20 grid of neurons, 57600 training steps (5 epochs of the data), with an initial learning rate of 0.2. The initial neighborhood size was maintained at 2 / 3 the edge length of the grid and cosine similarity used as the distance metric to determine the best matching unit. Finally, the optimized model was used to classify the previously unused test data, to give an indicator of the classification performance. Classification using the test data were repeated 10 times from separate SOM initializations and an average of the results output as a confusion matrix. An illustration of the workflow is shown in Fig. S1.

Table 1. Summary of retina spectra used as inputs for multivariate analysis across the three injury states (sham, mTBI and sTBI).

	Spectra Per Tissue Sample	Mice	Eyes	Total
Sham	400	6	2	4800
mTBI	400	6	2	4800
sTBI	400	6	2	4800
				14,400

Table 2. Breakdown of data across each injury state, and split into training and test data sets.

Injury State	Total	Training Data (80 %)	Test Data (20 %)
Sham	4800	3840	960
mTBI	4800	3840	960
sTBI	4800	3840	960
Total	14,400	11,520	2880

2.4. Analysis of brain tissue

SkiNET was used to analyze spectra measured from whole brain samples as described in the previous section. The 400 spectra measured across each tissue sample were grouped according to injury state from the contusion core, and 20 % of the data reserved as test data (summarized in Table 3). Non-negative least squares (NNLS) analysis was performed on brain tissue by fitting a library of component spectra to the average spectrum for each brain sample (Fig. S2d-f). The component spectra consisted of raw data provided by Krafft *et al.* [19] for human brain lipids and cardiolipin. Cytochrome c was purchased from Sigma-Aldrich Ltd and measured without modification at 785 nm using a laser power of 10 mW, focused through a 50x Leica objective

Biomedical Optics EXPRESS

(0.75 NA) over 10 s (1s acquisition, 10 accumulations). The **lsqnonneg** function in MATLAB was used to determine coefficients of the raw component spectra to the average spectra measured from the brain. The **interp1** function was used to rescale the data in the range of 1200-1714 cm^{-1} in increments of one inverse centimeter.

Table 3. Breakdown of data across each injury state, and split into training and test data sets from brain tissue in the contusion core.

Injury State	Total	Training Data (80 %)	Test Data (20 %)
Sham	2400	1920	480
mTBI	2400	1920	480
sTBI	2400	1920	480
Total	7200	5760	1440

3. Results

Experimental TBI was induced by controlled cortical impact in mice (n=6 for each injury state), with the degree of injury (either moderate or severe) being defined by the deformation depth. Tissue samples of postfixed brain (Fig. 1(a)) and eyes were collected 3 days after injury from sham, mTBI and sTBI groups. An illustration of the mouse head is shown in Fig. 1(b), highlighting the bilateral axon projections that are present between the brain and the retina. Each eye was carefully dissected to isolate and flat mount the retina as shown in Fig. 1(c). The corresponding Raman spectra (averaged over all samples) from the contusion core of the brain (Fig. 1(d)) and from flat mounted retina (Fig. 1(e)) are shown for mTBI and sTBI against the sham group. Assignments to the highlighted bands are summarized in Table 4, along with common biochemical attributions, with reference to the database published by Talari *et al.* [20].

Table 4. Summary of chemical assignments and biochemical attribution to Raman bands which display a change after TBI. Assignments were made with reference to Larkin [21], common biochemical attributions made with reference to the database by Talari *et al.* [20].

Peak (cm^{-1})	Assignment	Attribution
850	C-H wagging	-
1003	C-C skeletal	phenylalanine
1266	C-H bending	mixed (proteins/lipids)
1337	C-N stretching, N-H bending	Amide III
1447	$C\text{-}H_2$ bending	mixed (proteins/lipids)
1660	C=C stretching	mixed (proteins/lipids)

3.1. Multivariate analysis of retina tissue

From the average spectra of brain tissue in Fig. 1(d), dramatic changes to the bands around 1266 and 1660 cm^{-1} are clearly visible, however the data from the retina (Fig. 1(e)) are almost indistinguishable across the three injury states. The average spectra provide an easily digestible format in order to present the data, but forces us to throw away vital information that arises from point-point variation within each sample combined with sample-sample variation. Fortunately, multivariate techniques allow us to capture all of this information and extract the most important spectral features which characterize a group of data, such as an injury state. Recently, we highlighted the value of SOMs in the analysis of Raman spectra from biological samples [14].

Biomedical Optics EXPRESS

The 400 spectra measured across each tissue sample were grouped according to injury state from both eyes. 20 % of the data was randomly selected from each group and reserved as test data, leaving the remaining 80 % for training.

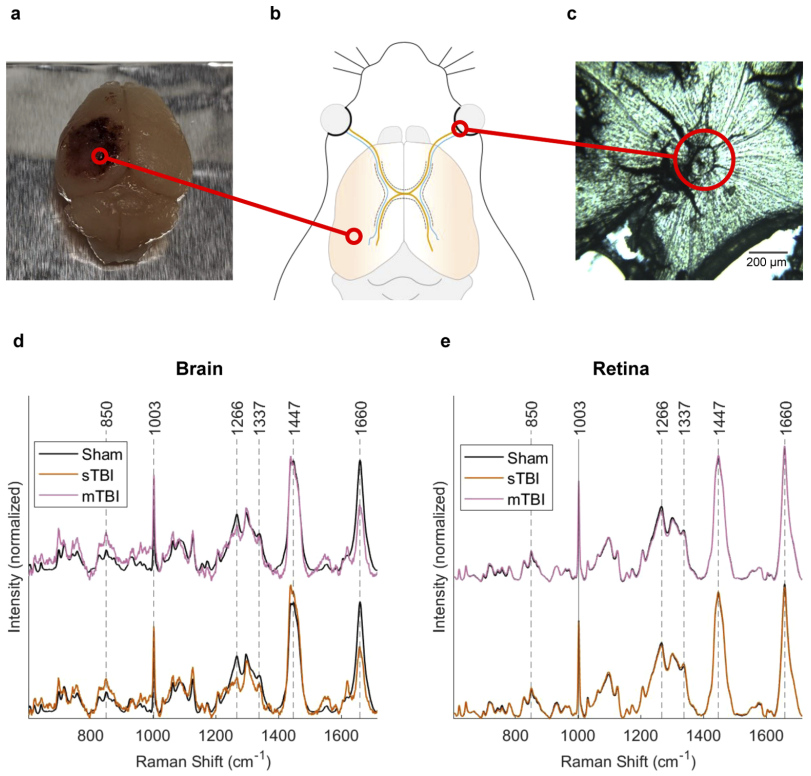

Fig. 1. **a**, Photograph of whole brain following sTBI to the left parietotemporal cortex. **b**, Illustration of mouse brain and optic tract, highlighting ipsilateral (blue) and contralateral (orange) projections connecting the brain to the retina. **c**, Example of a bright field microscopy image of a flat mounted retina from the mTBI group. **d**, Average Raman spectra collected in the contusion core for mTBI and sTBI compared to the sham group. **e**, Average Raman spectra collected from flat mounted retina samples (both eyes), showing mTBI and sTBI compared to the sham group. Raman spectra were collected as map measurements of 400 spectra over each sample, using a 785 nm excitation laser (50 mW), 1s acquisitions with 5 accumulations. Map measurements from each sample were averaged to produce a single spectrum per sample (n=6 for each injury state).

Briefly, a SOM is a type of artificial neural network that is typically visualized as a 2D array of hexagonal neurons, which loosely tries to mimic the visual cortex in the brain; with neighboring neurons activating on similar inputs. The training process is performed iteratively by presenting an individual spectrum (ξ) from the training data, and finding the neuron that has previously activated on data most similar to the input, ξ. The winning neuron is then updated to become more likely to activate on data like ξ, along with neighboring neurons (but to a lesser degree).

Biomedical Optics EXPRESS

The result is neurons that are grouped according to particular features, as see in Fig. 2(a). Each neuron (hexagon) in the SOM is colored according to the type of data it activates from the training data (sham, mTBI or sTBI), providing immediate visualization of how the data is organized in groups.

A clear separation between sham and sTBI groups can be seen in the SOM shown in Fig. 2(a). To indicate neurons that activate on more than one injury state, color mixing is used according to the relative proportion of hits from each state. Using the SOMDI [15], it is possible to identify features in the Raman spectrum responsible for the clustering observed in the SOM. For sTBI: increases to the bands around 850, 1098 and 1337 cm^{-1}, coupled to decreases in the bands around 1003, 1266 and 1660 cm^{-1} are observed, relative to the sham group (Fig. 2(b)). In comparison to sTBI, mTBI shows a poorer separation in the SOM (Fig. 2(c)), with a greater proportion of neurons activating on a mixture of mTBI and sham groups, particularly for neurons associated with mTBI. This is seen by mixing of the colors for injury states in the SOM. However, distinct regions are still present for both mTBI and sham groups. The same is true for the SOMDI of mTBI *vs* sham (Fig. 2(d)), with very few spectral regions of similarity between the two groups, indicating a greater degree of heterogeneity. Despite the increased variation, increases to the bands at 850, 1098 coupled to a decrease in the band at 1266 cm^{-1} are still observed for mTBI.

Following separation of the data from injured and healthy tissue, SKiNET can be used as a classifier. The classification method works by inputting a test sample into the trained network, and identifying which neuron is activated. The SOMDI associated with the activated neuron provides class data (based on the training inputs), which is used to make a prediction for the new sample. Models were optimized by using 10-fold cross validation on the training data to tune: the number of neurons in the SOM; initial learning rate; and training steps. Following optimization, the trained network was used to predict the previously unused test data, and showed good sensitivity for sTBI (82.0 ± 1.4 %). A poorer classification accuracy was obtained for sham (69.4 ± 0.9 %) and mTBI groups (75.1 ± 0.9 %), with a large proportion of sham data incorrectly classified as mTBI and *vice versa* (Table 5). Similar results were obtained by splitting the data according to ipsilateral (side of injury) and contralateral retinae (Table S1), and in comparison to the cross validation accuracy against the training data (Table S2).

Table 5. Summary of classification accuracy as a confusion matrix for: sham, mTBI and sTBI groups using trained SKiNET against test data. Data shown is the average classification accuracy across 10 SOM initializations, trained using Raman spectra from flat mounted mouse retina (both eyes).

		Predicted		
		Sham (%)	**mTBI (%)**	**sTBI (%)**
Actual	**Sham (%)**	**69.4**	24.0	6.6
	mTBI (%)	17.9	**75.1**	6.9
	sTBI (%)	7.9	10.0	**82.0**

3.2. Corresponding changes to brain spectra

In contrast to the retina, Raman spectra of brain tissue from the site of injury showed more dramatic and consistent changes across injury groups. Even in the average spectra over all samples (Fig. 1(d)), there are visible differences to the bands around 1266 cm^{-1} and 1660 cm^{-1}. This observation is supported by SKiNET analysis applied to the spectra from brain tissue in the contusion core, using the same methodology described in the previous section. Spectra from the test data were classified with an accuracy of (100 ± 0.0 %) for sham, (94.5 ± 0.9 %) for mTBI

Biomedical Optics EXPRESS

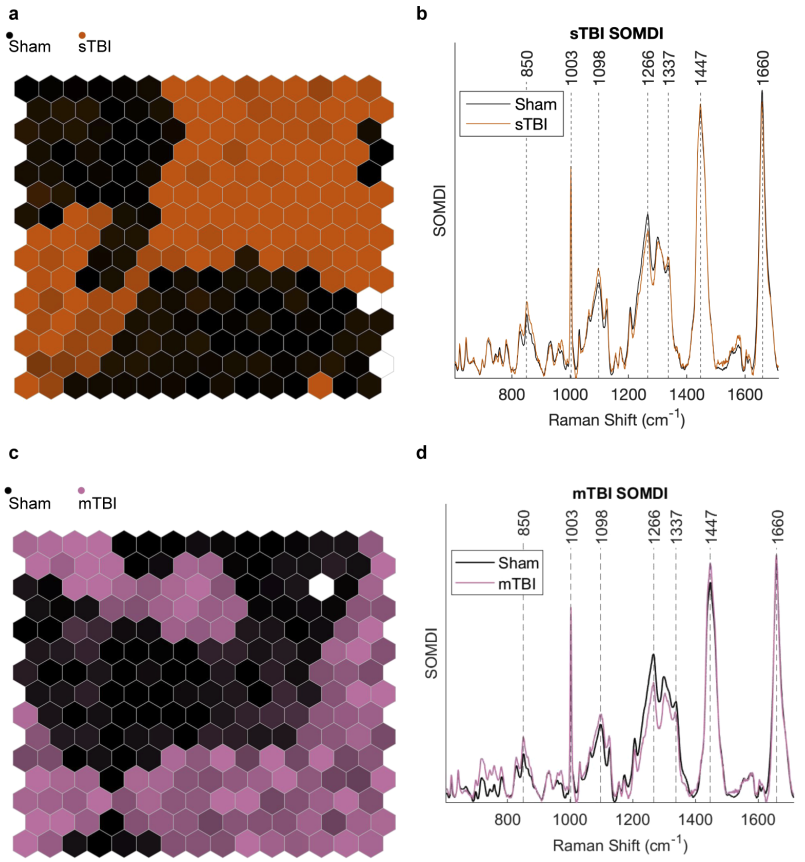

Fig. 2. **a**, Clustering of Raman spectra from the retina for sTBI (orange) and sham (black) groups using a SOM. **b**, Features extracted (SOMDI) from SOM shown in (**a**), highlighting the Raman bands most influential to neurons in the SOM for sham and sTBI groups. **c**, Clustering of mTBI (purple) and sham (black) Raman spectra from the retina using a SOM. **d**, Features extracted from SOM in **c**, highlighting Raman bands for sham and mTBI groups.

and (91.2 ± 1.3 %) for sTBI. Furthermore, the extracted features using the SOMDI (Fig. S4) closely resemble the average spectra.

A decrease to the band at 1266 cm^{-1} in TBI samples appears to be a key feature from the analysis of both brain and retina. Visually, this can be observed using false colored Raman maps of the ratio of the band at 1447 vs 1266 cm^{-1} (Fig. 3). The band at 1266 cm^{-1} is assigned to CH bending modes, and commonly associated with amide groups in lipids and proteins [20]. Since the brain contains nearly 60 % fat and the Raman signature for all 12 major and minor brain specific lipids have been well characterized [19,22], we attempted to decompose the changes due to the lipid contribution. NNLS fitting was performed against average spectra from brain tissue from each sample (Fig. S2d-f), using a library of component spectra, which included the

Biomedical Optics EXPRESS

raw data for brain specific lipids, cardiolipin (provided by Krafft *et al.* [19]) and cytochrome c. Fitting was performed in the range 1200-1714 cm^{-1}, to identify the relative contributions in each tissue sample for sham, mTBI and sTBI. The resultant fitting coefficients for each lipid spectrum are therefore proportional to the lipid concentration measured within each tissue sample. A one-way ANOVA shows a statistically significant difference in the contribution (compared to the sham) from cardiolipin (Fig. 4(a)), linked to the decrease in the bands at 1266 and 1660 cm^{-1} (Fig. 4(b)) in TBI for both moderate and severe TBI *vs* the sham. No significant change was observed between injury severity for cardiolipin. A small decrease in the fitting coefficient for cholesterol was observed, along with an increase in sphingomyelin, but were not statistically significant (Table S3-S5).

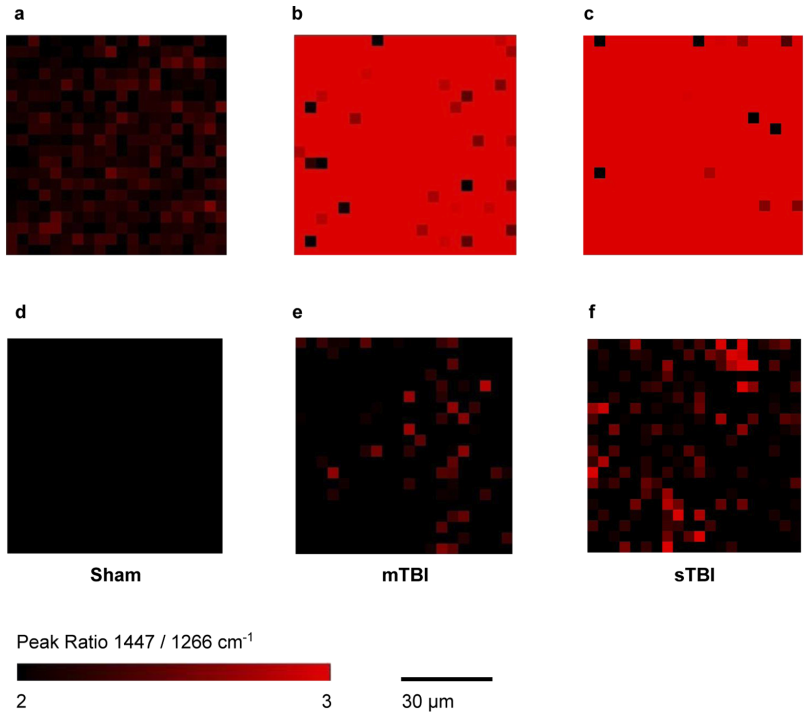

Fig. 3. False colored Raman maps showing the peak ratio at 1447 / 1266 cm^{-1} for a single brain tissue sample from Sham (**a**), mTBI (**b**), and STBI (**c**) groups. **d-f**, Corresponding Raman maps of ipsilateral tissue of retina from the same mice. Raman maps for all samples are shown in Fig. S5-S6.

Biomedical Optics EXPRESS

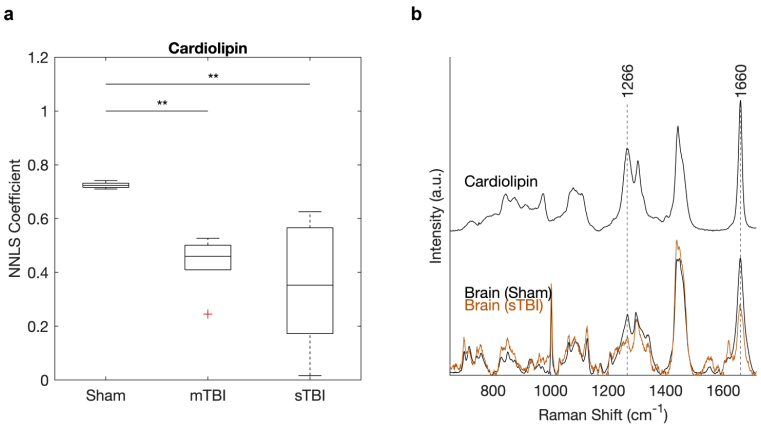

Fig. 4. **a**, Change in the relative contribution from cardiolipin for sham, mTBI and sTBI. Boxplot shows the NNLS coefficient fitted to the average map spectrum measured from each brain sample at the injury site, in the range 1200-1714 cm^{-1}. A statistically significant difference determined by one-way ANOVA exists in cardiolipin for mTBI ($p = 0.0090$) and sTBI ($p = 0.0011$) compared to the sham. There is no statistically significant difference between mTBI and sTBI (*$p < 0.05$, **$p < 0.01$). **b**, Spectra for cardiolipin (using data from Krafft *et al.* [19]) and average spectra for brain tissue from sham and sTBI.

4. Discussion

Through the use of SKiNET, subtle changes to spectral features have been identified for TBI, further highlighting the value of SOMs in the analysis of Raman spectra. The observed change to the band 1266 cm^{-1} has been shown to be present for both the brain and retina, proportional to injury severity (Fig. 3). However, whilst Raman maps of brain tissue show a strong and uniform relative decrease at 1266 cm^{-1}, tissue from the retina appears more heterogeneous. This suggests that future applications of the technology may require targeted scanning over specific areas of the retina (e.g. optic disc), and identify a number of spectra above a certain threshold for TBI. Furthermore, the change seen in Fig. 3 was not observed consistently across all samples, especially from contralateral tissue (Fig. S6). One implication is that a change to a single Raman band in isolation is not enough to classify tissue, emphasizing the importance of tools such as SKiNET, which use all of the available data.

From brain tissue, obvious and consistent changes were observed to spectra in response to injury, which is in contrast to the subtle changes seen in the previous work by Surmacki *et al.* [8]. An explanation for this discrepancy is that we collected a large number of spectra over an area for each sample, whilst following the surface topography. Hemorrhaging that was clearly visible in the contusion core from mTBI and sTBI samples of the brain (Fig. 1(a)) led to a strong background autofluorescence, which we have attributed to the near infrared absorption of deoxyhemoglobin [23]. Whilst this did not effect measurements from the retina, this may have led to artifacts in the baseline correction, such as the small bands observed between 1447 and 1660 cm^{-1}.

Biomedical Optics EXPRESS

4.1. Biochemical attribution

Attribution and deconvolution of Raman spectra to biological species from spectra of tissue remains challenging, which we have attempted through the use of NNLS fitting. The choice of fitting library followed previous qualitative analysis [8], and included cardiolipin and cyctochrome c as markers of mitochondrial activity. Cardiolipin is found exclusively in the inner mitochondrial membrane, playing a crucial role in cell metabolism and signaling; including apoptosis. A decrease in cardiolipin concentration following cortical impact has recently been shown using mass spectrometry, where both the importance in relation to TBI and opportunity for future therapeutics were highlighted [16]. Furthermore, the release of cardiolipin microparticles following TBI induced cell damage has been show to compromise the blood brain barrier, and so plays a major role in the resulting biochemical cascade and metabolic disruption [24]. These findings are also consistent with earlier studies using Raman spectroscopy to assess TBI in mice, where the authors concluded a link between the observed spectral changes and apoptosis *via* comparison to immunohistochemistry of the samples [25]. Cytochrome c is a protein found in the inner membrane of mitochondria, where a complementary change to cardiolipin was expected. Small coefficients were fitted for cytochrome c in the mTBI and sTBI groups, which were not present in the sham group. This adds additional weight to the conclusion that the observed changes in response to injury are a result of metabolic distress. Although these results are encouraging, it should be noted that the spectral bands associated with cardiolipin are also present in several proteins, and so these changes cannot solely be attributed to cardiolipin [26].

4.2. Translation and future work

Despite the obvious challenges for Raman spectroscopy of the eye, it appears to be an area of active development, with Stiebing *et al.* [13] recently showing how spectra can be safely collected from *ex-vivo* human retina using a synthetic model of the optical parameters of the eye, in place of a microscope objective. The spectra acquired through such a low numerical aperture geometry are inevitably noisy, or require long acquisition times. In the present study, the important issue of eye safety limits have not been addressed, and a traditional Raman microscope geometry used. However, short acquisition times meant that individual spectra used as training inputs were noisy and yet, *via* SKiNET these were used to accurately identify TBI severity. Now that we have established a preliminary proof of concept, a study using a larger animal model of TBI (e.g. porcine) could be used demonstrate *in-vivo* viability.

5. Conclusions

For the first time, we have shown that Raman spectroscopy can be used to effectively and accurately identify TBI from tissue samples of the retina, coupled to chemical changes from a cortical impact to the brain. Machine learning using the SOMDI and SKiNET has been used to extract the subtle spectral changes present from the retina, and shown these to be in line with the measured changes to brain tissue. Consistent changes were observed in particular for the band at 1266 cm^{-1} both in brain and retina tissue for mTBI and sTBI, when compared to the sham group. Raman spectroscopy represents a unique opportunity for TBI monitoring throughout the patient journey from pre-hospital assessment, to intensive care and follow up examinations. In demonstrating a fundamental ability to study chemical changes from eye tissue as a result of TBI, we begin to push the boundaries of Raman spectroscopy of the eye beyond purely ophthalmic applications; opening a new window to study neurological changes.

Funding

Royal Academy of Engineering (RF1415/14/28); Wellcome Trust (174ISSFPP); Engineering and Physical Sciences Research Council (EP/L016346/1).

Biomedical Optics EXPRESS

Acknowledgments

C. Banbury gratefully acknowledges funding from EPSRC through a studentship from the Sci-Phy- 4-Health Centre for Doctoral Training (EP/L016346/1). P.G.O. is a Royal Academy of Engineering Research (RAEng) Fellowship holder and would like to acknowledge the support for this research (RF1415/14/28). We also acknowledge funding from the Wellcome Trust (174ISSFPP). We would like to thank Dr A. Spear and Dr C. Howle (Defence Science and Technology Laboratories (DSTL)) for supporting this study and this research.

Disclosures

The authors declare no competing interests.

See Supplement 1 for supporting content.

References

1. M. C. Dewan, A. Rattani, S. Gupta, R. E. Baticulon, Y. C. Hung, M. Punchak, A. Agrawal, A. O. Adeleye, M. G. Shrime, A. M. Rubiano, J. V. Rosenfeld, and K. B. Park, "Estimating the global incidence of traumatic brain injury," J. Neurosurg. **130**(4), 1080–1097 (2019).
2. M. L. Pearn, I. R. Niesman, J. Egawa, A. Sawada, A. Almenar-Queralt, S. B. Shah, J. L. Duckworth, and B. P. Head, "Pathophysiology associated with traumatic brain injury: Current treatments and potential novel therapeutics," (2017).
3. G. Teasdale, A. Maas, F. Lecky, G. Manley, N. Stocchetti, and G. Murray, "The Glasgow coma scale at 40 years: standing the test of time," Lancet Neurol. **13**(8), 844–854 (2014).
4. D. Purve, G. J. Augustine, D. Fitzpatrick, L. C. Katz, A. LaMantia, J. O. McNamara, and S. M. Williams, *Neuroscience* (Sinauer Associates, 2001), 2nd ed.
5. S. S. Hayreh, "Pathogenesis of oedema of the optic disc (papilloedema): A preliminary report," Br. J. Ophthalmol. **48**(10), 522–543 (1964).
6. T. Geeraerts, J. Duranteau, and D. Benhamou, "Ocular sonography in patients with raised intracranial pressure: the papilloedema revisited," Critical Care **12**(3), 150 (2008).
7. R. Meyer-Schwickerath, T. Kleinwächter, H. D. Papenfuß, and R. Firsching, "Central retinal venous outflow pressure," Graefe's Arch. Clin. Exp. Ophthalmol. **233**(12), 783–788 (1995).
8. J. M. Surmacki, L. Ansel-Bollepalli, F. Pischiutta, E. R. Zanier, A. Ercole, and S. E. Bohndiek, "Label-free monitoring of tissue biochemistry following traumatic brain injury using Raman spectroscopy," The Analyst **142**(1), 132–139 (2017).
9. R. S. Krishnan and R. K. Shankar, "Raman effect: History of the discovery," J. Raman Spectrosc. **10**(1), 1–8 (1981).
10. R. Erckens, F. Jongsma, J. Wicksted, F. Hendrikse, W. March, and M. Motamedi, "Raman spectroscopy in ophthalmology: From experimental tool to applications in vivo," Lasers Med. Sci. **16**(4), 236–252 (2001).
11. A. Obana, T. Hiramitsu, Y. Gohto, A. Ohira, S. Mizuno, T. Hirano, P. S. Bernstein, H. Fujii, K. Iseki, M. Tanito, and Y. Hotta, "Macular carotenoid levels of normal subjects and age-related maculopathy patients in a japanese population," Ophthalmology **115**(1), 147–157 (2008).
12. M. Marro, A. Taubes, A. Abernathy, S. Balint, B. Moreno, B. Sanchez-Dalmau, E. H. Martínez-Lapiscina, I. Amat-Roldan, D. Petrov, and P. Villoslada, "Dynamic molecular monitoring of retina inflammation by in vivo Raman spectroscopy coupled with multivariate analysis," J. Biophotonics **7**(9), 724–734 (2014).
13. C. Stiebing, I. W. Schie, F. Knorr, M. Schmitt, N. Keijzer, R. Kleemann, I. J. Jahn, M. Jahn, A. J. Kiliaan, L. Ginner, A. Lichtenegger, W. Drexler, R. A. Leitgeb, and J. Popp, "Nonresonant Raman spectroscopy of isolated human retina samples complying with laser safety regulations for in vivo measurements," Neurophotonics **6**(04), 1 (2019).
14. C. Banbury, R. Mason, I. Styles, N. Eisenstein, M. Clancy, A. Belli, A. Logan, and P. Goldberg Oppenheimer, "Development of the self optimising kohonen index network (SKiNET) for Raman spectroscopy based detection of anatomical eye tissue," Sci. Rep. **9**(1), 10812 (2019).
15. G. R. Lloyd, K. Wongravee, C. J. Silwood, M. Grootveld, and R. G. Brereton, "Self organising maps for variable selection: Application to human saliva analysed by nuclear magnetic resonance spectroscopy to investigate the effect of an oral healthcare product," Chemom. Intell. Lab. Syst. **98**(2), 149–161 (2009).
16. H. Chao, T. S. Anthonymuthu, E. M. Kenny, A. A. Amoscato, L. K. Cole, G. M. Hatch, J. Ji, V. E. Kagan, and H. Bayir, "Disentangling oxidation/hydrolysis reactions of brain mitochondrial cardiolipins in pathogenesis of traumatic injury," JCI Insight **3**(21), e97677 (2018).
17. E. R. Zanier, I. Bertani, E. Sammali, F. Pischiutta, M. A. Chiaravalloti, G. Vegliante, A. Masone, A. Corbelli, D. H. Smith, D. K. Menon, N. Stocchetti, F. Fiordaliso, M.-G. De Simoni, W. Stewart, and R. Chiesa, "Induction of a transmissible tau pathology by traumatic brain injury," Brain (2018).

Biomedical Optics EXPRESS

18. C. Banbury, "Raman toolkit - analysis and data management tool for Raman spectra," https://github.com/cbanbury/raman-tools (2020).
19. C. Krafft, L. Neudert, T. Simat, and R. Salzer, "Near infrared Raman spectra of human brain lipids," Spectrochim. Acta, Part A **61**(7), 1529–1535 (2005).
20. A. C. S. Talari, Z. Movasaghi, S. Rehman, and I. ur Rehman, "Raman spectroscopy of biological tissues," Appl. Spectrosc. Rev. **50**(1), 46–111 (2015).
21. P. Larkin, "IR and Raman spectra-structure correlations," Infrared Raman Spectrosc. pp. 73–115 (2011).
22. C. Chang, D. Ke, and J. Chen, "Essential fatty acids and human brain," Acta neurologica Taiwanica **18**, 231 (2009).
23. T. W. L. Scheeren, P. Schober, and L. A. Schwarte, "Monitoring tissue oxygenation by near infrared spectroscopy (NIRS): background and current applications," J. Clin. Monit. Comput. **26**(4), 279–287 (2012).
24. Z. Zhao, M. Wang, Y. Tian, T. Hilton, B. Salsbery, E. Z. Zhou, X. Wu, P. Thiagarajan, E. Boilard, M. Li, J. Zhang, and J.-f. Dong, "Cardiolipin-mediated procoagulant activity of mitochondria contributes to traumatic brain injury–associated coagulopathy in mice," Blood **127**(22), 2763–2772 (2016).
25. L. Tay, R. G. Tremblay, J. Hulse, B. Zurakowski, M. Thompson, and M. Bani-Yaghoub, "Detection of acute brain injury by Raman spectral signature," The Analyst **136**(8), 1620 (2011).
26. A. Rygula, K. Majzner, K. M. Marzec, A. Kaczor, M. Pilarczyk, and M. Baranska, "Raman spectroscopy of proteins: a review," J. Raman Spectrosc. **44**(8), 1061–1076 (2013).

Supplemental Document

Biomedical Optics EXPRESS

Spectroscopic detection of traumatic brain injury severity and biochemistry from the retina: supplement

CARL BANBURY,[1] IAIN STYLES,[2] NEIL EISENSTEIN,[1] ELISA R. ZANIER,[3] GLORIA VEGLIANTE,[3] ANTONIO BELLI,[4] ANN LOGAN,[4] AND POLA GOLDBERG OPPENHEIMER[1,*]

[1]*School of Chemical Engineering, The University of Birmingham, Edgbaston, Birmingham, B15 2TT, UK*
[2]*Computer Science, The University of Birmingham, Edgbaston, Birmingham, B15 2TT, UK*
[3]*Department of Neuroscience, Istituto di Ricerche Farmacologiche Mario Negri IRCCS, Milan, Italy*
[4]*Institute of Inflammation and Ageing, The University of Birmingham, Edgbaston, Birmingham, B15 2TT, UK*
[*]*P.GoldbergOppenheimer@bham.ac.uk*
https://anmsa.com

Supplement DOI: https://doi.org/10.6084/m9.figshare.12991118

Parent Article DOI: https://doi.org/10.1364/BOE.399473

Supplementary Material

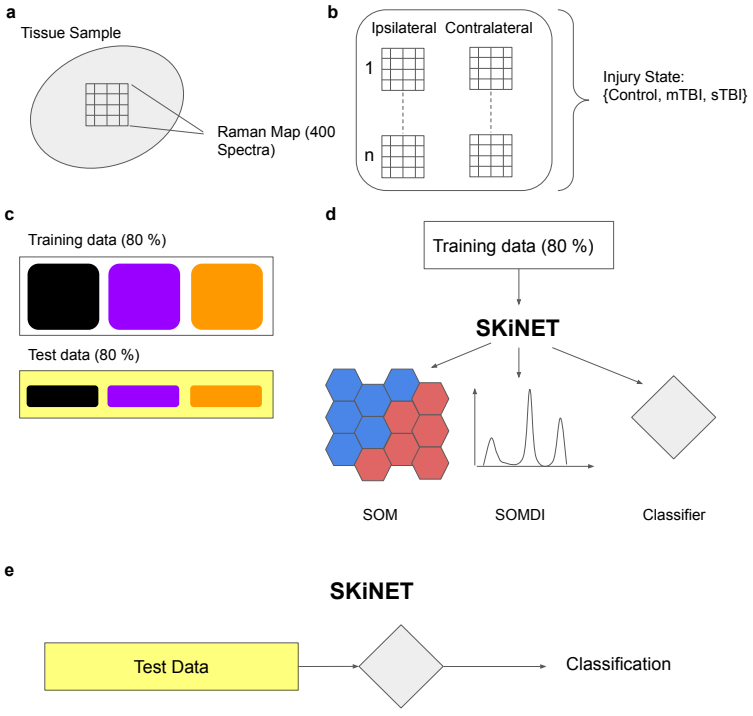

Fig. S1. Illustration of data analysis workflow for retina tissue using SKiNET. Spectra measured from Raman maps (**a**) of flat mounted retina (n=6) are grouped according to injury state (**b**). A 20 % partition of the data is randomly selected and reserved as test data (**c**). The remaining 80 % is input into SKiNET, which directly provides dimensionality reduction (SOM), feature extraction (SOMDI) and classification **d**. SKiNET is optimized on the training data using cross validation, and adjusting the available parameters (number of neurons, initial learning rate and number of training steps) to maximize the classification accuracy on the training data. Finally, the optimized model is shown the previously unused test data and asked to classifify each spectrum as either sham, mTBI or sTBI (**e**).

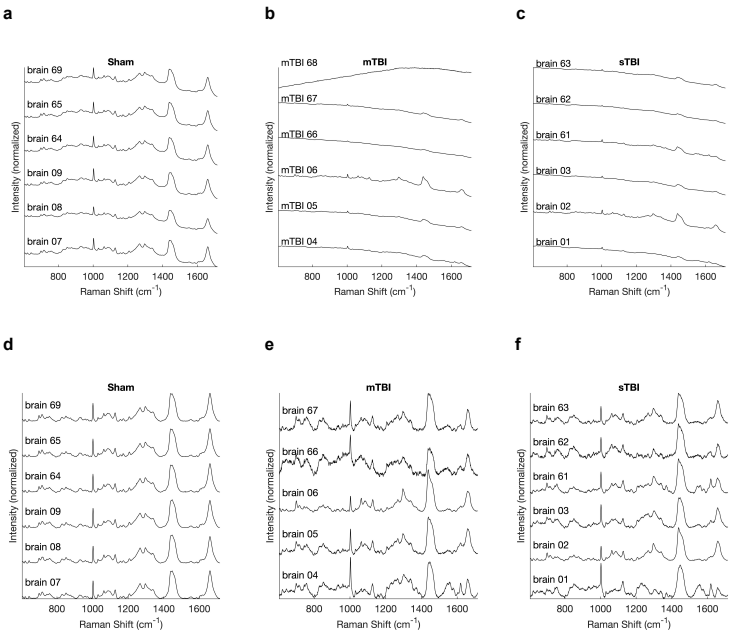

Fig. S2. Average Raman spectra collected from the injury site on left hemisphere of brain (n=6) for mTBI (**a**), sTBI (**b**), and sham (**c**) groups. Data for each tissue sample were collected as a Raman surface map (400 points) following the surface topography. **d-f**, Average Raman spectra for sham, mTBI and sTBI samples following baseline subtraction using an intelligent spline fit.

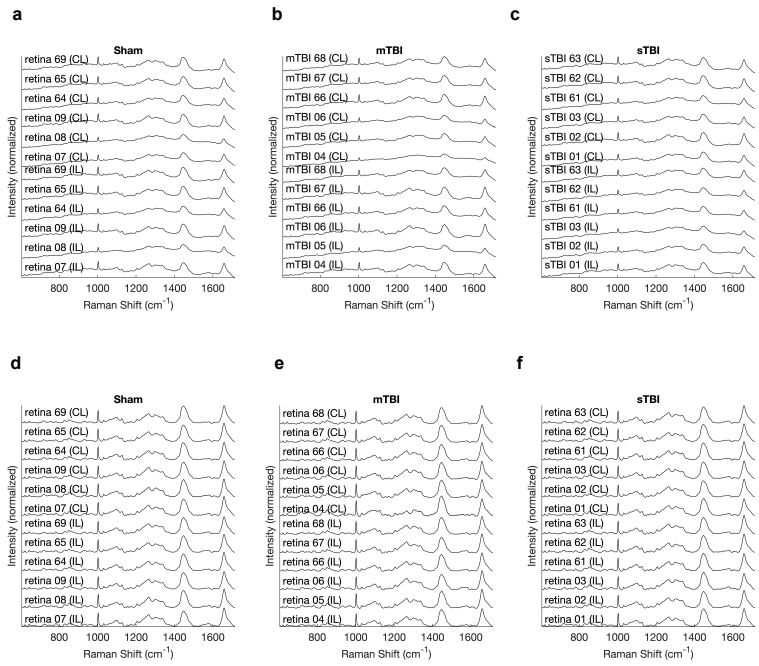

Fig. S3. Average Raman spectra collected from ipsilateral (IL) and contralateral (CL) flat mounted retina (n=6) for mTBI (**a**), sTBI (**b**), and sham (**c**) groups. Data for each tissue sample were collected as a Raman surface map (400 points) following the surface topography. **d-f**, Average Raman spectra for sham, mTBI and sTBI samples following baseline subtraction using an intelligent spline fit.

Model	Sham (%)	mTBI (%)	sTBI (%)
Bilateral	69.4 (± 0.9)	75.1 (± 0.9)	82.0 (± 1.4)
Ipsilateral	81.5 (± 0.8)	76.7 (± 1.9)	86.2 (± 1.4)
Contralateral	76.6 (± 1.6)	76.6 (± 1.2)	88.7 (± 0.9)

Table S1. Classification accuracy of TBI using Raman spectra of retina, modeled using data from both eyes (bilateral), eyes from the side of injury only (ipsilateral) and contralateral eyes. Results show the average over 10 SOM initializations and standard deviation in brackets.

		Predicted		
		Sham (%)	**mTBI (%)**	**sTBI (%)**
Actual	**Sham (%)**	**67.8**	24.9	7.3
	mTBI (%)	17.6	**76.1**	8.6
	sTBI (%)	8.8	13.6	**77.7**

Table S2. Summary of cross-validation accuracy as a confusion matrix for: sham, mTBI and sTBI from flat mounted mouse retina (both eyes) on 80 % partition of training data. Model trained using 400 neurons, with an initial learning rate of 0.2, and 57600 training steps.

Lipid	#07	#08	#09	#64	#65	#69	Average
Cardiolipin	0.74	0.71	0.72	0.73	0.71	0.72	0.72
Cholesteryl ester	0	0	0	0	0	0	0
Cholesterol	0.17	0.19	0.21	0.16	0.17	0.16	0.18
Cytochrome C	0	0	0	0	0	0	0
Galactocerebroside	0	0	0	0	0	0	0
Ganglioside	0	0	0	0	0	0	0
Sphyingomyelin	0.07	0.08	0.04	0.09	0.10	0.10	0.08
Phosphatidylcholine	0	0	0	0	0	0	0
Phosphatidylserine	0	0	0	0	0	0	0
Phosphatidylinositol	0	0	0	0	0	0	0
Phosphatidylethanolamine	0	0	0	0	0	0	0
Sulfatide	0	0	0	0	0	0	0
Triacylglyceride	0	0.01	0.01	0	0	0	0
R^2	0.88	0.89	0.87	0.86	0.86	0.86	0.87

Table S3. Decomposition of contribution from brain lipids (rows) in average Raman spectra of brain samples (columns) from contusion core for sham group using NNLS fitting. Each sample was fitted against the set of component spectra in the range 1200 - 1714 cm^{-1}.

Lipid	#04	#05	#06	#66	#67	Average
Cardiolipin	0.24	0.53	0.41	0.49	0.50	0.43
Cholesteryl ester	0	0	0	0	0	0
Cholesterol	0.17	0.16	0.20	0.08	0.19	0.16
Cytochrome C	0.35	0.10	0	0.25	0.02	0.14
Galactocerebroside	0.14	0	0	0.15	0	0.06
Ganglioside	0	0	0	0	0	0
Sphyingomyelin	0	0.16	0.39	0	0.14	0.14
Phosphatidylcholine	0.13	0	0.05	0	0.10	0.06
Phosphatidylserine	0.016	0	0	0	0	0
Phosphatidylinositol	0	0	0	0	0	0
Phosphatidylethanolamine	0	0	0	0	0	0
Sulfatide	0	0	0	0	0	0
Triacylglyceride	0	0.04	0	0	0.08	0.03
R^2	0.8	0.84	0.92	0.75	0.89	0.84

Table S4. Decomposition of contribution from brain lipids (rows) in average Raman spectra of brain samples (columns) from contusion core for mTBI group using NNLS fitting. Lipids that have non-zero fitting coefficients in the sham group are highlighted in bold. Each sample was fitted against the set of component spectra in the range 1200 - 1714 cm^{-1}.

Lipid	#01	#02	#03	#61	#62	#63	Average
Cardiolipin	0.17	0.51	0.57	0.19	0.02	0.63	0.35
Cholesteryl ester	0	0	0	0	0	0	0
Cholesterol	0.18	0.19	0.22	0.16	0.13	0.1	0.16
Cytochrome C	0.41	0	0.07	0.22	0	0	0.12
Galactocerebroside	0	0	0	0	0	0	0
Ganglioside	0	0	0	0	0	0	0
Sphyingomyelin	0	0.32	0.1	0.18	0.12	0.25	0.16
Phosphatidylcholine	0.02	0	0	0.22	0.57	0	0.13
Phosphatidylserine	0.01	0	0	0	0	0	0
Phosphatidylinositol	0	0	0	0	0	0	0
Phosphatidylethanolamine	0	0	0	0	0	0	0
Sulfatide	0	0	0	0	0	0	0
Triacylglyceride	0.27	0.03	0.03	0.04	0.29	0.06	0.12
R^2	0.62	0.90	0.86	0.84	0.77	0.84	0.81

Table S5. Decomposition of contribution from brain lipids in average Raman spectra of brain samples from contusion core for sTBI group using NNLS fitting. Lipids that have non-zero fitting coefficients in the sham group are highlighted in bold. Each sample was fitted against the set of component spectra in the range 1200 - 1714 cm^{-1}.

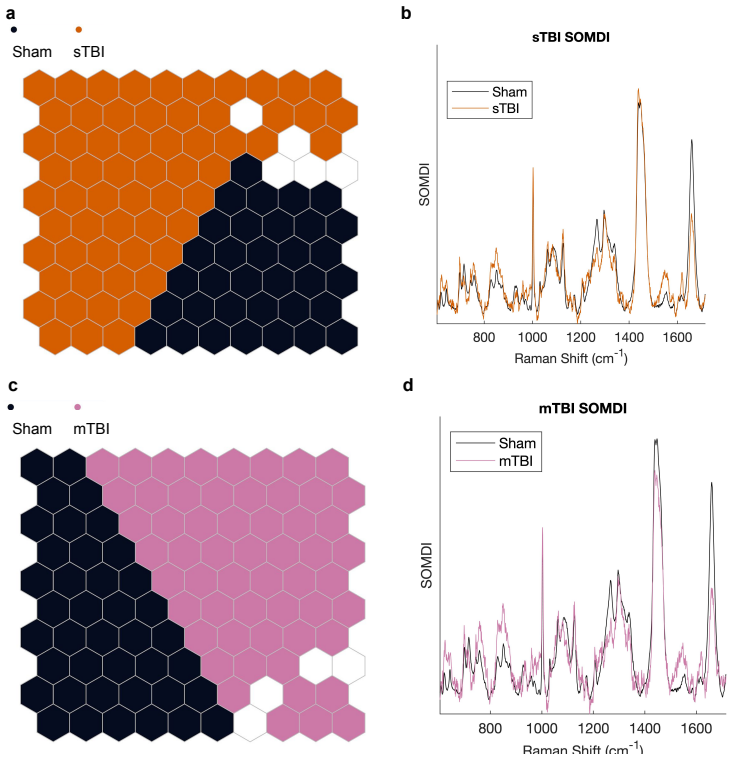

Fig. S4. **a**, Clustering of Raman spectra from the brain in the contusion core for sTBI (orange) and sham (black) groups using a SOM. **b**, Features extracted (SOMDI) from SOM shown in (**a**), highlighting the Raman bands most influential to neurons in the SOM for sham and sTBI groups. **c**, Clustering of mTBI (purple) and sham (black) Raman spectra from the brain in the contusion core using a SOM. **d**, Features extracted from SOM in **c**, highlighting Raman bands for sham and mTBI groups.

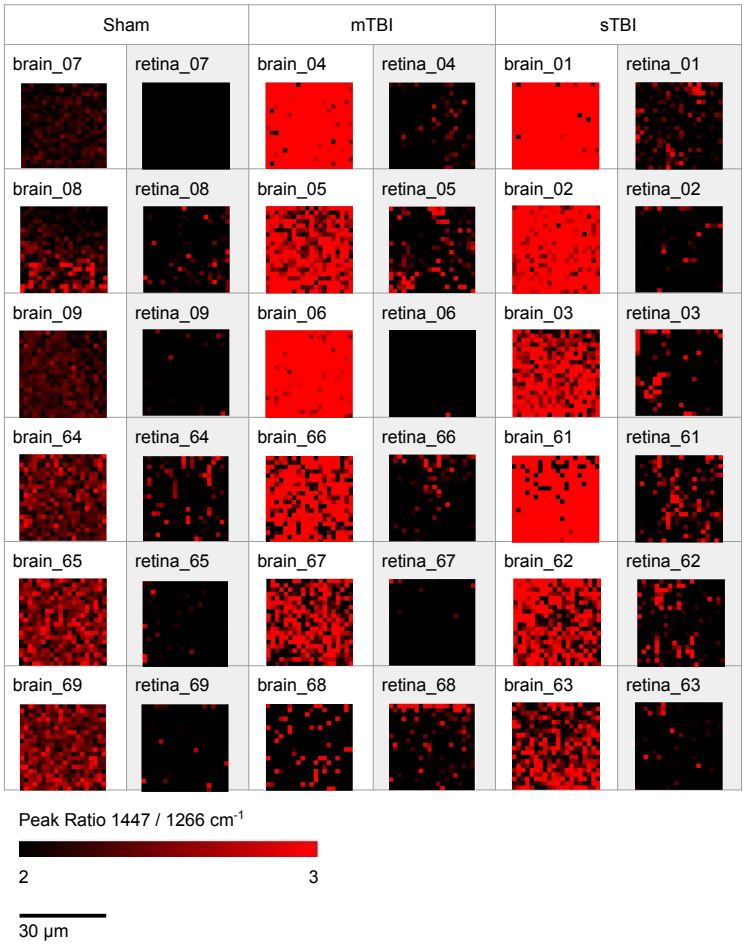

Fig. S5. False colored Raman maps for whole brain tissue from the contusion core, and for corresponding ipsilateral flat mounted retina samples. Maps are colored according to the ratio between the bands at 1447 and 1266 cm^{-1}.

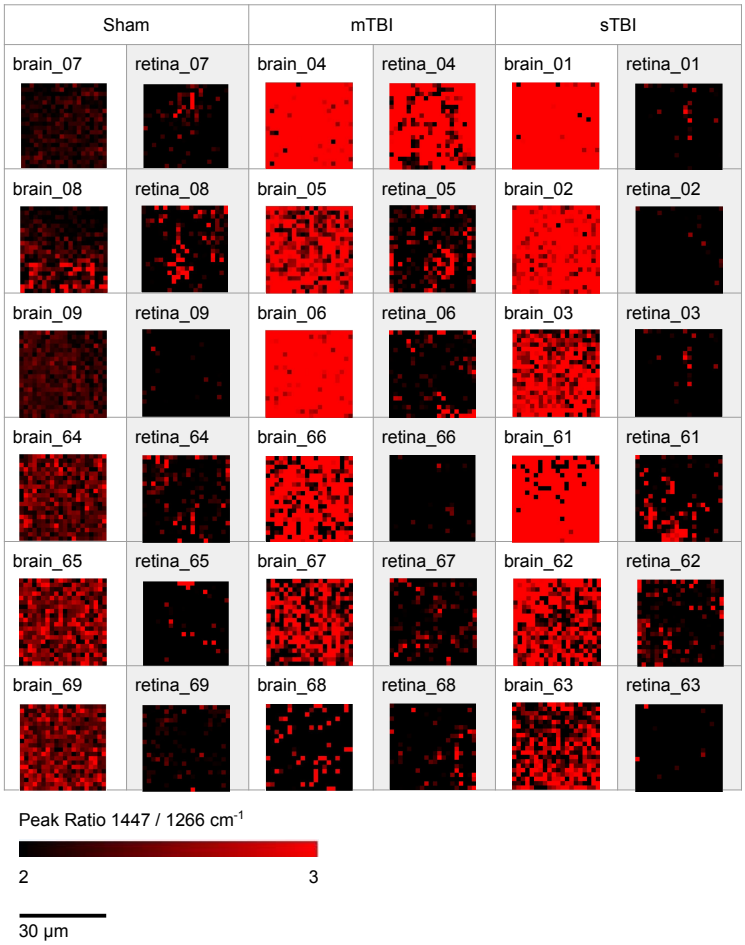

Fig. S6. False colored Raman maps for whole brain tissue from the contusion core, and for corresponding contralateral flat mounted retina samples. Maps are colored according to the ratio between the bands at 1447 and 1266 cm^{-1}.